Universidad de los Andes

Facultad de Ingeniería y Ciencias Aplicadas



FEASIBILITY STUDY AND DESIGN OF POLYHYDROXYBUTYRATE (PHB) FIBERS PRODUCED BY FERMENTATION FOR THE REINFORCEMENT OF CEMENTITIOUS COMPOSITES

Maximiliano Biasi Taiano

Thesis submited in partial fulfillment of the requirement for the degree of

Master of Science in Engineering

ADVISOR: Álvaro Paul Quiroz

CO-ADVISOR: Felipe Scott Contador

Santiago, August, 2026

I certify that I have read this thesis and that, in my opinion, its scope and quality are completely suitable to be considered a thesis leading to the Master of Science in Engineering Degree.

Álvaro Paul, Ph.D.

Felipe Scott, Ph.D.

César Huiliñir, Ph.D.

Paulo Díaz, Ph.D.

Franco Zunino, Ph.D.

A mi padre, quien cada día me sigue demostrando que rendirse no es una opción. Cuando uno hace una promesa, hay que luchar por cumplirla. Espero que, con esto, pueda finalmente cumplir la mía.

Abstract

Fiber reinforcement can improve the durability and service performance of cementitious composites, contributing to longer-lasting structures and potentially reducing their long-term environmental burden. However, many of the synthetic fibers currently used for this purpose are petroleum-derived, introducing additional environmental impacts associated with their manufacture and motivating the search for more sustainable alternatives. Polyhydroxybutyrate (PHB) is a bacterially produced and biodegradable polymer with potential to replace petroleum-derived materials across a wide range of applications. This thesis establishes an initial experimental basis for evaluating the use of PHB-based fibers as potential alternatives to conventional petroleum-derived reinforcement fibers in cementitious composites, encompassing bacterial production, polymer recovery, fiber processing, and characterization of the resulting materials. PHB was produced by fed-batch fermentation of *Cupriavidus necator*. Progressive refinement of the process resulted in reproducible production, with the final reactor runs reaching approximately 14-17 g L^{-1} of PHB. A chloroform-based extraction and subsequent purification procedure was developed, achieving high polymer recovery and a final PHB purity of approximately 98%. Direct extrusion of the locally produced polymer did not provide stable fiber formation because of processing and thermal stability limitations. Continuous PHB fibers were instead produced from a commercial thermoplastic-grade PHB to complete the fiber-level characterization. The obtained materials were evaluated through physicochemical, thermal, mechanical, aging, and alkaline degradation analyses. The extruded PHB fibers exhibited tensile strengths of approximately 34-42 MPa and strains at failure close to 0.7-0.8%, indicating that their untreated mechanical response is not yet sufficient for the intended reinforcing function. In contrast, their alkaline stability was favorable under the conditions evaluated, with mass losses remaining close to zero after up to 168 h of exposure at 20 °C and maximum mean mass losses of approximately 10% under accelerated exposure at 70 °C. Overall, the results support PHB as a technically plausible precursor for cementitious reinforcement while identifying fiber processing and mechanical performance as the principal remaining challenges. The production and extraction stages were established reliably, and the limitations identified for fiber development can be addressed through subsequent stabilization, drawing, and thermal post-processing. These findings provide a basis for developing PHB fibers toward more sustainable cementitious reinforcement.

Acknowledgements

Ya pasados seis años y medio, actualmente en esta etapa final de mi estancia en la Universidad de Los Andes, puedo decir feliz y orgullosamente que he tenido un periodo universitario exitoso cuanto menos.

Sin embargo, con esto no hago alusión simplemente a los resultados positivos obtenidos en lo académico; sino también a todo lo conseguido de manera externa a ello.

Los logros jamás son individuales, algo que he tenido en mente durante mucho tiempo y hoy más que nunca. Hoy me toca agradecer, quizás de manera más intensa a cualquier agradecimiento diario que uno pueda hacer.

Hoy le doy gracias, primero que nada, a la vida. Le doy gracias por las personas que me ha puesto en el camino, por las oportunidades que me ha entregado y por siempre haberme dado un motivo para seguir adelante, tal como mi padre lo ha hecho hasta hoy. En conjunto, han sido los elementos que me han entregado la fortaleza con la cual afronto el día a día, han sido el motor de lo cotidiano.

También debo agradecer a las desgracias, que por muy desagradables que fuesen, uno siempre puede sacar algo positivo de ellas. Me forzaron a crecer, a madurar y a comprender la importancia de muchas cosas, sobretodo del amor familiar.

De manera particular, quiero agradecer a diversas personas, que sin ellas, estos casi siete años hubiesen sido extremandamente distintos.

En primer lugar, agradecerle a mi padre, mi pilar de vida, mi motor, mi refugio y debilidad, a quien dedico no sólo este trabajo, sino toda la constancia presente en estos años. Hoy más que nunca te extraño y deseo con todo mi ser que fueses consciente del presente que vive tu hijo o tu "potro", como me dijiste mucho tiempo, y que pudiéramos compartir esta felicidad juntos. Espero, genuinamente espero, al menos poder llegar a ser la mitad de padre y persona que fuiste, pero para ello sé que tengo un largo camino que recorrer y costumbres que cambiar. Que no quepan dudas de que hasta el último día de mi vida lo voy a intentar.

A mi madre, que por muchas rabietas que me haga pasar, sigue siendo aquello, mi madre, razón por la cual sigo luchando día a día por nosotros, a veces con éxito, otras no tanto. Agradezco tu presencia, tu preocupación y tu cuidado del día a día. Agradezco tu cuidado de nuestro techo y las infinitas cenas que me tuviste listas en esos

días eternos. Agradezco tu amor y cuidado por nuestros peludos, quienes corresponden a un pilar de nuestro hogar.

A mis tíos y primos, Liliana, Juan Carlos, Daniela y Pablo, que se encargaron del cuidado de mi padre todos estos años y que, indirectamente, me permitieron continuar con la construcción y el desarrollo de mi vida. No hay palabras que describan lo agradecido que me siento de tener semejante familia y no me alcanzará esta vida ni la próxima para terminar de retribuir lo entregado.

A Alfonso, mi segundo padre, y a Álvaro y Renato, mis hermanos, por darme una familia cuando más lo necesitaba. Agradecerles por tanto cariño, preocupación y ánimos. Gracias por tantas enseñanazas, por transmitirme valores y por tantas risas y asados. Durante estos últimos tres años, parte de la energía semanal fue pensar que el viernes nos juntábamos a compartir.

Como dije en un inicio, la vida puso a ciertas personas en mi camino durante mi etapa universitaria, que de una forma u otra, forjaron mi presente. Quiero empezar agradeciendóle a Álvaro, quien ha sido un excelente profesor guía y sin dudas aún mejor amigo. Agradecerle por creer en mí y en mis capacidades desde el día uno, por apoyarme incondicionalmente dentro de sus posibilidades y por ser mi mentor en todo ese proceso. Las palabras nuevamente no alcanzan para agradecer todas las oportunidades entregadas y para la consideración tenida conmigo en estos últimos años.

Asimismo, agradecer al equipo que integró esta investigación. A Felipe, por aportarnos a Coni y a mí todo su ingenio cuando no encontrábamos respuestas. A Coni y Max, por todo su apoyo. Esta Tesis es tanto mía como lo es de ustedes. No podría haber pedido mejores acompañantes en este tramo final de carrera.

La universidad también me entregó otro tipo de familia, los amigos. En especial, mencionar a Mutis, Samuel, Claudio y Pipe, a quienes les tengo un cariño particular. Agradezco muchísimo la capacidad de escuchar y la constante preocupación de Mutis, la presencia de Saig, la habilidad de Claudio para siempre ser el meme y la creatividad de Pipe. De una forma u otra, hicieron este periodo más ameno y sin dudas, con muchas risas entremedio.

A Pipe debo agradecerle de manera especial. Posterior al ingreso a la especialidad fue mi partner 1, 2 y 3. Creo fielmente que parte del éxito académico no hubiese sido posible sin él, de ahí que los logros jamás han sido individuales. Trabajando juntos nos

potenciábamos. Lo dije muchas veces, lo único peor que una persona con toc, son 2 personas con toc. Al trabajar de manera separada, de igual manera teníamos un efecto de llevar al otro un poco más allá.

También agradecer a Vito, Elisa y Chopi. Mi cariño por ustedes, quizás poco transmitido, es inmenso. Junto a Pipe, fueron un pilar fundamental durante la especialidad, tanto en el apoyo académico como en el emocional.

Con respecto al resto, podría escribir páginas y páginas sobre ellos. Agradezco a la Catita, por darme uno de los cariños más sinceros que he podido disfrutar, a Gonza por su locura, a Pezzani por sus pilas, que nunca se agotan, a Pelao y sus Pelao cosas, a Arvo y sus cateteos de 2 lucas. A los que se me olviden, les pido que no se ofendan. Estoy muy agradecido de lo compartido con cada uno de ustedes.

A mis amigos del colegio, agradecerles por tanta anécdota, por tantas tallas, stickers, fotos y videos. Agradecerles por nuestra reciente reconexión, que muchas alegrías me han traído y que seguirán trayendo. Agradecer especialmente a Diego y Alonso, mis hermanos de otra madre, y a Damián, que a pesar de la distancia, de alguna forma siempre intentamos mantener la cercanía. Sepan que los quiero con toda mi alma.

A Domi, agradecerle por constantemente tirarme para adelante, por siempre hacer que me creyera el cuento. A Claudia, que todas las semanas se preocupó de mandar un mensajito. A Belén por siempre estar y transmitirme optimismo.

Para cerrar, agradecer a todas las personas que pusieron su granito de arena en esta investigación, ya sea de manera directa o indirecta. Agradecer a los laboratorios del Centro de Investigación e Innovación Biomédica (CiiB) de la Universidad de Los Andes y a los del Departamento de Ingeniería y Gestión de la Construcción, y Química y Farmacia de la PUC por su guía y ayuda en la realización de diversos análisis. A Héctor, por su siempre buena disposición a ayudarnos en el UandesLab. A Luz y Dana, por tenerme paciencia y por enseñarme elementos y técnicas que en su área pueden haber sido básicos, pero que por mi formación eran desconocidos y, por último, a Natalia, quien por amor al arte, me soportó varios sábados quejándome en el laboratorio.

Gracias a todos.

Contents

Abstract v
Acknowledgements vi
Nomenclature xix

1 Introduction **1**
1.1 Hypothesis 6
1.2 Objectives 6
1.2.1 General objective 6
1.2.2 Specific objectives 6
1.3 Thesis Structure 7
1.3.1 Scope 7

2 Novel Fibers in Cementitious Composites **8**

3 Methodology **17**
3.1 Materials 17
3.1.1 Fermentation chemicals 18
3.1.2 Bacterial strain 18
3.2 PHB Production 18
3.2.1 Growth media 18
3.2.1.1 Nutrient agar 18
3.2.1.2 Mineral medium 19
3.2.1.3 Culture medium for bioreactor production 20
3.2.2 Bacterial kinetics 21
3.2.2.1 Growth monitoring 21
3.2.2.2 Quantification of fructose 22
3.2.2.3 Quantification of PHB 24
3.2.2.4 Quantification of ammonium 26

3.2.3 Fermentation process . . . 27
3.2.4 Extraction method . . . 29
3.3 Extrusion process . . . 32
3.4 PHB characterization . . . 34
3.4.1 Physicochemical properties of the PHB . . . 34
3.4.1.1 Density . . . 34
3.4.1.2 Molecular weight . . . 35
3.4.1.3 Purity . . . 36
3.4.1.4 Thermal Properties (T_g, T_m, T_d and X_c) . . . 36
3.4.2 Mechanical properties of the PHB (σ_u, E and ε) . . . 38
3.4.3 Degradation of PHB . . . 40
3.4.3.1 Thermal degradation . . . 40
3.4.3.2 Degradation by alkalis . . . 40
3.5 Aging . . . 44

4 Production of PHB Films and Fibers 47
4.1 Bacterial kinetics . . . 47
4.2 Fed-batch Fermentations . . . 50
4.3 Extraction yield . . . 52
4.4 Extrusion process . . . 54

5 Evaluation of PHB Films and Fibers 64
5.1 Physicochemical properties of the PHB . . . 64
5.1.1 Density . . . 64
5.1.2 Molecular weight . . . 66
5.1.3 Purity . . . 67
5.1.4 Porosity and surface area . . . 69
5.1.5 Thermal properties . . . 82
5.2 Mechanical properties . . . 106
5.3 Degradation of PHB . . . 112
5.3.1 Thermal degradation . . . 112
5.3.2 Degradation by alkalis . . . 113
5.3.3 FTIR analysis . . . 124

6 Discussion and Future Perspectives 130
6.1 Mechanical feasibility of PHB fibers for cementitious reinforcement . . . 130
6.2 Aging and stabilization of the mechanical response . . . 133

6.3 Alkaline stability and implications for cementitious use 134
6.4 Environmental implications of PHB production 135
6.5 Research outlook 137

7 Conclusions **139**

References **143**

A Fermentation Details **161**
A.1 *A. lata trace* 161
A.2 Mineral Medium 162
A.3 Culture Medium 162

B PHB Characterization **164**
B.1 Density Calculation 164
B.2 Water Density 165
B.3 Molecular-Weight Calculations 166
B.4 Compute of the Mobile and Rigid Amorphous Fractions from DSC . . . 167
B.5 Calculation procedure 168

C Detailed Results of the Fed-Batch Fermentation Campaign **169**

D DSC Mean Thermograms **175**
D.1 Differential Scanning Calorimetry 175

List of Figures

2.1 Embodied energy of concrete 10
2.2 Comparison between the embodied energy of concrete and fibers used in cementitious composites. 11

3.1 Spectrophotometer 22
3.2 High performance liquid chromatograph 23
3.3 Centrifuges 23
3.4 Gas chromatograph 26
3.5 Minifors 2 Bioreactor 28
3.6 Main stages of the PHB extraction and recovery procedure. 31
3.7 Wellzoom B2 REX-C100 Extruder 32
3.8 Custom-made 0.5 mm extruder nozzle used in fiber production. 33
3.9 Equipment used for the thermal characterization of PHB samples. . . . 36
3.10 DSC thermal protocol used for the two-heating-cycle analysis. 37
3.11 UTM and load-cell configuration used for the single-fiber tensile tests. . 39
3.12 Nova-600, Anton Paar 43
3.13 IR Prestige 21, Shimadzu 45

4.1 Temporal profiles of biomass concentration, fructose consumption, and intracellular PHB accumulation obtained from triplicate kinetic experiments. 47
4.2 OD profiles obtained during the fed-batch fermentation campaign. . . . 51
4.3 PHB recovery yields obtained during the preliminary chloroform extraction trials and after implementation of the final methodology. 52
4.4 PHB films obtained after chloroform extraction and solvent evaporation. 53
4.5 Comparison between the original commercial PHB/PLA filament and the thinner fiber obtained after re-extrusion. 55
4.6 Material accumulation at the nozzle outlet during extrusion. 56

4.7 Fiber collection behavior observed during extrusion trials with commercial materials. 57
4.8 Fiber agglomeration observed in the collection zone when no water bath was used. 58
4.9 Visual evolution of the locally produced PHB during extrusion trials, showing fibers, degraded material, partially degraded material, recovered non-melted material, and clean PHB film before extrusion. 60
4.10 Continuous PHB fiber obtained by extrusion of the commercial Enmat Y3000P PHB pellet. 63

5.1 N_2 adsorption-desorption isotherm obtained for the PHAC fiber at 77 K. 70
5.2 Low-pressure region of the N_2 adsorption isotherm used for BET analysis of the PHAC fiber. 70
5.3 DFT pore size distribution and cumulative pore volume obtained for the PHAC fiber. 71
5.4 N_2 adsorption-desorption isotherm obtained for the locally produced PHB recovered as native film at 77 K. 73
5.5 Low-pressure region of the N_2 adsorption isotherm used for BET analysis of the locally produced PHB recovered as native film. 74
5.6 DFT pore size distribution and cumulative pore volume obtained for the locally produced PHB recovered as native film. 74
5.7 N_2 adsorption-desorption isotherm obtained for the purified PHB at 77 K. 76
5.8 Low-pressure region of the N_2 adsorption isotherm used for BET analysis of the purified PHB. 77
5.9 DFT pore size distribution and cumulative pore volume obtained for the purified PHB. 77
5.10 Sponge-like morphology observed for the purified PHB obtained by ethanol-assisted precipitation. 79
5.11 N_2 adsorption-desorption isotherm obtained for the PHB fiber at 77 K. 80
5.12 Low-pressure region of the N_2 adsorption isotherm used for BET analysis of the PHB fiber. 80
5.13 DFT pore size distribution and cumulative pore volume obtained for the PHB fiber. 81
5.14 Average DSC thermograms of the PHAC fiber at different aging times. 83
5.15 Phase-fraction evolution, PHAC fiber 87
5.16 TGA, PHAC Fiber 89
5.17 Extended TGA profile of the PHAC fiber up to 1000 °C. 90

5.18 Average DSC thermograms of the locally produced PHB recovered as native film at different aging times. 91
5.19 Average DSC thermogram of the locally produced PHB recovered as native film during the first heating cycle. 92
5.20 Average TGA curves of the locally produced PHB recovered as native film for the evaluated aging times. 94
5.21 TGA triplicates of the recovered PHB film after aging. 95
5.22 TGA curve of the purified PHB obtained after ethanol-assisted purification. 97
5.23 DSC thermograms of the commercial PHB pellet during the first and second heating cycles. 98
5.24 Average DSC thermograms of the PHB fiber at different aging times. . 100
5.25 DSC thermograms obtained from three consecutive heating cycles of the PHB fiber using an upper temperature of 250 °C. 102
5.26 DSC thermograms obtained from three consecutive heating cycles of the PHB fiber using an upper temperature of 220 °C. 102
5.27 TGA curves of PHB fiber specimens previously subjected to two DSC heating cycles with upper temperatures of 220 and 250 °C. 103
5.28 Average TGA curves of the PHB fiber at Day 0 and after 7 and 28 days of aging. 105
5.29 Average stress-strain curves of PHAC fiber specimens as a function of aging time, including the linear fits used to estimate the apparent elastic modulus. 106
5.30 Average stress-strain curves of PHB fiber specimens including the linear fits used to estimate the apparent elastic modulus. 109
5.31 Representative failure modes observed during single-fiber tensile testing of PHAC and PHB fibers. 110
5.32 Chemical structure of PHB. 113
5.33 Mass loss of the PHAC fiber after alkaline exposure at 70°C. 114
5.34 Mass loss of the PHAC fiber after alkaline exposure at 20°C. 116
5.35 Mass loss of the locally produced PHB recovered as native film after alkaline exposure at 70°C. 117
5.36 Mass loss of the locally produced PHB recovered as native film after alkaline exposure at 20°C. 119
5.37 Mass loss of the PHB fiber after alkaline exposure at 70°C. 120
5.38 Mass loss of the PHB fiber after alkaline exposure at 20°C. 123

5.39 FTIR spectrum of the locally produced PHB recovered as native film from reactor run R1, showing the principal PHB absorption regions. . . 124
5.40 FTIR spectra of the locally produced PHB recovered as native film at different aging times. 126
5.41 Comparison of the specimens obtained during preparation of PHB materials for transmission FTIR analysis. 127
5.42 Preparation of finely cut PHB fiber for diffuse-reflectance FTIR analysis. 128
5.43 FTIR spectra obtained for the PHB fiber at different aging times. . . . 129

D.1 Individual average DSC thermograms of the PHAC fiber at different aging times. 175
D.2 Individual average DSC thermograms of the locally produced PHB recovered as native film at different aging times. 178
D.3 Individual DSC thermograms of the commercial PHB pellet during the first and second heating cycles. 180
D.4 Individual average DSC thermograms of the PHB fiber at different aging times. 181

List of Tables

3.1 Experimental test matrix. 46

4.1 Summary of biomass yields, PHB accumulation, and specific growth rate obtained from triplicate kinetic experiments. 48
4.2 Performance of the PHB-producing reactors. 52
4.3 Extrusion temperatures selected for each commercial fiber material. . . 54

5.1 Density measurements obtained for the PHAC fiber. 65
5.2 Density measurement obtained for the PHB fiber. 65
5.3 PHB purity measured for the PHAC fiber. 67
5.4 Purity of recovered PHB samples. 68
5.5 PHB purity measured for the commercial PHB pellet. 69
5.6 PHB purity measured for the PHB fiber. 69
5.7 Porosity parameters obtained from N_2 physisorption analysis of the PHAC fiber. 71
5.8 Porosity parameters obtained from N_2 physisorption analysis of the locally produced PHB recovered as native film. 75
5.9 Porosity parameters obtained from N_2 physisorption of the purified PHB. 78
5.10 Porosity parameters obtained from N_2 physisorption analysis of the PHB fiber. 81
5.11 Summary of transition temperatures and crystallinity obtained from DSC for the PHAC fiber evaluated as a function of aging. Values are reported as $\bar{X} \pm \sigma$. 83
5.12 Apparent mobile and rigid amorphous fractions calculated for the PHAC fiber under the PHB-reference assumption. Values correspond to $\bar{X} \pm \sigma$. 87
5.13 Summary of mean transition temperatures obtained from DSC for the locally produced PHB recovered as native film. 91

5.14 Summary of transition temperatures obtained from DSC for the commercial PHB pellet. 98
5.15 Summary of mean transition temperatures and crystallinity obtained from DSC for the PHB fiber. 100
5.16 Summary of tensile properties obtained from single-fiber tensile tests of the PHAC fiber. 106
5.17 Summary of tensile properties obtained from single-fiber tensile tests of the PHB fiber. 109
5.18 Summary of degradation temperatures obtained from TGA for the different PHB-based materials evaluated as a function of aging. Values are reported as $\bar{X} \pm \sigma$. 113
5.19 Summary of mass loss obtained for the PHAC fiber after alkaline exposure at 70°C. 114
5.20 Summary of mass loss obtained for the PHAC fiber after alkaline exposure at 20°C. 116
5.21 Summary of mass loss obtained for the locally produced PHB recovered as native film after alkaline exposure at 70°C. 118
5.22 Summary of mass loss obtained for the locally produced PHB recovered as native film after alkaline exposure at 20°C. 119
5.23 Summary of mass loss obtained for the PHB fiber after alkaline exposure at 70°C. 121
5.24 Summary of mass loss obtained for the PHB fiber after alkaline exposure at 20°C. 123

A.1 Composition of the *A. lata* trace element solution used in this work . . 161
A.2 Mineral medium used in all fermentation iterations. 162
A.3 Initial reactor medium. 162
A.4 Final reactor medium. 163

B.1 Standard density of water in the range of 21-25 °C, according to ASTM D792 166

C.1 Summary of reactor runs R1-R4 performed during the fed-batch fermentation campaign for PHB production with *Cupriavidus necator* H16. . . 170
C.2 Summary of reactor runs R5-R6 performed during the fed-batch fermentation campaign for PHB production with *Cupriavidus necator* H16. . . 171

C.3 Summary of reactor runs R7-R8 performed during the fed-batch fermentation campaign for PHB production with *Cupriavidus necator* H16. . . 172
C.4 Summary of reactor runs R9-R10 performed during the fed-batch fermentation campaign for PHB production with *Cupriavidus necator* H16. 173
C.5 Summary of reactor runs R11-R13 performed during the fed-batch fermentation campaign for PHB production with *Cupriavidus necator* H16. 174

Nomenclature

BET: Brunauer-Emmett-Teller

ECC: Engineered cementitious composites

DCE: Dichloroethane

DEF: Delayed ettringite formation

DFT: Density Functional Theory

DMC: Dimethyl carbonate

DSC: Differential scanning calorimetry

DTG: Differential thermogravimetry

FID: Flame ionization detector

FRC: Fiber reinforced concrete

FTIR: Fourier transform infrared spectroscopy

GC: Gas chromatography

GPC: Gel Permeation Chromatography

k_La: Volumetric mass transfer coefficient

HPLC: High performance liquid chromatography

MAF: Mobile amorphous fraction

M_n: Average molecular weight

M_w: Molecular weight

PBS: Polybutylene succinate

PDI: Polydispersity index

PE: Polyethylene

PHA: Polyhydroxyalkanoates

PHAC: Commercial Polyhydroxyalkanoates Fiber

PHB: Polyhydroxybutyrate

PHBV: Poly(hydroxybutyrate-co-hydroxyvalerate)

PLA: Polylactic acid

PP: Polypropylene

PVA: Polyvinyl alcohol

RAF: Rigid amorphous fraction

RID: Refractive index detector

SEM: Scanning Electron Microscope

SFTT: Single fiber tensile test

T_d: Thermal degradation onset

T_g: Glass transition temperature

TGA: Thermogravimetric analysis

T_m: Melting temperature

UHPC: Ultra high performance concrete

UTM: Universal testing machine

WCA: Water contact angle

XRD: X-ray diffraction

Chapter 1

Introduction

Currently, humanity faces a major challenge regarding environmental preservation. Among the contributors to anthropogenic pollution and resource depletion, the construction industry plays a particularly relevant role. The buildings and construction sector accounts for approximately 34% of global CO_2 emissions, including emissions associated with both building operation and the production of construction materials (United Nations Environment Programme & Global Alliance for Buildings and Construction, 2025). Within this contribution, cement and concrete, together with other major construction materials, represent a significant fraction of the sector's embodied emissions. This is consistent with other reports indicating that cement production alone is responsible for approximately 8-9% of global CO_2 emissions (Monteiro et al., 2017), which corresponds to roughly one quarter of the total emissions attributed to buildings and construction.

This challenge can be addressed from multiple perspectives, including improvements in construction technologies, transportation logistics, waste management, recycling practices, project planning, and material design (Ozturk & Ozyurt, 2022). In this broader context, waste generation and end-of-life management are also relevant aspects, since the construction sector generates between 2 and 3 billion tons of construction waste annually worldwide (Kumar Singh et al., 2023). Therefore, reducing the environmental burden of construction requires strategies that address not only emissions during

production, but also material efficiency, durability, and the fate of materials after their service life.

For the purposes of this research, the focus is placed on the development of new material technologies for the reinforcement of cement-based systems, which represents one of the main routes for reducing the environmental impact of construction while maintaining or improving structural performance. In this context, and considering the complexity of the concept, the sustainability of a building material can be represented in a simplified form through Equation **1.1** (Müller et al., 2014):

$$\text{Sustainability} = \frac{\text{Performance} \cdot \text{Lifetime}}{\text{Environmental Impact}} \tag{1.1}$$

According to this framework, the sustainability of cement-based materials can be improved through three complementary strategies: increasing performance, extending service life, and reducing environmental impact. From a materials perspective, significant efforts have therefore been devoted to reducing the cement content of concrete through the incorporation of supplementary cementitious materials (SCMs), while also developing new cement-based technologies with improved mechanical performance, durability, and resource efficiency. These developments include ultra-high-performance concrete (UHPC) (Bajaber & Hakeem, 2021; Randl et al., 2014; Du et al., 2021), geopolymers (Almutairi et al., 2021; Singh et al., 2015; Wong, 2022), 3D-printed concrete (Siddika et al., 2020; Zhang et al., 2019), fiber-reinforced concrete (FRC) (Brandt, 2008), and engineered cementitious composites (ECC) (Li, 2011; Li, 2003; Leon-Miquel et al., 2023). In different ways, these materials aim to increase structural performance, extend service life, reduce maintenance requirements, reduce waste, and ultimately decrease the environmental burden associated with construction.

In this context, FRC and ECC are relevant examples of cement-based composites in which discrete fibers are incorporated into the matrix to improve mechanical performance and extend service life (Shoji et al., 2022). These fibers enhance crack control, post-cracking behavior, toughness, and energy dissipation capacity. In addition, by limiting crack widths and reducing permeability, fiber-reinforced cement-based composites

can restrict the ingress of aggressive agents such as chlorides and sulfates, which are responsible for reinforcement corrosion and deterioration of the cementitious matrix cita?.

However, the environmental footprint associated with the production of fiber-reinforced cementitious materials is usually higher than that of conventional concrete. In the case of ECC, the enhanced mechanical response is commonly achieved through high cement contents and petroleum-derived fibers, both of which can increase the environmental impact of the composite. As shown in the material sustainability indicators summarized by Shoji et al. (2022), typical ECC mixtures can exhibit embodied energy, CO_2 emissions, and solid waste generation values substantially higher than those of conventional concrete, in some cases exhibiting a 100% increase depending on the indicator and reference mixture considered. In addition, Hu et al. (2023) reported embodied energy values of 73-116 GJ t^{-1} and CO_2 emissions of 2000 kg t^{-1} for conventional PE fibers used in FRC and ECC production, highlighting the environmental burden associated with petroleum-derived synthetic fibers.

In FRC, the incorporation of fibers also introduces an additional material component with its own environmental burden. However, this impact is generally lower than in ECC because conventional FRC typically uses smaller fiber volumes, whereas ECC requires a higher fiber content to achieve its characteristic strain-hardening and multiple-cracking behavior. For instance, Ghali et al. (2023) reported that the addition of different fiber types in FRC beams increased the environmental impact by approximately 4-9% and costs from 34% and 150%, depending on the fiber considered. Therefore, although fibers can improve crack control, toughness, durability, and service life, their own environmental contribution must also be considered when evaluating the sustainability of fiber-reinforced cementitious materials.

Considering cement content and fiber incorporation as the two main material-related contributors to the environmental footprint of fiber-reinforced cementitious composites, the reduction of cement content has received substantially greater attention. The use of SCMs as partial replacements for Portland cement has been widely studied as an effective strategy to reduce the environmental impact of the cementitious matrix (Zhu et al.,

2012; Şahmaran & Li, 2009; Leon-Miquel et al., 2023). In contrast, the replacement of petroleum-derived fibers has been comparatively less explored, despite the critical role that fibers play in the post-cracking response, toughness, crack-width control, and durability of FRC and ECC systems. This imbalance highlights a relevant research gap in the development of more sustainable fiber-reinforced cementitious composites.

Some studies have addressed this gap by exploring the replacement of synthetic fibers with natural plant-derived alternatives such as flax, hemp (Radhakrishnan et al., 2024), kenaf, pineapple (Chellapandian et al., 2024), and curauá (Soltan et al., 2017), among others; cf. Mukhopadhyay & Khatana (2015). These fibers may offer environmental advantages due to their renewable origin and, in some cases, improved degradation behavior after disposal. However, their use also presents important challenges. Natural fibers can exhibit significant variability in geometry, composition, and mechanical properties depending on origin, cultivation conditions, harvesting, and processing cita?. In addition, their hydrophilic nature may increase water absorption, affect fiber-matrix interaction, and reduce dimensional stability. Their long-term performance in highly alkaline cementitious environments may also be limited by the susceptibility of lignocellulosic components to alkaline degradation cita?. For instance, Xiao et al. (2001) showed that treatment of maize stems, rye straw, and rice straw with 1 M NaOH at 30 °C for 18 h dissolved substantial fractions of lignin and hemicelluloses, indicating that these components can be chemically affected under alkaline conditions. Furthermore, large-scale production of plant-based fibers may require land, water, and agricultural resources, which can limit their sustainability benefits when considered at industrial scale cita?.

For this reason, the search for alternative reinforcement fibers should not only focus on avoiding petroleum-based feedstocks, but also on ensuring scalable production, consistent properties, adequate durability, and suitable mechanical performance. In this context, bacteria-produced polymers, particularly polyhydroxyalkanoates (PHAs), represent a promising route. PHAs are intracellular polyesters accumulated by microorganisms as carbon and energy storage materials and can be produced through fermentation using renewable carbon sources. Although the broader replacement of conventional petroleum-derived polymers by PHAs is still limited by their relatively high production

cost, this limitation is closely linked to substrate selection, fermentation efficiency, and downstream processing, making it a challenge that can be addressed through process optimization (Zhang et al., 2022).

One of the major advantages of PHA production is its compatibility with alternative carbon sources and residual streams, which can contribute both to cost reduction and to circular economy strategies. Several organic residues, industrial by-products, and gaseous carbon streams can potentially be used as substrates for microbial growth and polymer accumulation. These include, among others, agricultural residues, molasses, whey, glycerol from biodiesel production, waste oils, food-processing residues, wastewater-derived substrates, methane, and biogas-derived streams (Wang et al., 2021; Fu et al., 2023; Patel et al., 2024; Thanahiranya et al., 2025). Therefore, PHA production may benefit from the valorization of residual streams generated by different industrial sectors, opening the possibility of producing reinforcement materials from waste-derived or renewable carbon resources rather than fossil feedstocks.

Among PHAs, poly(3-hydroxybutyrate) (PHB) is one of the most widely studied bacterial polyesters due to its biodegradability, thermoplastic behavior, and potential for processability into films, filaments, and fibers. Compared with plant-derived fibers, bacteria-produced PHB-based fibers may offer greater control over material composition and production conditions, while avoiding direct dependence on agricultural cultivation. At the same time, compared with petroleum-derived synthetic fibers, PHB-based fibers may reduce reliance on fossil resources and provide an alternative end-of-life profile. Nevertheless, following a comprehensive review of the state of art, no published experimental studies have yet demonstrated the use of PHB-based fibers as reinforcement in cementitious composites for construction applications. This knowledge gap motivates the investigation of their potential for this purpose.

Since no commercial sources of pure PHB fibers were identified for this study, the work begins with local PHB production through bacterial fermentation as a starting point for investigating their potential use as reinforcement in cementitious composites. The study also addresses polymer extraction, processing, physicochemical characterization, mechanical evaluation, and alkaline degradation. These evaluations constitute a prelim-

inary stage toward future incorporation into cementitious matrices. By identifying the capabilities and limitations of the materials obtained, this research seeks to establish a basis for the development of bacteria-produced fibers that could eventually serve as alternatives to petroleum-derived reinforcement fibers in construction.

1.1 Hypothesis

The hypothesis addressed by this thesis is the following:

- H: Bacterial PHB based fibers can replace petroleum-based fibers in their functional role as reinforcement within cementitious composites.

1.2 Objectives

1.2.1 General objective

Assess the physicochemical stability and mechanical performance of PHB fibers, and determine their suitability as reinforcement in cementitious composites

1.2.2 Specific objectives

a) Develop a robust fermentation process for the synthesis of PHB.

b) Establish a reliable extraction process to recover PHB from the produced biomass.

c) Develop an extrusion process for the fabrication of PHB-based microfibers.

d) Evaluate the physicochemical properties, degradation behavior, and stability of the obtained materials in different formats and over time, considering the effect of aging under testing conditions representative of realistic exposure scenarios.

e) Evaluate the mechanical properties and fiber durability of the obtained materials over time, considering the effect of aging.

1.3 Thesis Structure

This thesis is organized into seven distinct chapters, each contributing uniquely to the overarching research endeavor:

a) Chapter 1: Introduction

b) Chapter 2: Novel Fiber in Cementitious Composites

c) Chapter 3: Methodology

d) Chapter 4: Production of PHB Films and Fibers

e) Chapter 5: Evaluation of PHB Films and Fibers

f) Chapter 6: Discussion and Future Perspectives

g) Chapter 7: Conclusions

1.3.1 Scope

This research focuses on the feasibility, production, processing, and evaluation of PHB-based fibers produced by bacterial fermentation for their potential application as reinforcement in fiber-reinforced cementitious composites. The scope includes the development and optimization of the production route, encompassing bacterial PHB synthesis, polymer extraction and fiber processing.

Both the laboratory-produced polymer and, where required, a commercial PHB reference are characterized in different formats, including native films and fibers. Their mechanical, thermal, physicochemical, degradation, and aging behavior is evaluated, together with comparative characterization of both PHB sources.

The study is limited to the stages required to assess the feasibility of PHB-based fibers for cementitious reinforcement. Their direct incorporation into cementitious matrices and the mechanical evaluation of FRC specimens are outside the scope of this thesis and are proposed as future work.

Chapter 2

Novel Fibers in Cementitious Composites

Currently, a wide range of cementitious materials incorporate fibers to enhance their performance. These fibers are predominantly metallic and synthetic polymeric, which are already widely used in commercial applications, while a few natural fibers have also been investigated as alternative reinforcement options (Mukhopadhyay & Khatana, 2015; Soltan et al., 2017; Chellapandian et al., 2024; Radhakrishnan et al., 2024). Notable fiber-reinforced systems include Ultra-High Performance Concrete (UHPC) (Bajaber & Hakeem, 2021), Fiber-Reinforced Concrete (FRC) (Brandt, 2008) and Engineered Cementitious Composites (ECC) (Li, 2003).

Some of the key functions that fibers perform in concrete include crack control, improved tensile and flexural response, enhanced ductility, increased fracture toughness, and improved resistance to fatigue, impact, and thermal shock (Mukhopadhyay & Khatana, 2015). These contributions depend on the fiber type, geometry, volume fraction, and interaction with the cementitious matrix. By limiting crack opening and damage progression during service, fibers can also contribute to improved durability (Brandt, 2008; Li, 2003; Paul et al., 2020).

In UHPC, the cementitious matrix is designed to achieve very high compressive

strength, low porosity, and enhanced durability through dense particle packing, low water-to-binder ratio, and the use of fine reactive materials (Bajaber & Hakeem, 2021). Although the term UHPC is commonly used in practice for concrete without fibers, most structural UHPC applications incorporate fibers because the dense and brittle matrix requires reinforcement to develop a useful tensile and post-cracking response. Steel fibers are the most commonly used reinforcement in UHPC due to their effectiveness in bridging cracks and improving mechanical performance (Yoo & Yoon, 2016; Bajaber & Hakeem, 2021).

For FRC, discrete fibers are distributed throughout the cementitious matrix and act after the matrix cracks by transferring stresses across crack surfaces. Unlike conventional reinforced concrete, where steel bars provide the main tensile reinforcement at specific locations, fibers provide distributed reinforcement within the matrix. Therefore, the main distinction of FRC is not only the improvement of individual mechanical properties, but the change in how tensile stresses and cracks are controlled throughout the composite (Brandt, 2008; Mukhopadhyay & Khatana, 2015).

The ductility mechanism in ECC is achieved through the controlled limitation of crack expansion. Victor Li, the creator of ECC, applied micromechanics principles to achieve this behavior (Li, 1993). Li highlights how the interplay between fiber-matrix interaction, crack control, and material design principles allows ECC to exhibit its characteristic strain-hardening behavior and exceptional ductility.

The replacement of petroleum-based fibers with natural plant-derived alternatives has been increasingly explored in fiber-reinforced cementitious composites. Several studies have focused on ECC systems, where the fiber requirements are particularly demanding because strain-hardening behavior depends strongly on fiber strength, deformability, bond, and crack-bridging capacity. For example, Radhakrishnan et al. (2024) investigated natural fibers such as flax, kenaf, pineapple, and hemp as alternatives for ECC. Among these fibers, only two achieved strain capacities slightly above 3%, while the others remained below this threshold, limiting their effectiveness in producing the characteristic strain-hardening response of ECC. Similarly, Soltan et al. (2017) examined curauá fiber in ECC and reported a significantly lower deformation capacity compared

with conventional ECC formulations. These studies show that natural fibers are being actively investigated as sustainable reinforcement alternatives, but also that matching the mechanical performance of ECC with petroleum-derived synthetic fibers remains challenging.

Replacing petroleum-based fibers with natural alternatives can offer relevant environmental advantages, including reductions in embodied energy and associated carbon emissions. Embodied energy represents only one way of assessing the environmental impact of a material, since a complete sustainability evaluation should also consider raw-material sourcing, production route, transport, service life, durability, and end-of-life scenario. Nevertheless, it provides a useful first indicator for comparing the energy demand associated with different materials. As shown in Figure 2.1, concrete presents a relatively low embodied energy per unit mass.

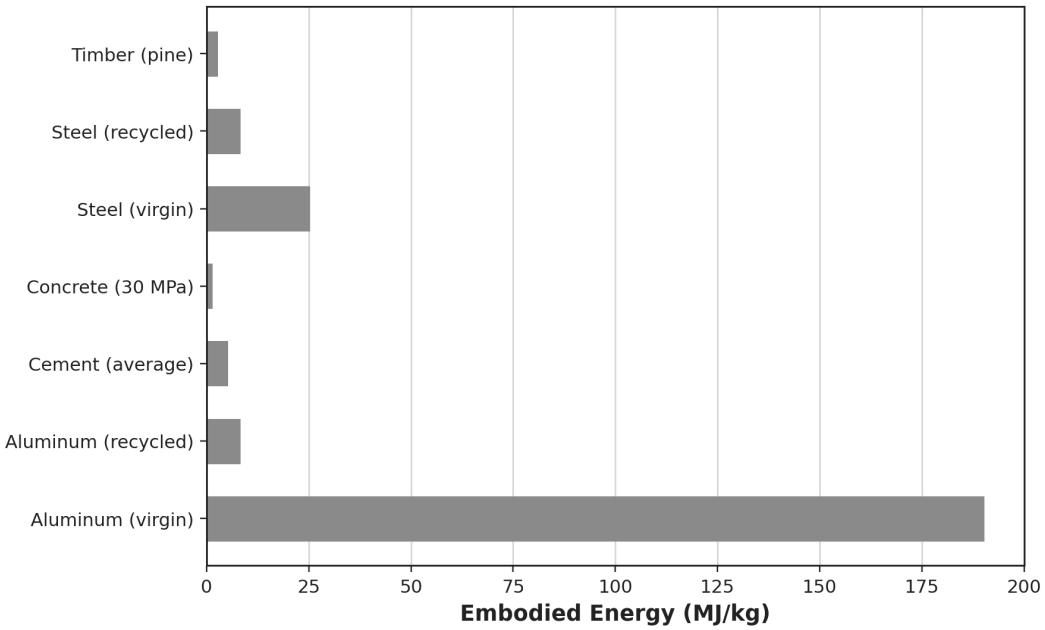


Figure 2.1: Embodied energy of concrete, adapted from (Juenger et al., 2011).

However, the reinforcement phase may introduce materials with substantially higher energy demand, as shown in Figure 2.2. Conventional fibers used in cementitious composites, including steel, PE, PP, and PVA fibers, can present considerably higher embodied energy than concrete. Therefore, replacing petroleum-based synthetic fibers with renewable or bio-based alternatives may contribute to reducing the environmental

burden of fiber-reinforced cementitious composites, provided that the alternative fibers can satisfy the mechanical and durability requirements of the composite.

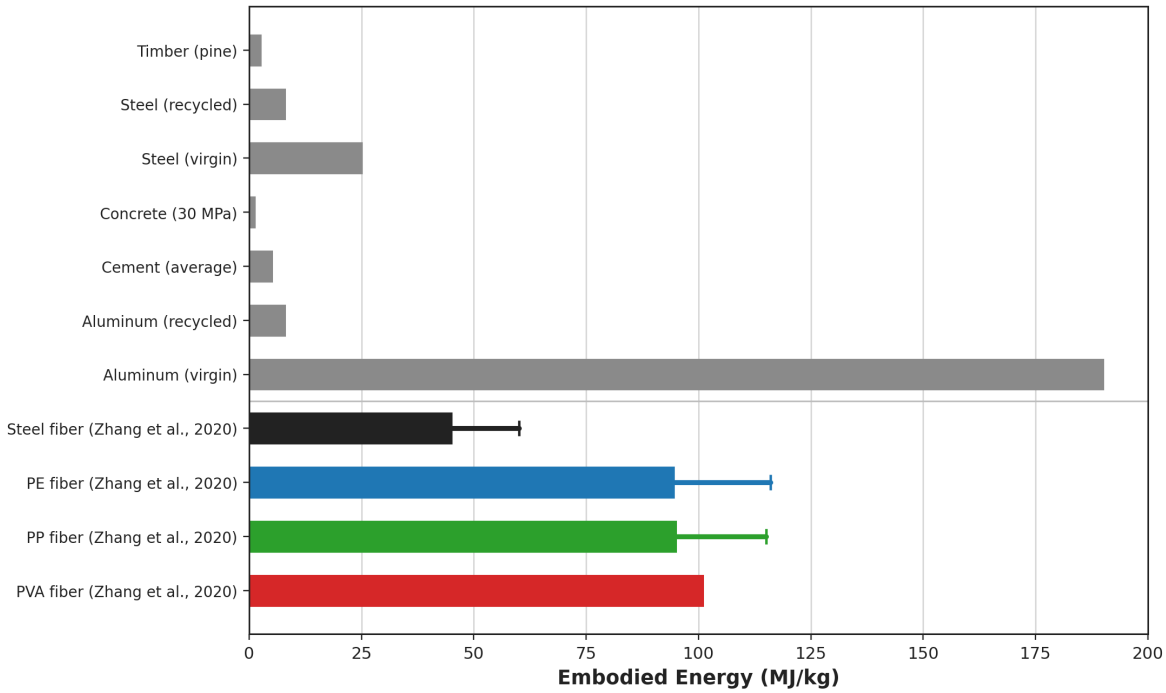


Figure 2.2: Comparison between the embodied energy of concrete and fibers used in cementitious composites, adapted from Juenger et al. (2011) and Zhang et al. (2020).

Nevertheless, replacing petroleum-based fibers with renewable alternatives does not automatically guarantee a lower overall environmental impact. In the case of plant-derived fibers, their renewable origin must be balanced against land use, water demand, potential competition with agricultural production, dependence on fertilizers or pesticides, regional availability, and variability in material quality. Therefore, alternative reinforcement fibers should not only avoid fossil-derived feedstocks, but also offer scalable production, consistent properties, adequate durability, and suitable mechanical performance for cementitious composites.

Bacteria-derived polymers have attracted increasing attention as potential sources for fiber production, particularly in response to the need for alternatives to petroleum-derived materials. Examples include fibers produced from polymers such as polybutylene succinate (PBS), polylactic acid (PLA), polyhydroxyalkanoates (PHAs), and poly(3-hydroxybutyrate) (PHB), among others. These materials can be processed into

fibers through techniques such as melt spinning and electrospinning (Naeimirad et al., 2023; Puppi et al., 2019). Among PHA-based materials, PHB is particularly promising due to its bacterial origin, biodegradability, thermoplastic behavior, and potential processability into fiber formats (Puppi et al., 2019).

PHB was first discovered in the early twentieth century by Maurice Lemoigne, then head of the fermentation department at the Pasteur Institute, and has since been the subject of extensive research (Lenz & Marchessault, 2005). In particular, the application of PHB in fiber form, has gained significant attention over the past two decades, showing potential for medical and agricultural uses (Acevedo et al., 2018). For instance, PHB has been evaluated as a sustainable alternative to conventional plastics in food packaging applications (Bucci et al., 2005), and as a biodegradable suture material in animal studies (Volova et al., 2003).

Despite this progress, the application of PHB-based fibers in civil engineering, particularly in cementitious composites, remains largely unexplored. This is mainly because the mechanical properties typically reported for PHB fibers are still lower than those of conventional reinforcement fibers used at larger scale, such as PE, PVA, PP, or steel fibers (Sanhueza et al., 2019; Sanhueza et al., 2020; Li et al., 2002; Said & Razak, 2015). Therefore, the main challenge is not only to produce PHB fibers, but also to tailor their molecular structure, morphology and surface characteristics, so that they can fulfill the reinforcing functions required in cement-based materials.

Nevertheless, the development of bacterial-origin fibers with improved tensile capacity is feasible. The properties of the resulting fibers can be adjusted based on several controllable factors (Sanhueza et al., 2020; Acevedo et al., 2018; Kabe et al., 2012). In particular, during the production process, it is possible to modify both the physical and chemical properties of the produced PHB or fiber, enabling the latter to be tailored to meet specific performance requirements. This characteristic allows for the development of beneficial properties customized for the intended use of the fiber.

For instance, surface modifications can be used to tune the interaction between PHB-based fibers and their surrounding medium. Parameters such as water contact angle (WCA), surface roughness, and chemical functionality influence the hydrophilic or hy-

drophobic behavior of the material, as well as its potential adhesion with a cementitious matrix. Previous studies on other polymeric and porous materials have demonstrated that surface modification can strongly alter the WCA, ranging from highly hydrophilic to superhydrophobic behavior (Gökaltun et al., 2019; Okutan et al.,). Although these studies were not conducted on PHB fibers or cementitious composites, they illustrate the broader principle that surface properties can be deliberately tailored. In the context of fiber-reinforced cementitious composites, this is particularly relevant because the fiber-matrix interface controls stress transfer, pull-out behavior, crack bridging, and overall reinforcement efficiency (Li et al., 2002). Therefore, tailoring the surface of PHB-based fibers could be a key strategy to adjust their compatibility with cement-based materials and improve their reinforcing performance.

Moreover, not only surface characteristics but also bulk mechanical properties can be tailored through polymer formulation. For instance, the incorporation of 3-hydroxyvalerate units into PHB to form poly(3-hydroxybutyrate-co-3-hydroxyvalerate) (PHBV) copolymers has been reported as an effective strategy to improve flexibility and reduce brittleness. In their comparative study, Righetti et al. (2019) showed that PHBV copolymers with increasing HV content (8% and 12%) exhibited higher ductility and a greater mobile amorphous fraction (MAF) than pure PHB. This was accompanied by a reduction in the rigid amorphous fraction (RAF), also referred to as the constrained amorphous interphase, as well as a reduction in the crystalline fraction. As a result, PHBV retained higher elongation at break while maintaining acceptable stiffness. Such microstructural control could be important when designing PHB-based fibers for cementitious composites, where the balance between stiffness, ductility, and controlled crack-bridging behavior is critical for tensile performance.

Additionally, the choice of carbon source during bacterial synthesis can significantly influence the properties of the resulting PHB. Sanhueza et al. (2020) demonstrated that using glucose, mannitol, or xylose as the sole carbon source in *Paraburkholderia xenovorans* cultures led to differences in molecular weight, crystallinity, and mechanical behavior of the produced PHB and its electrospun fibers. For instance, PHB derived from mannitol showed the highest molecular weight and purity, while fibers electrospun from xylose-based PHB exhibited greater flexibility and hydrophilicity, with properties

comparable to those of human skin. These findings highlight that, beyond genetic and process conditions, substrate selection can be strategically used to tailor PHB fiber properties for specific applications. Since molecular weight generally shows a positive relationship with the mechanical performance of PHA materials, an increase in MW may contribute to improving the tensile properties of the resulting fibers (Boesel et al., 2014).

Beyond carbon sources and culture conditions, the choice of bacterial species can also affect the molecular and mechanical properties of the produced PHB. While *Cupriavidus necator* and recombinant *E. coli* are widely used due to their high PHB productivity and genetic tractability, other species such as *Azotobacter vinelandii*, *Pseudomonas putida*, and some *Bacillus* species have also gained attention for their ability to produce PHAs with different monomer compositions or molecular characteristics (Peña et al., 2014). The review by Lu et al. (2009) further highlights that differences in PHA synthase classes, metabolic fluxes, and regulatory pathways among bacterial species can influence not only productivity, but also polymer chain length, crystallinity, and mechanical behavior. Thus, strain selection represents a key tool for tuning PHB microstructure and functionality, particularly for applications requiring specific stiffness, ductility, or biodegradation profiles.

In addition to strain selection and culture optimization, genetic engineering provides a powerful strategy to enhance PHB production and tailor polymer properties. Zhang et al. (2020) reviewed how advanced synthetic biology tools, including CRISPR/Cas systems, transcriptional regulators, and modular pathway optimization, can be used to manipulate metabolic fluxes toward PHA biosynthesis. These approaches have enabled improvements in polymer yield, control over monomer composition, and modification of polymer-related properties. Such genetic control complements the natural variability among wild-type strains, allowing the fine-tuning of molecular weight, mechanical behavior, and biodegradation profile, thereby expanding the design space for PHB-based fibers and composite materials.

The extraction method also plays a decisive role in preserving the molecular integrity and quality of the PHB destined for fiber production. Traditional solvent-based meth-

ods, particularly those using chlorinated solvents such as chloroform and methylene chloride, have been shown to yield PHB with high purity and molecular weights exceeding 1.2 MDa when optimized with pretreatments such as acetone washing and controlled reflux times (Ramsay et al., 1994). However, these methods also pose a risk of thermal degradation through random and chain-end scission, especially at elevated temperatures or prolonged exposure. More recently, greener alternatives such as dimethyl carbonate (DMC) have gained attention due to their lower toxicity and capacity to extract PHB under milder conditions. Mongili et al. (2021) demonstrated that DMC extraction, when coupled with optimized temperature and time parameters, can achieve competitive purity while minimizing polymer degradation, making it a promising approach for applications requiring high molecular weight PHB. Thus, the extraction strategy must be carefully selected to retain the mechanical and rheological properties needed for downstream processing, particularly in fiber formation and composite reinforcement.

Furthermore, the mechanical properties of PHB-based fibers can be significantly enhanced through post-processing strategies such as cold drawing, hot drawing, and annealing (Iwata et al., 2004; Yamane et al., 2001; Kabe et al., 2012; Liu et al., 2015). These treatments promote molecular orientation, increase the alignment of crystalline domains, and reduce structural defects. During cold drawing, polymer chains that are initially arranged in random or semi-amorphous conformations become partially oriented along the fiber axis. Subsequent annealing can stabilize these oriented morphologies by promoting crystallinity and reducing residual stresses. This sequence of morphological transformations is essential for developing high-performance fibers from PHB or its derivatives, with mechanical properties approaching those of some conventional polymers.

Another advantage of PHB-based fiber production is that it is not strongly constrained by regional agricultural availability. Since PHB is synthesized by bacteria, production can be implemented in different locations provided that the required microbial strains, feedstocks, and fermentation infrastructure are available. This offers a potential advantage over plant-derived fibers, whose large-scale production may depend more strongly on climate, land availability, crop productivity, and regional supply chains.

Therefore, PHB-based fibers could contribute to the development of more sustainable cementitious composites by offering a bacteria-derived alternative to petroleum-based reinforcement fibers. Although their direct application in FRC or ECC still requires further validation, their tunable production, processability, and potential integration with circular feedstock strategies make them a promising research direction for reducing dependence on fossil-derived fibers in cement-based materials.

Chapter 3

Methodology

The following chapter presents all the procedures required for the production and characterization of PHB films and fibers.

The methodological approach is organized into three sequential stages that allow for the development of a PHB fiber: i) bacterial fermentation, ii) PHB extraction, and iii) fiber production. The first stage encloses the synthesis of PHB through the use of a bacterial strain in a bioreactor. The second stage corresponds to the separation of the PHB from the bacteria. The third stage is related to the melting process that transforms the native PHB into fiber.

Each stage includes specific characterization protocols to assess the material's key physicochemical, thermal, and mechanical properties.

3.1 Materials

This section describes the materials used in this study, including their origin or supplier, when applicable. These correspond to the inputs required for PHB production and characterization.

3.1.1 Fermentation chemicals

All chemical reagents used for fermentation were purchased from Sigma-Aldrich. The main reagent brands included Merck, Sigma-Aldrich, and Supelco.

3.1.2 Bacterial strain

The bacterial strain used in this research was *Cupriavidus necator H16* (*Ralstonia eutropha* wild type, RE H16), obtained from DSMZ German Collection of Microorganisms and Cell Cultures (DSM 428). *Ralstonia eutropha* is a Gram-negative, oxidase-positive, and strictly respiratory bacterium (Yabuuchi et al., 1995). This means its primary metabolic pathway is based on respiration, and it does not exhibit the Crabtree effect. However, the bacterium is capable of undergoing metabolic shifts under specific conditions. One example is the production of PHB, which occurs under nutritional stress specifically when the nitrogen or oxygen source is depleted while carbon is still in excess. This metabolic shift leads to the synthesis of intracellular carbon and energy storage polymers (Palmeiro-Sánchez et al., 2022), with PHB its prime example.

3.2 PHB Production

The stages used for PHB production were: i) preparation of culture media, ii) development of the inoculum, iii) fermentation under controlled conditions, and iv) downstream recovery. These stages are detailed in the next sections.

3.2.1 Growth media

3.2.1.1 Nutrient agar

A standard procedure (Cappuccino & Welsh, 2019) using nutrient agar and sterile Petri dishes was followed to initiate bacterial growth. The medium was prepared by dissolving 5 g of nutrient agar in 250 mL of water, with heating applied to ensure complete dissolution of the powder. Once fully dissolved, the medium was sterilized at 121 °C for 15 minutes. After sterilization, the agar was allowed to cool. Since the medium solidifies upon cooling, it was reheated before use until it returned to a liquid state and was subsequently allowed to cool to a temperature suitable for safe handling.

Under aseptic conditions in a JSR JSCB-900SB biosafety cabinet, sterile Petri dishes were filled with 25 to 30 mL of the liquid agar, enough to cover the bottom surface uniformly. The medium was then left to solidify before inoculation.

For inoculum development, 100–200 μL or 300 μL of inoculum were transferred onto the agar plate, depending on whether the bacterial source was cryopreserved stock or a previous LB culture, respectively. In all cases, the inoculum was evenly spread over the agar surface using a sterile L-shaped spreader.

After inoculation, the plates were sealed with parafilm and incubated at 30°C for 2 days. Following incubation, the plates were stored under refrigeration until further use. The viability of use of the culture was limited up to three weeks to one month.

3.2.1.2 Mineral medium

Prior to the preparation of the fermentation medium, the bacterial strain needs to be precultured in a mineral medium formulated to support initial cell growth under controlled conditions. The inoculum was sourced either from preserved Petri dishes or directly from P2 cryovials, depending on availability and storage duration.

This medium, adapted from previously established formulations for *Cupriavidus necator* (Wang & Lee, 1997; Kim et al., 1994), includes nitrogen and phosphorus sources, a predefined trace element solution (see Appendix A, Table A.1), and magnesium sulfate. The detailed composition of this mineral medium is presented in Appendix A, Table A.2.

For inoculum preparation, a standard procedure was followed (Manutsyan et al., 2024; Poladyan et al., 2019; Park et al., 2011). A total of 100 mL of the sterile medium were transferred into a 500 mL Erlenmeyer flask and supplemented with 4 mL of a fructose solution (500 g/L). The culture was incubated at 30°C under agitation at 250 rpm in a JSR JSSI-100C shaking incubator.

3.2.1.3 Culture medium for bioreactor production

The culture medium used in this study was formulated to support high-cell-density fermentation and PHB production through iterative adjustments in composition and the feeding strategy. The initial formulation of the mineral medium consisted of phosphate salts, a nitrogen source, fructose as the main carbon source, and a predetermined solution of trace elements, as detailed in Appendix A, Table A.3. The design of the medium was based on mineral media formulations reported in the literature for fed-batch PHB production using strains such as *Alcaligenes eutrophus* and *Alcaligenes latus*, which have demonstrated high productivity and polymer accumulation under controlled nitrogen-limiting conditions (Wang & Lee, 1997; Kim et al., 1994).

The reactor medium and the fed-batch strategy were tailored considering three main factors: i) the operational capabilities of the bioreactor used, ii) the production targets established during the development of the work, and iii) the growth behavior observed for RE H16 in the implemented system. These criteria were used to balance operational simplicity with adequate process control at laboratory scale. Accordingly, the medium was designed to promote biomass growth during the initial stage of fermentation, followed by PHB accumulation under nitrogen limited conditions, in agreement with the two stage approach commonly reported for PHB producing bacteria, in which biomass formation and polymer biosynthesis are partially decoupled (Wang & Lee, 1997; Kim et al., 1994).

The initial design of the culture medium was based on stoichiometric yield assumptions adopted as preliminary engineering parameters for aerobic PHB-producing bacteria cultivated under nutrient-limited conditions. In particular, a biomass yield of 0.4 g biomass per g fructose consumed was adopted for medium design, which is consistent with values reported for *Cupriavidus necator* grown on fructose in batch and fed-batch systems, typically ranging from approximately 0.3 to 0.5 g/g (Boy et al., 2021; Pérez-Camacho et al., 2024). In addition, a nitrogen related coefficient of 1.5 g biomass per g ammonium sulfate supplied was used as a practical design estimate to define the initial nitrogen requirement. This value is also consistent with yields derived from reported biomass production values of 5.21-6.60 g biomass per g NH_3, corresponding to approxi-

mately 1.34-1.70 g biomass per g $(NH_4)_2SO_4$ (Boy et al., 2021). These coefficients were used to estimate the initial amounts of carbon and nitrogen sources required to achieve the target biomass concentration prior to the PHB accumulation phase.

During the experimental campaign, these initial design assumptions were contrasted with observations obtained from successive reactor runs, leading to progressive refinement of the medium composition. The final formulation adopted in this work corresponds to the medium composition reported in Appendix A, Table A.4. This formulation reflects the adjustments implemented to ensure adequate biomass growth and controlled PHB accumulation under the operational conditions of the reactor.

Unless otherwise stated, media and samples were prepared using a Radwag AS 220 R2 Plus analytical balance with a precision of ± 0.2 mg.

3.2.2 Bacterial kinetics

The study of bacterial kinetics was performed by slightly modifying the previously described procedure for the development of the initial inoculum. Specifically, 500 mL Erlenmeyer flasks were prepared in triplicate, each containing 110 mL of mineral medium supplemented with 20 g/L of fructose. The flasks were then inoculated with bacterial cultures previously grown on Petri plates.

Based on this formulation and the available reagents, the bacterial kinetics were evaluated through batch experiments focused on substrate to biomass yield determination. The following methodologies were implemented to quantify bacterial growth, as well as fructose and PHB concentrations during cultivation:

3.2.2.1 Growth monitoring

A Jenway 6320D spectrophotometer was used to monitor cell growth in the reactor, the equipment is shown in Figure 3.1.



Figure 3.1: Spectrophotometer used for growth monitoring (Jenway, 2026).

Cell growth during cultivation was monitored by measuring the optical density at 600 nm (OD_{600}). This parameter was used as a rapid indicator of biomass evolution throughout the experiments, both in shake-flask cultures and during reactor operation.

3.2.2.2 Quantification of fructose

A Shimadzu Prominence liquid chromatograph (Cromtek, see Figure 3.2) equipped with an LC-20AD pump, a CTO-20A column oven, and a RID-20A refractive index detector was used for the quantification of fructose present in the flasks and reactor by High Performance Liquid Chromatography (HPLC). This technique was selected because it allows rapid and reliable sugar quantification, particularly when combined with a refractive index detector (RID) (Tiwari et al., 2023). Chromatographic separation was carried out on a Rezex ROA-Organic Acid H^+ column (300 × 7.8 mm, Phenomenex) maintained at 60 °C. The mobile phase consisted of 2.5 mM H_2SO_4 delivered at a constant flow rate of 0.6 mL min^{-1}. The RID detector was operated with a cell temperature of 40 °C. The injection volume for all samples was 5 μL.

The sample preparation protocol consisted of the following steps. First, at least 2 mL of culture were withdrawn using the bioreactor sampling port. The sample was then centrifuged for 3 minutes at 13000 rpm using a Labnet C2500-R Prism microcentrifuge (see Figure 3.3(a)), and the supernatant was collected. A dilution was prepared using Type I water (MilliQ) (Tiwari et al., 2023), with dilution factors of 1:10, 1:20, or 1:50 depending on the expected fructose concentration. The diluted sample was subsequently filtered into HPLC vials using a syringe filter (0.22μm, MCE, 13 mm) prior to chromatographic analysis. Finally, the vials were loaded into the HPLC system for measurement.

Quantification was performed using an external calibration curve constructed from fructose standards prepared from analytical grade fructose (Sigma-Aldrich) in the concentration range of 0.1 to 2.0 $\mathrm{g\,L^{-1}}$.



Figure 3.2: Shimadzu Prominence HPLC system used for the analysis of fructose concentration (Cromtek, 2026).



(a) C2500-R Prism. (b) Rotofix 32A.

Figure 3.3: Centrifuges used in the biomass concentration and washing process (TCLGroup, 2026; Andreas Hettich GmbH & Co. KG, 2026).

3.2.2.3 Quantification of PHB

Using HPLC

For PHB quantification, the same HPLC system described previously for fructose analysis was employed, using the SPD-20A UV-Vis detector for crotonic acid determination. This method is based on the acid-catalyzed conversion of PHB into crotonic acid, which can be quantified by UV absorbance (Karr et al., 1983; Duvigneau et al., 2021).

Culture samples were first withdrawn from the reactor or flask (at least 5 mL) and centrifuged using a Hettich Rotofix 32A centrifuge (see Figure 3.3(b)). The biomass was washed repeatedly with Type II water until the supernatant became clear, at least 3 washes were applied. An empty labeled crimp-seal vial (10 mL or smaller) was dried at 100 °C for 24 h to determine its dry weight. The washed biomass was then transferred into the vial and dried under the same conditions for an additional 24 h. After cooling to room temperature, the dry biomass weight was recorded.

Subsequently, 1 mL of sulfuric acid was added to the vial, which was sealed and placed in an oven at 100 °C for 30 min to promote the conversion of PHB into crotonic acid. The vial was manually agitated every 10 min to ensure proper mixing. This sample preparation procedure corresponds to an adaptation of the method originally proposed by (Karr et al., 1983). After the reaction, the sample was allowed to cool, and 4 mL of Type I water was slowly added. This step is highly exothermic and was performed under controlled conditions to allow gradual gas release. Personal protection elements were used.

The resulting solution was diluted (typically 1:50 or 1:100, depending on the expected PHB concentration) using 2 mL Eppendorf tubes. Prior to analysis, samples were filtered through 0.2 μm filters and transferred into HPLC vials. Quantification was performed using external calibration curves prepared from a commercial PHB standard (Santa Cruz Biotechnology, sc-255438) in the range of 1-16 mg. Standard solutions were subjected to the same acid digestion procedure as the biomass samples to ensure consistent conversion of PHB into crotonic acid and to account for potential losses during sample preparation.

Using Gas Chromatography (GC)

A Shimadzu Nexis GC-2030 chromatograph equipped with a flame ionization detector (FID) (see Figure 3.4) was also used for measuring PHB by gas chromatography (GC). The procedure followed an acid-catalyzed propanolysis approach for PHB quantification in dried biomass adapted from Scott et al. (2021).

An acidified propanol solution (Solution B) was prepared by mixing four parts of n-propanol with one part of concentrated hydrochloric acid (1:4 v/v). An internal standard solution (Solution S) was prepared by dissolving 2.0 g of benzoic acid in a 50 mL volumetric flask and filling to the mark with n-propanol.

For each determination, 10-20 mg of dried biomass were transferred into 15 mL glass tubes. Subsequently, 2.0 mL of dichloroethane (DCE), 2.0 mL of Solution B, and 200 μL of Solution S were added. DCE was used as a extraction solvent due to the solubility of PHB in the organic phase, enabling efficient recovery during derivatization. The mixture was vortexed for 3 s to eliminate visible aggregates and heated at 100 °C for 3 h in sealed tubes. After cooling to room temperature, 4 mL of distilled water were added to promote phase separation. The tubes were vortexed vigorously for 30 s and allowed to rest for 60 s. Finally, 500–1000 μL of the lower organic phase were transferred into GC vials for chromatographic analysis.

Chromatographic separation was performed on a J&W DB-FastFAME GC column (20 m $\times$ 0.18 mm $\times$ 0.20 μm, Agilent G3903-63010). Nitrogen was used as the carrier gas at a constant column flow of 0.48 $\mathrm{mL\,min^{-1}}$. The injector temperature was set at 260 °C and operated in split mode with a split ratio of 30:1. The oven temperature was set at 50 °C. The FID detector temperature was maintained at 280 °C, with hydrogen and air flows of 32 $\mathrm{mL\,min^{-1}}$ and 200 $\mathrm{mL\,min^{-1}}$, respectively, and a nitrogen makeup gas flow of 24 $\mathrm{mL\,min^{-1}}$. A 5 μL aliquot of the organic phase was injected for each analysis.

Quantification was performed using an internal standard method with benzoic acid. The calibration curve was constructed using a commercial PHB standard (Santa Cruz Biotechnology, sc-255438) in the range of 1-16 mg.



Figure 3.4: Shimadzu GC system used for the analysis of PHB concentration and purity (Shimadzu, 2026).

3.2.2.4 Quantification of ammonium

Direct ammonium quantification was not reliable under the experimental conditions used in this work. For this reason, the biomass yield with respect to ammonium was estimated through an inverse calculation procedure based on dry biomass, PHB content, and the amount of ammonium supplied to the culture.

After completion of the kinetic experiment, an empty vial was dried in an oven at 100°C for at least 24 h and weighed to determine its tare mass. Then, at least 5 mL of culture were transferred into the same vial and dried for 24 h, after which the mass of dry biomass was recorded. From this value and the analyzed culture volume, the dry biomass concentration was calculated. The total dry biomass in the flask was then estimated by proportional extrapolation to the final culture volume. Alternatively, the entire final culture volume could be dried directly to determine the total dry biomass.

The PHB content of the dry biomass was determined using the HPLC or GC protocols described in the methodology. Once the total dry biomass and PHB content were

known, the PHB-free biomass was calculated as the complement of the PHB fraction within the total dry biomass, according to Equation 3.1.

$$X_{\text{res}} = X_T \left(1 - f_{\text{PHB}}\right) \tag{3.1}$$

where X_{res} is the residual biomass, or PHB-free biomass, X_T is the total dry biomass, and f_{PHB} is the PHB mass fraction in the biomass.

The biomass yield with respect to ammonium was then estimated according to Equation 3.2.

$$Y_{X/N} = \frac{X_{\text{res}}}{N} \tag{3.2}$$

where $Y_{X/N}$ is the biomass yield with respect to ammonium and N is the amount of ammonium supplied to the culture. The resulting yield was expressed in units of $\text{g}_{\text{biomass}}/\text{g}_{\text{substrate}}$.

Estimates of biomass yields and specific growth rate provides a more robust basis for experimental design and process control. In particular, the estimation of yield coefficients and growth kinetics allows for a more accurate definition of the required amounts of fructose and ammonium to meet specific fermentation targets. This approach improves the reliability of achieving the desired PHB production levels and enhances process consistency. Furthermore, it contributes to a more efficient use of resources by reducing the need for frequent sampling or redundant measurements during cultivation.

3.2.3 Fermentation process

An Infors Minifors 2 reactor, shown in Figure 3.5, was used for the fermentation process. The microorganism, previously cultivated in the mineral medium, was transferred to the reactor to initiate the main fermentation process.



Figure 3.5: Minifors 2 Bioreactor, Incitec (INFORS HT, 2026).

The bioreactor used in this study is equipped with integrated systems and connections for sensors and pumps, enabling automated control of pH, temperature, and foam during operation. It features dedicated inlet ports for air and pure oxygen, as well as an outlet line for gas release. Additionally, the system includes feed lines operated by pumps for nutrient addition; however, they were not used in this particular experimental setup. Instead, nutrient feeding was performed manually by injecting the solutions with sterile syringes under a flame to maintain aseptic conditions.

Operational conditions were selected based on previously reported values for optimal growth of RE H16 (Grunwald et al., 2015; Budde et al., 2011; Shahhosseini, 2004). The temperature was maintained at 30°C, with the pH regulated around 7. Dissolved oxygen levels were kept above 30%, supported by a variable agitation speed between 200 and 800 rpm, aeration at 0.5-2 LPM, and pure oxygen between 0-0.5 LPM, depending on the metabolic activity of the culture.

After each fermentation, the reactor broth was recovered, transferred to 50 mL Falcon tubes, and subjected to a biomass washing procedure prior to extraction. In each cycle, the biomass suspension was centrifuged for 15 min at 4000g using a Rotofix 32A centrifuge (Figure 3.3(b)), after which the supernatant was removed. The recovered biomass was then resuspended in distilled water and centrifuged again under the same

conditions. This procedure was repeated for a total of three washing cycles in order to remove residual medium components.

After completing the washing steps, the concentrated biomass was stored in the same 50 mL Falcon tubes used during centrifugation, but resuspended in ethanol for subsequent storage and processing.

3.2.4 Extraction method

The extraction procedure consisted of seven main stages: i) pretreatment, ii) drying, iii) grinding, iv) extraction, v) filtration, vi) solvent recovery by distillation, and vii) precipitation. The setup used for the main stages is shown in Figure 3.6. Each stage was designed to enhance PHB recovery.

The procedure was carried out using biomass samples previously washed and stored in ethanol. Before extraction, the biomass was centrifuged to remove the ethanol, and the recovered wet biomass was subjected to a pretreatment with acetone. The acetone volume was selected to obtain a mass-to-volume ratio of 1:10 (g:mL) (Ramsay et al., 1994). Acetone contributes to biomass disruption prior to solvent extraction, thereby facilitating access to intracellular polymer (Morey-Yagi et al., 2026). In this work, the pretreatment was applied to wet biomass, since biomass particles in suspension have smaller diameters and are better dispersed, increasing the available surface area in contact with acetone and potentially improving the pretreatment efficiency. During the pretreatment stage, the biomass was kept in contact with acetone for 12 to 24 h (Ramsay et al., 1994), under agitation at 250 rpm, and at 30°C in a JSR JSSI-100C shaking incubator.

After pretreatment, the Falcon tubes were centrifuged again in order to separate the biomass from the acetone. The pretreated biomass was then dried for approximately 3 h in a glass Petri dish inside an oven at 50°C. During this step, the biomass was spread uniformly over the surface of the dish in order to avoid particle agglomeration.

After oven-drying, the biomass was ground to reduce its particle size prior to PHB extraction. A smaller particle size increases the available surface area of the biomass,

thereby improving the contact area between the biomass and the solvent. After grinding, the dried biomass was grouped in extraction batches of 5 g. Each extraction batch can include biomass from multiple reactors; therefore, for every batch, the maximum PHB content and the biomass contribution of each reactor were recorded in order to estimate the maximum amount of PHB that could be recovered during the extraction.

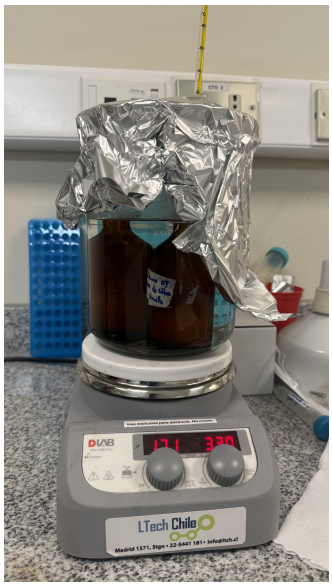
The extraction stage was carried out using glass vials of 100 and 120 mL, hermetically closed with crimp seals. Chloroform was used as the extraction solvent, and a biomass-to-solvent ratio of 1:20 was adopted (Ramsay et al., 1994; Meneses et al., 2022). A magnetic stir bar was placed inside each vial, and the sealed vials were immersed in a beaker containing water previously boiled. The beaker was placed on a magnetic hotplate (see Figure 3.6(a)), which provided both heating and stirring. The extraction was performed at 400 rpm, maintaining the water temperature above 70°C in order to improve PHB dissolution in chloroform.

Each extraction cycle was sustained for 30 min. After this period, the vials were removed from the water bath and allowed to rest for approximately 2 min. The chloroform solution containing dissolved PHB was then recovered and immediately subjected to vacuum filtration for purification (see Figure 3.6(b)). A Newstar glass fiber filter (110 mm diameter, 1.5 μm pore size), cut into four equal parts, was used to retain residual bacterial cells, large cell debris, and insoluble impurities, while allowing the PHB-chloroform solution to pass through. This pore size was considered suitable based on the micrometric dimensions reported for *Ralstonia eutropha* cells during P3HB accumulation (Volova et al., 2013). During filtration, the extracted solution was filtered along with preheated clean chloroform, which was added to increase PHB recovery and reduce premature polymer precipitation on the filter.

After filtration, the chloroform solution containing dissolved PHB was subjected to distillation and solvent recovery using a 150 mL glass Soxhlet apparatus supplied by BoroLab (Chile), shown in Figure 3.6(c). Although the Soxhlet system was not used for the direct extraction of PHB from biomass in this protocol, it was used as a distillation setup to concentrate the filtered PHB-chloroform solution and recover part of the chloroform used during extraction. The Soxhlet apparatus was heated using a

water bath Stuart RE300DB, while condensation was maintained by circulating refrigerant liquid with a JSRC-13C recirculating chiller. During this stage, chloroform was evaporated from the lower flask and condensed in the upper section of the apparatus, allowing cleaner chloroform to be recovered separately while the PHB-containing solution became progressively more concentrated in the lower flask.

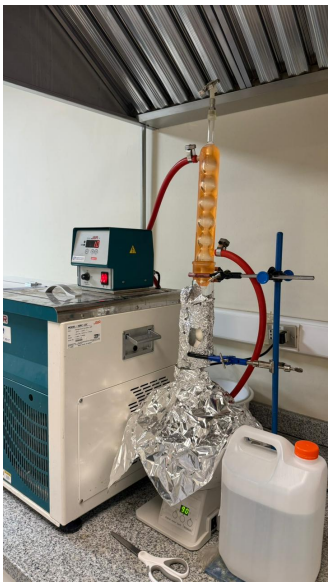
Two final recovery methodologies were implemented after filtration and solvent concentration. In the first approach, the filtered and concentrated chloroform solution containing PHB was placed in a glass Petri dish and introduced into an oven at 50°C to evaporate the remaining solvent and recover the polymer as a film. However, the resulting films contained impurities that prevented their processing in the subsequent stages of the project. Therefore, a second approach incorporating an additional purification step with cold ethanol as an antisolvent was implemented. For this purpose, the concentrated PHB-chloroform solution was transferred into 50 mL Falcon tubes, using 15 mL of concentrate per tube. Two volumes of cold ethanol, corresponding to 30 mL, were then added to precipitate the PHB and promote the removal of soluble impurities. The resulting mixture was left to rest for at least 12 h before recovering the purified polymer.



(a) Extraction setup.



(b) Vacuum filtration.



(c) Solvent recovery.

Figure 3.6: Main stages of the PHB extraction and recovery procedure.

3.3 Extrusion process

After the extraction process, the recovered PHB was processed into fibers using melt extrusion. For this purpose, a *Wellzoom B* extruder, shown in Figure 3.7, was employed. This equipment is typically fed with polymers in the form of pellets or granules and produces filaments with standard diameters of 1.75 mm or 3 mm, depending on the nozzle used. To produce fibers with diameters comparable to commercial petroleum-derived microfibers, the extruder nozzle was modified to obtain an outlet diameter of approximately 0.5 mm. Images of the modified nozzle are shown in Figure 3.8.



Figure 3.7: Wellzoom B2 REX-C100 extruder (Wellzoom, 2026).

Before processing PHB, the operation of the extruder and the performance of the modified nozzle were tested using two commercially available materials: a PHA fiber manufactured by ColorFabb in the Netherlands (colorFabb, 2024), hereafter designated as PHAC, and a PHB/PLA fiber manufactured by Fillamentum in the Czech Republic (Fillamentum, 2026). These preliminary trials were conducted to assess extrusion stability and verify the ability of the modified nozzle to produce continuous fibers with a reduced diameter.

During extrusion, the equipment was placed at an elevated height of approximately

1.5 m because filament formation depended largely on gravity. As the molten polymer exited the nozzle, the weight of the descending filament provided the pulling force required to sustain continuous and relatively homogeneous extrusion. The process was conducted in a temperature-controlled chamber maintained at 16 °C to promote rapid cooling and solidification of the polymer after it exited the nozzle. This arrangement facilitated filament formation and helped maintain a more uniform fiber diameter during production.



(a) Two-part nozzle. (b) Assembled nozzle.

Figure 3.8: Custom-made 0.5 mm extruder nozzle used in fiber production.

Melt spinning is one of the standard processes for producing PHB fibers (Yamane et al., 2001; Iwata et al., 2004; Furuhashi et al., 2004; Hufenus et al., 2020); however, it is not the only available approach. Alternative methods include electrospinning (Acevedo et al., 2018), solution blow spinning (Medeiros et al., 2009), and wet spinning (Kundrat et al., 2019), among others. Each of these techniques offers different advantages in terms of fiber diameter control, production scalability, and morphological characteristics. In this study, melt spinning was selected for use because the resulting fiber diameters are suitable for subsequent post-treatment processes.

The extrusion process requires a thorough understanding of the material's critical thermal transition points. These points refer to the glass transition temperature (T_g), melting temperature (T_m), and thermal degradation onset (T_d). These parameters are

essential for setting appropriate extrusion conditions, as the equipment must be programmed to operate within a temperature window that ensures sufficient polymer flow while preventing thermal degradation. For PHB, this is particularly important due to its narrow processing window.

3.4 PHB characterization

The produced PHB was characterized in its native film form. For the fiber stage, a commercial PHB supplied by Helian Polymers in pellet form was selected and extruded to produce fibers for evaluation. The PHAC fiber previously used in the preliminary extrusion was also characterized using the analytical methods described in this study. Its evaluation helped identify methodological limitations and supported the correction and optimization of the experimental and analytical protocols subsequently applied to the produced PHB and to the commercial PHB fibers. PHAC was also included as a reference material.

3.4.1 Physicochemical properties of the PHB

3.4.1.1 Density

The density of the PHB and PHAC samples was determined using a liquid displacement method based on Archimedes' principle. The procedure is conceptually consistent with ASTM D792 (ASTM International, 2026a), while experimentally following a volumetric approach analogous to the pycnometer method described in ASTM D854 (ASTM International, 2026b). Distilled water was used as the reference fluid due to its chemical compatibility with PHB.

The procedure considered the measurement of the mass of an empty volumetric flask (m_f) and the mass of the flask filled with distilled water up to the calibration mark (m_{fw}). A small volume of water was then removed to allow the introduction of the polymer specimen without overflow. After adding a known mass of the specimen (m_s), the flask was refilled with distilled water up to the calibration mark, ensuring that the total volume remained constant. The final mass of the system (m_{fws}) was then recorded.

The density was calculated from the mass of water displaced by the specimen. The corresponding equation, variable definitions, and water-density correction values are presented in Appendix B. The temperature of the distilled water was recorded prior to each measurement, and the density of water was corrected when deviations from the reference temperature of 23°C were observed.

At least three independent measurements were performed for each specimen to quantify the statistical variability.

3.4.1.2 Molecular weight

The molecular-weight distribution of the PHB samples was determined by gel permeation chromatography (GPC), using chloroform as the mobile phase. The chromatographic system consisted of a Dionex P590A liquid chromatography pump, a PLgel 5 μm Mixed-C column (300 $\times$ 7.5 mm), a Wyatt Technology DAWN EOS light-scattering detector, and an Optilab DSP interferometric refractive-index detector. The analyses were performed at 25 °C using a constant flow rate of 1 mL min^{-1}.

Calibration was performed using polystyrene standards with molecular weights of 29.3, 100, 300, 470, and 612 kg mol^{-1}. The PHB samples were prepared in chloroform at an approximate concentration of 1.5 mg mL^{-1}.

The weight-average molecular weight (M_w), number-average molecular weight (M_n), and the polydispersity index (PDI, M_w/M_n) was calculated from the chromatographic signal. The corresponding definitions, equations, and interpretation of the polystyrene-equivalent values are presented in Appendix B.3.

Molecular-weight distribution is relevant to melt processing because it affects the rheological response of PHB. In commercial PHB grades, differences in molar-mass distribution have been associated with different melt viscosities, processing temperatures, throughput limitations, and fiber-formation stability (Höhnemann & Windschiegl, 2023).

3.4.1.3 Purity

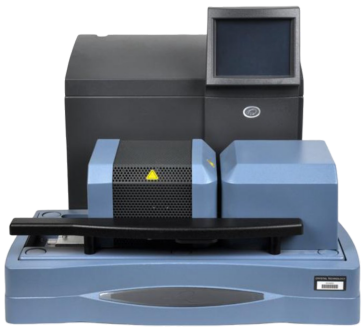
Purity of PHB samples was determined following the same derivatization procedure by propanolysis used for PHB quantification in biomass. In this case, purity was defined as the ratio between the amount of PHB quantified by GC and the mass of the analyzed sample.

3.4.1.4 Thermal Properties (T_g, T_m, T_d and X_c)

The thermal behavior of PHB samples was evaluated via differential scanning calorimetry (DSC) and thermogravimetric analysis (TGA) using a DSC 1 instrument from Mettler Toledo (see Figure 3.9(a)) and a SDT-Q600 from TA Instruments (see Figure 3.9(b)), respectively. These techniques enable the identification of thermal transitions such as melting and glass transition temperatures, as well as the evaluation of thermal stability and degradation onset.



(a) DSC 1, Mettler Toledo (Mettler Toledo, 2026).



(b) SDT-Q600, TA Instruments (TA Instruments, 2026).

Figure 3.9: Equipment used for the thermal characterization of PHB samples.

For the DSC test, approximately 30-40 mg of PHB were sealed in 100 μL hermetic aluminum pans prior to testing. The experimental procedure follows the thermal cycle shown in Figure 3.10, where Top and Bottom correspond to 250 °C and -70 °C, respectively. The parameter β_{heating} corresponds to a heating rate of 10°C min^{-1}. The cooling stages, denoted as $\beta_{\text{cooling},1}$ and $\beta_{\text{cooling},2}$, were 20°C min^{-1} and 60°C min^{-1}, respectively. These rates were selected to ensure controlled thermal transitions while enabling reproducible characterization of the polymer's thermal behavior. For the sec-

ond cooling step, the sample needs to be rapidly cooled to induce an amorphous state prior to isothermal crystallization or secondary heating scans (Kabe et al., 2012).

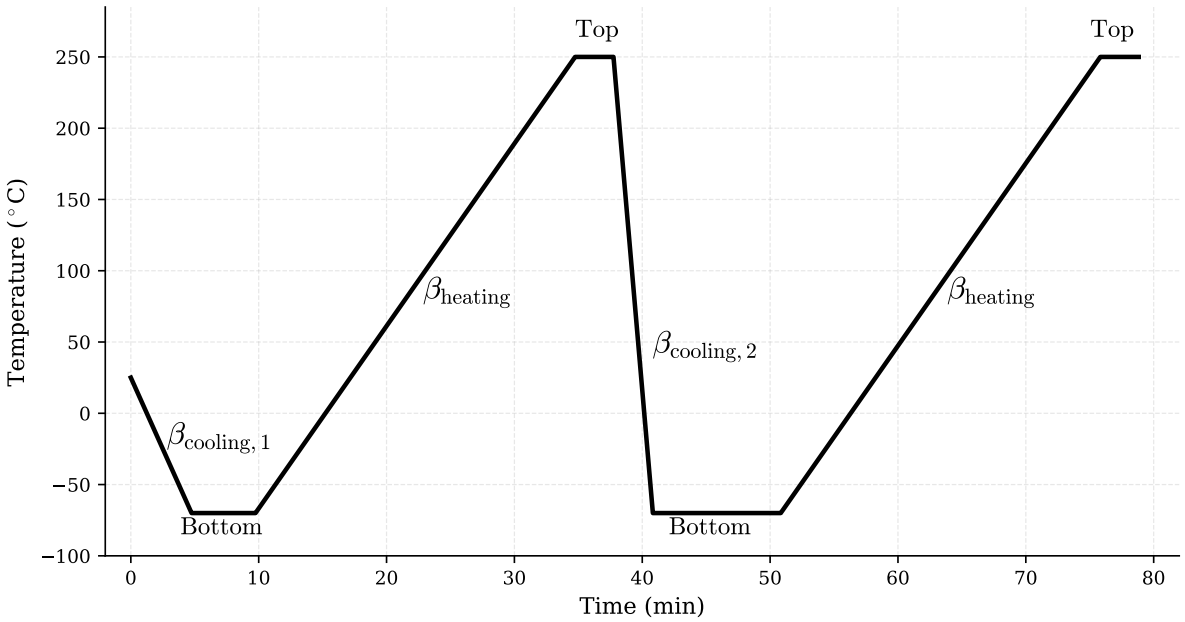


Figure 3.10: DSC thermal protocol used for the two-heating-cycle analysis.

The melting temperature was determined as the peak of the endothermic transition, while the glass transition was identified as a shift in the baseline of the heat flow curve. The enthalpy of fusion (ΔH_m) was calculated from the area under the melting peak, and the degree of crystallinity (X_c) was computed using a reference value of 146 J/g for 100% crystalline PHB, as determined by (Barham et al., 1984), and through extrapolation from twelve experimentally characterized samples.

A Shimadzu AUW120D analytical balance was used for the preparation and weighing of the samples analyzed by DSC. According to the specifications, the balance has a minimum display of 0.01 mg and high precision for low mass measurements.

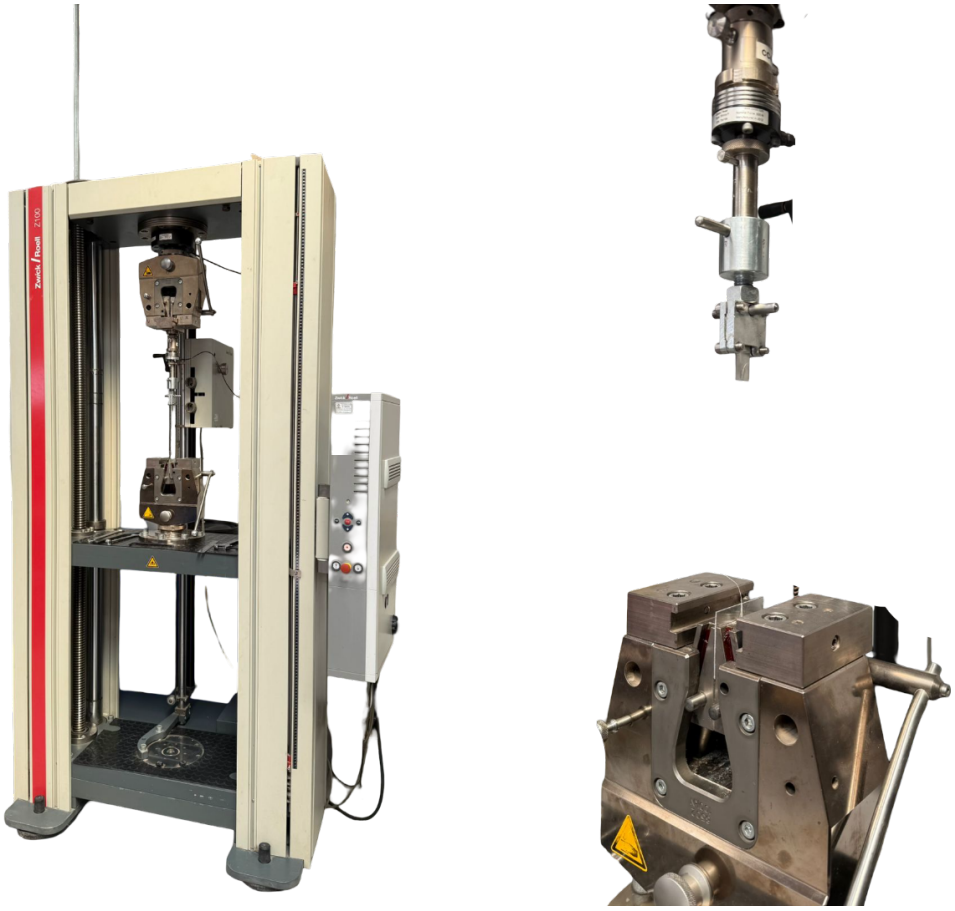
For TGA, the samples were initially heated from room temperature to 400°C under a nitrogen atmosphere (45 mL/min), using a heating rate of 10°C/min, following the methodology described by (Li et al., 2001). The degradation temperature (T_d) was determined from the TGA/DTG (differential thermogravimetry) curves using the conventional extrapolated tangent approach. A tangent was drawn to the TGA curve

at the temperature corresponding to the maximum mass-loss rate, identified from the DTG peak, and its intersection with the extrapolated baseline was used to define T_d.

This thermal profile provides essential information for understanding the processability and structural organization of the PHB material. Importantly, this analysis was conducted immediately prior to extrusion, in order to account for potential variations caused by aging. Since PHB undergoes structural reorganization over time (Srubar et al., 2012; Di Lorenzo & Androsch, 2019), even at room temperature, using outdated DSC data would not accurately reflect the polymer's current thermal behavior.

3.4.2 Mechanical properties of the PHB (σ_u, E and ε)

A ZwickRoell Z100 Universal Testing Machine (UTM) was used to perform single fiber tensile tests (SFTT) for the determination of the tensile strength, elastic modulus, and elongation at break of the PHB fibers. The testing configuration is shown in Figure 3.11.



(a) UTM ZwickRoell Z100. (b) Load-cell configuration.

Figure 3.11: UTM and load-cell configuration used for the single-fiber tensile tests.

The load cell used had a maximum capacity of 500 N and a precision of ± 1%, allowing for the evaluation of fibers with considerably small diameters. An additional fixture was attached to the load cell (see Figure 3.11(b)) in order to improve the gripping of the small elements tested during the procedure. The tests were performed under displacement control, using a constant crosshead speed of 0.05 mm/s. Failure was defined as a drop in the measured force to 80% of the maximum value recorded during the test.

This setup represented a slight adaptation of the configuration proposed by (Curosu et al., 2017); however, aluminum plates were used on both sides of the fixture, along with sandpaper, to minimize slippage during testing.

A cyanoacrylate adhesive (La Gotita, Akapol) was used to fix the fiber to the plate and

was allowed to cure for at least 48 h prior to testing to ensure adequate bonding and prevent premature failure at the fiber–plate interface.

In this test, the tensile strength was defined as the maximum stress reached before failure, while the elongation at break corresponded to the maximum strain attained. The elastic modulus (Young's modulus) was calculated as the slope of the initial linear portion of the stress–strain curve.

3.4.3 Degradation of PHB

One of the key limitations of using PHB in cementitious materials is its susceptibility to degradation, which, while beneficial in many environmental applications, poses a challenge in this context. For the intended use as reinforcement in cement-based composites, it is essential to delay its degradation in order to ensure structural performance throughout the material's service life. If the PHB fibers degrade prematurely, they may reduce the embodied energy of the system but will affect the performance of the composites, such as FRC or ECC. Therefore, understanding and controlling its degradation under different conditions is a central focus of this research.

The following sections describe the methodologies employed to evaluate the main degradation mechanisms to which PHB fibers could be exposed during processing and end use.

3.4.3.1 Thermal degradation

Thermal degradation of PHB will be evaluated using DSC and TGA, as outlined in the thermal properties evaluation section. While DSC may detect early signs of thermal instability through anomalies in heat flow, TGA provides a direct assessment of degradation by measuring weight loss as a function of temperature.

3.4.3.2 Degradation by alkalis

Considering that the pore solution in concrete typically exhibits a pH close to 13, it is essential to assess the resistance of the PHB to this highly alkaline environment. Given that temperature significantly influences the rate of chemical reactions, the combined

effects of elevated pH and temperature must be evaluated.

The degradation protocol was applied at two temperatures: 20°C, representing ambient conditions, and 70°C, representing a commonly accepted maximum temperature for concrete during early-age curing in construction practice. This temperature limit is typically adopted to reduce the risk of delayed ettringite formation (DEF), a phenomenon associated with the suppression or alteration of normal ettringite formation during early cement hydration and which can lead to severe long-term damage in concrete. Therefore, assessing the material's stability under such conditions is critical to ensure its long-term performance and compatibility with cementitious environments.

The steps for assessing alkali-induced degradation of PHB are detailed below and are inspired by the methodologies proposed in (Silva et al., 2005; Yu et al., 2005):

a) A total of 15 vials (20 mL capacity) were prepared, with three replicates assigned to each exposure time (1 h, 6 h, 24 h, 72 h, and 168 h). All vials were dried at 100°C for 24 hours prior to use to register their dry mass.

b) After drying, the empty vials were weighed. Subsequently, a PHB sample with a mass between 20 and 50 mg was placed in each vial. The mass of the vial containing the sample was then recorded, and the sample mass was determined by difference.

c) The samples were dried at 30°C for 48 hours to ensure the complete removal of moisture before testing.

d) Subsequently, 2 mL of Lawrence solution (Silva et al., 2005) (pH approximately 12.9-13.0) was added to each vial. The vials were then sealed using crimp caps and stored in either a convection oven or a temperature controlled chamber, set at the designated testing temperatures (20°C or 70°C).

e) At each testing time, the vials were opened and the remaining solution was collected and stored in Eppendorf tubes for subsequent analysis by HPLC in future research. The PHB samples were dried again at 30°C for at least 48 hours.

f) After this final drying phase, the samples were weighed again. The mass loss between the pre and post-exposure conditions were used to quantify the degree of degradation caused by the alkaline environment.

g) Finally, the dried samples were stored in Eppendorf tubes for Scanning Electron Microscope (SEM) evaluation in future research.

Since the degradation rate should depend on the surface area in contact with the Lawrence solution, Brunauer-Emmett-Teller (BET) analysis was performed on PHB samples in different formats to quantify their exposed surface area and verify potential differences among them.

The BET method is one of the most widely used approaches for determining the specific surface area of porous solids and fine powders (Thommes et al., 2015). In this method, the surface area is estimated from gas adsorption data by evaluating the amount of adsorbate required to form a monolayer on the sample surface. In addition to specific surface area, adsorption isotherms can also be used to estimate pore size distribution through appropriate theoretical models (Thommes et al., 2015). The protocol related to this test is described in the following section.

BET protocol

An Anton Paar Nova-600 physisorption analyzer, shown in Figure 3.12, was used to determine the specific surface area and pore size distribution of the samples through N_2 adsorption isotherms at 77 K. The BET surface area was calculated from the adsorption isotherm, while the pore size distribution was obtained using the Density Functional Theory (DFT) model. Prior to the analysis, samples of approximately 150 mg were degassed to remove physically adsorbed moisture by heating from room temperature to 120°C at a rate of 10°C/min, followed by a 2-hour isothermal period at this temperature. Similar pretreatment and analysis conditions have been reported in the literature for porous solid characterization by N_2 physisorption at 77 K (Chen et al., 2021; Saab et al., 2022).



Figure 3.12: Nova-600, Anton Paar (Anton Paar, 2026)

3.5 Aging

PHB undergoes physical aging even at temperatures below glass transition. This process is characterized by molecular relaxation within the rigid amorphous phase, where residual mobility of polymer chains allows for conformational rearrangements that gradually reduce the free volume. As this volume decreases, the mobility of the polymer chains is restricted, leading to the stiffening of the material and an increase in brittleness over time. This phenomenon is associated to the formation of imperfect crystals within the interlamellar regions and the restriction of movement in the RAF, which becomes unable to dissipate energy by viscous flow (Santos et al., 2017). Importantly, experimental results from DSC analyses indicate that this embrittlement does not occur primarily due to secondary crystallization, but rather due to densification of the amorphous domains through physical aging mechanisms (Di Lorenzo & Androsch, 2019; Srubar et al., 2012).

The aging process was conducted in a climate-controlled chamber at 20°C. Aging was assessed through the evolution of thermal and mechanical properties and the resistance of PHB to alkali degradation. These measurements, described in the previous sections, were performed after aging periods of 7 (7DA) and 28 days (28DA). The PHAC was additionally evaluated after 100 days of aging (100DA). For DSC, the day 0 condition was analyzed using two heating scans, with the second heating thermogram taken as the response of the PHB in its initial, thermally standardized state. The aged specimens were then evaluated using the first heating scan at each aging time in order to capture the changes developed from this initial state during storage. This procedure allowed the thermal evolution associated with aging to be assessed relative to a common day 0 reference. Additionally, Fourier Transform Infrared Spectroscopy (FTIR) was performed using a Shimadzu IRPrestige-21 spectrometer, shown in Figure 3.13, to detect chemical structural changes in the polymer chains.



Figure 3.13: IR Prestige 21, Shimadzu (Center for Optical and Laser Materials Research, 2026).

FTIR protocol

FTIR analysis was conducted within the mid-infrared (MIR) spectral range using different sample-preparation approaches depending on the physical characteristics of the material analyzed. First, PHB films obtained by evaporation were analyzed directly in transmission mode without further preparation, since their transparency allowed the infrared beam to pass through the sample; in this case, air was used as the background. Second, transparent PHB sheets were prepared by placing approximately 20 mg of material (pellet or fiber) into a Specac die set without dilution in a KBr matrix. The material was then compressed using a manual hydraulic press (PRS15, Mega) at a force of 9 tons, producing transparent pellets with a diameter of 13 mm; for these measurements, air was also used as the background. Third, when the recovered PHB did not provide sufficient transparency, the sample was mixed with KBr at PHB:KBr ratios of 1:5 or 1:10 and analyzed by diffuse reflectance using a Pike DiffusIR cell. In this case, pure KBr was used as the background (Shimadzu Scientific Instruments, 2026). The infrared absorption spectra were obtained by averaging 50 individual scans in the wavenumber range of 4000 to 500 cm^{-1}. Similar FTIR approaches have been reported for PHB and related polyhydroxyalkanoate materials, including transmission measurements and pressed-sample preparations (Kamnev et al., 2018; Xu et al., 2002; Sato et al., 2009).

Table 3.1 summarizes the experimental testing performed on PHAC and PHB samples. This matrix compiles the characterization techniques applied to each material, distinguishing between baseline measurements and tests evaluated as a function of aging. All aging-dependent characterization techniques were performed at the initial condition (Day 0), after 7 days of aging, and after 28 days of aging. For PHAC fiber, an additional evaluation was performed after 100 days of aging.

Table 3.1: Experimental test matrix.

Test	**PHAC Fiber**	**PHB Film**	**PHB Fiber**
Baseline characterization (single condition)			
Density	✓	-	✓
Molecular weight	-	✓	✓
Purity	✓	✓	✓
BET surface area	✓	✓	✓
Aging-dependent characterization			
DSC	✓	✓	✓
TGA	✓	✓	✓
SFTT	✓	-	✓
Alkali degradation	✓	✓	✓
FTIR	-	✓	✓

Chapter 4

Production of PHB Films and Fibers

4.1 Bacterial kinetics

Batch kinetic in shake flasks was performed in triplicate to evaluate substrate consumption and formation of biomass and PHB under controlled conditions. The temporal profiles of biomass, fructose, and PHB content are presented in Figure 4.1.

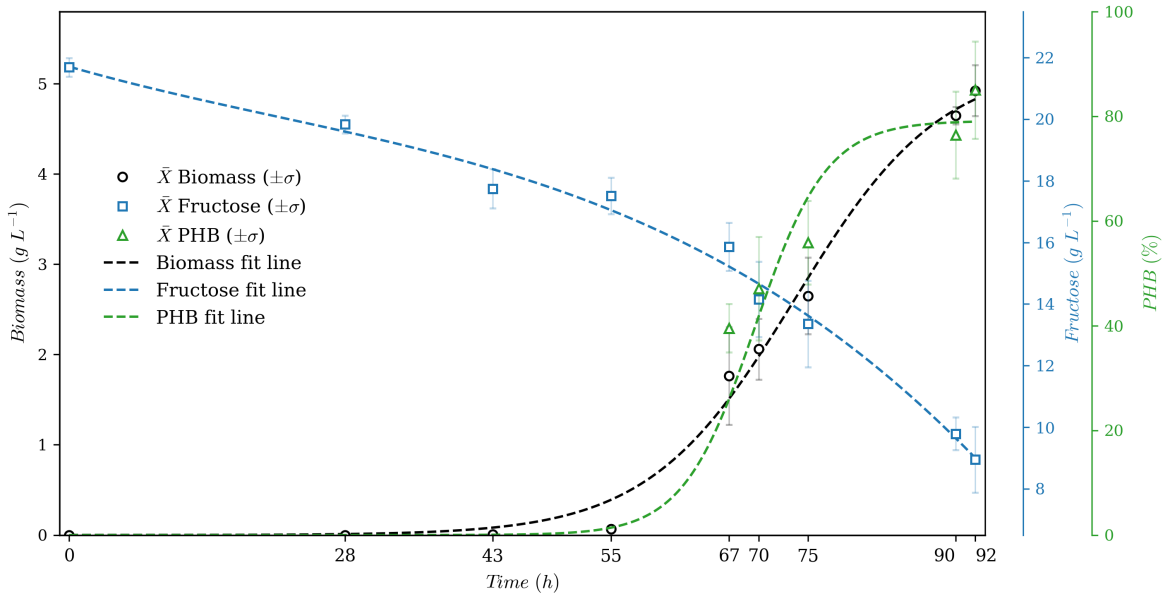


Figure 4.1: Temporal profiles of biomass concentration, fructose consumption, and intracellular PHB accumulation obtained from triplicate kinetic experiments.

The cultivation profile of *Cupriavidus necator* shows a clear transition between bacterial growth and intracellular PHB accumulation. During the initial lag phase, up to approximately 43 h, biomass concentration remained nearly constant, while fructose was consumed slowly and PHB accumulation was negligible, indicating cellular adaptation to the culture conditions. After this period, the culture entered an active growth phase, characterized by a rapid increase in biomass and a higher fructose consumption rate. Based on the initial biomass yield and the use of 1 g of ammonium sulfate, biomass formation was expected to proceed up to approximately 1.5 g L^{-1} before nitrogen limitation became dominant and PHB accumulation was strongly promoted. However, the experimental profile indicates that PHB accumulation began slightly before this expected biomass threshold, becoming evident from approximately 65 h onward. At later cultivation times, between approximately 75 and 92 h, the rate of PHB accumulation progressively decreased as the intracellular polymer content approached its maximum.

Direct ammonium measurements were not successfully obtained in these experiments due to analytical interference observed during an enzymatic assay, which led to unreliable absorbance readings. Nevertheless, the biomass yield with respect to ammonium sulfate was estimated through the procedure previously described.

Based on these experiments and procedures, biomass yields with respect to fructose ($Y_{X/S}$) and ammonium sulfate ($Y_{X/N}$), PHB yield ($Y_{PHB/S}$), and the specific growth rate (μ) were estimated for each replicate. These results are shown in Table 4.1.

Table 4.1: Summary of biomass yields, PHB accumulation, and specific growth rate obtained from triplicate kinetic experiments.

Flask	**Kinetic and yield parameters**				
	$Y_{X/S}$ **(g/g)**	$Y_{X/N}$*** (g/g)**	**PHB (%)**	$Y_{PHB/S}$ **(g/g)**	μ **(h^{-1})**
Flask 1	0.39	1.08	77.00	0.53	0.22
Flask 2	0.41	1.28	82.71	0.43	0.23
Flask 3	0.41	1.20	79.21	0.59	0.23
Mean $\pm\sigma$	0.40 ± 0.01	1.19 ± 0.10	79.64 ± 2.88	0.52 ± 0.08	0.23 ± 0.01

*All ammonium-based yields ($Y_{X/N}$) were estimated by inverse calculation due to the lack of direct ammonium measurements.

Initially, the design process relied on literature-based yield coefficients of 0.4 g/g for fructose and 1.5 g/g for ammonium sulfate. While the assumed fructose yield was consistent with the experimental observations, the ammonium based yield was found to be overestimated. This discrepancy became evident during the development and operation of the fed batch reactors, where deviations from the expected biomass growth and PHB production were observed.

Based on these observations, the kinetic study was conducted between reactor runs R10 and R11, within a total of 13 fed-batch fermentations performed throughout the experimental campaign. Unlike the initial design assumptions, the ammonium sulfate yield reported in this section was obtained through inverse estimation based on the experimentally measured biomass and PHB production. This approach enabled the estimation of the actual amount of ammonium sulfate required to achieve the target PHB production of 15 g/L.

The values of μ showed low variability between replicates, with an average of 0.23 h^{-1}. This value is within the expected range for *Cupriavidus necator* cultivated on sugars, where growth rates are typically reported between 0.2 and 0.3 h^{-1}. In particular, values close to 0.21 h^{-1} have been reported for *Ralstonia eutropha* under batch cultivation conditions (Marangoni et al., 2001; Wang et al., 2007). Therefore, the obtained μ values indicate that the system operated under suitable growth conditions without significant inhibition or nutrient limitation during the exponential phase.

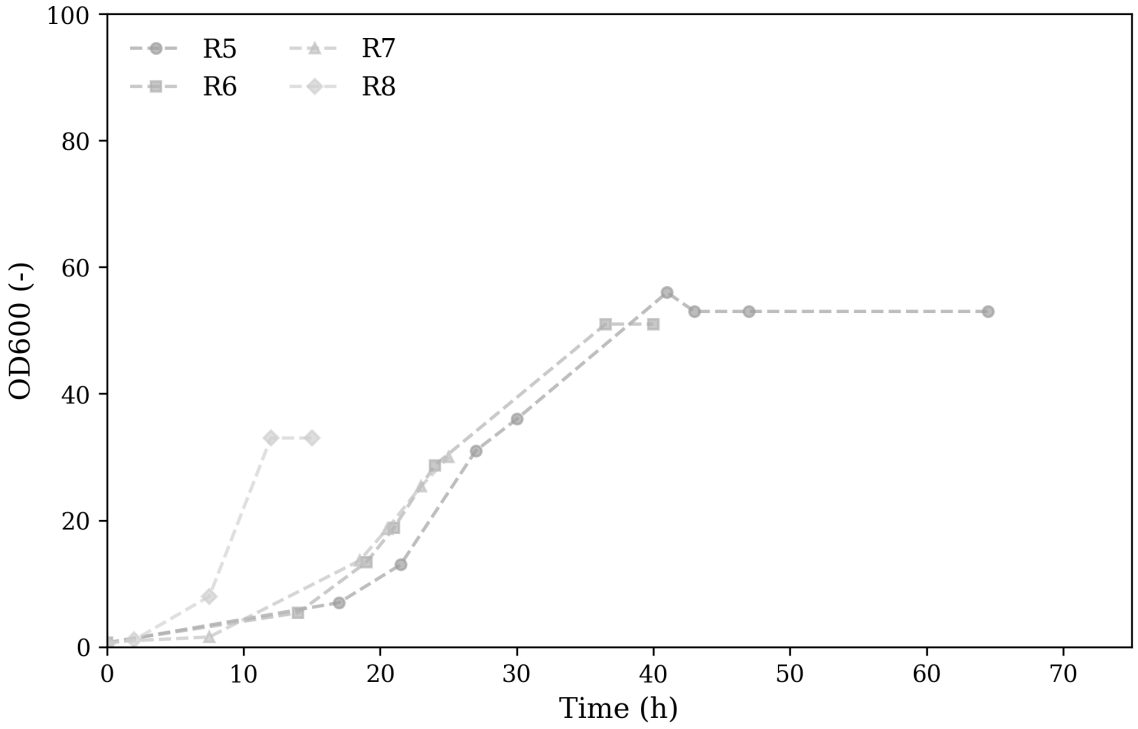
Regarding PHB accumulation, the obtained values ranged between 77.0% and 82.7%, with an average of 79.6%. These values are consistent with reported PHB contents for *C. necator* under nitrogen-limited conditions, where intracellular polymer fractions commonly exceed 70% of cell dry weight within 24 h of accumulation. Additionally, PHB yields on carbon substrate in the range of 0.4-0.5 g/g have been reported for *C. necator* under controlled conditions (Yousuf & Winterburn, 2016). This agreement indicates that the cultivation strategy effectively promoted PHB synthesis.

4.2 Fed-batch Fermentations

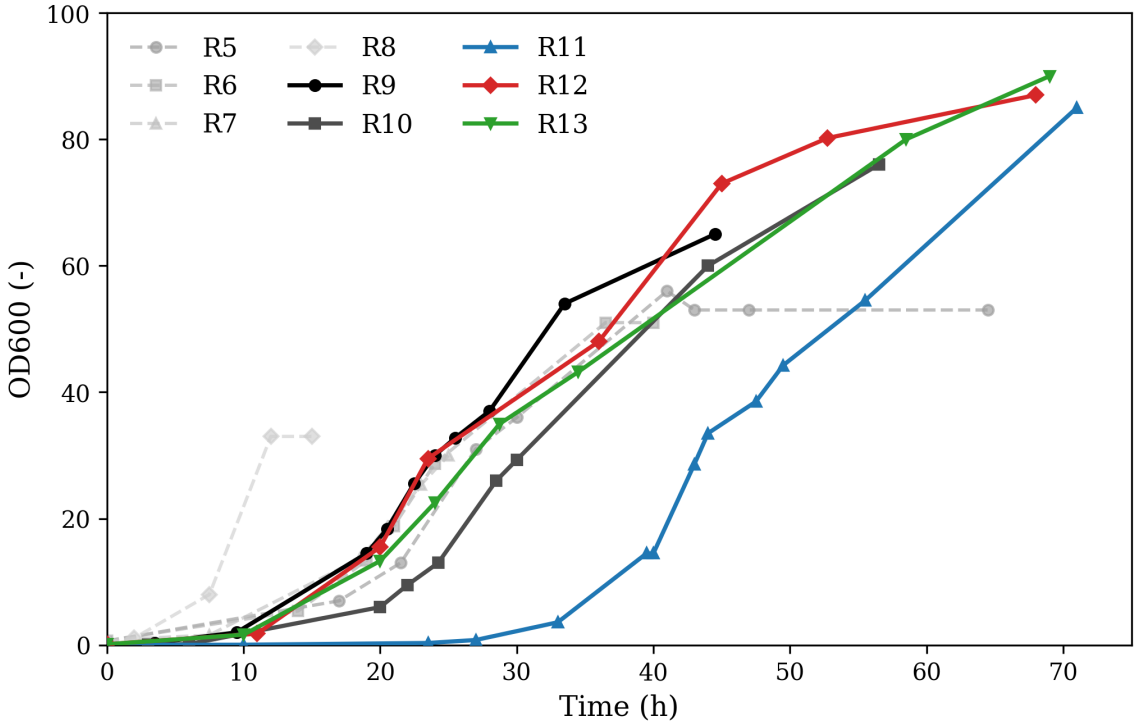
A total of 13 fed-batch reactor runs were performed during the experimental campaign in order to establish a robust protocol for PHB production with *Cupriavidus necator*. A detailed reactor-by-reactor description, including the operational issues encountered and the corrective actions implemented throughout the campaign, is provided in Appendix C. In summary, several operational problems were faced during reactor operation, preventing the experimental objectives from being achieved in a number of runs. The main issues were: i) culture loss due to excessive foam generation under high agitation (R2-R3), ii) oxygen limitation caused by excessive biomass growth resulting from an initial misinterpretation of the ammonium sulfate amounts added to the medium (R5-R6), iii) contamination events that caused premature fructose depletion and stagnation of the culture (R7-R8), and iv) failure to reach the target PHB production due to an incorrect ammonium sulfate yield assumption used in the experimental design (R9-R10).

These challenges were progressively addressed throughout the experimental campaign by improving foam control, modifying the ammonium sulfate design basis according to the kinetic analysis presented in Section 4.1, and improving the control of contamination. From reactor R9, gentamicin was incorporated into the cultivation protocol to prevent further contamination, taking advantage of the intrinsic resistance of RE H16 to this antibiotic. PHB was successfully produced in reactors R9-R13, and the polymer recovered from these fermentations was subsequently used in the extraction, processing, and characterization stages of this work.

Figure 4.2 shows the OD profiles obtained during the fed-batch campaign. Figure 4.2(a) illustrates the operational problems observed in the intermediate runs, whereas Figure 4.2(b) shows the complete campaign and the transition toward stable operation. After correcting the ammonium sulfate requirement, reactors R11-R13 reached maximum OD values between 85 and 90 and produced 14.18, 15.26, and 17.39 g L^{-1} of PHB, respectively, with fermentation times within approximately 68-71 h. The target production of 15 g L^{-1} of PHB was achieved in the last two reactors.



(a) OD profiles for reactors R5-R8.



(b) OD profiles for reactors R5-R13.

Figure 4.2: OD profiles obtained during the fed-batch fermentation campaign.

Table 4.2 summarizes the performance of the PHB-producing reactors used in the subsequent stages of the research.

Table 4.2: Performance of the PHB-producing reactors.

Reactor	**OD**	**Volume (mL)**	**Dry biomass (gL^{-1})**	**PHB (%)**	**PHB (gL^{-1})**
R9	65	940	15.88	63.48	10.08
R10	76	880	15.18	63.43	9.63
R11	85	1000	19.34	73.31	14.18
R12	87	985	22.80	66.91	15.26
R13	90	1000	24.46	71.09	17.39

These results demonstrate that once foaming, contamination, oxygen transfer limitations, and the ammonium sulfate design basis were addressed, the process became reproducible and capable of reaching the target PHB production level.

4.3 Extraction yield

Figure 4.3 presents the PHB recovery yields obtained from chloroform-based extractions.

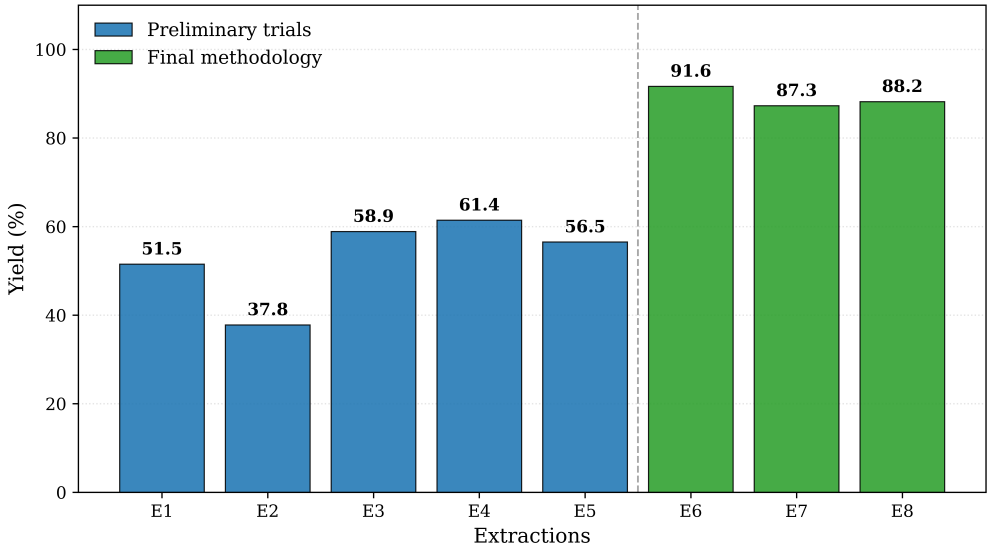


Figure 4.3: PHB recovery yields obtained during the preliminary chloroform extraction trials and after implementation of the final methodology.

Preliminary trials E1-E5 were conducted at a smaller scale using limited amounts of PHB-containing biomass. These trials focused on evaluating simple filtration systems, including metal mesh strainers and gauze used as filtering media. However, a considerable amount of PHB was retained within these materials, contributing to product losses. In addition, the extraction conditions used during these trials were not sufficiently efficient. Recovery yields were determined either gravimetrically from the extracted polymer mass or indirectly through GC analysis of the solvent phase during extraction. Since different quantification methods were used, these results should be interpreted as indicators of process development rather than as directly comparable experimental replicates.

The final protocol reported in this study was subsequently evaluated using a larger amount of biomass. This protocol comprised biomass preparation, chloroform extraction, vacuum filtration, solvent recovery by distillation, and final evaporation. Extraction E6 was the first trial performed using the complete methodology. Based on the favorable recovery obtained in this extraction, the same protocol was maintained for extractions E7 and E8, which also showed high recovery yields. In these three extractions, the recovered PHB was precipitated by solvent evaporation and was therefore obtained in the form of transparent films, as shown in Figure 4.4.

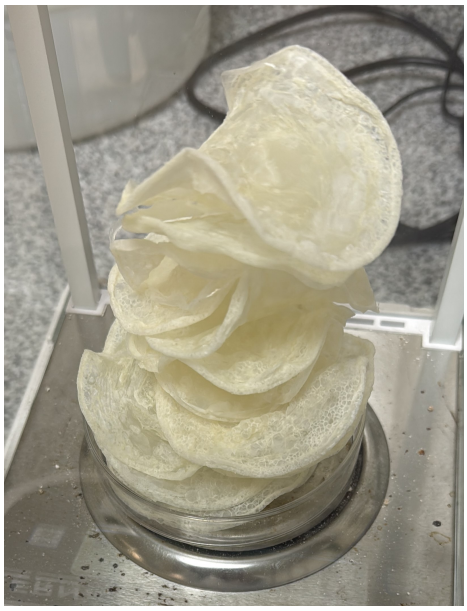


Figure 4.4: PHB films obtained after chloroform extraction and solvent evaporation.

4.4 Extrusion process

The preliminary extrusion trials with PHAC and PHB/PLA fibers showed that the modified nozzle was capable of producing fibers with substantially smaller diameters than the original commercial filaments. However, this result was not immediate. The first trials revealed that the extrusion window was strongly affected by the presence of the modified nozzle. In some cases, the melting temperature obtained by DSC or the printing temperature recommended by the manufacturer was not sufficient to ensure stable flow through the modified outlet. Although the polymer softened inside the extruder, the added nozzle section did not always reach the temperature required to maintain the material in a molten state, leading to premature solidification inside the nozzle, which caused clogging and interrupted the extrusion process. Conversely, when the temperature was increased excessively, the material exited the nozzle and exhibited very low viscosity, preventing stable filament formation.

For this reason, each material required an empirical adjustment of the extrusion temperature. The selected temperatures were defined by trial and error, using the lowest temperature that allowed continuous flow without clogging, while maintaining the viscosity needed for filament formation. The final temperatures used for the commercial fiber materials are summarized in Table 4.3.

Table 4.3: Extrusion temperatures selected for each commercial fiber material.

Material	**Extrusion temperature (°C)**
PHAC fiber	175
PHB/PLA fiber	185

After adjusting the extrusion temperature, continuous fiber formation was achieved for the commercial materials. Re-extrusion through the modified nozzle produced a clear reduction in filament diameter, with fibers generally reaching values close to the target diameter of 0.5 mm. This reduction is illustrated in Figure 4.5, where the original commercial PHB/PLA filament is compared with the re-extruded fiber. The visible difference between both spools confirms the effectiveness of the modified extrusion setup in producing thinner fibers.



Figure 4.5: Comparison between the original commercial PHB/PLA filament and the thinner fiber obtained after re-extrusion.

Another challenge of this stage was to ensure material continuity during extrusion. The extruder required a minimum amount of material, approximately 8 g, to fill its internal cavity and initiate extrusion. Once this volume was reached, additional material had to be supplied continuously to maintain pressure and avoid interruptions in the filament. The screw speed was kept at the minimum setting throughout the trials, since the outlet pressure depended both on the screw-driven displacement and on the amount of molten material reaching the nozzle. Under these conditions, stable extrusion required a balance between feed continuity, screw pressure, and material viscosity.

Even after continuous flow was achieved, material accumulation at the nozzle outlet was frequently observed. This accumulation interfered with the formation of a continuous filament and could lead to local agglomeration immediately after the material exited the nozzle, as shown in Figure 4.6. When this occurred, manual assistance was required to guide the fiber away from the outlet and restore continuity. However, because the fiber was still partially molten during collection, manual pulling introduced additional stretching and produced localized reductions in diameter. In some isolated segments, this effect led to diameters below the target value, reaching approximately 0.25 mm.

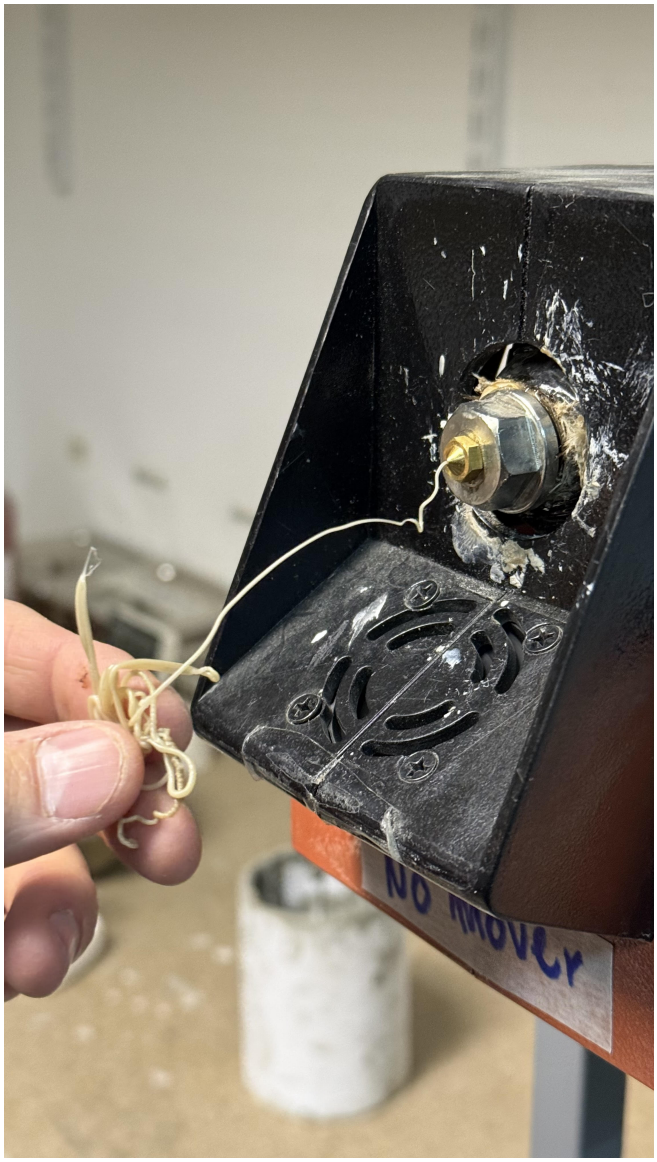
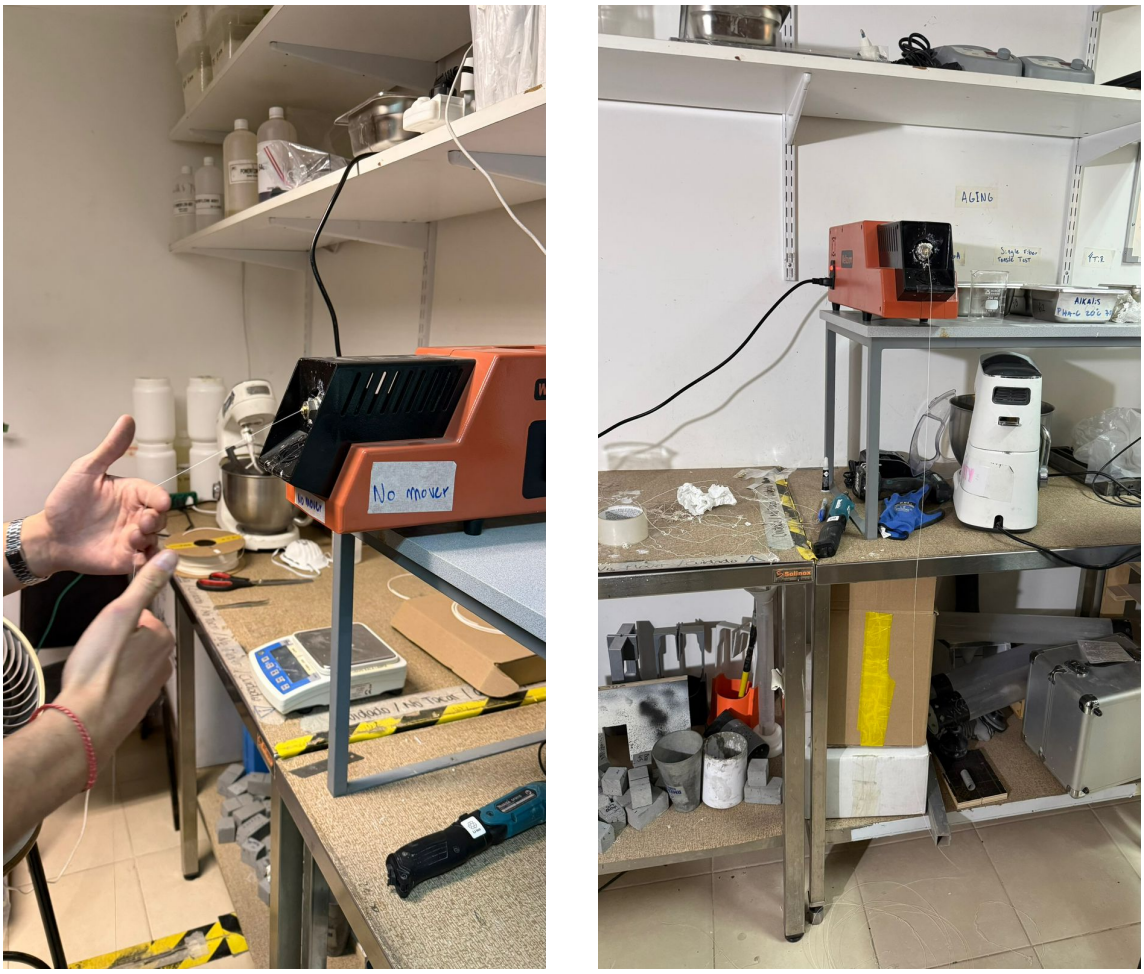


Figure 4.6: Material accumulation at the nozzle outlet during extrusion.

The final fiber diameter was therefore influenced by the way the material was collected after exiting the nozzle. When the fiber descended without interference and undisturbed, the final diameter was closer to the opening of the nozzle. In contrast, manual assistance helped guide the fiber away from the nozzle to prevent accumulation and improve short-term continuity, but it also increased geometric variability along the fiber. This contrast between manually assisted collection and gravity-driven collection is shown in Figure 4.7, and highlights that fiber collection was a critical factor for maintaining both continuity and diameter uniformity.



(a) Manually assisted fiber collection.

(b) Gravity-driven fiber collection.

Figure 4.7: Fiber collection behavior observed during extrusion trials with commercial materials.

An additional limitation was observed in the lower collection zone. When the extruded fiber accumulated without additional cooling, it retained part of the viscosity associated to the molten state. As a result, neighboring fiber segments adhered to one another, forming agglomerated regions and reducing the usability of the collected material. This behavior is shown in Figure 4.8. To mitigate this issue, the collection system was modified so that the fiber could fall into cold water. This additional step promoted faster solidification and allowed the fiber to sink after reaching the collection bath, reducing contact with subsequently falling segments and limiting agglomeration.



Figure 4.8: Fiber agglomeration observed in the collection zone when no water bath was used.

Overall, these observations show that successful fiber production depended not only on reducing the outlet diameter but also on controlling the extrusion and collection conditions. These factors are relevant because loss of continuity, agglomeration, and excessive diameter heterogeneity could compromise subsequent fiber characterization. Therefore, the preliminary trials established the operational criteria required to obtain fibers suitable for subsequent characterization and processing.

After the extrusion procedure had been refined using commercial materials, the in-house produced PHB was evaluated as a feedstock for fiber production. The first extrusion attempt was carried out using the PHB recovered as a film by evaporation-based precipitation. Approximately 28 g of material were available for this trial; however, stable processing could not be achieved. During the initial temperature-adjustment stage, most of the available material was consumed without a continuous filament formation. Instead of forming a self-supporting fiber, the material exited the nozzle with an excessively low viscosity and collapsed after extrusion.

Based on these results, extrusion trials with this material were discontinued. The behavior observed during processing suggested that the poor extrudability was not only related to temperature adjustment, but also to the composition of the recovered material. Analyses carried out in parallel with the extrusion trials supported this interpretation. Purity measurements of the evaporation-recovered PHB showed values between 80 and 85%, indicating that a significant fraction of the material corresponded to other components. In addition, the thermal analyses also showed deviations from the expected behavior of PHB, including altered melting-related peaks in DSC and mass losses between 60°C and 120°C in TGA. These results indicated the presence of additional phases or residual compounds that likely interfered with melt processing and prevented stable fiber formation.

The original PHB films obtained after evaporation-based recovery were transparent, as shown previously in Figure 4.4. However, after exposure to the extrusion conditions, the material progressively developed a brown to nearly black coloration. This color change indicated that thermally induced degradation or non-enzymatic browning reactions occurred during processing. Considering that PHB originally contained bacterial cells,

the non-PHB fraction was likely composed of chloroform-soluble residual cellular components, including lipids, hydrophobic membrane compounds, polysaccharide-derived residues, and possibly proteins. In this context, residual fructose or polysaccharide-derived sugars could react with amino groups from proteins or other nitrogen-containing compounds through Maillard-type reactions, producing brown degradation products during heating (Hodge, 1953; Dills, 1993).

This evolution is shown in Figure 4.9. From left to right, the first beaker contains fibers obtained from the locally produced PHB, which exhibited a clear brown coloration, limited length, and high fragility. The second beaker contains PHB with a high content of degradation products, showing an almost black coloration. The third beaker contains a mixture of partially clean PHB and material with mild degradation. The fourth beaker contains material recovered from the extruder after processing at a lower temperature, corresponding to material remaining inside the equipment that had not fully melted. Finally, the fifth beaker contains clean PHB film cut into small pieces before extrusion. This sequence illustrates the degradation and compositional changes experienced by the material during its passage through the extruder.



Figure 4.9: Visual evolution of the locally produced PHB during extrusion trials, showing fibers, degraded material, partially degraded material, recovered non-melted material, and clean PHB film before extrusion.

In addition, possible lipidic or hydrophobic cellular residues may have contributed to the excessive fluidity observed at the nozzle. Although these compounds were not directly identified, PHB-producing bacterial cells contain several non-PHB components that can be partially recovered with hydrophobic extraction routes, including membrane lipids, free fatty acids, phospholipids, glycolipid-derived fractions, and other hydrophobic cellular residues. Depending on their chemical structure, some of these lipidic fractions can present melting or softening transitions well below the extrusion temperature used in this study (Kerr et al., 2015). Therefore, if present as residual non-PHB phases, they could have remained in a liquid or low-consistency state within the processing range applied, modifying the apparent melt consistency of the recovered material and contributing to the loss of filament stability. Since their exact identity was not determined, this interpretation should be considered an explanation to be confirmed by further studies.

Taken together, the darkening of the material, the excessive fluidity at the nozzle, and the absence of stable filament formation indicate that the evaporation-recovered PHB did not present the compositional quality required for direct melt extrusion.

As a result, direct extrusion of the evaporation-recovered PHB was abandoned, and a second recovery strategy based on antisolvent precipitation was proposed. The objective of this approach was to reduce the impurity content of the recovered polymer and improve its suitability for melt processing. For this purpose, the PHB film was redissolved in hot chloroform and then precipitated using cold ethanol as an antisolvent. The purified PHB obtained from this procedure was subsequently characterized to verify the improvement in material quality. After purification, the PHB purity increased to values close to 98%, indicating that a substantial fraction of the impurities present in the evaporation-recovered material was successfully removed. Consistently, the thermal analyses of the purified material no longer showed the alterations observed in the evaporation-recovered PHB and instead presented a response consistent with the expected thermal behavior of PHB.

The purified PHB was also evaluated by extrusion. For this trial, approximately 3 g of purified material were introduced into the extruder and complemented with another

material in order to fill the internal cavity and generate the pressure required for extrusion. Under these conditions, fiber formation was possible; however, the initial extruded material presented an intense brown coloration, which was associated with degradation or caramelization reactions during processing. In addition, because a second material was required to complete the feed and promote extrusion, the resulting fiber may have been formed from the combined melting of both materials inside the extruder, even though the locally produced purified PHB was introduced first so that the following material would push it toward the nozzle. Therefore, this result cannot be considered definitive evidence that the locally produced PHB can be independently extruded into fibers. Further trials with a larger amount of purified material are required to confirm its processability. Moreover, the brown coloration observed at the beginning of the extrusion indicates that a small residual fraction was still susceptible to thermal degradation.

Personal communication with commercial manufacturers also indicated that PHB intended for fiber production commonly requires stabilizing additives before pelletization and extrusion. These additives may include nucleating agents and antioxidants, which improve thermal stability, crystallization behavior, and processability during melt processing. Since the identification, formulation, and optimization of these additives were outside the scope of this thesis, a commercial thermoplastic-grade PHB pellet was selected to continue the fiber-production stage. This decision ensured that the experimental program could still include PHB fibers suitable for characterization, while keeping the additive-design challenge as a limitation and future development of the locally produced PHB route.

For this purpose, Enmat Y3000P PHB pellets supplied by Helian Polymers, Netherlands, were selected because they correspond to a pure PHB grade specifically formulated for thermoplastic applications. According to information provided by the supplier through personal communication, the pellet formulation contains a nucleating agent and an antioxidant intended to facilitate crystallization and improve stability during melt processing.

The commercial PHB pellet was successfully extruded using a processing temperature of

185 °C, producing a continuous fiber, as shown in Figure 4.10. This confirmed that the extrusion setup was suitable for PHB fiber production when the material was supplied in a thermoplastic-grade formulation.



Figure 4.10: Continuous PHB fiber obtained by extrusion of the commercial Enmat Y3000P PHB pellet.

This result represents a discontinuity in the original objective of producing PHB fibers entirely from a locally produced bacterial polymer. Nevertheless, it does not invalidate the previous stages of the work. One of the main objectives of this research was to establish a reliable procedure for producing and extracting PHB from bacterial fermentation, and this was achieved through the development and refinement of the extraction methodology. The recovered PHB provided a valuable basis for understanding the limitations associated with purity, thermal stability, and melt processability.

It should also be considered that PHB is a highly tunable polymer, whose final behavior can be strongly modified by relatively small changes in formulation, purification, and processing design. Therefore, the production and extraction procedure developed in this work provides a robust foundation for future studies aimed at locally producing PHB with improved processability and specific characteristics. The specific challenge of defining the additive package required for direct extrusion of laboratory-produced PHB, including stabilizers, nucleating agents, and antioxidants, remains outside the scope of this thesis. However, since the experimental program also required the characterization and evaluation of PHB fibers, the use of the commercial thermoplastic-grade PHB pellet allowed this objective to be fulfilled.

Chapter 5

Evaluation of PHB Films and Fibers

5.1 Physicochemical properties of the PHB

This section presents the results of the analyses conducted on three specimens: the PHB produced in-house (native film), the commercial PHB processed into fibers, and the PHAC fiber used both as a reference material and to test and refine the experimental protocols.

5.1.1 Density

PHAC fiber

The density of the PHAC fiber was experimentally determined in order to compare the obtained value with the density reported by the manufacturer, namely 1.24 g/cm^3 (colorFabb, 2023). The results are presented in Table 5.1.

Table 5.1: Density measurements obtained for the PHAC fiber.

Test	**Density parameters**	
	Sample mass (g)	**Fiber density (g/cm^3)**
1	1.01	1.31
2	1.05	1.18
3	1.04	1.27
Mean $\pm\sigma$	1.03 ± 0.02	1.25 ± 0.07

The experimental result was consistent with the density reported by the manufacturer, considering the observed measurement variability. This agreement is particularly relevant because the experimental procedure adopted in this work combined two ASTM-based approaches into a modified methodology. The consistency with the manufacturer's specification therefore supports the reliability of the adopted procedure and its suitability for determining the density of the analyzed fiber material.

PHB fiber

Table 5.2 presents the measured density of the PHB fiber.

Table 5.2: Density measurement obtained for the PHB fiber.

Test	**Density parameters**	
	Sample mass (g)	**Fiber density (g/cm^3)**
1	1.01	1.15
2	1.05	1.24
3	1.01	1.36
Mean $\pm\sigma$	1.02 ± 0.02	1.22 ± 0.12

Despite the fact that slightly higher variability was observed among the replicate measurements, the obtained density remained consistent with the expected range for PHB-based materials, indicating that the extruded fiber exhibited a density response compatible with this polymer.

5.1.2 Molecular weight

Native film and purified PHB

The evaporation-recovered native film did not dissolve completely in the mobile phase after three days of agitation, and no chromatographic signal was obtained from its supernatant. Therefore, its molecular-weight parameters could not be determined.

The purified PHB presented an apparent M_w of 567.2 kDa, an apparent M_n of 167.9 kDa, and a dispersity of 3.38. Although the purity and TGA results showed that purification produced a cleaner material with a more defined thermal response, the effect of this process on the molecular-weight distribution could not be evaluated. The absence of a valid measurement for the native film prevents determining whether purification preserved, reduced, or otherwise modified the polymer chain length. Thus, the improvement in compositional and thermal quality cannot be accompanied by a direct assessment of molecular-weight evolution.

Commercial PHB pellet

The commercial PHB pellet did not dissolve completely under the selected sample-preparation conditions, and no chromatographic signal was obtained from its supernatant. Since the pellet was analyzed without prior grinding, insufficient solvent penetration may have limited its dissolution. Its initial molecular weight could not be determined and was not reported by the supplier. This analytical limitation prevented a direct comparison between the material before and after fiber extrusion.

PHB fiber

The extruded PHB fiber presented an apparent M_w of 236.5 kDa, an apparent M_n of 41.1 kDa, and a dispersity of 5.75. The comparatively high dispersity indicates that the processed material contained a broad molecular-weight distribution.

For reference, Li et al. (2021) reported an M_w of 269.5 kDa for ENMAT Y3000 PHB manufactured by Tianan Biologic Materials, China, which corresponds to the raw material used in the Helian Polymers pellet evaluated in this work. The value measured

for the fiber was approximately 12% lower and remained within the same order of magnitude. Considering that the material experienced pelletization before being supplied and was later subjected to melt extrusion during fiber production, this difference is compatible with a moderate reduction in molecular weight after thermal processing. However, the specific molecular-weight loss from pellet to fiber cannot be quantified because the M_w of the pellet itself, corresponding to the intermediate state between pelletization and fiber extrusion, was not determined.

5.1.3 Purity

Purity was evaluated as part of the physicochemical characterization of the materials analyzed in this work, in order to estimate the fraction of PHB present in each case. This parameter is relevant because it provides additional information regarding the composition of the PHAC fiber, the quality of the polymer obtained experimentally in native film form, and the composition of the commercial PHB supplied in pellet form and subsequently processed into fibers. The following sections present the results obtained for these materials.

PHAC fiber

The purity of the PHAC fiber is presented in Table 5.3.

Table 5.3: PHB purity measured for the PHAC fiber.

Test (N°)	**Sample mass (mg)**	**PHB mass (mg)**	**Purity (%)**
1	10.3	9.22	89.51
2	12.4	11.24	90.65

The obtained values indicate that PHB is the main constituent of the commercial fiber, although it does not account for its entire composition, with measured purities close to 90%. This agrees with the information provided by the manufacturer, who indicated that the commercial fiber also contains another type of PHA, a mineral filler, and a coating of titanium dioxide.

Native film and purified PHB

The purity results obtained for PHB recovered by evaporation and after ethanol-assisted precipitation after re-dissolution in chloroform are presented in Table 5.4.

Table 5.4: Purity of recovered PHB samples.

Sample	**Sample mass (mg)**	**PHB mass (mg)**	**Purity (%)**
Film 1	12.8	11.29	88.21
Film 2	18.6	15.31	82.29
Purified PHB	15.0	14.69	97.95

Film 1 and Film 2 correspond to PHB samples recovered after solvent evaporation, whereas purified PHB corresponds to the material obtained after ethanol precipitation. The initial measurements indicate that the PHB recovered by evaporation already presented a relatively high purity; however, based on the processing difficulties observed during extrusion, an additional purification step was incorporated using cold ethanol as an antisolvent. This procedure increased the purity of the recovered PHB, providing a cleaner material for subsequent processing and characterization stages.

Although purification improved the measured PHB content, the subsequent extrusion trial still showed brown coloration at the beginning of processing, indicating that a small residual fraction remained susceptible to thermal degradation. It should also be noted that the purification step would slightly penalize the extraction yields obtained from the evaporation-based recovery route, since part of the recovered material corresponds to impurities. Nevertheless, the recovery remained relatively high, and the improvement in material quality justified the incorporation of this additional step.

Commercial PHB pellet

Considering that extrusion remained a key limitation for the recovered PHB, the commercial PHB selected for fiber production was first evaluated in its original pellet form. This analysis was carried out to verify the polymer content of the purchased material before processing. The results are presented in Table 5.5.

Table 5.5: PHB purity measured for the commercial PHB pellet.

Test (N°)	Sample mass (mg)	PHB mass (mg)	Purity (%)
Pellet 1	15.6	15.53	99.54
Pellet 2	12.2	11.68	95.75

The measured values confirmed that the purchased material presented a high PHB content, consistent with its use as a thermoplastic-grade pellet intended for melt processing.

PHB fiber

After extrusion, the PHB fiber obtained from the commercial pellet was also analyzed to assess whether processing affected the quantified PHB fraction. The results are presented in Table 5.6.

Table 5.6: PHB purity measured for the PHB fiber.

Test (N°)	Sample mass (mg)	PHB mass (mg)	Purity (%)
Fiber 1	11.7	11.60	99.18
Fiber 2	13.2	12.55	95.06

The fiber samples presented comparable purity to the original pellet, indicating that extrusion did not measurably affect the quantified PHB fraction. This result supports that the commercial material preserved its composition during fiber production.

5.1.4 Porosity and surface area

PHAC fiber

The adsorption-desorption isotherm, the low-pressure region used for BET analysis, and the pore size distribution obtained by DFT for PHAC are shown in Figures 5.1, 5.2, and 5.3, respectively. The main parameters obtained from the analysis are summarized in Table 5.7.

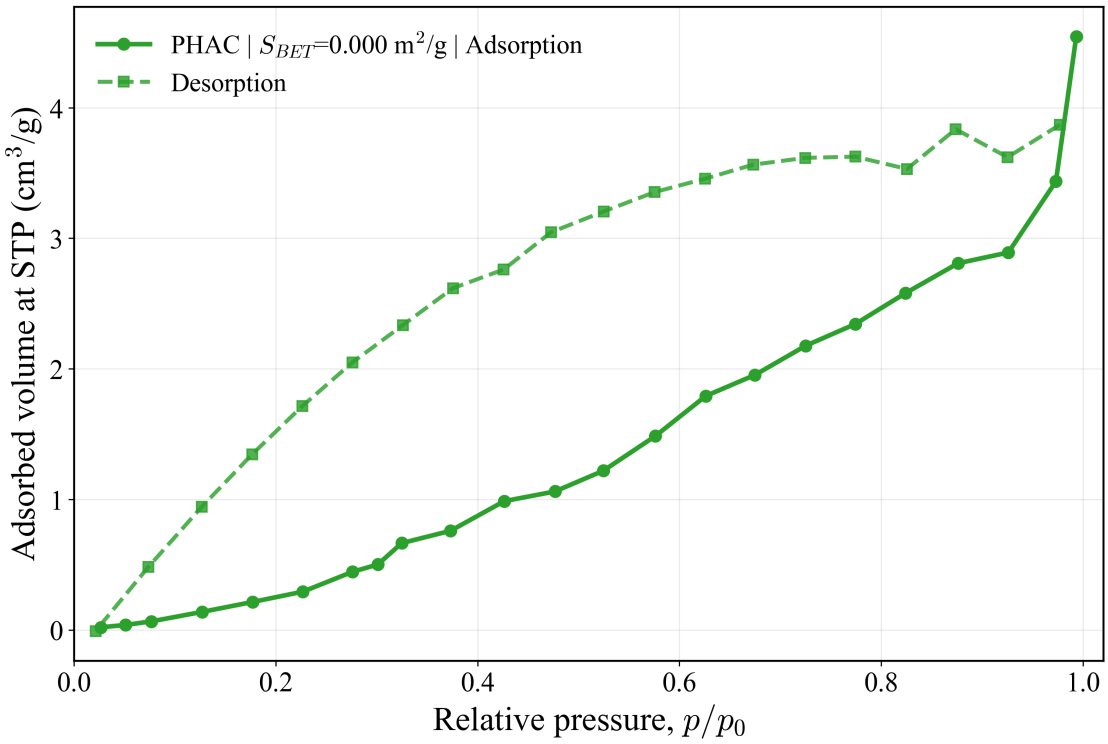


Figure 5.1: N_2 adsorption-desorption isotherm obtained for the PHAC fiber at 77 K.

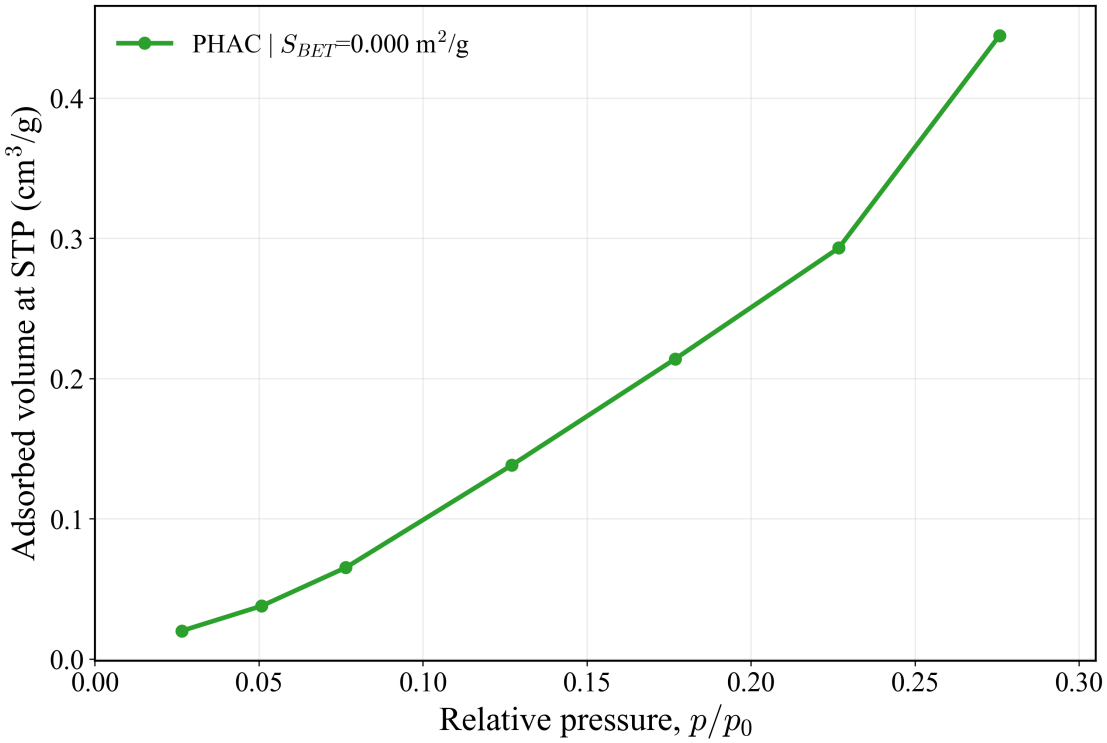


Figure 5.2: Low-pressure region of the N_2 adsorption isotherm used for BET analysis of the PHAC fiber.

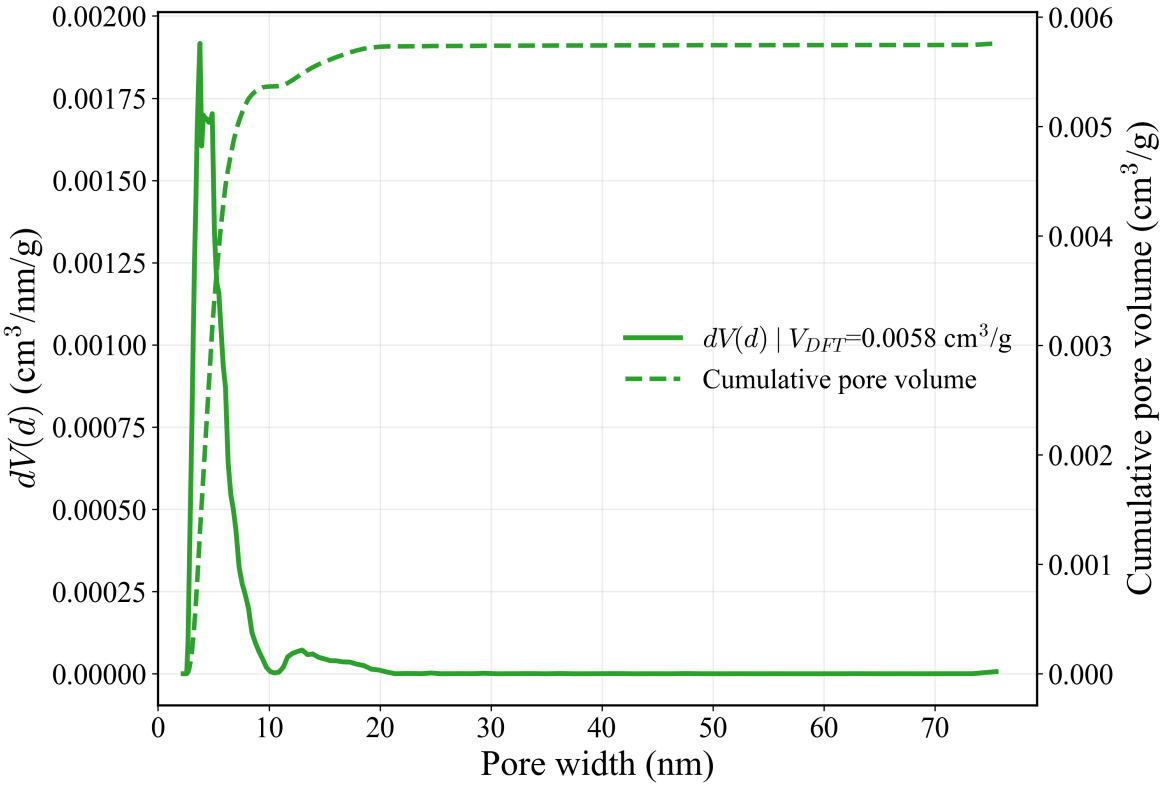


Figure 5.3: DFT pore size distribution and cumulative pore volume obtained for the PHAC fiber.

Table 5.7: Porosity parameters obtained from N_2 physisorption analysis of the PHAC fiber.

Parameter	**Value**	**Unit**
BET surface area	0.0000	m^2/g
BET constant (C)	-0.4201	-
DFT pore volume	0.0058	cm^3/g

The PHAC fiber exhibited limited N_2 adsorption, particularly within the low-pressure region used for BET analysis, as shown in Figure 5.2. The surface area reported by the instrument was essentially zero; however, the corresponding BET constant was negative, indicating that the BET fit was not physically valid. Therefore, this value should not be interpreted as an exact surface-area measurement, but rather as evidence that the material did not provide a reliable monolayer adsorption region.

A negative or physically invalid BET constant can result from an inadequate fitting

range, experimental noise, or the absence of a suitable BET region. In this case, the issue was not attributed to the selected fitting interval, since the points used for BET analysis showed very limited adsorption. Although the adsorbed volume increased at high relative pressures in Figure 5.1, this part of the isotherm is not appropriate for BET surface-area calculation because it may involve multilayer adsorption, capillary condensation, or filling of minor interparticle spaces. In addition, the isotherm did not show isolated anomalous points or abrupt discontinuities, suggesting that the invalid BET result was not caused by a specific measurement anomaly. The invalid BET response was mainly associated with the low N_2 uptake in the BET region and the absence of a well-defined monolayer adsorption domain.

According to the International Union of Pure and Applied Chemistry (IUPAC) classification, the adsorption-desorption curve showed a Type III-like behavior with a weak H3-like hysteresis loop (Thommes et al., 2015). The Type III-like response is consistent with the absence of a clear low-pressure knee or well-defined monolayer region, supporting the interpretation of weak N_2 interaction with the fiber surface. The small hysteresis observed at intermediate and high relative pressures may indicate a minor contribution from capillary condensation in low-volume mesopores, inter-fiber spaces, or surface irregularities. However, because the total N_2 uptake was low and the BET fit was not physically valid, this H3-like behavior should not be interpreted as evidence of a developed mesoporous network.

Under this interpretation, the PHAC fiber can be considered non-porous. This does not imply the complete absence of any surface irregularity or nanoscale voids, but rather that the accessible porosity was too limited to be quantified reliably by BET using N_2 physisorption at 77 K. The DFT results shown in Figure 5.3 suggest the possible presence of a very small contribution from micropores or low-range mesopores; however, the cumulative pore volume remains negligible compared with porous materials and does not modify the overall interpretation of the material as essentially non-porous.

Although N_2 physisorption did not provide a physically valid BET surface-area value for the PHAC fiber, complementary techniques could be used in future work to evaluate different aspects of porosity. Krypton adsorption would be more suitable for very

low surface-area materials, whereas CO_2 adsorption could improve the detection of narrow micropores. In addition, helium pycnometry combined with an independent measurement of the fiber envelope density could provide an indirect indication of the internal pore volume.

Native film and purified PHB

The adsorption-desorption isotherms, the low-pressure regions used for BET analysis, and the DFT pore size distributions obtained for the locally produced PHB recovered as native film are shown in Figures 5.4, 5.5, and 5.6, respectively. Two measurements were performed because of the visible heterogeneity of the recovered films. The main parameters obtained from both analyses are summarized in Table 5.8.

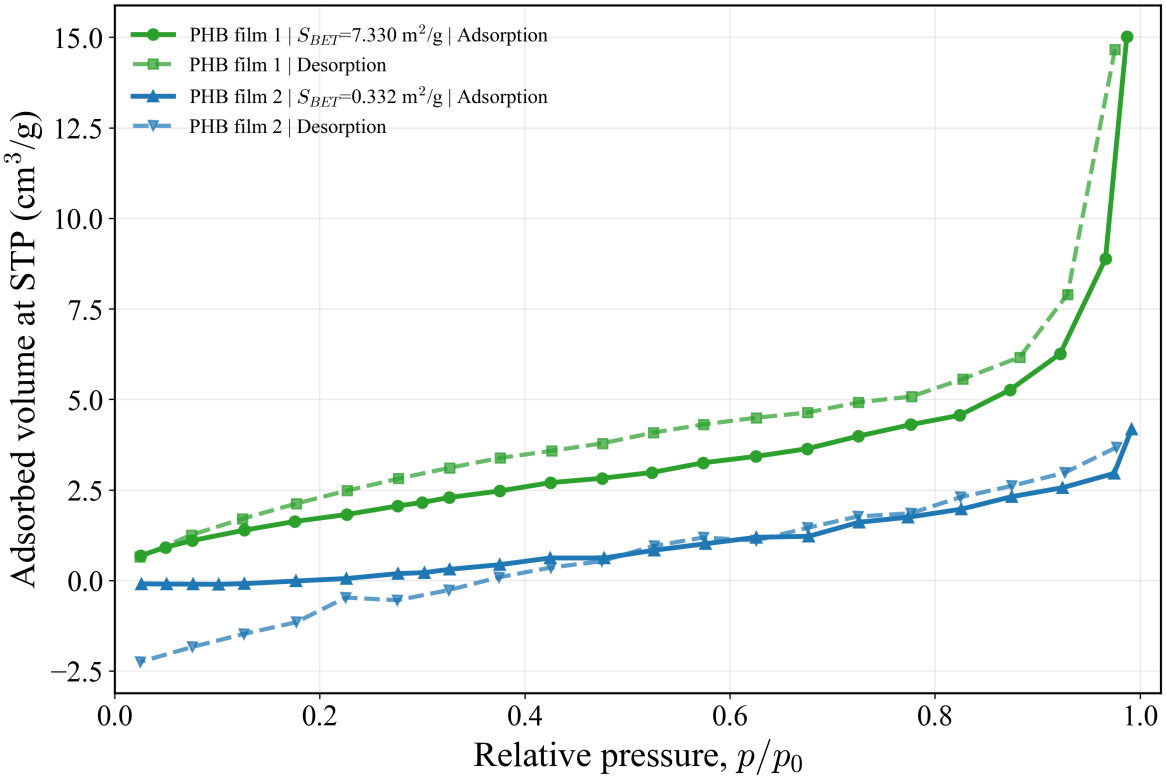


Figure 5.4: N_2 adsorption-desorption isotherm obtained for the locally produced PHB recovered as native film at 77 K.

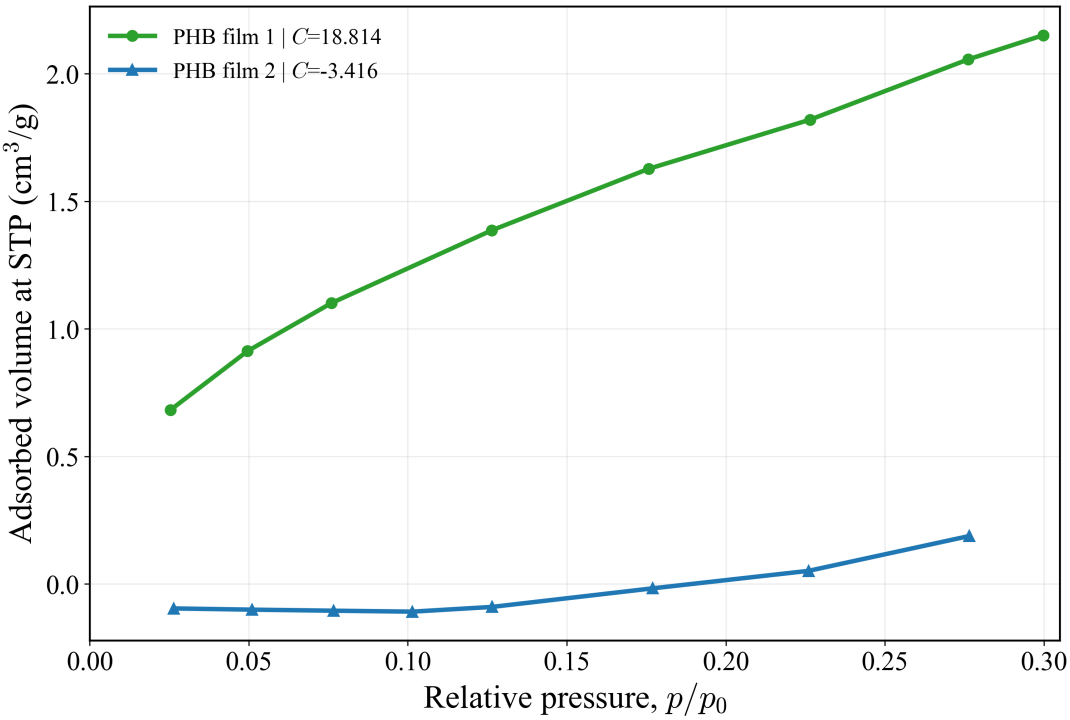


Figure 5.5: Low-pressure region of the N_2 adsorption isotherm used for BET analysis of the locally produced PHB recovered as native film.

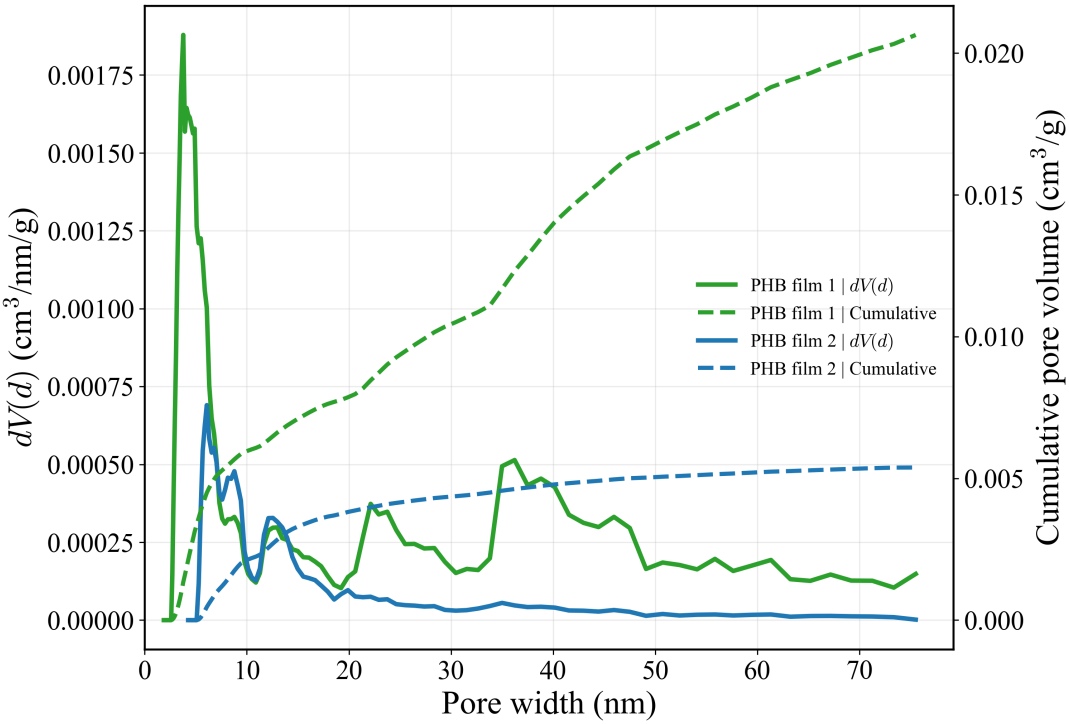


Figure 5.6: DFT pore size distribution and cumulative pore volume obtained for the locally produced PHB recovered as native film.

Table 5.8: Porosity parameters obtained from N_2 physisorption analysis of the locally produced PHB recovered as native film.

Parameter	**PHB film 1**	**PHB film 2**	**Unit**
BET surface area	7.3300	0.3320	m^2/g
BET constant (C)	18.8136	-3.4157	-
DFT pore volume	0.0206	0.0054	cm^3/g

The two measurements showed markedly different physisorption responses. PHB film 1 presented a physically valid BET fit, with a positive BET constant and a measurable surface area, whereas PHB film 2 presented a negative BET constant and a much lower apparent surface area. The DFT pore volume followed the same trend, indicating that the amount of pore volume accessible to N_2 depended strongly on the analyzed film fragment. This variability is consistent with the visible heterogeneity of the evaporation-recovered films.

The two native-film measurements also differed in their isotherm classification. PHB film 1 showed a Type IV(a)-like isotherm with an H3-like hysteresis loop according to the IUPAC classification (Thommes et al., 2015). This behavior is consistent with the presence of mesopore-related capillary condensation, although the absence of a clear plateau at high relative pressures suggests that the accessible porosity may be associated with slit-like voids, interparticle spaces, or non-rigid lamellar features rather than a uniform cylindrical pore network. In contrast, PHB film 2 showed a Type III-like response with a weak H3-like hysteresis loop, similar to the behavior observed for PHAC. This second response is consistent with weak N_2 interaction, low uptake in the BET region, and the absence of a well-defined monolayer adsorption domain.

In PHB film 2, some negative adsorbed-volume values were observed in the low-pressure region. These values do not have a physical meaning as negative adsorption, but rather indicate that the amount of N_2 adsorbed by this fragment was close to the detection and correction limits of the measurement. Under such low-uptake conditions, small uncertainties associated with dead-volume correction, pressure equilibration, thermal stability, or gas non-ideality corrections can produce slightly negative calculated adsorption values. This behavior supports the interpretation that PHB film 2 did not

provide a reliable BET region and that its accessible porosity was very limited under the experimental conditions.

The adsorption-desorption isotherm, the low-pressure region used for BET analysis, and the DFT pore size distribution obtained for the purified PHB are shown in Figures 5.7, 5.8, and 5.9, respectively. The main parameters obtained from the analysis are summarized in Table 5.9.

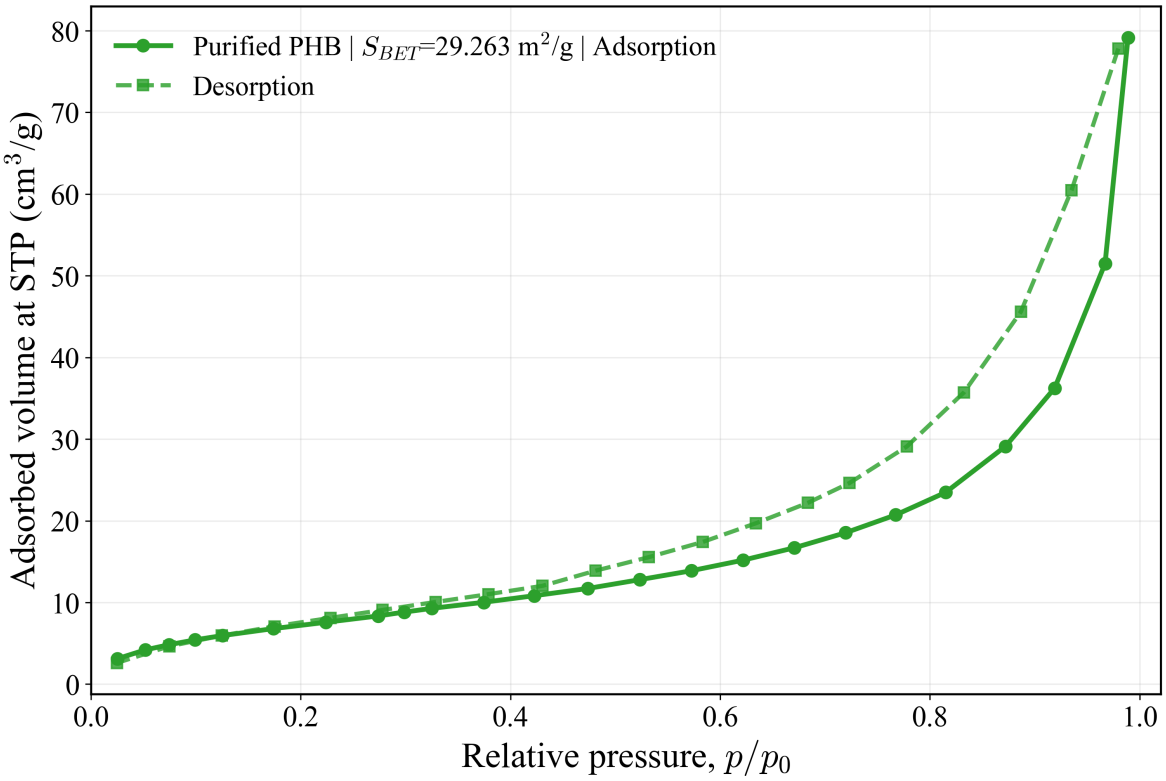


Figure 5.7: N_2 adsorption-desorption isotherm obtained for the purified PHB at 77 K.

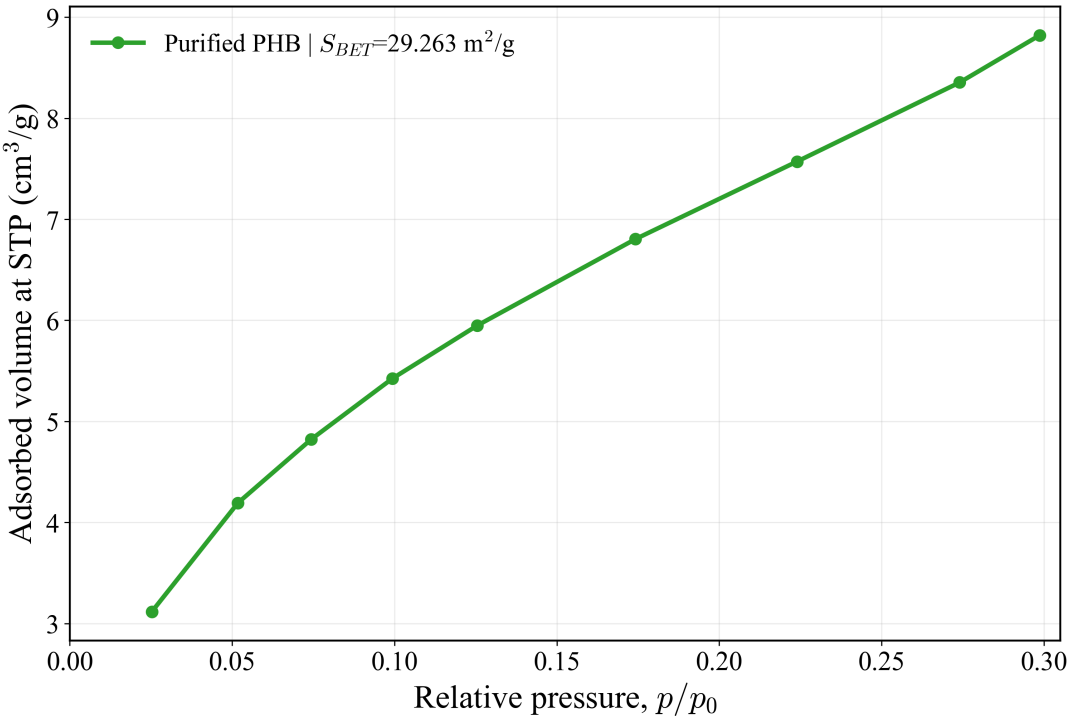


Figure 5.8: Low-pressure region of the N_2 adsorption isotherm used for BET analysis of the purified PHB.

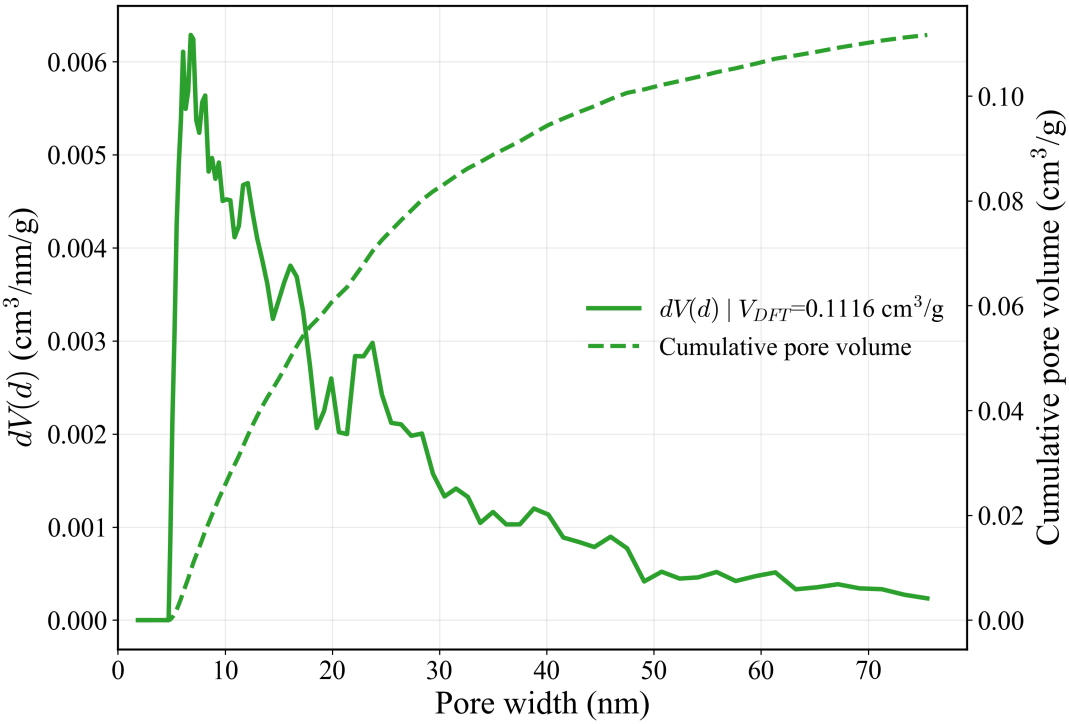


Figure 5.9: DFT pore size distribution and cumulative pore volume obtained for the purified PHB.

Table 5.9: Porosity parameters obtained from N_2 physisorption of the purified PHB.

Parameter	**Value**	**Unit**
BET surface area	29.2630	m^2/g
BET constant (C)	24.8627	-
DFT pore volume	0.1116	cm^3/g

Unlike PHAC and PHB film 2, the purified PHB presented a physically valid BET fit, with a positive BET constant and a clearly measurable surface area. Its response was closer to that observed for PHB film 1, although with a higher BET surface area and DFT pore volume. These results suggest that the purified material contained a larger fraction of surface and pore volume accessible to N_2 under the experimental conditions.

Similar to PHB film 1, the purified PHB showed a Type IV(a)-like isotherm with an H3-like hysteresis loop according to the IUPAC classification (Thommes et al., 2015). As discussed for the native film, this behavior is consistent with mesopore-related capillary condensation and suggests the presence of slit-like voids, interparticle spaces, or non-rigid lamellar features rather than a uniform cylindrical pore network. In the purified PHB, this interpretation is supported by the higher N_2 uptake, valid BET fit, and larger cumulative pore volume observed in the DFT analysis.

The increase in accessible surface area and pore volume after purification may be related to the change in recovery route. During ethanol-assisted precipitation, the polymer was separated from solution through antisolvent-induced precipitation rather than slow evaporation. This process may have produced a more fragmented, open, or irregular morphology, increasing the surface available for N_2 adsorption. The purified PHB was not only chemically cleaner than the evaporation-recovered native film; it also presented a different physical morphology.

The visual appearance of the purified material also supports this interpretation. After ethanol-assisted precipitation and drying, the recovered PHB presented a white, sponge-like morphology, as shown in Figure 5.10. This morphology differed from the compact films obtained by evaporation-based recovery and is consistent with a more open physical structure.

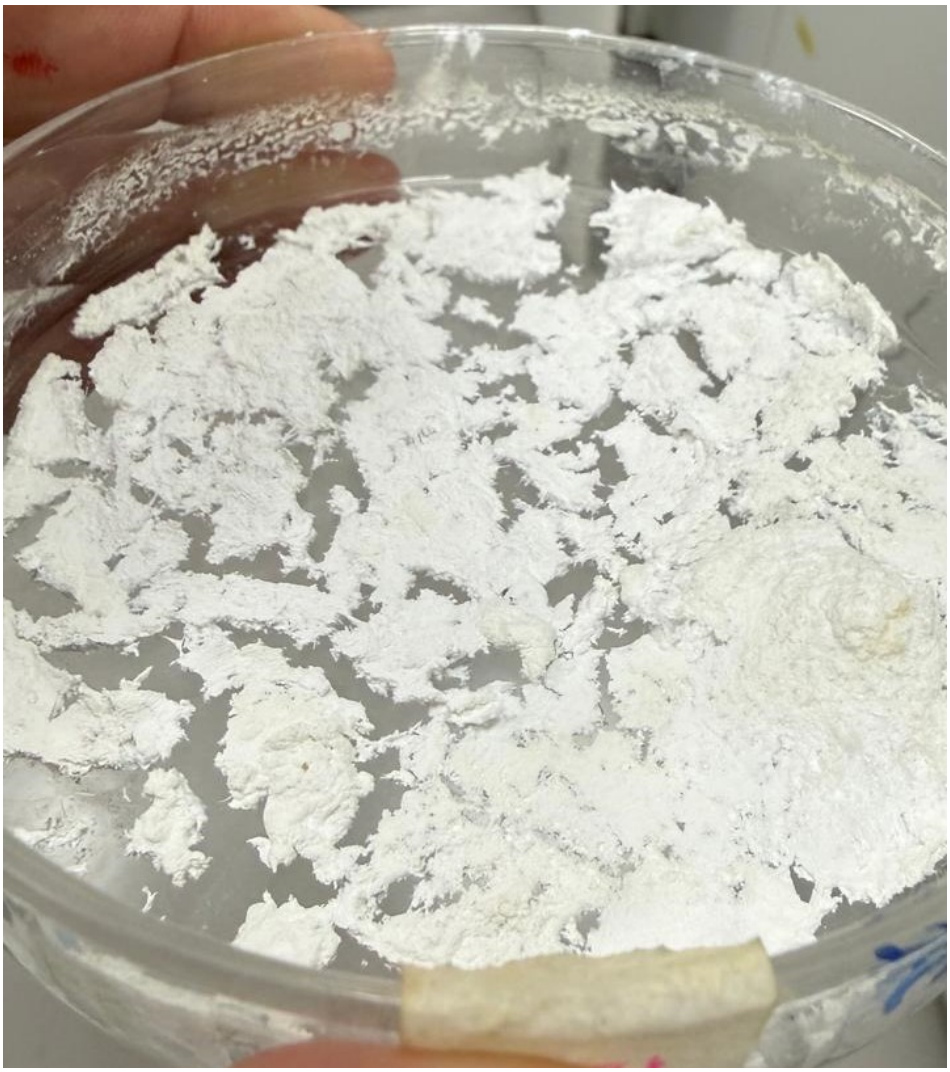


Figure 5.10: Sponge-like morphology observed for the purified PHB obtained by ethanol-assisted precipitation.

PHB fiber

The adsorption-desorption isotherm, the low-pressure region used for BET analysis, and the DFT pore size distribution obtained for the PHB fiber are shown in Figures 5.11, 5.12, and 5.13, respectively. The main parameters obtained from the analysis are summarized in Table 5.10.

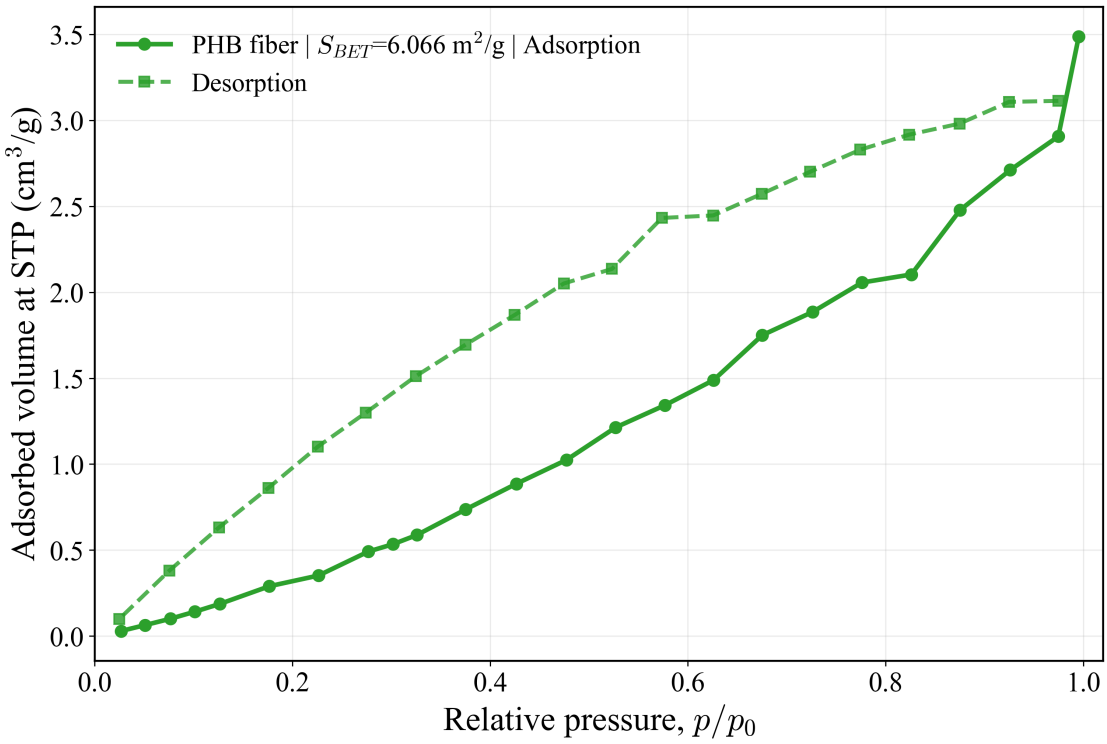


Figure 5.11: N_2 adsorption-desorption isotherm obtained for the PHB fiber at 77 K.

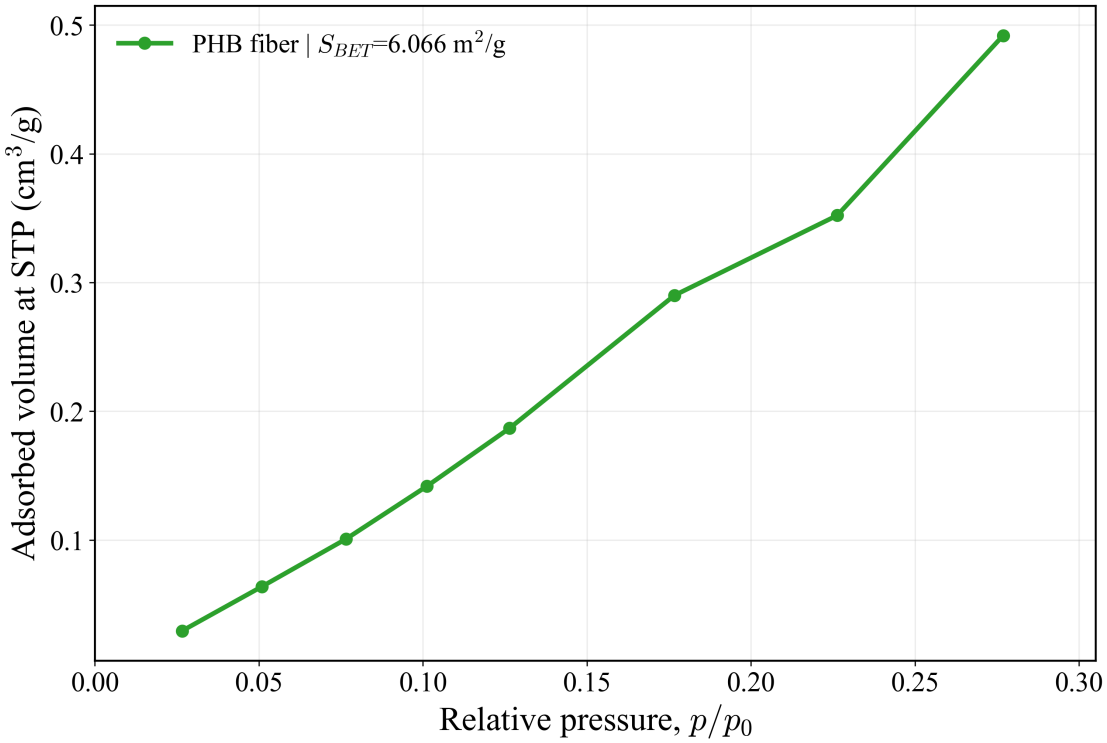


Figure 5.12: Low-pressure region of the N_2 adsorption isotherm used for BET analysis of the PHB fiber.

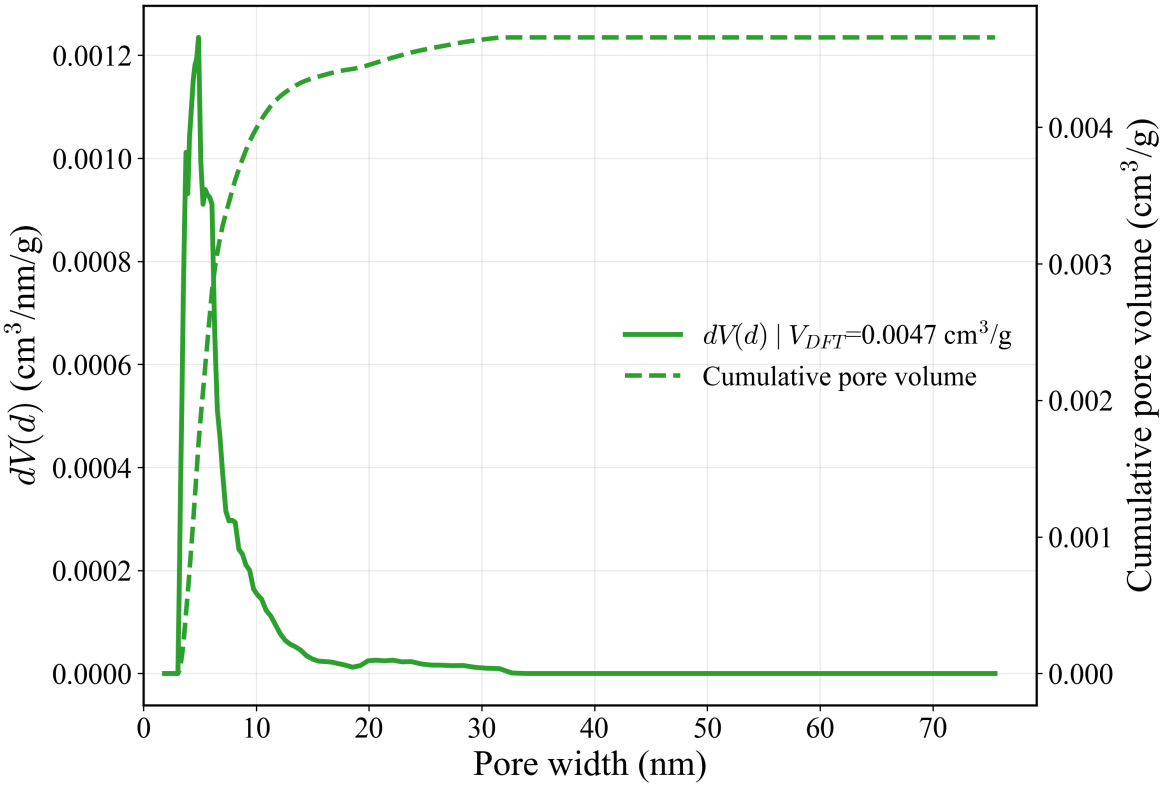


Figure 5.13: DFT pore size distribution and cumulative pore volume obtained for the PHB fiber.

Table 5.10: Porosity parameters obtained from N_2 physisorption analysis of the PHB fiber.

Parameter	**Value**	**Unit**
BET surface area	6.0660	m^2/g
BET constant (C)	0.8785	-
DFT pore volume	0.0047	cm^3/g

The PHB fiber presented a measurable BET surface area; however, the BET constant was lower than one, indicating that the BET fit was not fully physically valid. For this reason, the reported surface area should be interpreted only as an indicative value rather than as a precise quantification. The low-pressure region did not show a clearly defined monolayer adsorption domain, suggesting weak N_2 interaction with the fiber surface.

According to the IUPAC classification, the isotherm of the PHB fiber can be described

as Type III-like, with a weak H3-like hysteresis loop (Thommes et al., 2015). Although a small hysteresis was observed at higher relative pressures, the low DFT pore volume indicates that this feature should not be interpreted as evidence of a developed mesoporous network. Instead, it suggests only a minor contribution from surface irregularities, inter-fiber spaces, or low-volume mesopores.

The low accessible pore volume measured for the PHB fiber was comparable to that observed for PHAC. Although the commercial PHB pellet used to produce this fiber was not evaluated by BET, the similarity between both extruded fibers suggests that melt processing produced a compact morphology. Melting, flow through the nozzle, and solidification may reduce open surface features or voids accessible to N_2, leading to the low porosity measured after extrusion.

5.1.5 Thermal properties

PHAC fiber

The thermal results associated with the PHAC fiber are presented in Figure 5.14 and summarized in Table 5.11. It should be noted that this material was evaluated during the development of the DSC protocol and was therefore not analyzed according to the final methodology. Under the final protocol, the day 0 reference corresponds to the average of nine second-heating thermograms. These nine specimens are subsequently divided into three groups, with three specimens reevaluated after 7 days, three after 28 days, and three after 100 days of aging. For PHAC, however, the day 0 thermogram corresponds to the average of only three second-heating measurements. Nevertheless, because these specimens were obtained from the same commercial material, substantial variability was not expected, and their average was considered representative of the initial condition. The aged PHAC samples were subjected at day 0 to a heating-cooling cycle to erase their previous thermal history, but no day 0 second-heating thermogram was recorded for these specimens. Their thermal response was obtained only from the first heating scan performed after the corresponding aging period. Nevertheless, the observed results follow the expected thermal trends and are considered suitable for comparative interpretation. The individual thermograms are presented in Appendix D.

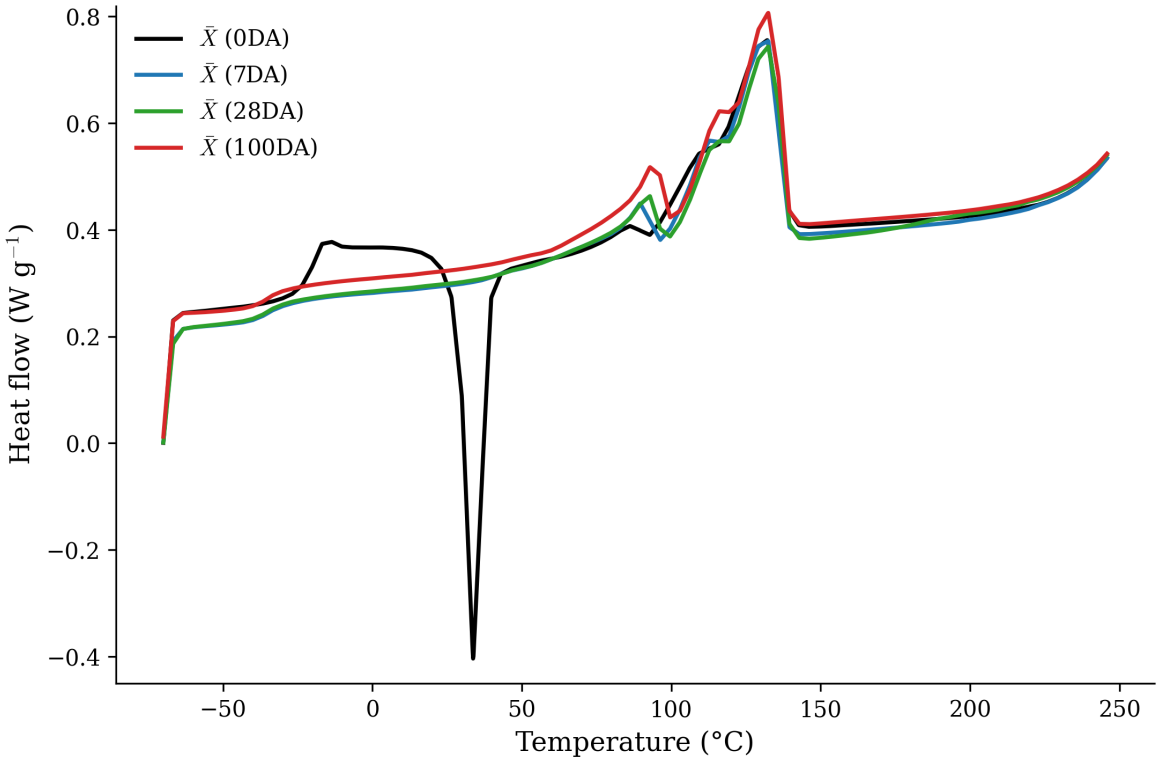


Figure 5.14: Average DSC thermograms of the PHAC fiber at different aging times.

Table 5.11: Summary of transition temperatures and crystallinity obtained from DSC for the PHAC fiber evaluated as a function of aging. Values are reported as $\bar{X} \pm \sigma$.

Aging time	**Transition temperature (°C) and crystallinity (χ)**				
	T_c	T_{g1}	T_{g2}	T_m	χ(%)
Day 0	34.46 ± 0.16	-21.19 ± 0.55	-	131.54 ± 1.36	54.66 ± 0.48
7 DA	-	-34.40 ± 0.42	38.44 ± 0.48	131.54 ± 0.18	35.06 ± 0.81
28 DA	-	-34.83 ± 0.25	42.20 ± 0.49	132.13 ± 0.22	33.83 ± 0.89
100 DA	-	-35.73 ± 0.21	44.52 ± 0.43	132.37 ± 0.44	35.70 ± 0.68

Only the main thermal transitions are reported in Table 5.11. Minor peaks or secondary events observed in individual thermograms were not included in the summary in order to maintain a consistent comparison among aging conditions.

A clear distinction is observed between the thermograms corresponding to the aged samples and that of the initial condition. These differences indicate that exposure to

the environment leads to measurable alterations in the thermal behavior of the PHA fibers when compared to the non-aged specimen.

For the Day 0 sample, the reported thermogram corresponds to the second heating scan, after erasing the previous thermal history of the material during the first heating cycle. Under these standardized conditions, a cold crystallization event (T_c) is observed at 34.46 °C, indicating that part of the polymer chains reorganize into a more ordered structure upon heating. For the aged samples, the first heating scan after storage was analyzed in order to preserve the thermal history developed during the aging period following the initial DSC cycle. The disappearance of the cold crystallization event in these aged specimens suggests that structural rearrangement occurred during aging, leading to a more stable morphology prior to the DSC measurement.

In all three aged samples, two distinct glass transition temperatures (T_g) are detected. This phenomenon has been previously reported for semicrystalline PHB and PHA systems and is attributed to the presence of multiple amorphous fractions with different chain mobilities (Srubar et al., 2012). In these materials, the polymer structure can be described using a three-phase model consisting of a crystalline phase, a MAF, and a RAF (Di Lorenzo & Androsch, 2019). Within this framework, the crystalline phase corresponds to the ordered lamellar domains of the polymer, while the amorphous phase is divided into two fractions with different molecular mobilities. The MAF is composed of less constrained chain segments that devitrify in the glass transition of the bulk polymer, whereas the RAF consists of amorphous segments coupled to the crystalline lamellae, whose mobility is strongly restricted and therefore devitrify at higher temperatures (Di Lorenzo & Androsch, 2019). Accordingly, the occurrence of two glass transition temperatures in the aged samples is consistent with the presence of these two distinct amorphous fractions.

Considering typical ambient temperatures (approximately 20-25 °C), the lower glass transition temperature (T_{g1}) lies well below the service temperature of the material. Under these conditions, the corresponding phase is in a rubbery state, allowing significant segmental mobility within this portion of the polymer matrix, and may therefore be associated with the MAF. The second glass transition (T_{g2}), located between ap-

proximately 38 and 45 °C, remains above ambient temperature. Consequently, the phase associated with this transition remains in a glassy and mechanically constrained state during normal environmental exposure, and may thus be related to the RAF. In addition, T_{g2} showed a progressive increase with aging, indicating that the constrained amorphous fraction required a higher thermal activation to undergo segmental mobility. This suggests that the RAF became progressively more restricted over time, consistent with physical aging and structural rearrangement within the amorphous phase.

For the melting temperature (T_m), only minor variations were observed throughout the aging period. This relatively constant T_m suggests that the crystalline phase retained a similar thermodynamic stability during aging. However, the measured melting temperature was noticeably lower than the typical values reported for pure PHB homopolymers, commonly located in the range of approximately 170-180 °C (Srubar et al., 2012; Turco et al., 2021; Di Lorenzo & Androsch, 2019).

Likewise, the crystallinity values obtained for the PHAC fiber were lower than those commonly reported for pure PHB (McAdam et al., 2020; Dalton et al., 2022). This discrepancy is consistent with the purity results and with the information provided by the manufacturer, which indicated that the commercial fiber contains a non-PHB fraction and an additional PHA component. The incorporation of comonomer units with longer side chains, such as 3-hydroxyhexanoate in PHBHHx copolymers, can disrupt the crystalline packing of PHB chains, reducing both crystallinity and melting temperature. In agreement with this interpretation, the lower-temperature melting behavior observed in this work suggests that the additional PHA present in the formulation may correspond to a hexanoate-containing comonomer, since the incorporation of 3-hydroxyhexanoate units is known to reduce the melting temperature of PHB-based copolymers (Doi et al., 1995; Dalton et al., 2022). In addition, PHBHHx fibers have been reported to present crystallinity values around 33-34% (Vanheusden et al., 2023), similar to those obtained for the aged PHAC fiber in this work. Therefore, the relatively low T_m and crystallinity observed for the PHAC fiber are consistent with its commercial "allPHA" nature and with its measured composition.

The crystallinity values shown in Table 5.11 exhibit a noticeable difference between the

initial condition and the aged samples. However, the Day 0 thermogram includes a cold crystallization event during heating, whereas this event is absent in the aged specimens. As a result, the apparent crystallinity calculated from DSC may be influenced by differences in thermal history and crystallization behavior during the measurement, rather than representing a direct decrease in the intrinsic crystalline fraction of the material. The crystallinity values among the aged samples remain nearly unchanged over time, suggesting that once the initial structural rearrangement has occurred, the crystalline fraction becomes relatively stable during further aging.

Considering that the analyzed material is a commercial fiber and therefore likely underwent extrusion and orientation during manufacturing, this stability may also be associated with the presence of an oriented crystalline fraction. In PHB-based systems, the metastable β form has been reported in hot-drawn films as well as in melt-spun and electrospun fibers, and is associated with highly extended chains generated under deformation (Di Lorenzo & Androsch, 2019). Therefore, the limited variation in crystallinity observed among the aged samples could also be related to the relative stability of a pre-oriented crystalline structure, potentially including β crystals. Nevertheless, this possibility remains hypothetical and should be confirmed through complementary structural analyses, such as X-ray diffraction (XRD), which are beyond the scope of this thesis.

Based on the relatively stable crystalline fraction observed among the aged specimens, the apparent MAF and RAF were calculated to evaluate whether aging mainly affected the amorphous phase. The calculation was performed according to the procedure described in Appendix B.4. Briefly, the MAF was obtained from the heat-capacity increment associated with the lower-temperature glass transition, while the RAF was calculated by complementarity from the crystalline and mobile amorphous fractions. Because the procedure uses the reference thermal properties of fully amorphous and fully crystalline PHB as operational values for the PHB-based fraction of the PHAC fiber, the resulting fractions are reported as apparent MAF and apparent RAF rather than as absolute phase contents.

The apparent MAF and RAF obtained for the aged conditions are presented in Fig-

ure 5.15 and summarized in Table 5.12.

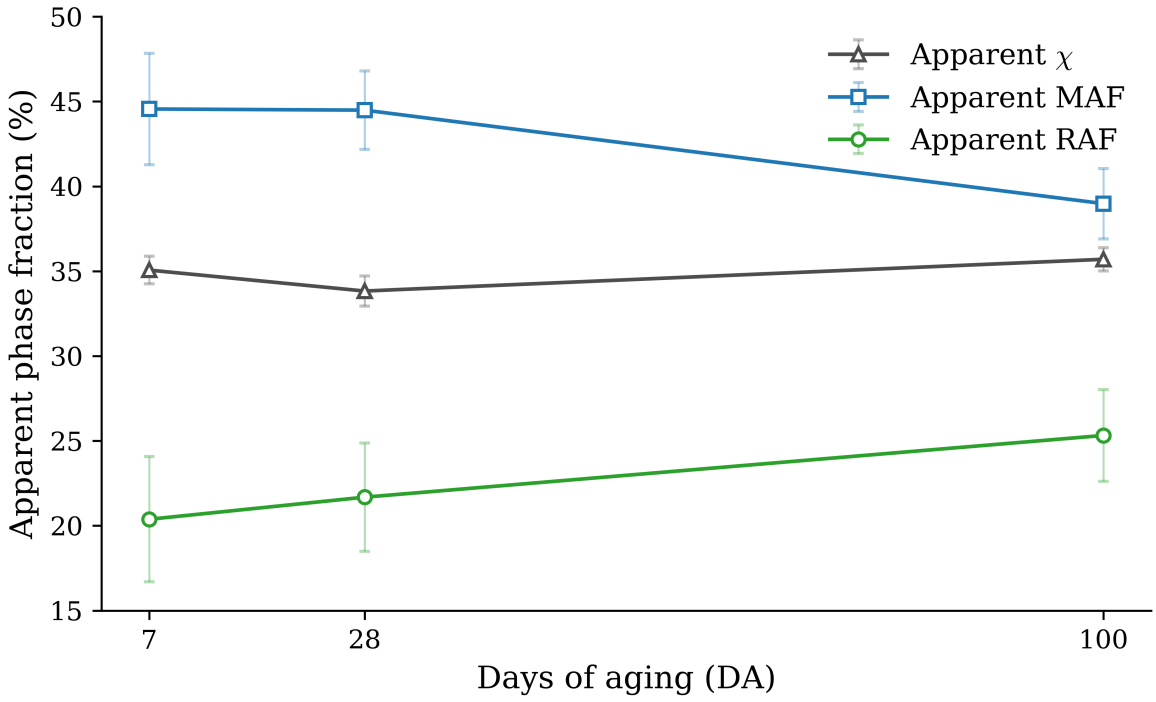


Figure 5.15: Evolution of the apparent crystallinity, MAF, and RAF in the PHAC fiber between 7 and 100 days of aging. Error bars represent the sample standard deviation.

Table 5.12: Apparent mobile and rigid amorphous fractions calculated for the PHAC fiber under the PHB-reference assumption. Values correspond to $\bar{X} \pm \sigma$.

Aging time	**Apparent MAF (%)**	**Apparent RAF (%)**
7 DA	44.56 ± 3.28	20.38 ± 3.69
28 DA	44.49 ± 2.31	21.68 ± 3.20
100 DA	38.98 ± 2.07	25.32 ± 2.70

Day 0 was not included in this comparison because its second-heating thermogram reflects the early reorganization stage after melting, where the polymer may behave predominantly as mobile amorphous material at the onset of recrystallization. Under these conditions, the measured heat-capacity increment produced an apparent MAF greater than 100%, which, combined with the current apparent crystallinity, resulted in a negative RAF. This non-physical phase balance may also be amplified by the fact

that the PHAC fiber is not composed of pure PHB, so the use of PHB reference values can introduce inconsistencies in the absolute phase fractions.

The phase-fraction estimates are consistent with the interpretation proposed from the glass-transition behavior. Among the aged conditions, the apparent crystallinity remained comparatively stable, showing lower variation than the amorphous fractions. The apparent RAF tended to increase with aging, while the apparent MAF decreased. These measurements support the idea that the main structural evolution during aging was associated with changes within the amorphous phase, rather than with a substantial increase in the crystalline fraction.

The difference between 7 and 28 days was small relative to the experimental variability, as reflected by the overlap of the corresponding standard deviations. Thus, these two conditions cannot be clearly differentiated based only on the present measurements. The higher apparent RAF obtained after 100 days, together with the lower apparent MAF and the stable crystallinity, suggests a progressive increase in amorphous-phase constraint over longer aging times. Since the analysis relies on a PHB-based reference and the evaluated conditions do not correspond to repeated measurements of the same individual specimens, this trend should be interpreted as descriptive evidence rather than as a direct quantitative measurement of phase conversion.

Figure 5.16 presents the thermogravimetric curves obtained from the average of three independent measurements evaluated as a function of aging. The percentage value reported in the figure corresponds to the residual mass remaining after thermal degradation for each condition.

The obtained results are consistent with those reported in the literature (Li et al., 2001), where PHA and PHB typically undergo thermal degradation within the temperature range of approximately 250-280 °C. In the present study, the main degradation event occurred near this range for all aging conditions, indicating that the thermal stability of the polymer matrix was not significantly affected by environmental exposure.

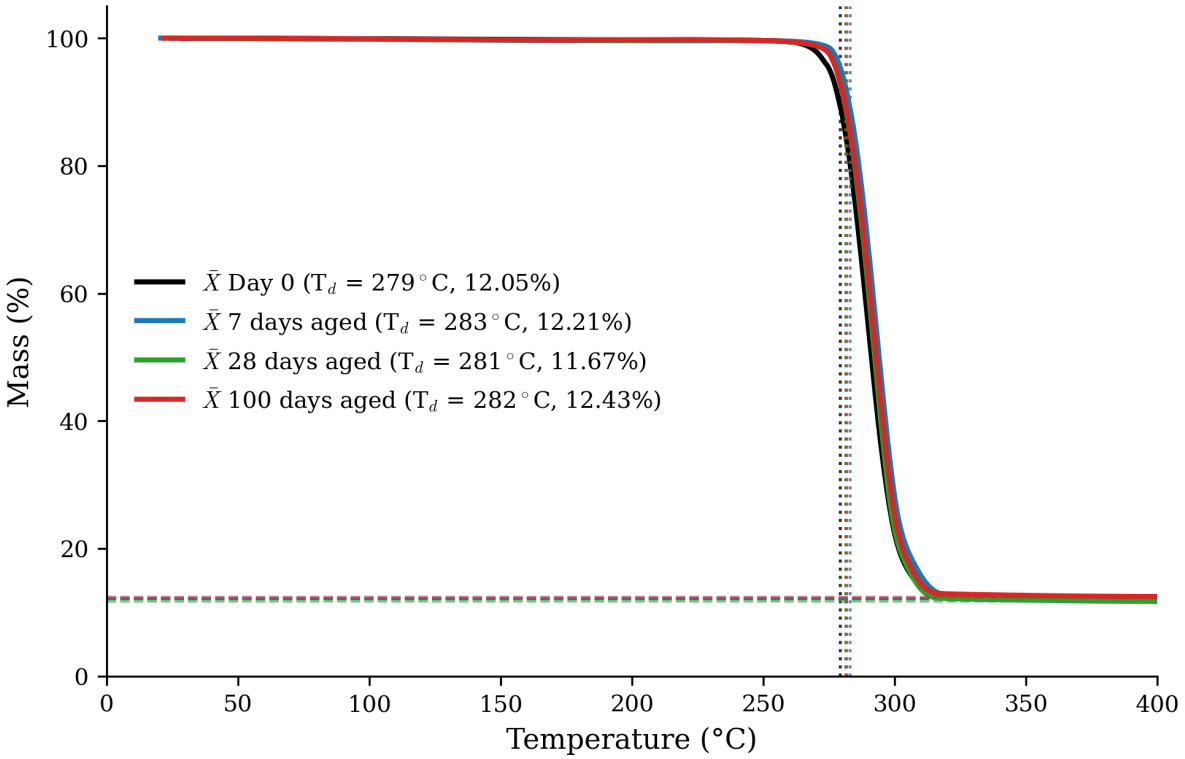


Figure 5.16: TGA curves of the PHAC fiber for all evaluated aging times.

It is important to note that the specimen exhibited a non-negligible residual mass after the initial TGA test conducted up to 400 °C. To assess the thermal stability of this fraction, an additional TGA test was performed up to 1000 °C, as shown in Figure 5.17. The residual fraction remained essentially stable throughout the extended temperature range, with 11.54% of the initial mass remaining at the end of the test. This result confirms the presence of components that did not undergo thermal degradation under the evaluated conditions.

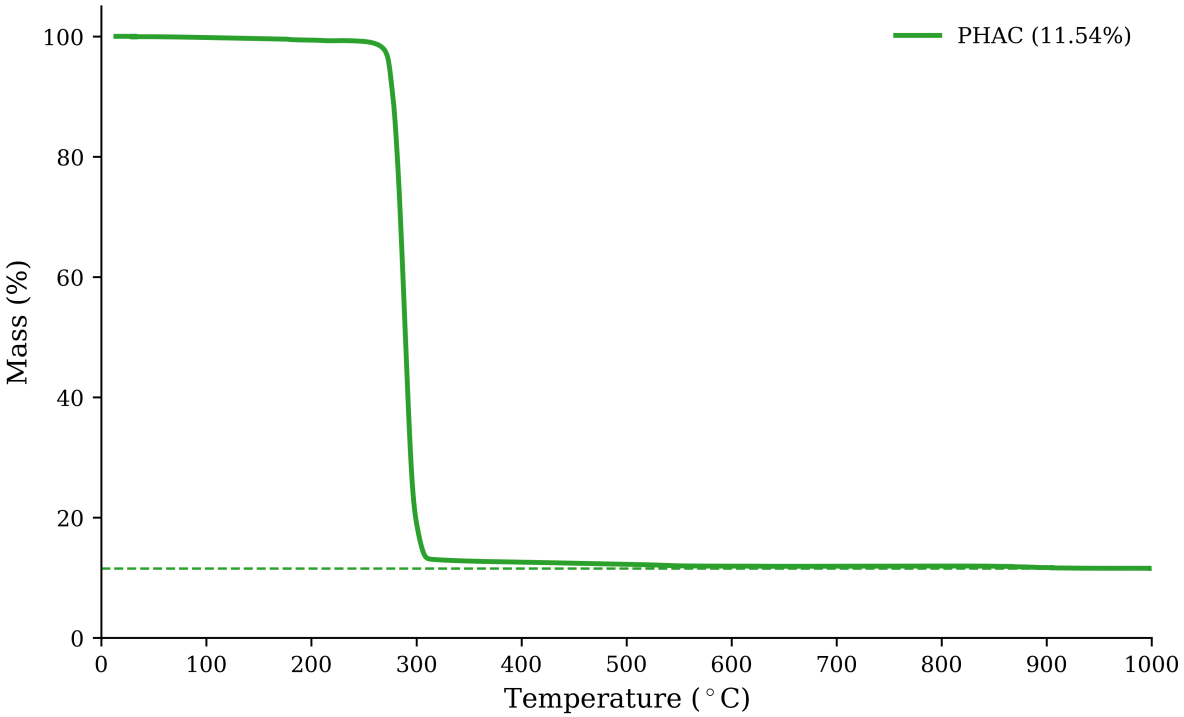


Figure 5.17: Extended TGA profile of the PHAC fiber up to 1000 °C.

No thermal transitions attributable to this residual fraction were identified by DSC, suggesting that these components do not participate in the transitions observed below the melting temperature of the polymer matrix. Considering the composition discussed previously, the residual mass detected by TGA is therefore consistent with the inorganic fraction of the commercial formulation, particularly the mineral filler and titanium dioxide coating, rather than with the polymeric PHA components.

Native Film and purified PHB

As discussed in Section 4.4, the thermal response of the locally produced PHB recovered by evaporation as a native film showed deviations from the expected behavior of PHB. These results were relevant for interpreting the poor extrudability of the material, since the DSC curves revealed altered melting-related transitions that suggested the presence of additional phases or residual compounds in the recovered polymer. The average DSC thermograms obtained for the native film at the evaluated aging times are shown in Figure 5.18, and the corresponding thermal parameters are summarized in Table 5.13. The individual thermograms are presented in Appendix D.

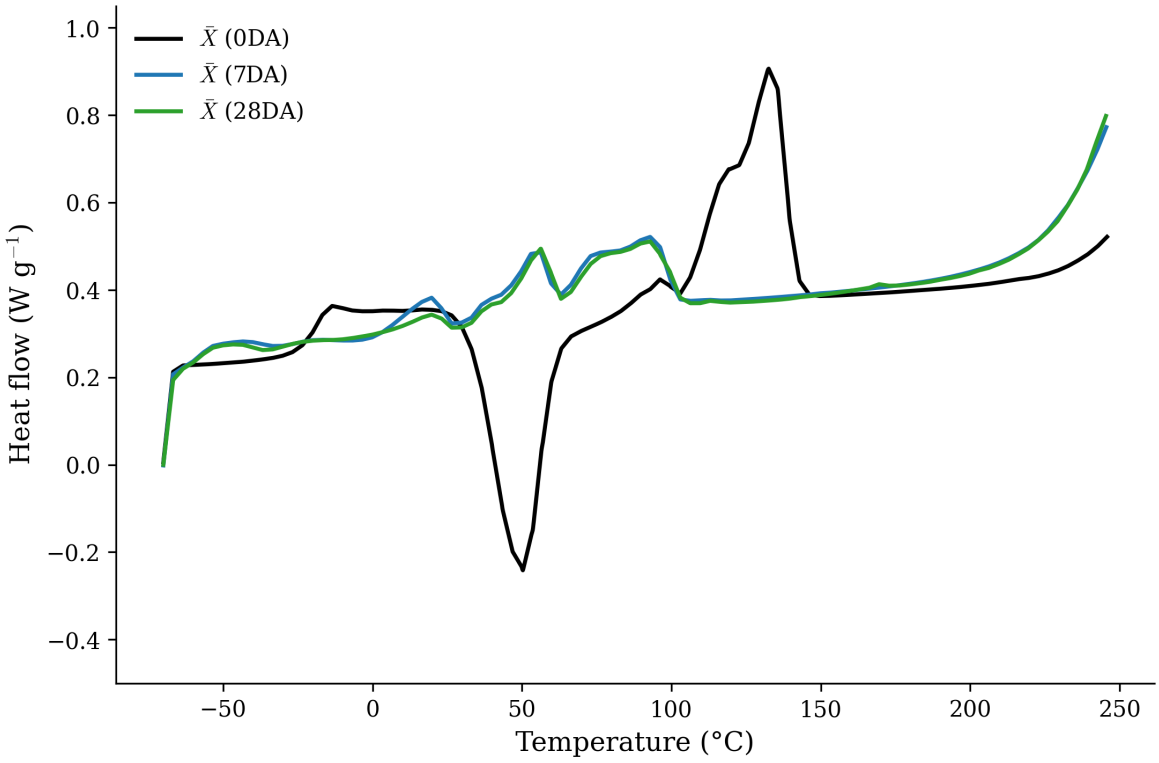


Figure 5.18: Average DSC thermograms of the locally produced PHB recovered as native film at different aging times.

Table 5.13: Summary of mean transition temperatures obtained from DSC for the locally produced PHB recovered as native film.

Aging time	**Thermal parameters** ($\bar{X} \pm \sigma$)			
	T_g (°C)	T_c (°C)	T_m (°C)	χ(%)
Day 0	-20.25 ± 2.93	49.43 ± 4.45	134.29 ± 2.12	93.49 ± 7.73
7 DA	-56.33 ± 0.42	-	86.24 ± 12.07	33.81 ± 2.70
28 DA	-56.26 ± 0.71	-	93.15 ± 2.83	33.51 ± 2.60

The transition temperatures reported in Table 5.13 were obtained from the average values calculated for each condition. Because the thermograms shown in Figure 5.18 correspond to averaged heat-flow curves, slight differences may occur between the apparent peak position observed visually in the figure and the mean transition temperatures reported in the table.

The thermal response of the recovered PHB film differed from that expected for pure

PHB, particularly in the second-heating thermogram used for the Day 0 analysis. In this scan, the melting transition was located near 130 °C, below the range commonly reported for PHB (Srubar et al., 2012; Di Lorenzo & Androsch, 2019). However, this difference was not observed in the first heating cycle, where the recovered film showed an average melting temperature of 172.54 °C, closer to the expected melting range of PHB, as shown in Figure 5.19. This comparison suggests that the lower melting temperature observed during the second heating scan was associated with the imposed thermal history rather than with the initial thermal state of the recovered film. Consecutive cooling and heating processes can modify the crystallization and melting response of PHB, since the subsequent heating scan may involve secondary crystallization, recrystallization, and remelting processes that depend on the previous thermal history (Gunaratne et al., 2004; Di Lorenzo & Androsch, 2019).

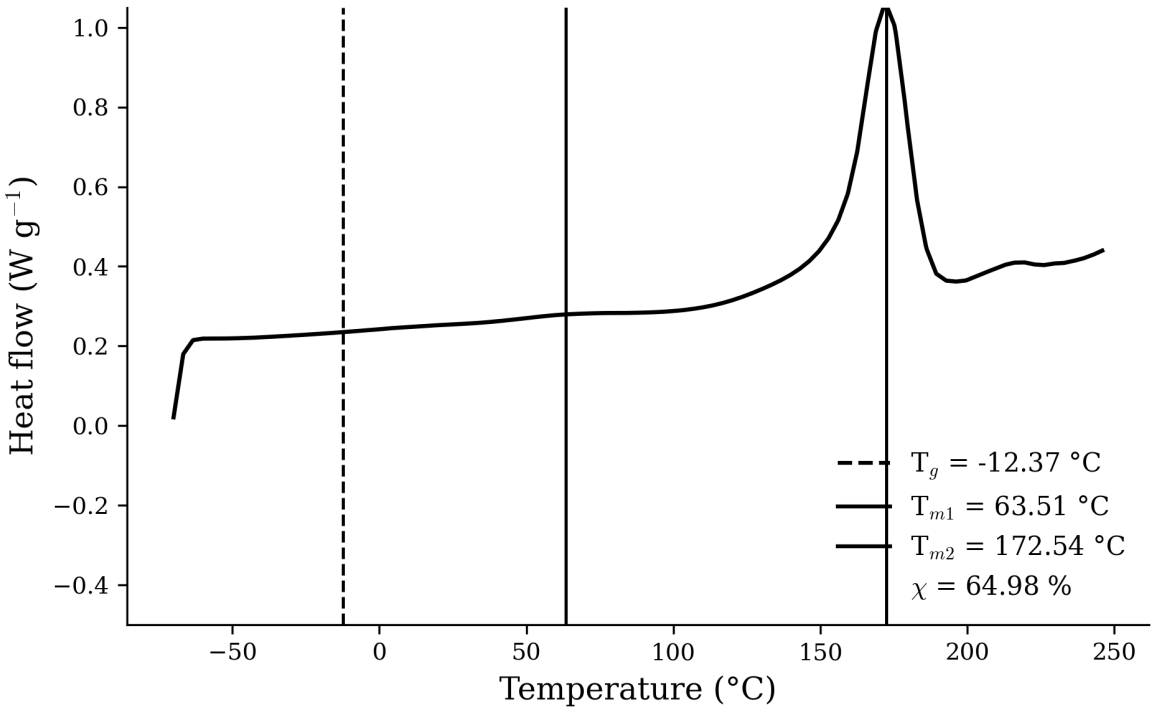


Figure 5.19: Average DSC thermogram of the locally produced PHB recovered as native film during the first heating cycle.

In addition to the lower melting temperature, the Day 0 second-heating thermogram showed a thermal response similar to that observed for the PHAC fiber, including a comparable first glass transition and a crystallization event identified by its correspond-

ing T_c. The crystallinity calculated for this condition was high for PHB; however, this value includes the contribution of the crystallization event observed during the scan, which magnifies the apparent crystallinity obtained from DSC integration.

The comparison with PHAC provides additional context. While PHAC repeatedly showed its principal melting transition near 130 °C after the imposed thermal cycle, the recovered PHB film showed a first-heating melting transition closer to pure PHB, followed by a lower melting transition and a pronounced crystallization event during the second heating. This result suggests that rapid cooling prevented the PHB chains from completely recovering their initial crystalline organization and that crystallization continued during reheating. This behavior is consistent with the low nucleation density and slow crystallization reported for PHB (Gunaratne et al., 2004). In addition, Di Lorenzo & Righetti (2013) showed that the thermal history influences the subsequent evolution of the crystalline and amorphous fractions during storage. They also reported that rapid cooling from the melt can produce an initially amorphous PHB structure that crystallizes during subsequent annealing or heating.

The more reproducible thermal response of PHAC should instead be interpreted in relation to its different polymeric composition. PHAC contains a second PHA component that may modify its melting behavior and the morphology developed during crystallization. However, its identity and concentration were not disclosed, so the mechanism responsible for the thermal response of PHAC cannot be established. The DSC results only show that PHAC repeatedly developed a similar melting response within the time scale of the applied protocol.

For the recovered PHB film, incomplete structural reorganization after melting may have contributed to its limited filament stability during extrusion by delaying solidification after exiting the nozzle, together with the effects of residual compounds and thermal degradation discussed previously.

The aged samples exhibited broad and overlapping thermal events that complicated the identification of glass transitions and melting-related processes. A possible explanation is that residual phases in the recovered film were progressively damaged during the previous DSC heating cycles, producing compounds that altered the subsequent heat-flow

response. This interpretation is consistent with the marked darkening observed during extrusion under thermal exposure. Since the specimens were not visually inspected after the DSC cycles, this mechanism remains a plausible rather than confirmed explanation.

The crystallinity values obtained for the aged samples were lower than those commonly reported for PHB, which are typically around 60-65% (McAdam et al., 2020; Dalton et al., 2022). However, these values were directly conditioned by the broad and overlapping events in the thermograms, which introduced uncertainty into the integration of the melting and crystallization contributions.

The TGA results in Figure 5.20 provide additional evidence of residual components. Although the main degradation event occurred within the expected temperature range for PHB-based materials (Li et al., 2001), the curves showed a slight gradual mass loss before this step. This early loss suggests the presence of volatile or thermally labile compounds with lower thermal stability than PHB, which may have affected both the thermal response and processability of the recovered film.

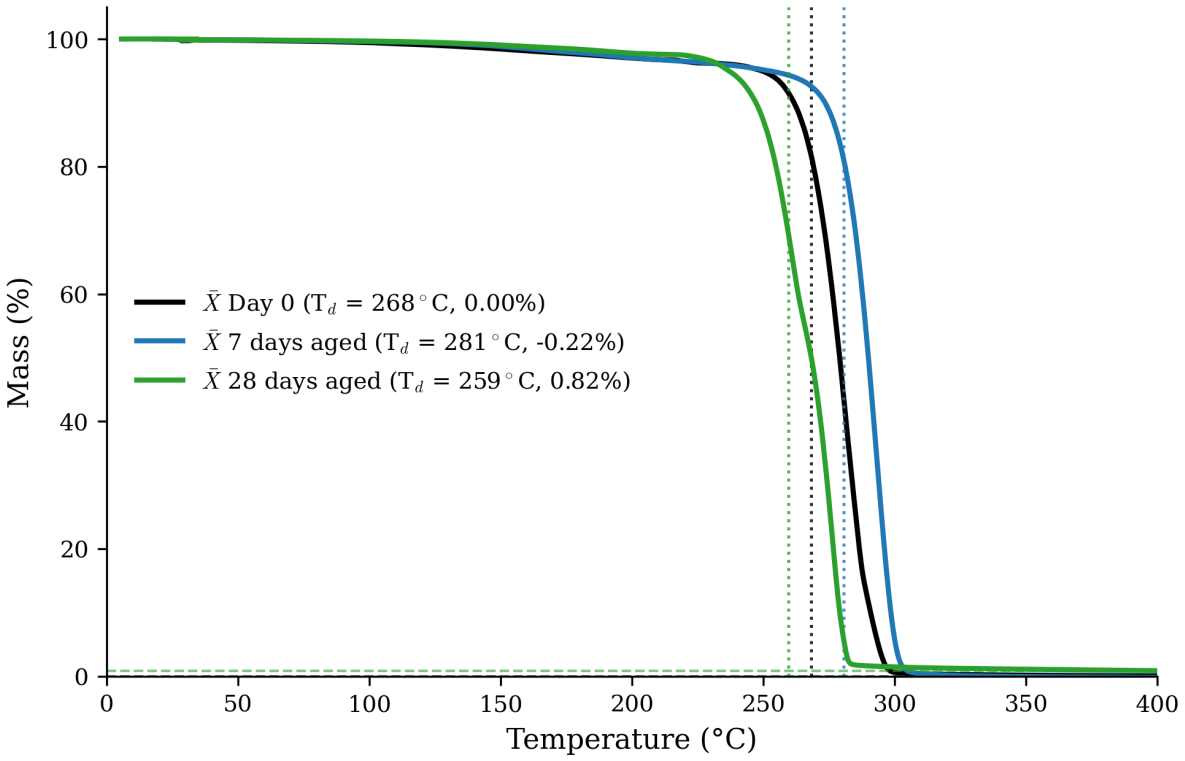
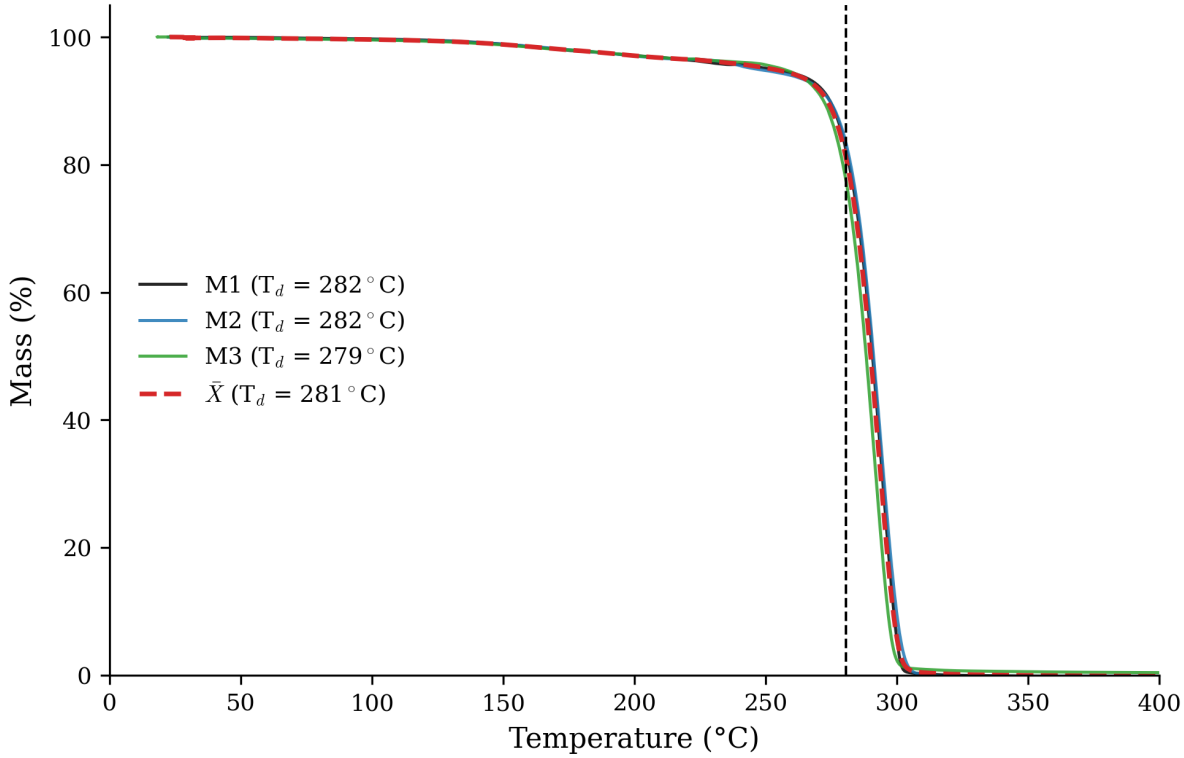


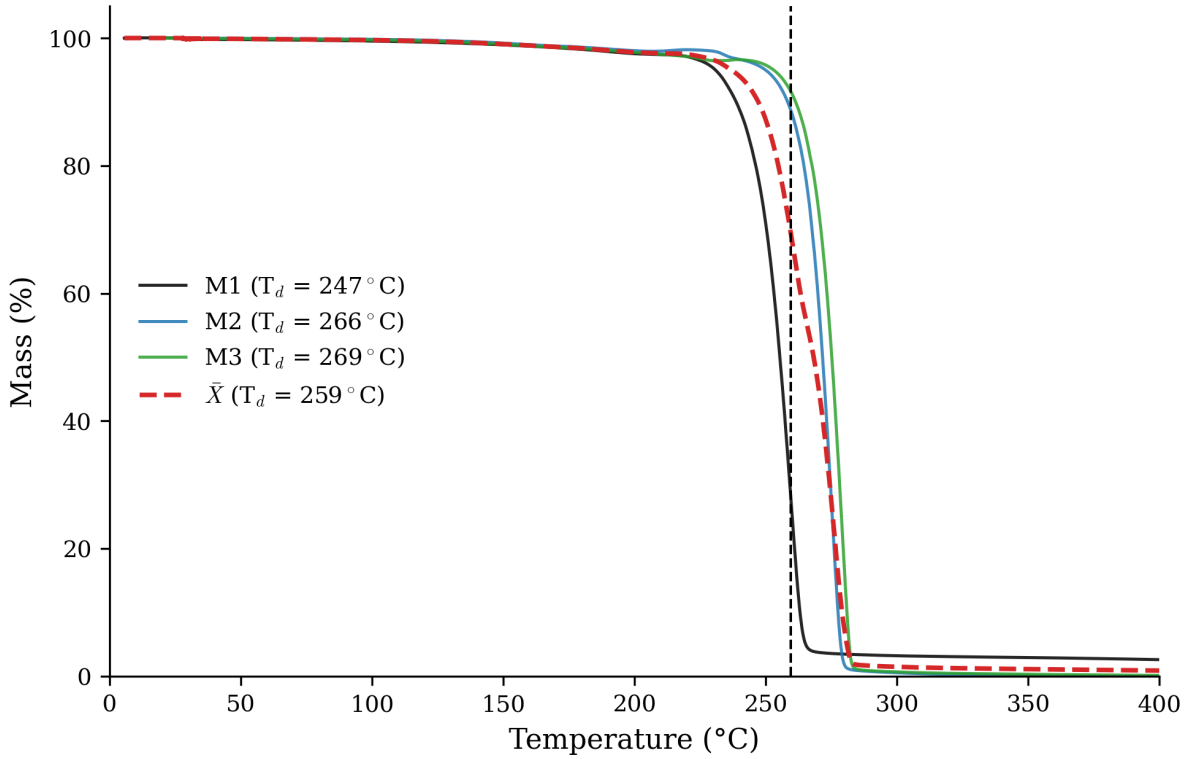
Figure 5.20: Average TGA curves of the locally produced PHB recovered as native film for the evaluated aging times.

The T_d values did not follow a monotonic trend with aging, increasing at 7 days and decreasing at 28 days. In addition, the differences observed between aging times and replicates suggest that the thermal response was affected by local variations in the recovered film. This agrees with the visual heterogeneity shown previously in Figure 4.4, where differences in texture, color, thickness, and surface morphology can be observed. The TGA triplicates in Figure 5.21 further support this interpretation, showing a more homogeneous response at 7 days and greater dispersion at 28 days.



(a) 7 days aged.

Figure 5.21: TGA triplicates of the recovered PHB film after aging.



(b) 28 days aged.

Figure 5.21: TGA triplicates of the recovered PHB film after aging.

These thermal results support the decision to incorporate an additional purification stage, as previously discussed in Sections 4.4 and 5.1.3. The thermal response of the evaporation-recovered PHB film showed that the material did not meet the quality requirements needed for subsequent processing and use in the intended application. For this reason, ethanol-assisted purification was applied to reduce the impurity content of the recovered polymer and improve its suitability for the following experimental stages.

DSC aging analysis was not performed for the purified PHB due to the limited amount of material available after purification and other characterization processes. In addition, this material was not further used as the main feedstock for fiber production. Therefore, the evaluation of the purified PHB focused on TGA. The obtained result is shown in Figure 5.22.

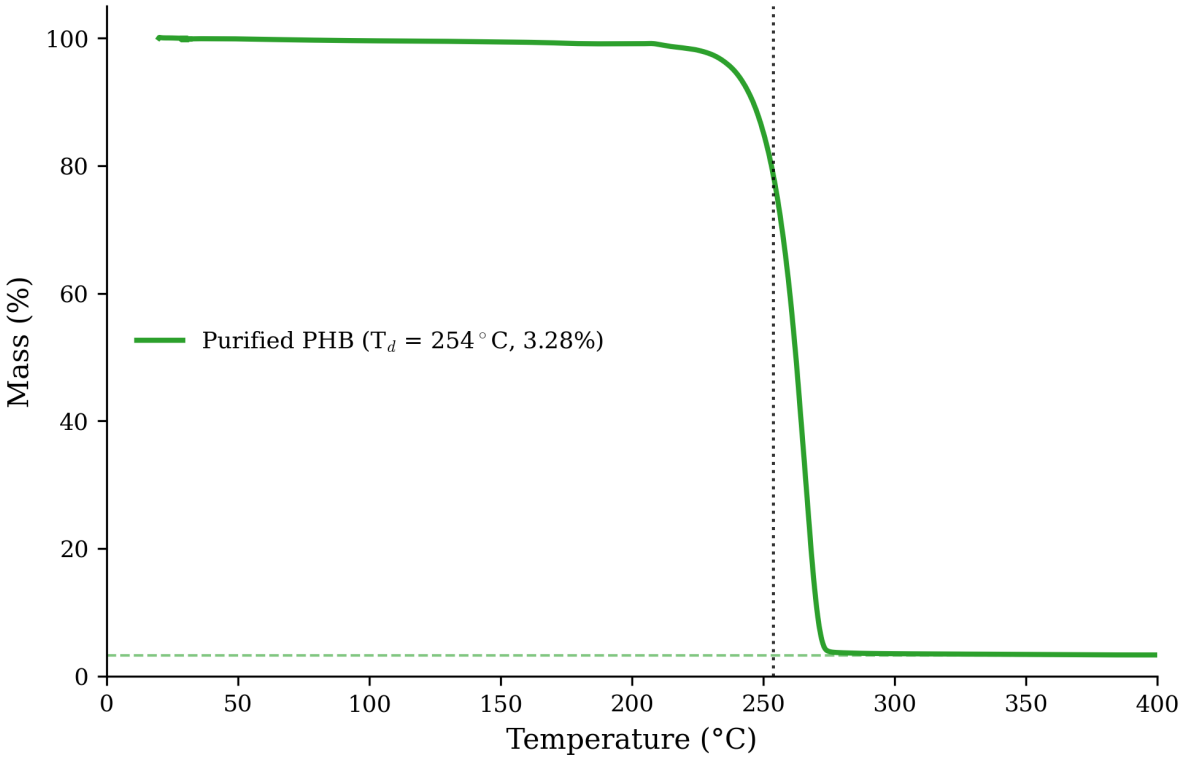


Figure 5.22: TGA curve of the purified PHB obtained after ethanol-assisted purification.

The purified material did not show a gradual mass-loss slope from the beginning of the test. Instead, the curve remained comparatively stable before the main degradation step, followed by the direct degradation event associated with PHB. This behavior suggests that the purification step reduced the residual compounds present in the evaporation-recovered material.

Commercial PHB pellet

The thermal results obtained for the commercial PHB pellet are presented in Figure 5.23, corresponding to the first and second heating cycles. The main thermal parameters obtained from these thermograms are summarized in Table 5.14. The individual heating-cycle thermograms are presented in Appendix D.

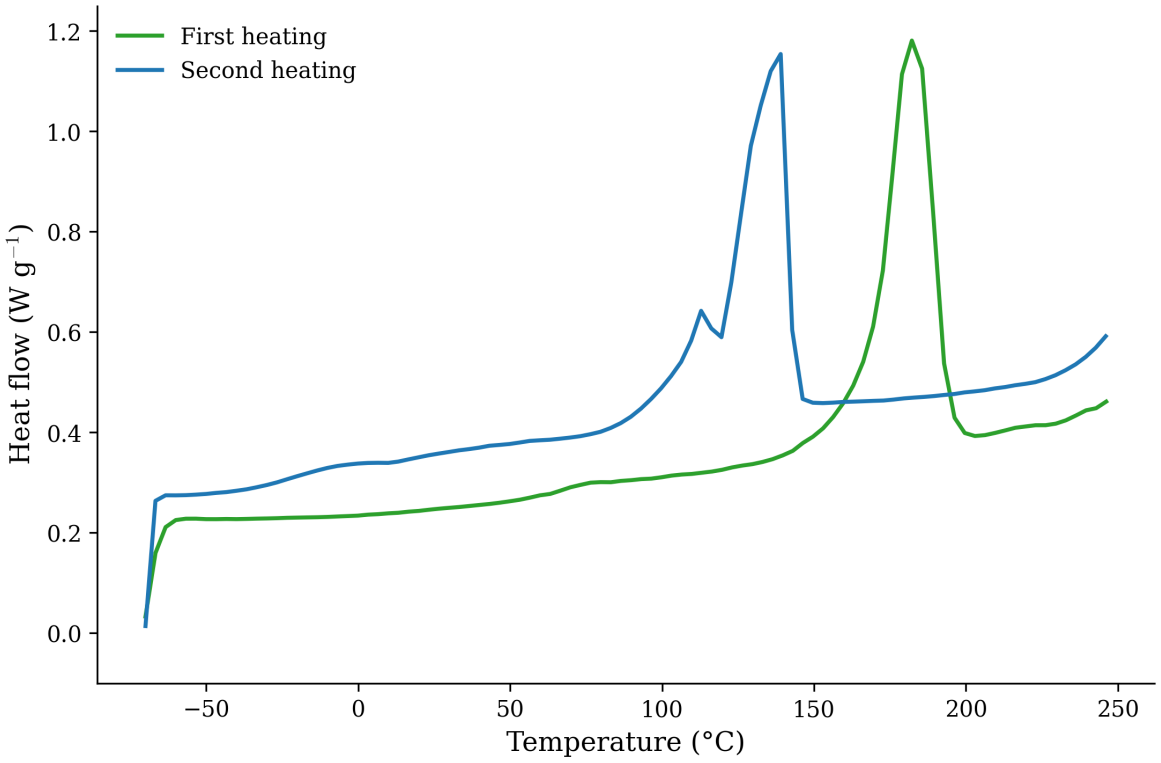


Figure 5.23: DSC thermograms of the commercial PHB pellet during the first and second heating cycles.

Table 5.14: Summary of transition temperatures obtained from DSC for the commercial PHB pellet.

Heating cycle	**Transition temperature (°C)**			
	T_{g1}	T_{g2}	T_m	χ(%)
First heating	-	63.20	182.69	65.66
Second heating	-20.19	43.13	138.18	65.21

Aging analysis was not performed for the pellet, since this material was not intended to be used directly in the subsequent experimental stages, but rather as the feedstock for fiber production. Nevertheless, DSC analysis was carried out to characterize the commercial material before extrusion and to compare its thermal response with the behavior typically reported for PHB. Consistent with the behavior discussed for the recovered film, the first heating cycle showed a melting transition within the expected range for PHB (Srubar et al., 2012; Turco et al., 2021; Di Lorenzo & Androsch, 2019),

whereas the second heating cycle exhibited a lower melting temperature after the imposed thermal history. This supports the interpretation that the sequence of rapid cooling and immediate reheating used in the DSC protocol can modify the crystallization and melting response of PHB (Gunaratne et al., 2004).

The crystallinity values obtained for both heating cycles were consistent with those commonly reported for PHB (McAdam et al., 2020; Dalton et al., 2022). Unlike the recovered native film, the commercial pellet showed no detectable cold crystallization event during the second heating cycle, suggesting that a substantial crystalline fraction had already formed during cooling. However, the lower T_m measured during the second heating indicates that this crystalline structure differed from that initially present in the pellet, potentially involving thinner or less perfect lamellae formed under the imposed cooling conditions. The thermal history consequently modified the melting response without producing a distinct cold crystallization peak. Since no such event contributed to the integrated heat flow, the calculated crystallinity was not magnified by crystallization occurring during the heating scan.

Regarding the glass transitions, the difference observed in T_{g2} between the first and second heating cycles may be related to the thermal history of the material. The first heating cycle reflects the state of the pellet as received, including any structural rearrangement that may have occurred during storage after manufacturing. A prolonged storage period could allow further organization of the RAF, increasing its apparent glass transition temperature. However, since aging was not evaluated for the pellet, this interpretation cannot be confirmed. The second heating cycle reflects the response of the polymer after erasing its previous thermal history and applying rapid cooling, which may leave the material in a less organized state. Under these conditions, T_{g2} may represent an earlier stage of structural reorganization rather than the response of a fully stabilized morphology.

PHB fiber

The thermal results obtained for the PHB fiber produced from the commercial PHB pellet are presented in Figure 5.24, and the main thermal parameters are summarized in Table 5.15. The individual thermograms are presented in Appendix D.

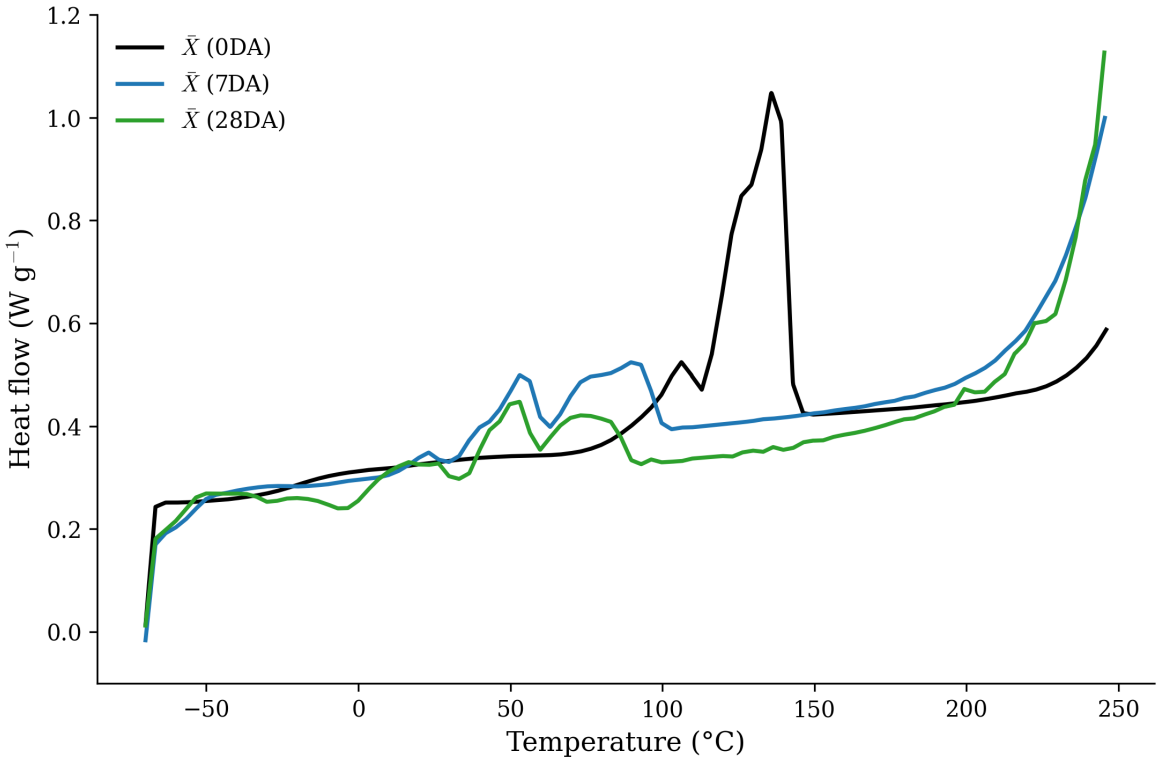


Figure 5.24: Average DSC thermograms of the PHB fiber at different aging times.

Table 5.15: Summary of mean transition temperatures and crystallinity obtained from DSC for the PHB fiber.

Aging time	**Thermal parameters** ($\bar{X} \pm \sigma$)			
	T_g (°C)	T_{g2} (°C)	T_m (°C)	χ (%)
Day 0	-21.76 ± 1.35	38.56 ± 3.59	137.22 ± 0.50	63.20 ± 6.28
7 DA	-53.87 ± 2.09	-	90.58 ± 0.37	28.76 ± 3.08
28 DA	-55.96 ± 0.74	-	72.79 ± 1.27	21.76 ± 5.98

The first heating cycle of the Day 0 PHB fiber showed an average melting temperature of 177.39 °C, which is within the expected range for PHB, indicating that extrusion did not eliminate the characteristic melting response of the polymer. However, as observed for both the recovered PHB film and the commercial PHB pellet, the second heating cycle did not reproduce the same melting temperature. Instead, the day 0 second heating thermogram showed a lower melting-related event, which may be associated with the imposed DSC thermal history (Gunaratne et al., 2004). No crystallization

event was identified during this scan, consistent with the behavior previously discussed for the commercial PHB pellet. The crystallinity obtained for Day 0 remained within the expected range for PHB, suggesting that the fiber retained a substantial crystalline fraction after extrusion and the imposed thermal cycle.

After aging, both the 7-day and 28-day thermograms showed markedly altered responses, characterized by multiple melting-related events similar to those observed for the locally produced PHB film. Since the same phenomenon occurred in both the recovered film and the fiber produced from the commercial PHB pellet, it cannot be attributed exclusively to impurities in the locally produced material. Those impurities likely played a critical role in its poor extrudability, but they do not fully explain the abnormal DSC response after aging. The occurrence of these altered thermograms in different PHB materials previously subjected to the initial DSC thermal cycle suggests that the behavior may instead be related to the protocol itself, particularly to the thermal exposure imposed before aging.

To examine whether the altered aged thermograms were associated with the upper temperature used in the DSC protocol, an exploratory protocol assessment was performed. Two PHB fiber specimens were subjected to three consecutive heating cycles, one with an upper temperature of 250 °C and the other limited to 220 °C, allowing the effect of each protocol to be observed directly in the third heating scan. Two additional specimens were subjected to two heating cycles using the same respective upper temperatures and were subsequently evaluated by TGA to determine whether the previous thermal exposure affected their thermal stability.

The thermograms obtained from the three consecutive heating cycles using upper temperatures of 250 and 220 °C are presented in Figures 5.25 and 5.26, respectively.

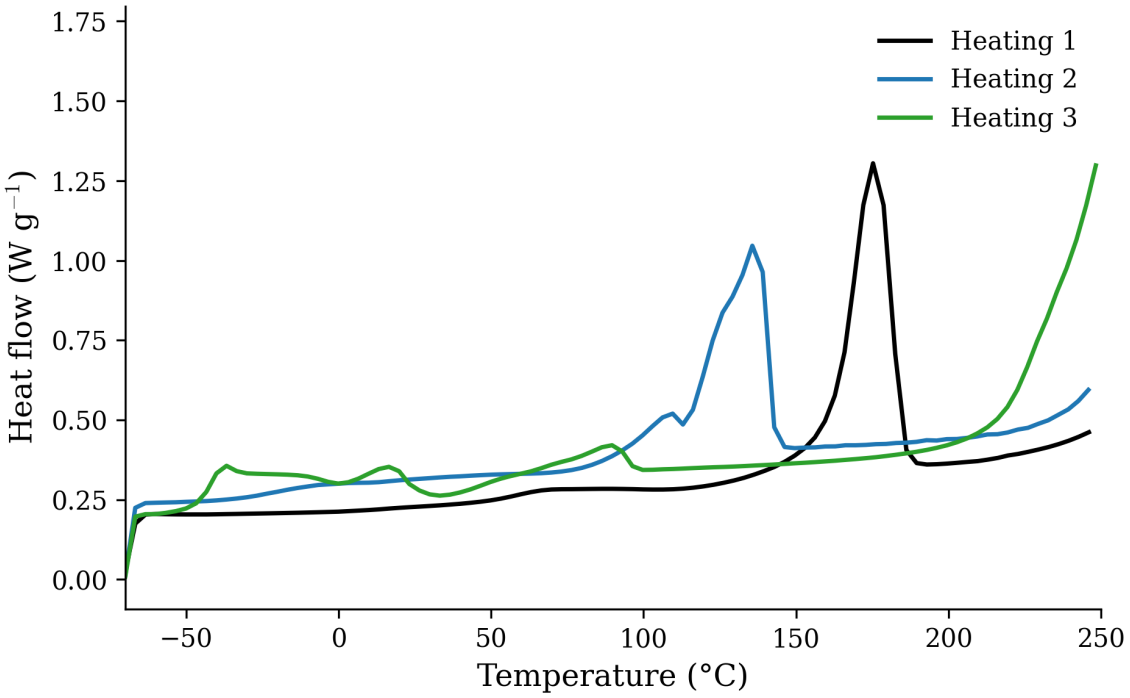


Figure 5.25: DSC thermograms obtained from three consecutive heating cycles of the PHB fiber using an upper temperature of 250 °C.

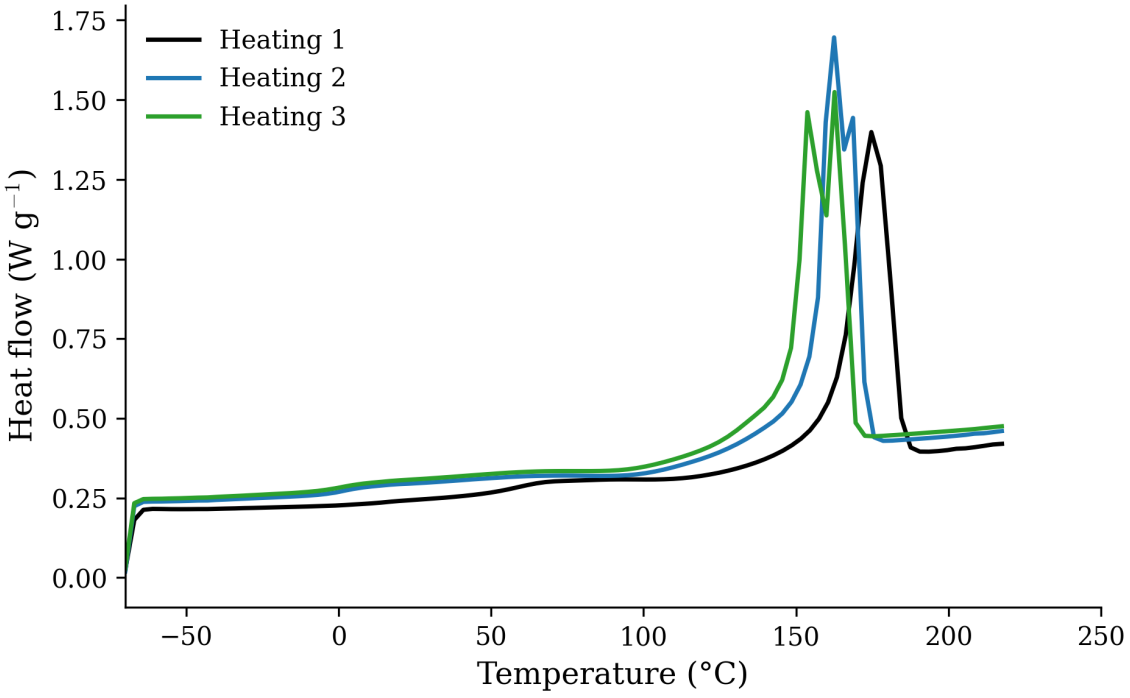


Figure 5.26: DSC thermograms obtained from three consecutive heating cycles of the PHB fiber using an upper temperature of 220 °C.

The effect of the upper temperature became particularly evident during the third heating cycle. When the specimen was repeatedly heated to 250 °C, the third thermogram no longer exhibited the characteristic melting response of PHB and instead showed multiple lower-temperature events and a strongly rising terminal baseline, as shown in Figure 5.25. In contrast, the specimen heated to 220 °C retained defined melting-related transitions throughout the three cycles without developing the same marked distortion, although changes in peak position and shape associated with the imposed thermal history were still observed, as shown in Figure 5.26.

The thermogravimetric response of the specimens previously subjected to two DSC heating cycles is compared in Figure 5.27.

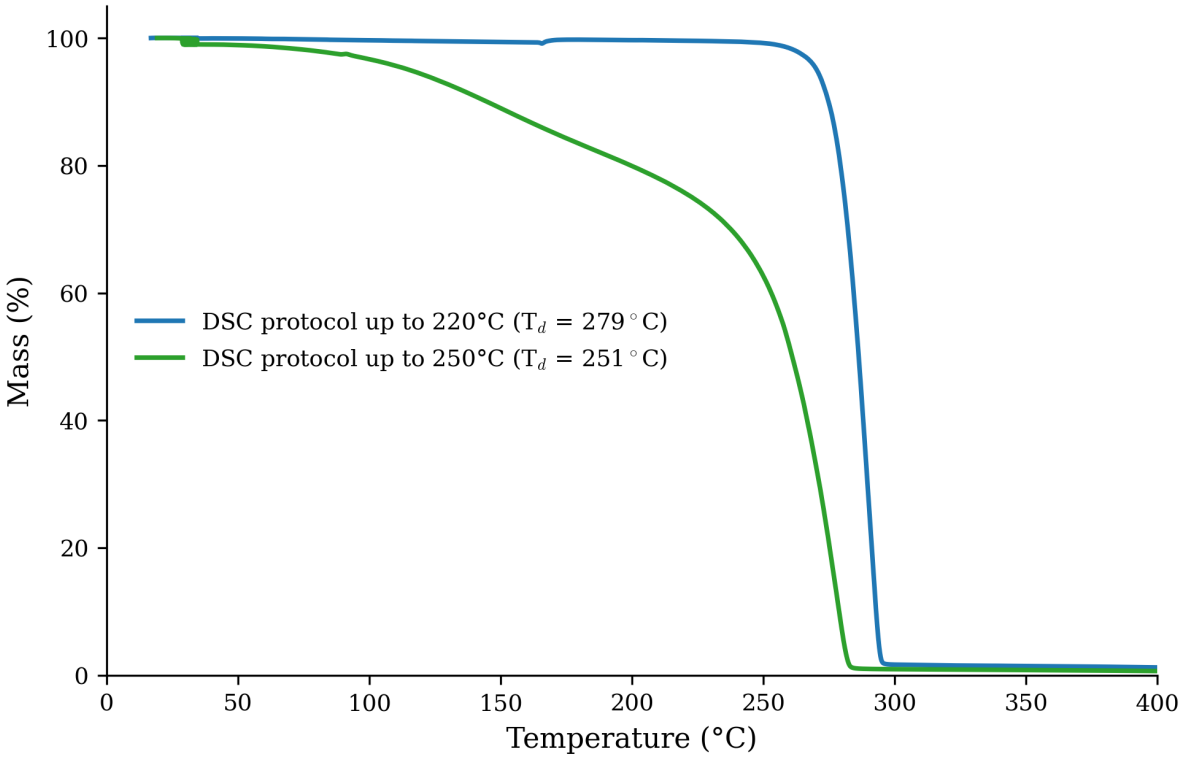


Figure 5.27: TGA curves of PHB fiber specimens previously subjected to two DSC heating cycles with upper temperatures of 220 and 250 °C.

The specimen previously heated to 220 °C remained essentially stable before its principal degradation event, whereas the specimen exposed to 250 °C showed gradual mass loss before the main degradation step. This shift in thermal response suggests that repeated exposure to 250 °C introduced an additional source of thermal damage during

the DSC protocol. The effect should not be attributed only to incomplete crystalline reorganization, since the TGA response indicates an actual reduction in thermal stability after the repeated heating cycles.

The absence of a clearly altered response in the second heating cycle suggests that the first exposure to 250 °C did not produce sufficient degradation to distort the subsequent thermogram. The critical stage may instead have occurred toward the end of the second heating cycle. After the first melting and rapid cooling step, the polymer entered the second heating scan from a less organized structural state, as reflected by the lower melting transition. A possible mechanism is that this incomplete structural reorganization also reduced the thermal stability of the material, making it more susceptible to degradation when exposed again to 250 °C. Under this hypothesis, the altered response observed in the following heating scan and the less stable TGA profile obtained after two cycles up to 250 °C would both result from protocol-induced thermal damage. This interpretation remains hypothetical, since the crystalline structure and molecular state of the material were not examined after each heating cycle. Confirming it would require complementary protocols capable of following the structural evolution of the polymer after each thermal step, such as XRD, FTIR, molecular-weight measurements, or DSC protocols specifically designed to isolate the effect of each heating cycle.

This protocol-related effect was not identified during the PHAC analysis, since the PHAC thermograms remained consistent after repeated heating up to 250 °C. The original upper-temperature limit consequently appeared suitable for the first material evaluated. The altered response became evident only when the same protocol was applied to the PHB fiber, indicating that the suitability of the DSC thermal cycle depends on the specific PHB-based formulation being analyzed.

For this PHB formulation, an upper temperature of 220 °C is more suitable for repeated-heating DSC analyses than the original limit of 250 °C. Applying the revised protocol could also reduce thermal damage during the evaluation of the locally produced PHB film, although this would require experimental confirmation. A new aging series performed under these conditions would allow the evolution of T_{g2} to be evaluated, as achieved for PHAC, without the same degree of interference from protocol-induced

degradation. This additional evaluation was outside the scope of the present thesis.

The average TGA curves obtained for the PHB fiber as a function of aging are presented in Figure 5.28.

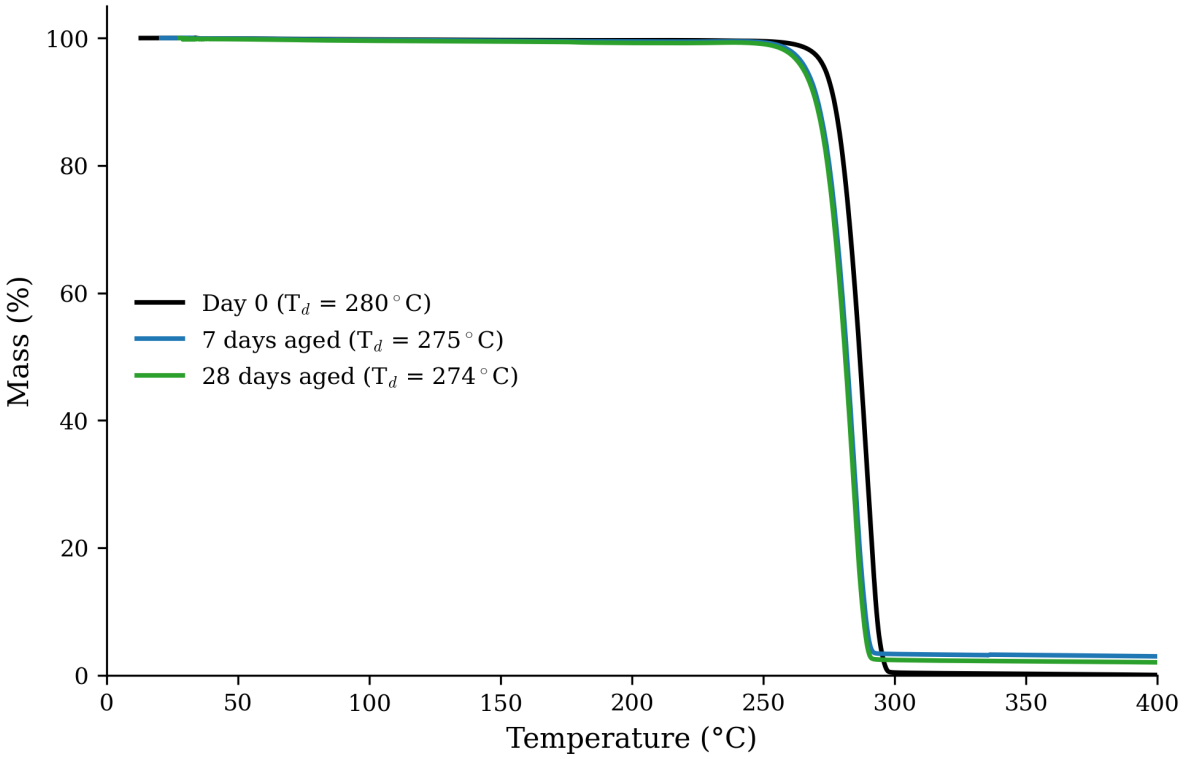


Figure 5.28: Average TGA curves of the PHB fiber at Day 0 and after 7 and 28 days of aging.

The degradation temperature decreased only slightly, from approximately 280 °C at Day 0 to 275 and 274 °C after 7 and 28 days, respectively. Most of this small difference occurred during the first 7 days, with practically no further change between 7 and 28 days. Aging consequently produced no substantial progressive reduction in the thermal stability of the PHB fiber within the evaluated period, particularly when compared with the decrease of approximately 28 °C caused by the DSC protocol reaching 250 °C.

5.2 Mechanical properties

PHAC fiber

The average stress-strain curves are presented in Figure 5.29, together with the linear fits used to estimate the apparent elastic modulus. The main tensile parameters of the PHAC fiber are summarized in Table 5.16.

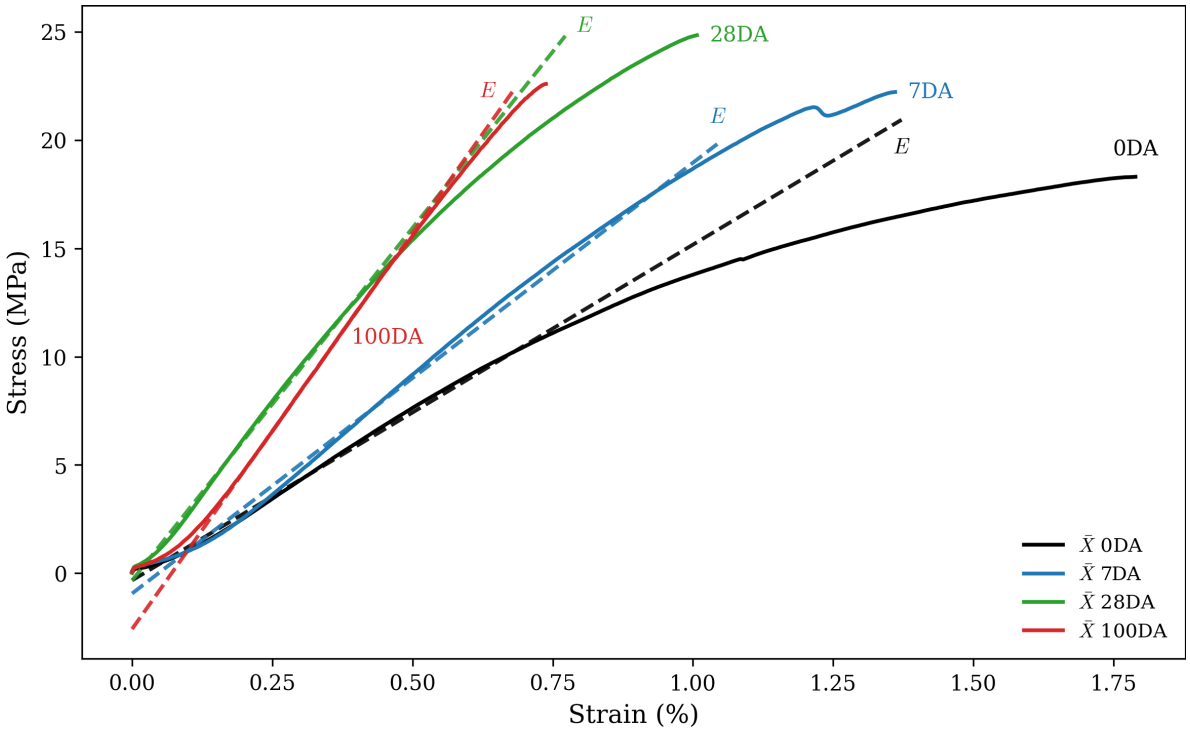


Figure 5.29: Average stress-strain curves of PHAC fiber specimens as a function of aging time, including the linear fits used to estimate the apparent elastic modulus.

Table 5.16: Summary of tensile properties obtained from single-fiber tensile tests of the PHAC fiber.

Aging time	**Tensile parameters** ($\bar{X} \pm \sigma$)		
	$\overline{\sigma_u}$ **(MPa)**	$\overline{\varepsilon_u}$ **(%)**	**E (GPa)**
Day 0	18.3 ± 1.8	1.79 ± 0.54	1.55
7 DA	22.2 ± 2.1	1.36 ± 0.42	1.99
28 DA	24.8 ± 1.4	1.01 ± 0.13	3.26
100 DA	23.2 ± 1.9	0.82 ± 0.06	3.66

The average curves show a clear time-dependent change in the mechanical response of PHAC. The most consistent effect of aging was the progressive reduction in strain at failure, indicating a gradual loss of deformation capacity. Tensile strength increased during the initial aging period, reached its highest mean value after 28 DA, and decreased slightly after 100 DA. The strength evolution was consequently not monotonic, whereas the loss of ductility and increase in apparent elastic modulus continued throughout the evaluated period.

This mechanical evolution is consistent with the phase-fraction analysis presented in subsection 5.1.5. Among the aged PHAC specimens, the apparent crystallinity remained comparatively stable, while the apparent RAF tended to increase and the apparent MAF decreased, particularly after 100 DA. This redistribution provides a coherent explanation for the mechanical response, since stiffness is influenced by the crystalline and constrained amorphous fractions, whereas deformation capacity depends more strongly on the remaining MAF (Righetti et al., 2019). The progressive increase in T_{g2} further supports an increase in amorphous-phase constraint. The increase in apparent modulus and reduction in strain at failure are thus more consistent with changes within the amorphous phase than with a substantial increase in crystallinity.

The slight decrease in tensile strength after 100 DA, together with the behavior observed during specimen preparation, is consistent with the development of a more brittle response after prolonged aging. The 100 DA fibers were noticeably fragile, and two specimens fractured during handling before testing. Since these specimens could not be included in the tensile analysis, the reported results may not fully represent the fragility of the complete aged sample population. The principal aging effect should consequently be interpreted as a progressive increase in stiffness and loss of deformation capacity, rather than as a continuous improvement in tensile strength.

The manufacturer reports a tensile strength of 24.3 MPa, an elastic modulus of 2.32 GPa, and an ultimate strain of 7.5% for the commercial material (colorFabb, 2023). The tensile strengths measured in this work were relatively close to the reported value, supporting the ability of the adopted procedure to provide consistent tensile-strength measurements. However, direct comparison remains limited because the manufacturer

did not specify the storage history of the tested material.

The difference in strain at failure should also be interpreted considering the experimental procedure. Strain was estimated from the crosshead displacement of the UTM rather than measured directly over the specimen gauge length using an extensometer or a dedicated fiber-testing system. Crosshead displacement may include contributions from equipment compliance, grip displacement, specimen alignment, and uncertainty in the effective gauge length. The obtained strain values are consequently more suitable for relative comparison among aging conditions than for direct comparison with standardized manufacturer values.

From the perspective of cementitious composite reinforcement, the initial increase in tensile strength and the progressive increase in stiffness could improve stress transfer before fiber failure. However, the simultaneous loss of deformation capacity and the fragility observed after prolonged aging could restrict crack-bridging performance by promoting fiber rupture at smaller crack openings. Despite the increase in tensile strength with aging, the measured values remained well below the approximately 530-3000 MPa range reported for representative commercial PP, PVA, and PE reinforcement fibers used in cement-based materials (Lan et al., 2021). Therefore, the PHAC fiber evaluated in this work cannot be considered suitable as mechanical reinforcement for cementitious composites.

PHB fiber

The average stress-strain curves of the PHB fiber, including the linear fits used to estimate the apparent elastic modulus, are presented in Figure 5.30. The main tensile parameters are summarized in Table 5.17.

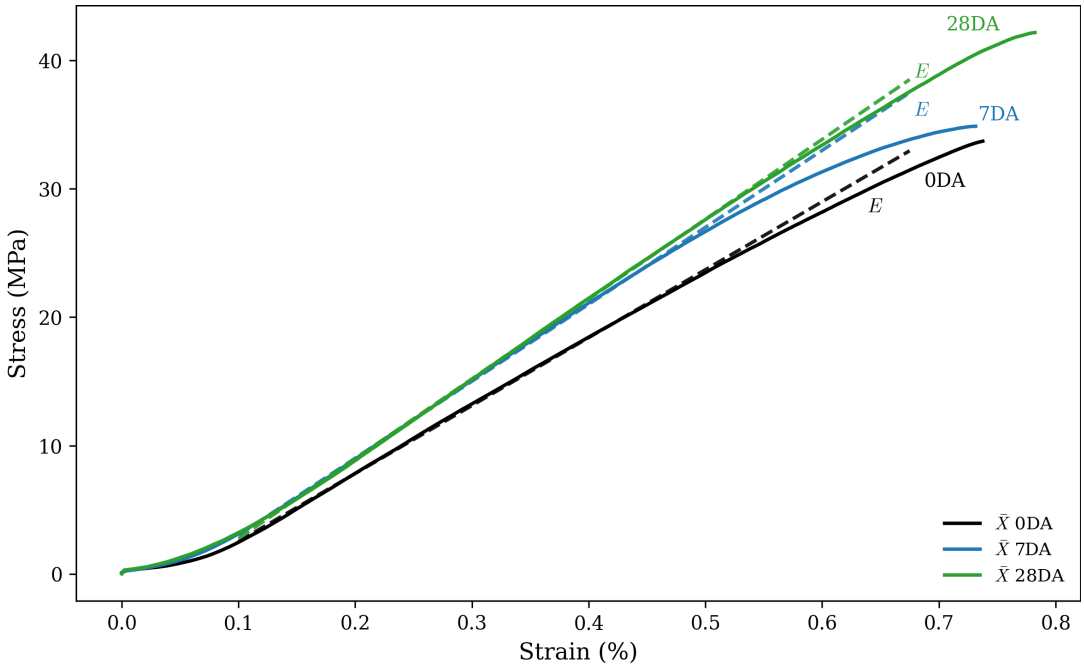
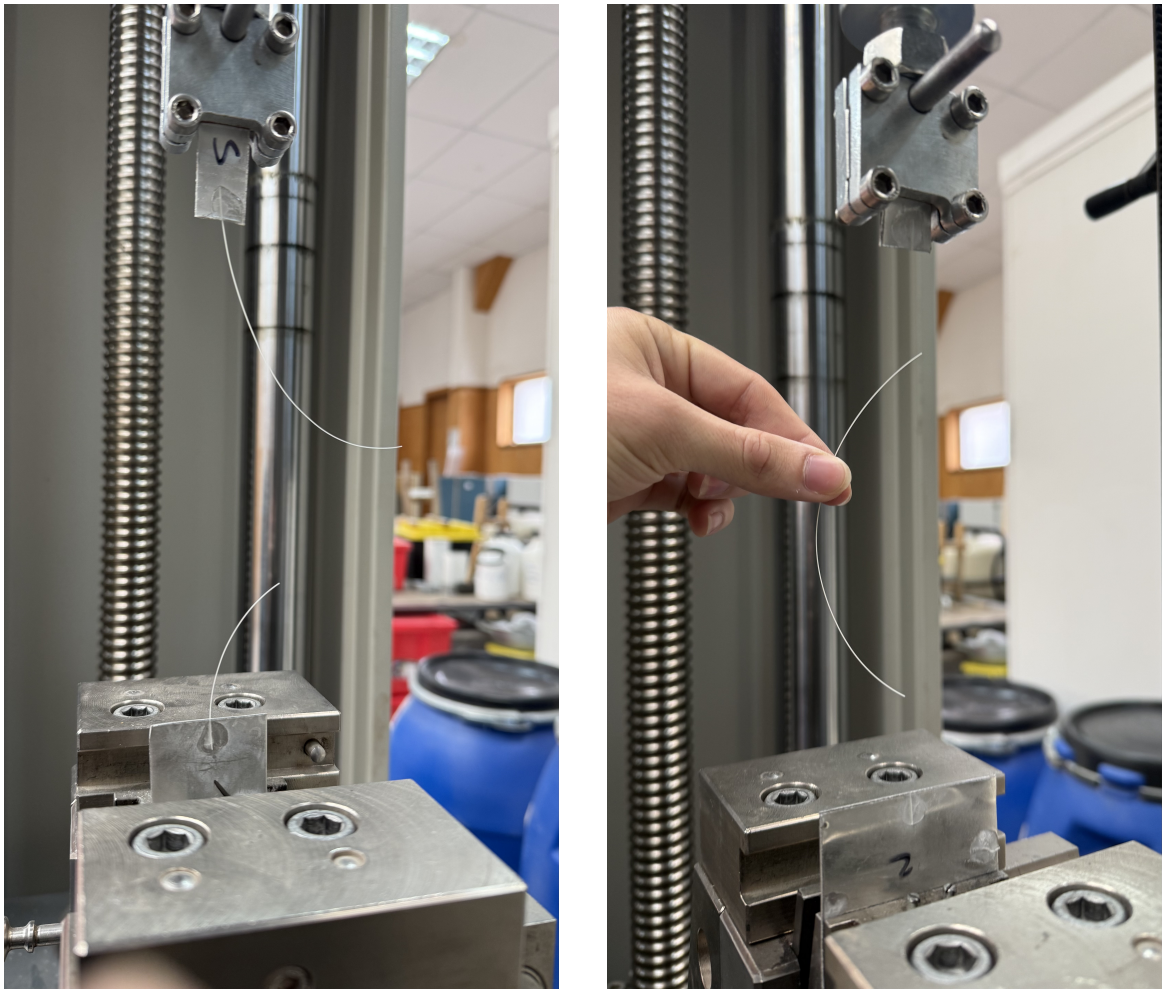


Figure 5.30: Average stress-strain curves of PHB fiber specimens including the linear fits used to estimate the apparent elastic modulus.

Table 5.17: Summary of tensile properties obtained from single-fiber tensile tests of the PHB fiber.

Aging time	**Tensile parameters** ($\bar{X} \pm \sigma$)		
	$\overline{\sigma_u}$ **(MPa)**	$\overline{\varepsilon_u}$ **(%)**	**E (GPa)**
Day 0	33.7 ± 6.5	0.74 ± 0.09	5.29
7 DA	34.9 ± 2.0	0.73 ± 0.08	5.99
28 DA	42.2 ± 4.5	0.78 ± 0.10	6.22

During the SFTT measurements, two representative failure modes were observed for both PHAC and PHB fibers, as shown in Figure 5.31. The first corresponded to fiber fracture within the gauge length. These fractures generally occurred at locations with a visibly smaller diameter, where the reduced cross-sectional area produced a local increase in stress. The second mode occurred at the connection between the fiber and the aluminum tabs and involved detachment from either the upper or lower tab. In some specimens, detachment occurred at both ends, leaving the fiber separated from both tabs at the end of the test, as shown in Figure 5.31(b).



(a) Fracture within the gauge length at a section with a locally reduced fiber diameter.

(b) Detachment of the fiber from both aluminum tabs.

Figure 5.31: Representative failure modes observed during single-fiber tensile testing of PHAC and PHB fibers.

The maximum stresses recorded for both failure modes were similar and remained within the range observed for each material, with no clear systematic reduction associated with tab-interface failure. Nevertheless, detachment from the aluminum tabs may involve partial slippage or loss of anchorage rather than fracture within the free gauge length. This behavior represents an additional source of uncertainty, particularly for the strain at failure, and further supports interpreting the measured strain values as comparative rather than absolute values.

The apparent elastic modulus increased progressively with aging. Mean tensile strength

remained similar between Day 0 and 7 DA, followed by a higher average value after 28 DA. However, the dispersion of the Day 0 results overlapped with part of the range measured after 28 DA. The results consequently suggest a possible strengthening trend, but the experimental variability prevents a clear time-dependent increase in tensile strength from being established.

No clear reduction in deformation capacity was observed. The mean strain at failure remained similar throughout the evaluated period and was slightly higher after 28 DA, with the differences remaining within the experimental variability. This response differs from that of PHAC, which exhibited a progressive reduction in strain at failure. The PHB fiber nevertheless presented low deformation capacity and a comparatively high apparent modulus from Day 0. Its behavior should therefore be interpreted as the preservation of an initially brittle tensile response rather than as evidence of ductility.

Unlike PHAC, the aged DSC thermograms of the PHB fiber did not permit a reliable evaluation of RAF and MAF evolution because their thermal response was affected by the original protocol reaching 250 °C, as discussed in subsection 5.1.5. The mechanical behavior cannot consequently be correlated directly with measured changes in these fractions. The progressive increase in apparent modulus and the evolution of the mean tensile strength suggest continued structural changes during storage, although their specific origin cannot be established from the aged DSC results.

The contrasting responses of PHAC and the PHB fiber may be related to the different morphologies and interfacial organization developed after extrusion. As discussed in subsection 5.1.5, the magnitude of physical aging depends not only on crystallinity, but also on the organization of the crystalline and amorphous regions. Alata et al. (2007) showed that changes in comonomer content can modify the crystallization behavior and susceptibility of PHBHHx copolymers to aging-induced embrittlement. Since PHAC contains an unidentified additional PHA component, whereas the PHB fiber was produced from a predominantly PHB formulation containing processing additives, the aging response of one material cannot be directly extrapolated to the other.

The thermal history and formulation of the commercial PHB pellet may have influenced the response of the extruded fiber. Extrusion was performed at 185 °C, whereas PHB

has been reported to require melting temperatures of at least 192-193 °C to eliminate the memory of previous crystalline order (Di Lorenzo & Androsch, 2019). Part of this order may consequently have remained as residual self-nuclei after extrusion. Increasing the extrusion temperature above 185 °C was not feasible under the processing conditions used in this work, since the reduction in melt viscosity prevented stable fiber formation and further narrowed the margin before thermal degradation.

The nucleating agent reported by the supplier may also have promoted crystallization, since these additives can reduce the supercooling required for PHB crystallization (Puente et al., 2013). Improved crystallization rate and storage stability have also been reported in self-nucleated PHBH systems (Xu et al., 2021). Together, these mechanisms may have favored the formation of a comparatively organized morphology shortly after extrusion, leaving less scope for subsequent immobilization of the amorphous phase and helping preserve the deformation capacity during aging. Limited structural rearrangement during storage would remain compatible with the progressive increase in apparent modulus and the higher mean strength measured after 28 DA, although the overlapping variability prevents the latter from being interpreted as a clear time-dependent increase.

The proposed influence of crystalline memory and nucleation remains hypothetical. Confirming whether crystalline memory persisted after extrusion would require a dedicated DSC self-nucleation protocol. A new aging series using the revised DSC protocol, complemented by XRD measurements, would also be needed to follow the subsequent evolution of the crystalline organization. These additional evaluations were outside the scope of this thesis.

5.3 Degradation of PHB

5.3.1 Thermal degradation

While the detailed results are presented in the previous chapter, Table 5.18 summarizes the characteristic degradation temperatures obtained from TGA for the different PHB formats and PHAC fiber evaluated in this study.

Table 5.18: Summary of degradation temperatures obtained from TGA for the different PHB-based materials evaluated as a function of aging. Values are reported as $\bar{X} \pm \sigma$.

Aging time	T_d (°C)		
	PHAC fiber	**PHB film**	**PHB fiber**
Day 0	279.9 ± 3.4	273.5 ± 8.2	279.8 ± 1.1
7 DA	282.8 ± 0.2	280.9 ± 1.5	275.0 ± 1.9
28 DA	281.6 ± 0.4	260.9 ± 11.9	274.3 ± 1.1
100 DA	281.6 ± 0.3	-	-

5.3.2 Degradation by alkalis

The chemical structure of PHB is shown in Figure 5.32. PHB is an aliphatic polyester whose repeating units are connected through ester bonds along the polymer backbone.

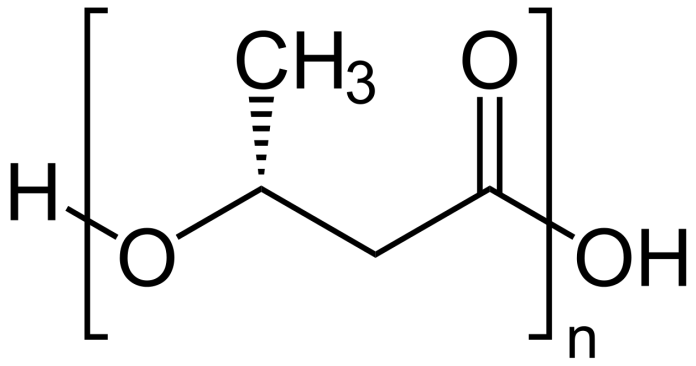


Figure 5.32: Chemical structure of PHB.

These ester bonds constitute the main chemically labile sites under alkaline conditions. Hydroxide ions can attack the carbonyl carbon, promoting ester-bond cleavage and progressive loss of molecular integrity through chain scission. Yu et al. (2005) studied the abiotic hydrolysis of PHB using NaOH solutions with concentrations ranging from 0.1 to 4 M and identified 3-hydroxybutyric acid (3HB) and crotonic acid (CA) as the main monomeric products formed under alkaline conditions.

PHAC fiber

The mass loss results obtained for the PHAC fiber at 70°C are presented in Figure 5.33 and summarized in Table 5.19.

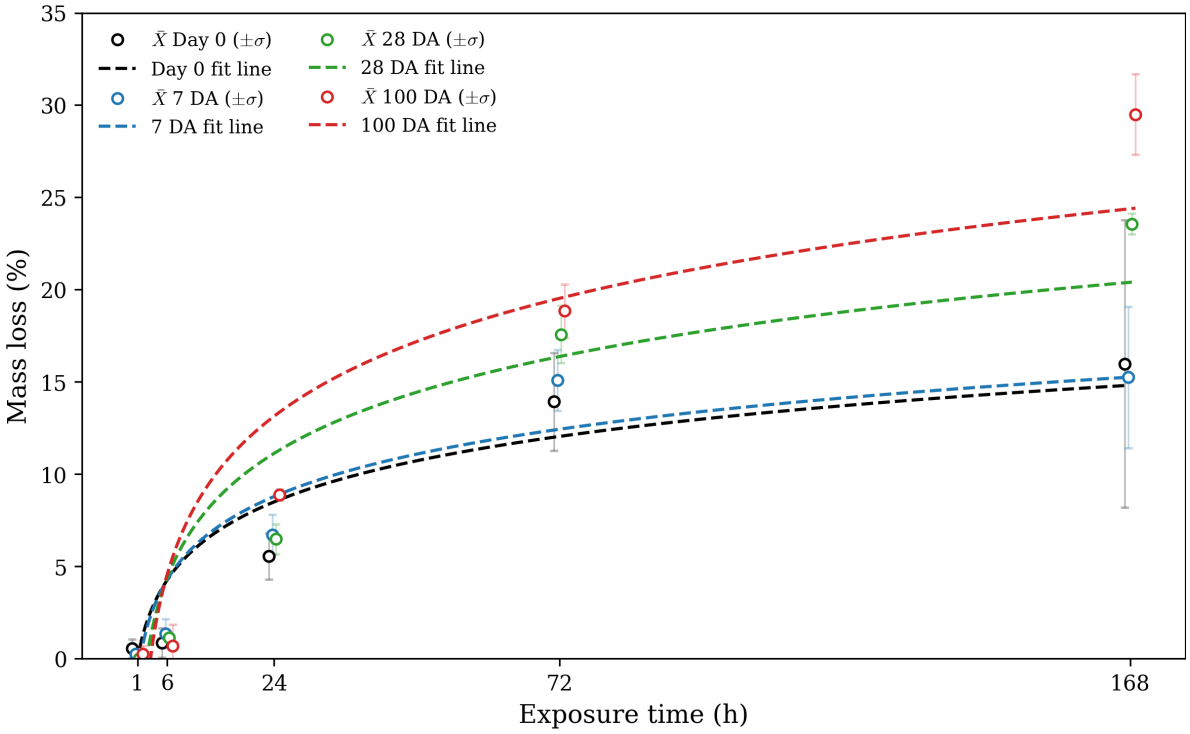


Figure 5.33: Mass loss of the PHAC fiber after alkaline exposure at 70°C.

Table 5.19: Summary of mass loss obtained for the PHAC fiber after alkaline exposure at 70°C.

Exposure time	**Mass loss ($\bar{X} \pm \sigma$) (%)**			
	Day 0	**7 DA**	**28 DA**	**100 DA**
1 h	0.55 ± 0.50	0.24 ± 0.01	0.00 ± 0.00	0.25 ± 0.43
6 h	0.85 ± 0.79	1.36 ± 0.77	1.12 ± 0.21	0.68 ± 1.18
24 h	5.55 ± 1.25	6.72 ± 1.07	6.48 ± 0.82	8.88 ± 0.30
72 h	13.93 ± 2.65	15.09 ± 1.64	17.57 ± 1.56	18.85 ± 1.44
168 h	15.98 ± 7.79	15.24 ± 3.83	23.56 ± 0.56	29.50 ± 2.18

The results obtained at 70°C show that mass loss increased markedly with exposure time in Lawrence solution. Prolonged alkaline exposure progressively affected the integrity

of the PHAC fiber, which could compromise its continuity and stress-transfer capacity within a cementitious composite. Since 70°C represents a severe alkaline-thermal condition, these results describe an accelerated degradation scenario rather than typical long-term exposure inside concrete.

The influence of aging became noticeable mainly after prolonged alkaline exposure. The differences between aging conditions were small at short exposure times, whereas a clearer separation appeared after 72 h. At 168 h, the 28 and 100 DA specimens showed greater mass loss than the initial condition, while the 7 DA result remained within the comparatively large variability of Day 0. Aging may consequently reduce alkaline resistance, although this effect was not uniform and became relevant only after sufficiently long exposure.

This behavior is consistent with the thermal and mechanical evolution discussed previously. Among the aged PHAC specimens, crystallinity remained comparatively stable, while the apparent RAF tended to increase and the apparent MAF decreased, particularly after 100 DA. These changes coincided with an increase in apparent modulus, a progressive reduction in strain at failure, and greater fragility during specimen handling. The higher alkaline degradation observed after prolonged aging may consequently be related to the redistribution and increasing constraint of the amorphous phase.

Tapadiya & Vasanthan (2017) studied alkaline hydrolysis of PHB films using DSC and FTIR. The normalized crystalline band at 3010 cm^{-1} remained nearly unchanged after degradation, whereas the amorphous band at 1183 cm^{-1} decreased, supporting preferential degradation of amorphous regions. Their analysis distinguished only between crystalline and amorphous contributions and did not separate MAF from RAF. The present results therefore support the involvement of the amorphous phase but do not demonstrate that RAF was preferentially attacked or that its increase directly caused the higher mass loss. Confirming this mechanism would require phase-fraction and structural analyses performed before and after alkaline exposure.

The mass loss results obtained at 20°C are presented in Figure 5.34 and summarized in Table 5.20.

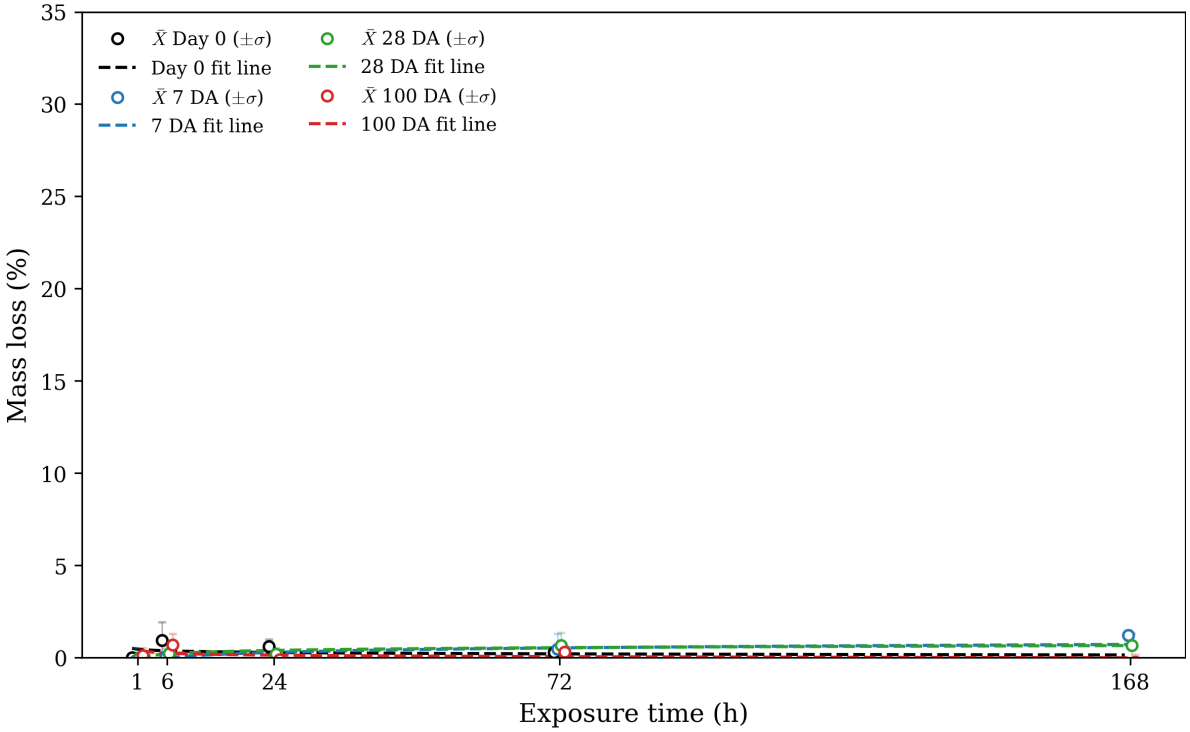


Figure 5.34: Mass loss of the PHAC fiber after alkaline exposure at 20°C.

Table 5.20: Summary of mass loss obtained for the PHAC fiber after alkaline exposure at 20°C.

Exposure time	**Mass loss** ($\bar{X} \pm \sigma$) (%)			
	Day 0	**7 DA**	**28 DA**	**100 DA**
1 h	0.00 ± 0.00	-0.15 ± 0.68	0.00 ± 0.00	0.12 ± 0.41
6 h	0.94 ± 0.97	0.01 ± 0.50	0.24 ± 0.41	0.70 ± 0.59
24 h	0.61 ± 0.37	-0.46 ± 0.02	0.19 ± 0.34	-0.11 ± 0.40
72 h	0.27 ± 0.24	0.47 ± 0.81	0.68 ± 0.67	0.31 ± 0.30
168 h	-0.32 ± 0.27	1.21 ± 0.27	0.65 ± 0.68	-0.23 ± 0.40

The results obtained at 20°C show a markedly different behavior from that observed at 70°C, confirming the strong effect of temperature on alkaline degradation. Under ambient-temperature exposure, the PHAC fiber did not show clear evidence of substantial mass loss, even after prolonged contact with Lawrence solution. This result is favorable for potential use in cementitious materials, since it suggests that the fiber may remain relatively stable under milder alkaline exposure conditions.

Some negative mass-loss values were obtained at 20°C. These values should not be interpreted as real mass gain of the polymer, but rather as an experimental effect. First, the samples were not washed after removal from the alkaline solution and before drying, which may have allowed residual salts from the Lawrence solution to remain attached to the fiber surface, increasing the measured final mass. Second, in several cases the measured mass differences were very small and close to the resolution limit of the balance.

No clear effect of aging was observed at 20°C. Unlike the behavior at 70°C, where aged samples showed higher mass loss after prolonged exposure, the results obtained at ambient temperature remained close to the experimental variability range for all aging conditions, with values that were generally close to zero. This indicates that aging did not noticeably reduce the alkaline stability of the PHAC fiber.

Native film

The mass loss results obtained for the locally produced PHB recovered as native film at 70°C are presented in Figure 5.35 and summarized in Table 5.21.

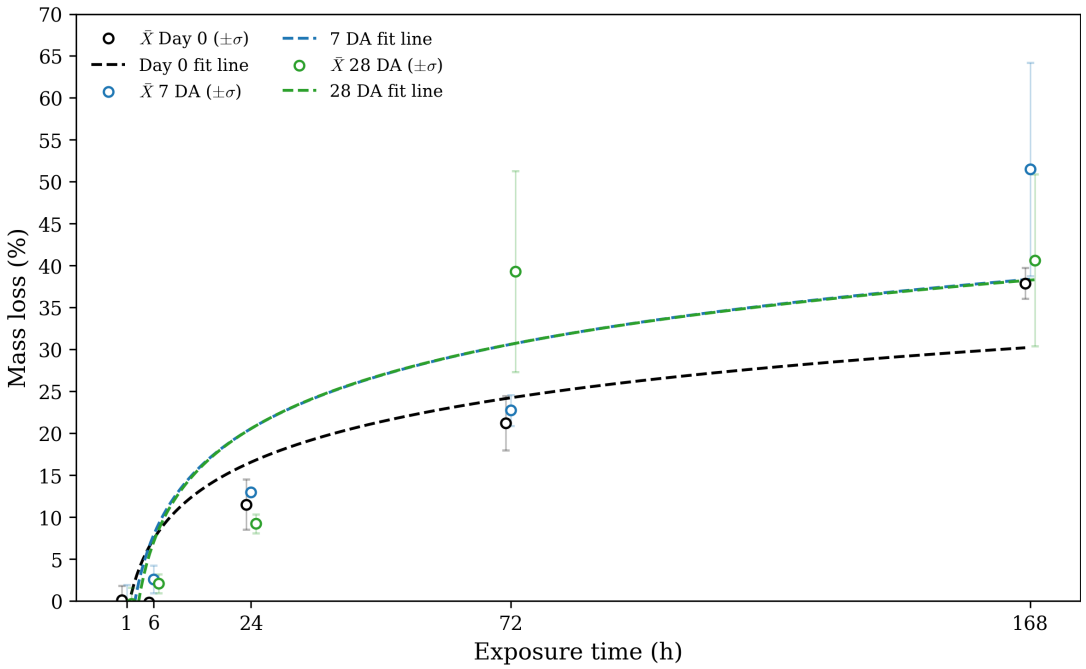


Figure 5.35: Mass loss of the locally produced PHB recovered as native film after alkaline exposure at 70°C.

Table 5.21: Summary of mass loss obtained for the locally produced PHB recovered as native film after alkaline exposure at 70°C.

Exposure time	**Mass loss** ($\bar{X} \pm \sigma$) (%)		
	Day 0	**7 DA**	**28 DA**
1 h	0.14 ± 1.71	-0.88 ± 2.80	-0.34 ± 1.95
6 h	-0.14 ± 0.48	2.59 ± 1.65	2.07 ± 1.14
24 h	11.51 ± 2.99	12.97 ± 0.18	9.24 ± 1.13
72 h	21.23 ± 3.25	22.76 ± 1.84	39.31 ± 11.99
168 h	37.90 ± 1.84	51.49 ± 12.72	40.65 ± 10.25

As observed for PHAC, the native PHB film showed substantial mass loss at 70°C, with degradation increasing as exposure time progressed. After prolonged exposure, the values were generally higher than those obtained for PHAC under equivalent conditions. However, the differences among aging conditions did not follow a consistent progression. For example, the 28 DA condition showed particularly high mass loss after 72 h, but its value after 168 h was lower than that obtained for 7 DA. Aging cannot consequently be isolated as the main cause of the differences observed between these specimens.

The higher degradation relative to PHAC may be partly associated with differences in accessible porosity and morphology. PHAC was classified as essentially non-porous by N_2 physisorption, whereas one of the native-film measurements showed a higher accessible surface area and pore volume. A more open morphology could increase the area exposed to Lawrence solution and facilitate contact between hydroxide ions and hydrolytically susceptible ester bonds. However, the second native-film measurement presented substantially lower adsorption, confirming that this material was not structurally uniform. These differences are consistent with the heterogeneous appearance of the evaporation-recovered films, which varied in thickness, texture, color, and surface morphology. Specimens from different film fragments were also combined in some degradation vials, introducing an additional source of variability.

The porosity results provide a plausible explanation for the higher and more dispersed mass loss of the native film, although N_2-accessible porosity at 77 K cannot be translated directly into accessibility under aqueous alkaline conditions. Moreover, the aged DSC

thermograms cannot be used to establish a relationship between aging and degradation because their thermal response was affected by the original DSC protocol. The results at 70°C are consequently better explained by the combined effects of prolonged alkaline exposure and specimen heterogeneity than by a clearly defined aging mechanism.

The mass loss results obtained for the locally produced PHB recovered as native film at 20°C are presented in Figure 5.36 and summarized in Table 5.22.

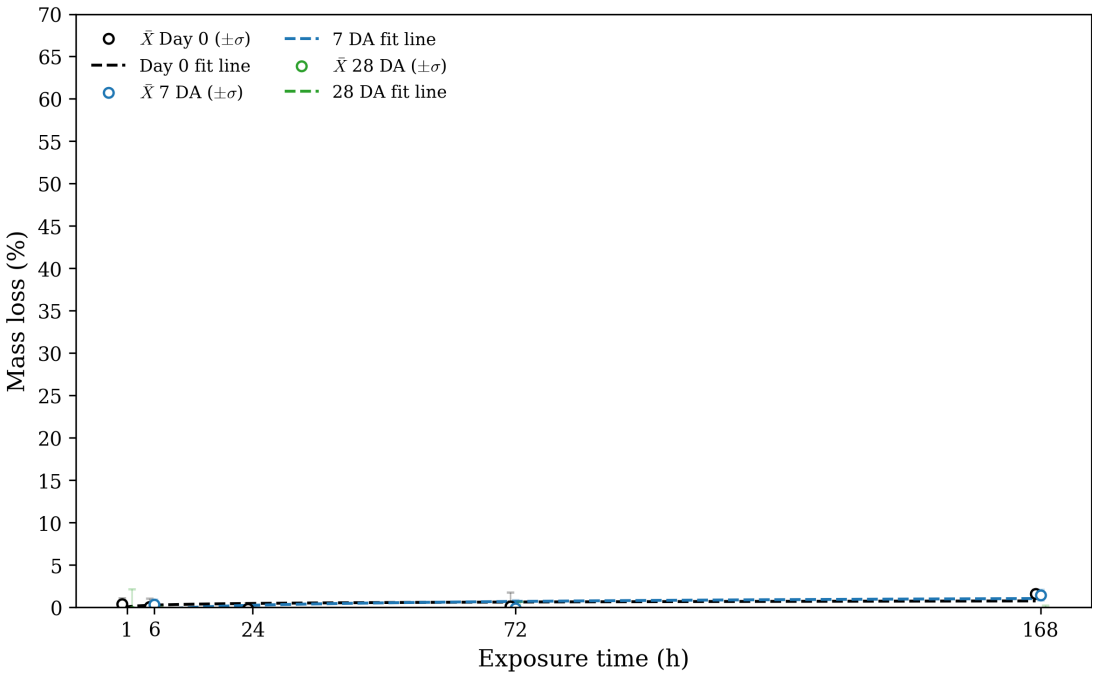


Figure 5.36: Mass loss of the locally produced PHB recovered as native film after alkaline exposure at 20°C.

Table 5.22: Summary of mass loss obtained for the locally produced PHB recovered as native film after alkaline exposure at 20°C.

Exposure time	**Mass loss** ($\bar{X} \pm \sigma$) **(%)**		
	Day 0	**7 DA**	**28 DA**
1 h	0.40 ± 0.72	-1.35 ± 0.50	-0.53 ± 2.67
6 h	0.04 ± 1.01	0.34 ± 0.60	-1.86 ± 2.00
24 h	-0.14 ± 0.65	-0.17 ± 0.65	-0.87 ± 0.80
72 h	0.12 ± 1.65	-0.09 ± 1.00	-1.07 ± 1.73
168 h	1.62 ± 0.47	1.47 ± 0.63	-1.06 ± 1.28

At 20°C, the native film showed no substantial mass loss within the evaluated exposure period. Most values remained close to zero and within the experimental variability, without a consistent effect of either exposure time or aging. As discussed for PHAC, the negative values may be associated with residual salts retained on the unwashed specimens and with mass differences within the resolution of the balance. Despite its heterogeneous morphology and strong degradation at 70°C, the locally produced PHB remained comparatively stable under the ambient-temperature alkaline condition.

PHB fiber

The mass loss results obtained for the PHB fiber at 70°C are presented in Figure 5.37 and summarized in Table 5.23.

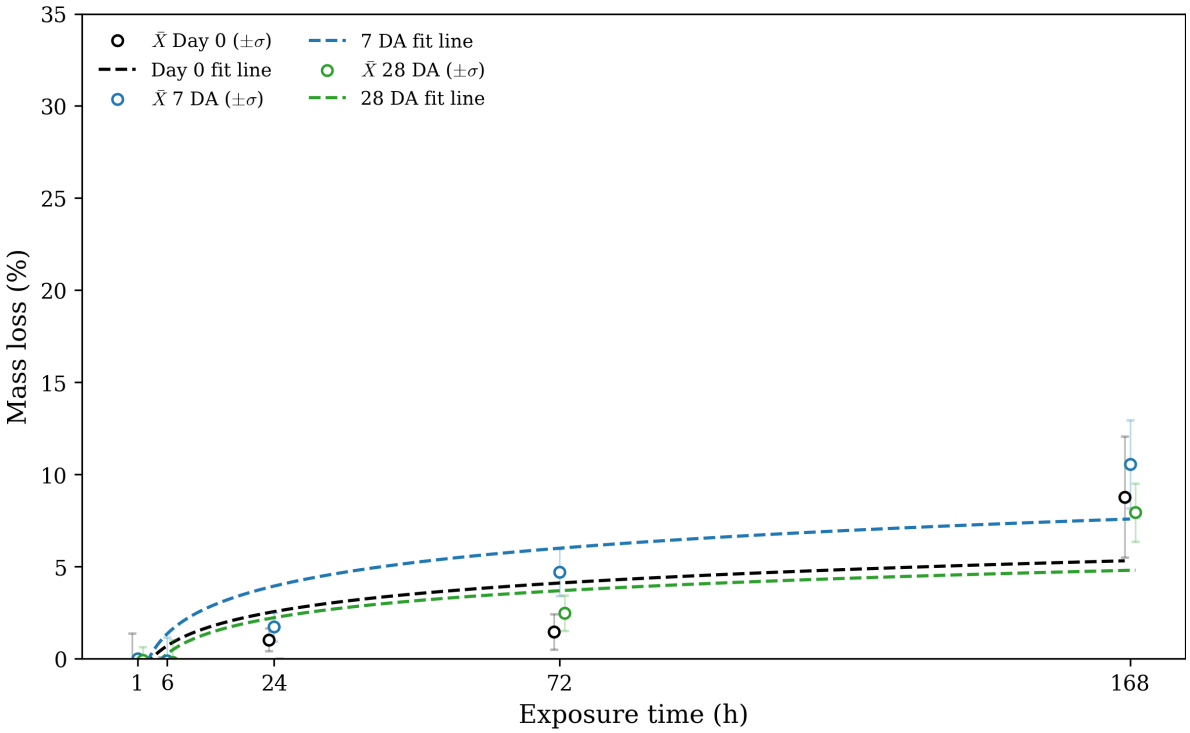


Figure 5.37: Mass loss of the PHB fiber after alkaline exposure at 70°C.

Table 5.23: Summary of mass loss obtained for the PHB fiber after alkaline exposure at 70°C.

Exposure time	**Mass loss** ($\bar{X} \pm \sigma$) (%)		
	Day 0	**7 DA**	**28 DA**
1 h	-0.42 ± 1.80	0.00 ± 0.00	-0.07 ± 0.71
6 h	-0.54 ± 0.63	-0.10 ± 1.26	-0.18 ± 1.19
24 h	1.03 ± 0.62	1.73 ± 0.78	-0.75 ± 0.79
72 h	1.46 ± 0.96	4.69 ± 1.27	2.49 ± 0.96
168 h	8.78 ± 3.28	10.56 ± 2.40	7.93 ± 1.57

At 70°C, the PHB fiber showed limited mass variation during the first 24 h, followed by a clearer increase after 72 and 168 h. Nevertheless, its mass loss remained substantially lower than that measured for PHAC and the native film under the same exposure condition. This indicates that the extruded PHB fiber presented greater resistance to accelerated alkaline degradation within the evaluated period.

No monotonic effect of aging was observed. The 7 DA specimens showed the highest mean mass loss after 72 and 168 h, whereas the 28 DA specimens remained below both the 7 DA and Day 0 conditions at the end of the test. The overlap between the corresponding standard deviations further prevents these differences from being interpreted as a progressive aging effect.

The different alkaline responses of PHAC and the PHB fiber cannot be explained by their thermal stability or accessible porosity. Both materials maintained comparatively stable degradation temperatures during aging and were classified as essentially non-porous by N_2 physisorption. These properties do not account for the higher mass loss of PHAC or for its more evident aging-related trend.

Tapadiya & Vasanthan (2017) reported that alkaline hydrolysis of PHB decreased with increasing crystallinity and preferentially affected its amorphous regions. This provides a possible explanation for the differences observed both during PHAC aging and between the two fibers. In PHAC, crystallinity and thermal stability remained comparatively stable, whereas MAF decreased and RAF increased. Since this redistribution

was the principal structural change identified during aging, the increasing constraint of the amorphous phase represents the most plausible explanation supported by the available results for the progressive reduction in alkaline resistance. However, Tapadiya & Vasanthan (2017) do not distinguish between MAF and RAF. The relationship between increasing RAF and mass loss consequently remains hypothetical and does not demonstrate selective degradation of RAF.

The difference in crystallinity may also contribute to the greater overall degradation of PHAC. The aged PHAC specimens presented an apparent crystallinity of approximately 35%, whereas the reliable Day 0 value obtained for the PHB fiber was close to 63%. PHAC consequently contained a larger total amorphous fraction potentially susceptible to alkaline attack. A direct comparison during aging was not possible because the aged DSC thermograms of the PHB fiber did not allow its crystallinity, MAF, and RAF to be quantified reliably.

The comparatively stable alkaline response of the PHB fiber is consistent with the limited aging effect discussed in the preceding mechanical analysis. Crystalline memory and the nucleating agent present in the commercial PHB formulation may have promoted rapid organization after extrusion, leaving less space for subsequent changes in amorphous-phase organization. The additional PHA phase in PHAC may instead have modified chain packing and contributed to its lower crystallinity. These compositional effects provide a complementary explanation for the different responses of the fibers, although their specific contribution cannot be confirmed because the identity and concentration of the additional PHA in PHAC were not disclosed.

The corresponding mass loss results obtained at 20°C are presented in Figure 5.38 and summarized in Table 5.24.

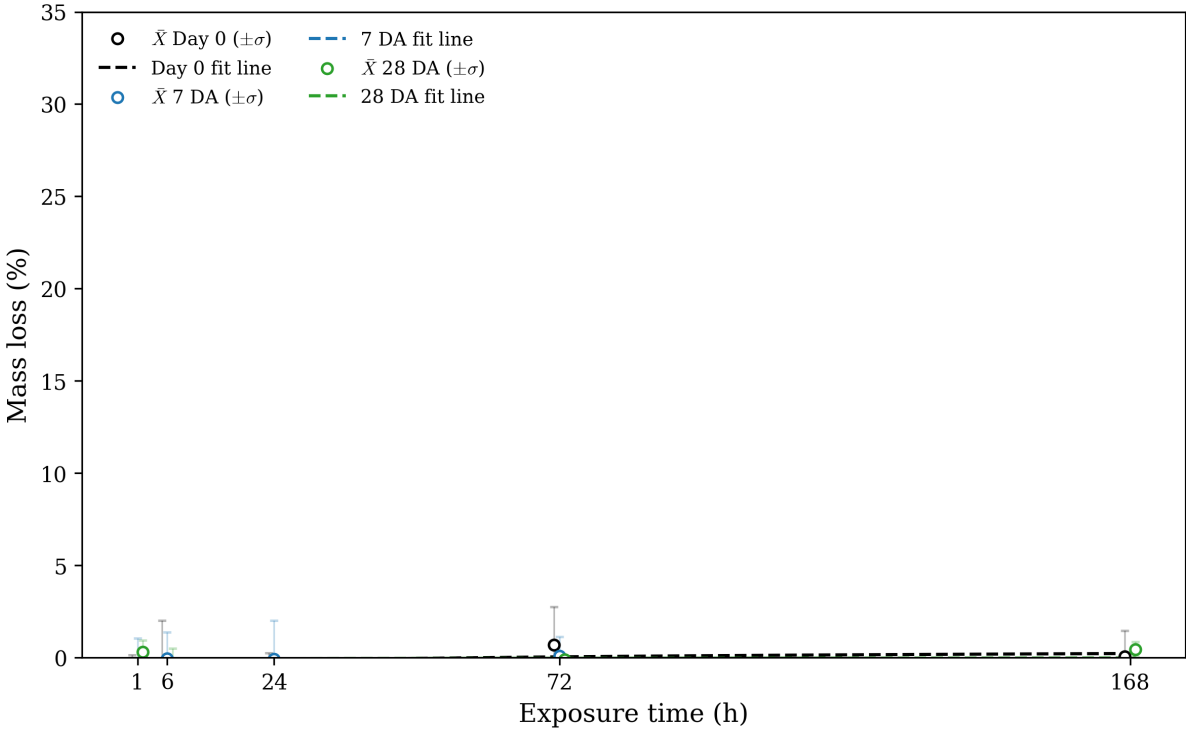


Figure 5.38: Mass loss of the PHB fiber after alkaline exposure at 20°C.

Table 5.24: Summary of mass loss obtained for the PHB fiber after alkaline exposure at 20°C.

Exposure time	**Mass loss** ($\bar{X} \pm \sigma$) (%)		
	Day 0	**7 DA**	**28 DA**
1 h	-0.64 ± 0.79	-0.53 ± 1.57	0.32 ± 0.63
6 h	-0.73 ± 2.75	-0.04 ± 1.41	-0.46 ± 0.96
24 h	-0.72 ± 0.96	-0.07 ± 2.10	-0.51 ± 0.17
72 h	0.71 ± 2.04	0.09 ± 1.04	-0.11 ± 0.19
168 h	0.07 ± 1.39	-0.49 ± 0.43	0.45 ± 0.40

At 20°C, the results remained close to zero for all aging and exposure conditions. The small positive and negative variations were within the experimental uncertainty and did not reveal a systematic effect of aging. The PHB fiber can consequently be considered stable under the ambient-temperature alkaline condition evaluated in this work.

5.3.3 FTIR analysis

PHAC fiber

FTIR analysis was not performed for the PHAC fiber under the selected transmission configuration because the presence of titanium dioxide in the formulation prevented the preparation of a sufficiently transparent specimen. As previously indicated by the manufacturer, this component is responsible for the white coloration of the fiber. Its presence hindered transmission of the infrared beam through the specimen, preventing the acquisition of a reliable spectrum using this preparation route.

Native film and purified PHB

The FTIR spectrum obtained from one of the native PHB films produced during the preliminary quality-control analysis of the fermentation process is presented in Figure 5.39. This spectrum was used to identify the principal PHB absorption bands and the spectral regions of interest for assessing possible changes in crystalline and amorphous organization during aging.

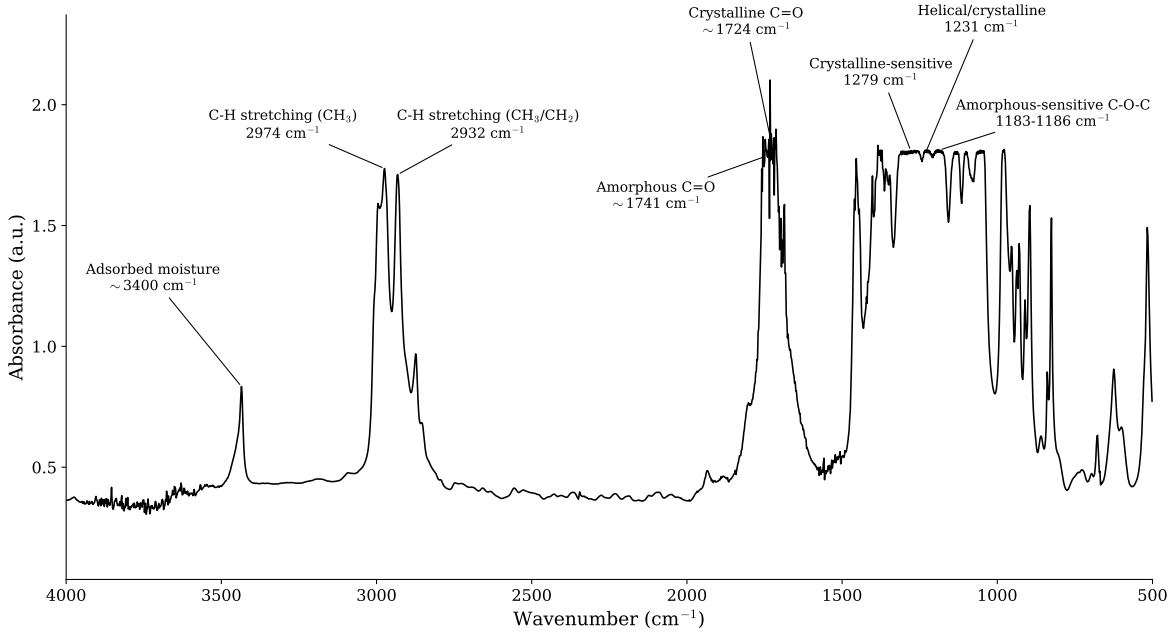


Figure 5.39: FTIR spectrum of the locally produced PHB recovered as native film from reactor run R1, showing the principal PHB absorption regions.

The bands measured near 2974 and 2932 cm^{-1} fall within the aliphatic C-H stretching region of PHB and are therefore assigned to C-H stretching vibrations. Similar PHB absorption bands have been reported in the 2928-2984 cm^{-1} range for alkyl groups, and near 2975 and 2934 cm^{-1} in FTIR analyses of PHB films (Tapadiya & Vasanthan, 2017). The intense region between approximately 1750 and 1720 cm^{-1} corresponds to ester carbonyl stretching. This carbonyl envelope can contain contributions from different local environments within semicrystalline PHB. In situ FTIR measurements performed during melting and crystallization assigned the lower-wavenumber contribution near 1724 cm^{-1} to crystalline PHB and the higher-wavenumber contribution near 1741 cm^{-1} to amorphous PHB (Xu et al., 2002). The bands near 1278 and 1230 cm^{-1} have also been associated with crystalline organization, with the latter assigned to helical chain conformation, whereas the region near 1183-1186 cm^{-1} has been used as an amorphous-sensitive C-O-C band (Xu et al., 2002; Tapadiya & Vasanthan, 2017). The small band observed near 3400 cm^{-1} was attributed to O-H stretching associated with adsorbed moisture rather than to a characteristic vibration of the PHB backbone (Zohaib et al., 2023).

These phase assignments were established by following controlled structural changes rather than from a single spectrum. Xu et al. (2002) monitored the opposite evolution of crystalline- and amorphous-sensitive bands during in situ melting and crystallization and compared the spectral response with DSC. Tapadiya & Vasanthan (2017) varied PHB crystallinity through annealing, verified the resulting changes by DSC, and identified bands whose normalized absorbance increased or decreased systematically with crystallinity. Accordingly, the labels in Figure 5.39 indicate literature-supported spectral assignments and regions of interest. They do not imply that overlapping crystalline and amorphous contributions were independently separated in the R1 spectrum.

The FTIR spectra obtained for the native film at the evaluated aging times are compared in Figure 5.40. The principal PHB absorption regions remained at comparable wavenumbers, and no new band attributable to the formation of a different functional group was clearly identified during aging.

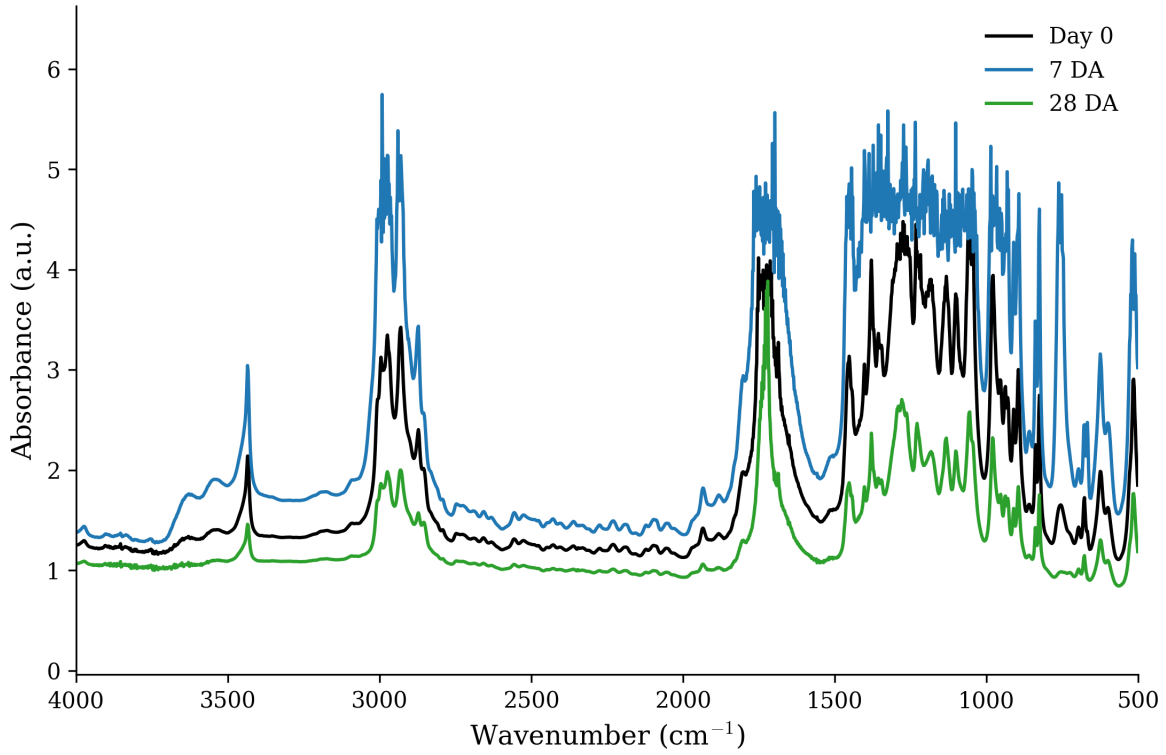


Figure 5.40: FTIR spectra of the locally produced PHB recovered as native film at different aging times.

The absolute absorbance values cannot be compared quantitatively because the heterogeneous films did not have identical thicknesses and optical paths. Several regions, particularly in the 7 DA spectrum, also reached high absorbance and presented substantial noise, reducing the reliability of direct band-height or band-area ratios. Within these limitations, the amorphous-sensitive carbonyl and C-O-C regions did not show a clear and systematic change with aging.

The amorphous-sensitive bands reported in the literature represent the overall response of chemical groups located in disordered molecular environments and do not distinguish MAF from RAF. The DSC analysis of PHAC suggested that aging may involve a redistribution from MAF toward RAF while the total amorphous fraction remains comparatively stable. If a similar redistribution occurred in the native film, the same ester groups would remain within the total amorphous phase but under different mobility constraints. Such a change may affect thermal or mechanical behavior without producing a large variation in the total amorphous FTIR contribution. The absence of

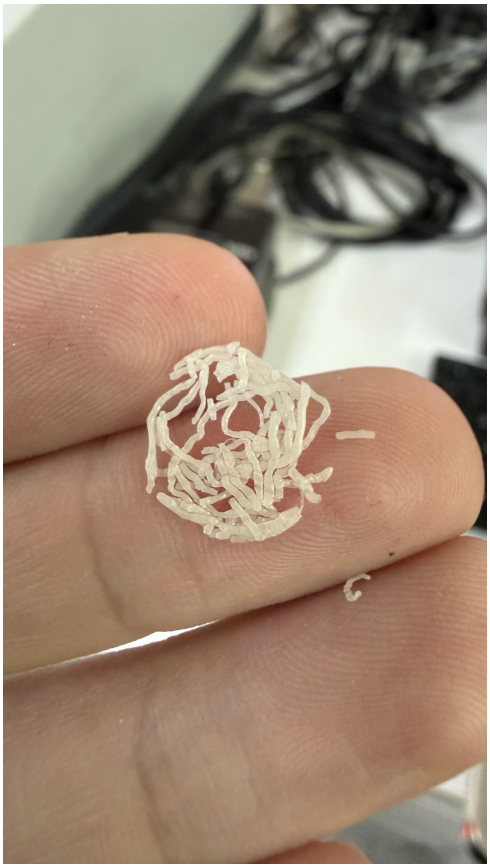
a clear spectral difference cannot be interpreted as evidence that no amorphous-phase rearrangement occurred.

PHB fiber

The initial PHB fiber was intended to be evaluated in transmission mode after compression into a thin sheet. A reference test performed with the commercial pellet produced a continuous translucent sheet, whereas the extruded fiber required a higher compaction force and remained as a discontinuous network after pressing, as shown in Figure 5.41. The Day 0 spectrum obtained from this unsuccessful preparation was not considered directly comparable with the subsequent measurements.



(a) Continuous sheet obtained by pressing the commercial PHB pellet.



(b) Discontinuous material obtained after pressing the PHB fiber.

Figure 5.41: Comparison of the specimens obtained during preparation of PHB materials for transmission FTIR analysis.

For the 7 and 28 DA conditions, the fibers were finely cut and analyzed by diffuse reflectance, as illustrated in Figure 5.42. This approach avoided the need to obtain a continuous transparent sheet and provided the same measurement configuration for both aged conditions.

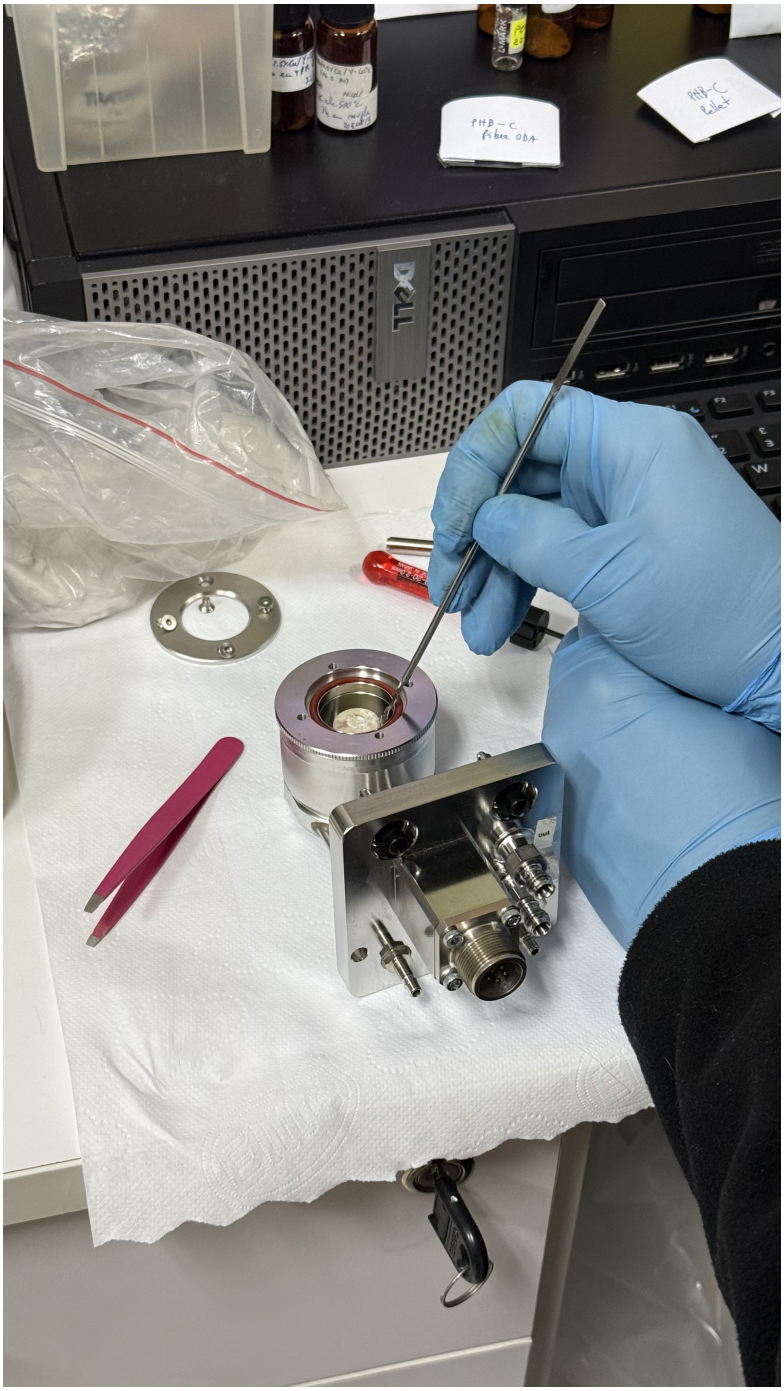


Figure 5.42: Preparation of finely cut PHB fiber for diffuse-reflectance FTIR analysis.

The FTIR spectra obtained for the PHB fiber at the evaluated aging times are shown in Figure 5.43. The spectra presented comparable overall features, and no clear new absorption band was identified with aging. Absolute intensity differences were not interpreted, since the measurements were affected by differences in sample preparation.

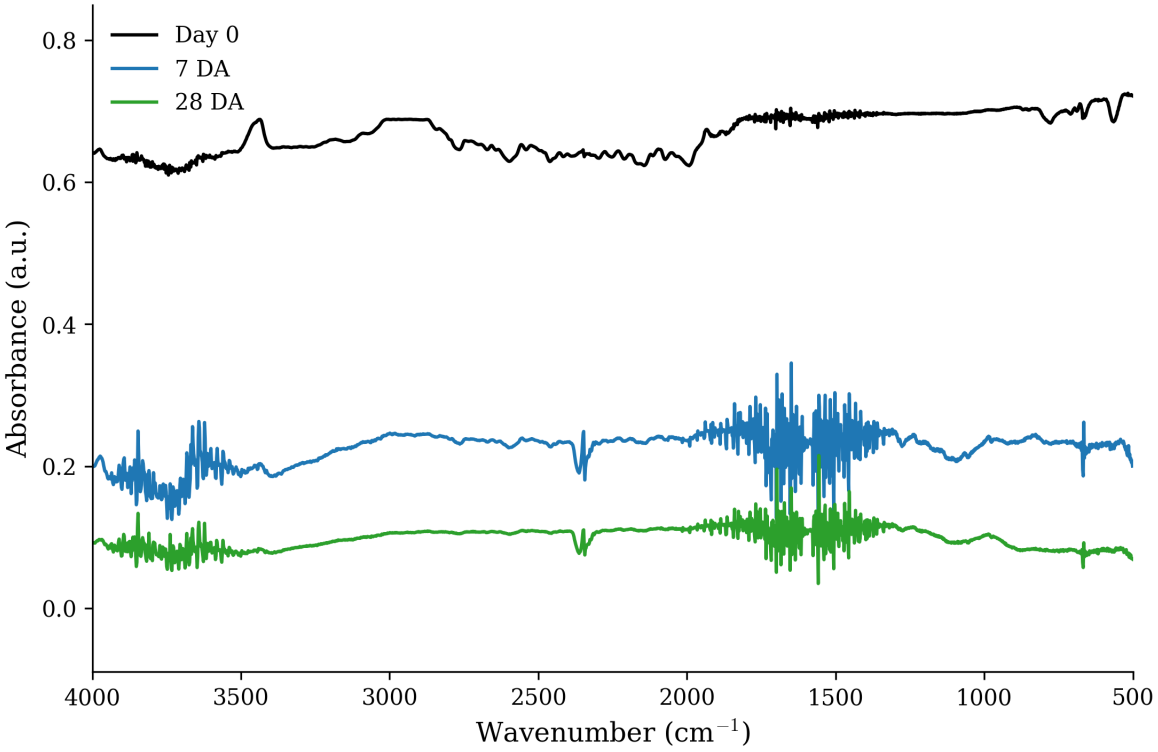


Figure 5.43: FTIR spectra obtained for the PHB fiber at different aging times.

The absence of a reliable Day 0 spectrum acquired by the same method prevents establishing a complete time-dependent FTIR trend for the PHB fiber. In addition, the signal-to-noise ratio of the diffuse-reflectance spectra limits the identification of subtle changes in peak intensity, shape, or position that could result from structural evolution during aging. The spectra therefore allow only a qualitative comparison between 7 and 28 DA, with no major changes in the characteristic absorption bands being clearly distinguishable.

Chapter 6

Discussion and Future Perspectives

6.1 Mechanical feasibility of PHB fibers for cementitious reinforcement

The broader research line addressed in this thesis ultimately seeks to use bacteria-derived fibers, specifically PHB, as alternatives to petroleum-based reinforcement fibers in cementitious composites. Within the scope of the present work, however, the investigation was limited to the stages preceding their incorporation into a cementitious matrix. The production route, processing, physicochemical behavior, mechanical response, aging, and alkaline stability of the fibers were evaluated, but their reinforcing performance within concrete was not tested directly. The results included herein are best interpreted as an assessment of the feasibility of PHB as a precursor for cementitious reinforcement rather than as a demonstration of performance at a composite level .

The mechanical properties of the fibers have been identified as the main limitation in their present, untreated state. The PHAC fiber exhibited tensile strengths between 18 and 25 MPa, whereas the extruded PHB fiber reached mean values between 34 and 42 MPa over the evaluated aging period. These values remain substantially below those reported for established synthetic fibers used in cementitious composites (Lan et al., 2021). The PHB fiber also exhibited a low strain at failure, between 0.7-0.8%,

which is consistent with the relatively brittle response of PHB in an as-processed state without subsequent molecular-orientation treatments. Consequently, neither of the fibers evaluated in this work, under the processing conditions adopted in this thesis, can presently be considered mechanically suitable for replacing conventional reinforcement fibers.

This limitation concerns the fibers produced under the processing conditions adopted in this thesis rather than PHB as a material class. Previous studies have demonstrated that the mechanical response of PHB can be modified substantially through post-processing. Furuhashi et al. (2004) produced highly oriented PHB fibers through cold drawing followed by further drawing and annealing under tension, while Iwata et al. (2004) reported a tensile strength of 1.32 GPa for ultra-high-molecular-weight P(3HB) fibers processed through combined cold- and two-step-drawing procedures. Related PHA systems have also reached high tensile performance. For example, optimized two-step drawing with intermediate annealing increased the tensile strength of P(3HB-co-3HH) fibers to 552 MPa (Kabe et al., 2015). These results demonstrate that the low tensile strength measured in the present work should not be interpreted as an intrinsic upper limit for PHB-based fibers.

The relevance of these values becomes clearer when compared with representative fibers currently used in high-performance cementitious composites. Lan et al. (2021) reported tensile strengths of approximately 530-850 MPa for different PP fibers, approximately 1500-1620 MPa for PVA fibers, and approximately 3000 MPa for high-modulus PE fibers. The 1.32 GPa reported for highly processed P(3HB) lies within the same order of magnitude as some established polymeric reinforcement fibers, although it does not reach the performance of high-modulus PE. Such comparisons should not be interpreted as defining a universal minimum tensile strength for cementitious reinforcement. The required fiber properties depend on the intended composite response and on the combined effects of fiber strength, elastic modulus, deformation capacity, geometry, and fiber-matrix interaction (Li et al., 2002; Lan et al., 2021). Nevertheless, the literature demonstrates that PHB possesses a mechanical design space considerably broader than that represented by the as-extruded fibers obtained in this thesis.

The improvement of the mechanical performance is not exclusively associated to a drawing process of the fibers. The high-strength fibers reported in the literature were obtained from specific polymer grades and carefully controlled processing histories. In particular, the 1.32 GPa fiber reported by Iwata et al. (2004) was produced from ultra-high-molecular-weight P(3HB), whereas the PHB fiber obtained in the present work showed an apparent M_w of approximately 236.5 kDa after extrusion. In addition, the tensile tests conducted here revealed fractures preferentially occurring at locally reduced fiber diameters, showing that geometrical non-uniformity also introduced stress concentrations. Future mechanical improvement should consider polymer molecular weight, extrusion stability, fiber-diameter uniformity, and post-extrusion treatment as interconnected variables rather than assuming that a single additional drawing step would reproduce the mechanical properties reported elsewhere.

The effectiveness of drawing arises from the structural reorganization generated when the polymer is extended. As-spun polymer fibers generally contain a comparatively low degree of molecular orientation, whereas drawing progressively aligns polymer chains and higher-order structures along the fiber axis. In PHB, drawing has been associated with the development of highly-oriented structures containing the conventional helical α-form together with extended planar-zigzag chains commonly associated with the β-form (Yamane et al., 2001; Furuhashi et al., 2004; Iwata et al., 2004). Increasing axial organization improves the ability of the fiber to transfer tensile load through the oriented polymer structure and can consequently produce large increases in tensile strength and stiffness. The final response nevertheless depends on drawing ratio, temperature, molecular weight, crystallization history, and the subsequent thermal treatment, which also control the remaining deformation capacity.

The practical implementation of such treatments represents a clear next step for this research line. Although the PHB literature establishes drawing ratios, temperatures, and thermal treatments capable of generating highly oriented fibers, detailed descriptions of scalable mechanical systems for continuously imposing these histories are less commonly provided. Multi-stage drawing systems used for other thermoplastic polymers may provide useful engineering references. For example, the two-stage process proposed by Liu et al. (2015) applies sequential cold and hot drawing to UHMWPE

fibers. This study does not constitute evidence of PHB mechanical performance, since the polymer and structural mechanisms are different, but its process architecture illustrates how independently controlled drawing stages could be implemented through sequential rollers and temperature-controlled regions. A comparable apparatus adapted specifically to the thermal and crystallization behavior of PHB could provide a practical starting point for future process development.

6.2 Aging and stabilization of the mechanical response

A second requirement for a potential reinforcement fiber is the preservation of its properties after processing and during storage. This aspect is particularly relevant for PHB because its mechanical response can evolve substantially through physical aging and continued structural organization. The two fibers evaluated in this thesis exhibited markedly different behaviors. PHAC progressively lost deformation capacity, with mean strain at failure decreasing from 1.79% at Day 0 to 0.82% after 100 days, together with a pronounced increase in the apparent modulus of elasticity. The PHB fiber, in contrast, showed no loss of deformation capacity between days 0 and 28. The mean strain at failure remained close to 0.7-0.8%, while the apparent modulus of elasticity increased and the mean tensile strength reached a higher value after 28 days, although the experimental variability prevented a statistically clear strengthening trend from being established.

Post-processing provides a possible route for deliberately stabilizing an oriented fiber structure rather than allowing its morphology to evolve uncontrolled during storage. Annealing provides molecular mobility for structural reorganization after drawing and can modify crystallinity, chain orientation, and the relative contribution of the different ordered structures. In PHB fibers, Furuhashi et al. (2004) showed that annealing conditions and applied tension strongly influence the resulting higher-order structure. Annealing under tension can restrict macroscopic relaxation of a previously drawn fiber while allowing further structural rearrangement, whereas unconstrained thermal treatment may permit part of the imposed orientation to relax. Annealing should con-

sequently be understood as a processing variable whose temperature, duration, and mechanical constraint must be optimized together with the preceding drawing history rather than as a universal treatment that automatically prevents embrittlement.

The comparatively stable strain at failure observed for the PHB fiber in this thesis may indicate that its structure was already relatively stabilized shortly after extrusion. As discussed in Chapter 5, extrusion was performed at 185 °C, below the tremoval erasure of the previous crystalline order in PHB (Di Lorenzo & Androsch, 2019). Residual self-nuclei, together with the nucleating agent reported in the commercial formulation, may therefore have accelerated organization after extrusion and reduced the magnitude of subsequent structural evolution (Puente et al., 2013; Xu et al., 2021). This interpretation remains hypothetical and should not be confused with an annealing effect, since no deliberate annealing treatment was applied to these fibers. Rather, the present results suggest that processing history can substantially condition subsequent aging and provide a basis for testing whether controlled drawing and annealing could produce a stronger and intentionally stabilized morphology.

A future study on fiber processing should evaluate drawing and annealing simultaneously with aging, rather than measuring only the immediate tensile improvement after treatment. Fibers produced at different drawing ratios and annealing conditions could be characterized immediately after processing and after controlled storage periods using single-fiber tensile testing, the revised DSC protocol developed in this thesis, and XRD. This approach would determine whether the mechanical gains produced by molecular orientation remain stable with time, and would allow to quantify the evolution of the α and β structures and their influence on tensile strength, stiffness, and deformation capacity.

6.3 Alkaline stability and implications for cementitious use

The results of alkaline-degradation provide a more favorable outcome than the mechanical characterization. At 20 °C, the PHB fiber showed mass variations close to

zero throughout the complete 168 h exposure period for all evaluated aging conditions. Under the accelerated exposure at 70 °C, measurable degradation appeared after longer exposure times, but the maximum mean mass loss after 168 h was approximately 10%. The PHB fiber exhibited substantially greater resistance to alkaline degradation than PHAC and the locally produced native film under the accelerated condition, while remaining essentially stable under the ambient-temperature condition evaluated in this work.

These results support continued investigation of PHB fibers for cementitious environments. The alkaline-degradation behavior observed in this work was promising under the evaluated conditions, particularly at 20 °C. However, their long-term durability within concrete remains to be established through direct evaluation in cementitious matrices.

The alkaline-degradation results also provide useful indications for future fiber development. Tapadiya & Vasanthan (2017) showed that increasing PHB crystallinity reduced the extent of alkaline hydrolysis, with degradation occurring preferentially in the amorphous regions. This finding suggests that modifications capable of increasing or stabilizing crystalline organization could potentially improve the alkaline resistance of PHB fibers. However, such modifications should not be considered independently from their mechanical effects, since changes in crystallinity may also influence the deformation capacity.

Other strategies could also be explored. Surface coatings may provide an additional barrier against alkaline attack, although their influence on fiber–matrix adhesion would need to be evaluated. Drawing and annealing could also modify alkaline stability through the structural changes induced in the fiber; however, this effect was not evaluated in the present work and should be treated as a hypothesis for future investigation.

6.4 Environmental implications of PHB production

The environmental motivation for replacing petroleum-derived reinforcement fibers also requires careful interpretation. A biologically produced and biodegradable polymer is

not intrinsically associated with a low production footprint. As discussed in Chapter 2, published life-cycle assessments of PHB show considerable variability because the results depend on carbon source, energy supply, fermentation performance, downstream recovery, system boundaries, and methodological assumptions (Kookos et al., 2019). The environmental potential of PHB should be evaluated in relation to the complete production route rather than inferred only from its biological origin.

A complementary investigation conducted within the same research project evaluated the environmental performance of PHB production at industrial scale. Although the modeled production route resulted in a relatively high carbon footprint, the analysis showed that its two largest contributors were the glucose used as carbon substrate and the electricity required by the process, which accounted for approximately 37.0% and 34.9% of the calculated climate-change impact, respectively. Together, these two inputs represented approximately 71.9% of the modeled carbon footprint. This result is particularly relevant because neither contribution is intrinsic to PHB itself, but depends strongly on engineering decisions about the processing of the polymer.

The electricity-related contribution can potentially be reduced through the use of lower-carbon energy sources. This possibility becomes increasingly relevant as renewable electricity continues to expand within electricity systems worldwide. Similarly, glucose is not the only possible carbon source for PHB production. Numerous studies have investigated the use of alternative substrates, including agro-industrial residues, glycerol, waste oils, wastewater-derived organic streams, and gaseous carbon sources (Marangoni et al., 2001; Wang et al., 2021; Fu et al., 2023; Patel et al., 2024). Consequently, reducing the environmental burden associated with the carbon substrate may be approached not only by improving process efficiency, but also by replacing refined feedstocks with lower-impact or residual carbon streams.

Several industrial initiatives are exploring measures to improve the environmental impact beyond laboratory scale. Mango Materials has developed a PHA production route based on waste methane, including methane originating from wastewater-treatment systems (Mango Materials, 2025). Paques Biomaterials has explored the production of PHA from different organic residual streams, including sewage sludge and agro-food side

streams (Paques Biomaterials, 2024; Paques Biomaterials, 2023). RWDC Industries provides another example through the use of plant-based oils, including post-consumer and waste cooking oils, as feedstocks for PHA production (RWDC Industries, 2023). These examples concern different members of the PHA family and different production technologies and cannot be transferred directly to the PHB process evaluated in this work. Nevertheless, they demonstrate that PHA production is not restricted to refined glucose or fructose as carbon substrates and may be integrated with the valorization of residual streams from other industries.

The environmental performance of future PHB production routes should be evaluated for each specific feedstock and process configuration rather than inferred solely from the renewable or residual origin of the carbon source.

6.5 Research outlook

Taken together, the results define a sequence of research questions rather than a completed route to cementitious reinforcement. The first priority is to improve the fiber itself through better control of molecular weight, extrusion uniformity, drawing, and annealing, while verifying that the resulting mechanical properties remain stable during aging. The second is to determine whether the favorable alkaline mass stability observed here is accompanied by retention of tensile properties after exposure. Once these two requirements are satisfied, the fiber-matrix interface becomes central. Surface chemistry, bond strength, pull-out behavior, fiber geometry, and dispersion must then be evaluated before the reinforcing effect can be assessed at mortar or concrete scale. In parallel, process simulation and life-cycle assessment should be updated as the production route changes so that improvements in mechanical performance are not obtained at the expense of an increased environmental burden.

This thesis does not establish that PHB fibers can already replace conventional petroleum-derived reinforcement fibers, but establishes something more specific and useful for the continuation of the research line. The study developed a complete experimental route for producing, recovering, processing, and characterizing PHB-based materials. The mechanical limitation of the fibers in their present state was identified;

their comparatively favorable stability under ambient-temperature alkaline exposure was demonstrated within the conditions tested; and processing, structural, and production variables capable of addressing the remaining limitations were identified. Together with the parallel development of industrial process and life-cycle models, these results provide a foundation from which the mechanical, durability, interfacial, and environmental requirements of a future PHB-based cementitious reinforcement can be investigated systematically.

Chapter 7

Conclusions

The hypothesis addressed in this thesis proposes bacterial PHB-based fibers as a potential alternative to petroleum-derived fibers for reinforcement in cementitious composites, provided that certain technical aspects are improved. The fibers obtained in their current state do not yet satisfy all the requirements expected for cementitious reinforcement, particularly in terms of mechanical performance. However, no limitation identified throughout this research provides sufficient grounds to discard PHB as a viable precursor for this application.

The observed alkaline stability was favorable under the conditions evaluated, while the mechanical limitation could be overcome through the techniques discussed in the preceding chapter. The hypothesis can be considered supported at the material-feasibility level established in this thesis, while its ultimate validation as a functional reinforcement will require the subsequent evaluation of treated fibers within cementitious composites.

Conclusion 1: PHB Production and Recovery

A reliable and repeatable laboratory route for PHB production through *Cupriavidus necator* fermentation was successfully established. The progressive development of the fermentation process resulted in a protocol capable of consistently producing PHB under the operating conditions adopted in this work.

The recovery of PHB from the produced biomass was also successfully consolidated. The developed extraction and purification methodology combines high polymer recovery with a final material of high purity, comparable to the commercial PHB used as reference throughout this work. Together, the fermentation and extraction stages establish a reliable route for obtaining locally-produced high-purity PHB from bacteria.

Conclusion 2: Fiber Processing

Fiber processing remains one of the main unresolved steps for the completion of the fully local production route. Continuous PHB fibers were successfully produced from commercial thermoplastic-grade pellets, demonstrating that the extrusion setup and processing strategy developed in this work are suitable for PHB fiber fabrication. However, stable fiber production from the locally produced PHB could not be achieved under the evaluated conditions.

Conclusion 3: Material Characterization and Alkaline Stability

The extensive characterization performed throughout this research established a detailed understanding of the thermal, physicochemical, degradation, and aging behavior of the different PHB-based materials. Comparative characterization also provided a basis for assessing the consistency between the laboratory-produced PHB and the commercial material used.

The alkaline-degradation results support continued investigation of PHB fibers for cementitious environments. The behavior observed under the evaluated conditions was promising, particularly at 20 °C, while the accelerated tests provided additional information regarding their susceptibility to alkaline attack. Their long-term durability within concrete remains subject to direct evaluation in cementitious matrices, but the results obtained in this work provide a favorable basis for continuing this line of investigation.

Conclusion 4: Mechanical Performance

Mechanical characterization established a clear reference point for future fiber devel-

opment. The fibers obtained under the processing conditions adopted in this thesis do not yet provide the mechanical performance required for their intended reinforcing function. This limitation corresponds to the present untreated state of the fibers and should not be interpreted as an intrinsic mechanical limit of PHB.

The present thesis does not establish that PHB fibers can already replace conventional synthetic reinforcement fibers. Instead, it establishes a reliable experimental foundation from which that possibility can now be pursued through a clearly defined sequence of material, processing, durability, and composite-level developments.

Recommendations

Further development of the local production route should address both polymer availability and its subsequent conversion into continuous fibers. Within the current experimental setup, the amount of PHB obtained per batch is constrained by the working capacity and $k_L a$ of the available bioreactor. The fermentation protocol established in this thesis provides a basis for increasing production capacity, although scale-up should preserve the relevant process conditions and verify that reproducibility and polymer quality are maintained.

For the recovered polymer, priority should be given to achieving stable extrusion. The comparatively high apparent molecular weight measured for the purified PHB, may be advantageous for future fiber performance, provided that adequate processability can be achieved. Formulation and processing strategies should therefore be evaluated to improve thermal and rheological stability during extrusion while limiting damage to the polymer chains. The characterization methods established in this work should guide these adjustments and allow their effects on the resulting material to be assessed.

Once continuous fibers can be produced reliably, drawing and annealing should be investigated as routes to improve their mechanical performance, following the strategies discussed in the preceding chapter. The mechanical and aging results obtained in this thesis provide a baseline for evaluating these treatments. Their effectiveness should be assessed not only through the initial improvement in fiber properties, but also through the preservation of those properties during storage and alkaline exposure.

Future Research

Following the development of fibers with suitable mechanical properties and stability, research should proceed to their incorporation into cementitious matrices. This stage should evaluate fiber-matrix interaction through bond and pull-out tests, together with the effects of fiber geometry, content, and dispersion on the mechanical response of the composite. Long-term exposure studies should also determine whether the alkaline resistance observed in isolated fibers is maintained within the cementitious environment. These evaluations will be necessary to establish whether the developed PHB fibers can fulfill the reinforcing role proposed in the original hypothesis.

Bibliography

Acevedo, F., Villegas, P., Urtuvia, V., Hermosilla, J., Navia, R., & Seeger, M. (2018). Bacterial polyhydroxybutyrate for electrospun fiber production. *International Journal of Biological Macromolecules*, *106*, 692–697.

Alata, H., Aoyama, T., & Inoue, Y. (2007). Effect of Aging on the Mechanical Properties of Poly(3-hydroxybutyrate-co-3-hydroxyhexanoate). *Macromolecules*, *40*(13), 4546–4551.

Almutairi, A. L., Tayeh, B. A., Adesina, A., Isleem, H. F., & Zeyad, A. M. (2021). Potential applications of geopolymer concrete in construction: A review. *Case Studies in Construction Materials*, *15*, e00733.

Andreas Hettich GmbH & Co. KG (2026). Rotofix 32 a. Available at: `https://www.hettweb.com/products/rotofix32a/` (accessed April 22, 2026).

Anton Paar (2026). Bet surface area analyzer: Nova. Available at: `https://www.anton-paar.com/es-es/productos/detalles/nova/` (accessed June 2, 2026).

ASTM International (2026a). Standard test methods for density and specific gravity (relative density) of plastics by displacement. ASTM D792-20. Available at: `https://store.astm.org/d0792-20.html` (accessed April 22, 2026).

ASTM International (2026b). Standard test methods for specific gravity of soil solids by the water displacement method. ASTM D854-23. Available at: `https://store.astm.org/d0854-23.html` (accessed April 22, 2026).

Bajaber, M. A. & Hakeem, I. Y. (2021). UHPC evolution, development, and utilization in construction: a review. *Journal of Materials Research and Technology*, *10*, 1058–1074.

Barham, P. J., Keller, A., Otun, E. L., & Holmes, P. A. (1984). Crystallization and morphology of a bacterial thermoplastic: poly-3-hydroxybutyrate. *Journal of Materials Science*, *19*(9), 2781–2794.

Boesel, L. F., Meur, S. L., Thöny-Meyer, L., & Ren, Q. (2014). The effect of molecular weight on the material properties of biosynthesized poly(4-hydroxybutyrate). *International Journal of Biological Macromolecules*, *71*, 124–130.

Boy, C., Lesage, J., Alfenore, S., Guillouet, S. E., & Gorret, N. (2021). Investigation of the robustness of Cupriavidus necator engineered strains during fed-batch cultures. *AMB Express*, *11*(1), 151.

Brandt, A. M. (2008). Fibre reinforced cement-based (FRC) composites after over 40 years of development in building and civil engineering. *Composite Structures*, *86*(1), 3–9.

Bucci, D., lorena, Tavares, L., & Sell, I. (2005). PHB packaging for the storage of food products. *Polymer Testing*, *24*, 564–571.

Budde, C. F., Riedel, S. L., Hübner, F., Risch, S., Popović, M. K., Rha, C., & Sinskey, A. J. (2011). Growth and polyhydroxybutyrate production by Ralstonia eutropha in emulsified plant oil medium. *Applied Microbiology and Biotechnology*, *89*(5), 1611–1619.

Cappuccino, J. G. & Welsh, C. (2019). *Microbiology: A Laboratory Manual* (12 ed.). New York: Pearson.

Center for Optical and Laser Materials Research (2026). Ftir spectrometer irprestige-21. Available at: `https://laser.spbu.ru/en/equipment-eng/irprestige-eng.html` (accessed April 23, 2026).

Chellapandian, M., Arunachelam, N., Maheswaran, J., & Kumar, N. P. (2024). Shear behavior of low-cost and sustainable bio-fiber based engineered cementitious composite beams –experimental and theoretical studies. *Journal of Building Engineering*, *84*, 108497.

Chen, H., Geng, J., Zhang, Z., Jiang, R., Zhai, J., & Zhang, J. (2021). The Structure and Properties of Sepiolite with Partial Lattice Ions Substituted by Aluminum Ions. *Frontiers in Chemistry*, *9*.

colorFabb (2023). allpha datasheet. Available at: https://downloads.colorfabb.com/index.php/s/rtfDDRCa723Xdor (accessed April 23, 2026).

colorFabb (2024). allpha natural. Available at: https://colorfabb.com/es/allpha-natural (accessed April 23, 2026).

Cromtek (2026). Shimadzu prominence hplc modular system. Available at: https://www.cromtek.cl/producto/hplc-modular-de-alto-desempeno-shimadzu-prominence/ (accessed April 22, 2026).

Curosu, I., Liebscher, M., Mechtcherine, V., Bellmann, C., & Michel, S. (2017). Tensile behavior of high-strength strain-hardening cement-based composites (HS-SHCC) made with high-performance polyethylene, aramid and PBO fibers. *Cement and Concrete Research*, *98*, 71–81.

Czerniecka-Kubicka, A., Fracz, W., Jasiorski, M., Błażejewski, W., Pilch-Pitera, B., Pyda, M., & Zarzyka, I. (2017). Thermal properties of poly(3-hydroxybutyrate) modified by nanoclay. *Journal of Thermal Analysis and Calorimetry*, *128*(3), 1513–1526.

Dalton, B., Bhagabati, P., De Micco, J., Padamati, R. B., & O'Connor, K. (2022). A Review on Biological Synthesis of the Biodegradable Polymers Polyhydroxyalkanoates and the Development of Multiple Applications. *Catalysts*, *12*(3), 319.

Di Lorenzo, M. L. & Androsch, R. (2019). Crystallization of Poly[(R)-3-hydroxybutyrate]. In M. L. Di Lorenzo & R. Androsch (Eds.), *Thermal Properties of Bio-based Polymers* (pp. 119–142). Cham: Springer International Publishing.

Di Lorenzo, M. L. & Righetti, M. C. (2013). Effect of thermal history on the evolution of crystal and amorphous fractions of poly[(R)-3-hydroxybutyrate] upon storage at ambient temperature. *European Polymer Journal*, *49*(2), 510–517.

Dills, W. (1993). Protein fructosylation: fructose and the Maillard reaction. *The American Journal of Clinical Nutrition*, *58*(5), 779S–787S.

Doi, Y., Kitamura, S., & Abe, H. (1995). Microbial Synthesis and Characterization of

Poly(3-hydroxybutyrate-co-3-hydroxyhexanoate). *Macromolecules*, *28*(14), 4822–4828.

Du, J., Meng, W., Khayat, K. H., Bao, Y., Guo, P., Lyu, Z., Abu-obeidah, A., Nassif, H., & Wang, H. (2021). New development of ultra-high-performance concrete (UHPC). *Composites Part B: Engineering*, *224*, 109220.

Duvigneau, S., Kettner, A., Carius, L., Griehl, C., Findeisen, R., & Kienle, A. (2021). Fast, inexpensive, and reliable HPLC method to determine monomer fractions in poly(3-hydroxybutyrate-co-3-hydroxyvalerate). *Applied Microbiology and Biotechnology*, *105*(11), 4743–4749.

Fillamentum (2026). Nonoilen® filament. Accessed: 2026-07-23.

Fu, X., Xu, H., Zhang, Q., Xi, J., Zhang, H., Zheng, M., Xi, B., & Hou, L. (2023). A review on polyhydroxyalkanoates production from various organic waste streams: Feedstocks, strains, and production strategy. *Resources, Conservation and Recycling*, *198*, 107166.

Furuhashi, Y., Imamura, Y., Jikihara, Y., & Yamane, H. (2004). Higher order structures and mechanical properties of bacterial homo poly(3-hydroxybutyrate) fibers prepared by cold-drawing and annealing processes. *Polymer*, *45*(16), 5703–5712.

Ghali, A. E. A., El Ezz, N. E., Hamad, B., Assaad, J., & Yehya, A. (2023). Comparative study on shear strength and life cycle assessment of reinforced concrete beams containing different types of fibers. *Case Studies in Construction Materials*, *19*, e02497.

Grunwald, S., Mottet, A., Grousseau, E., Plassmeier, J. K., Popović, M. K., Uribelarrea, J., Gorret, N., Guillouet, S. E., & Sinskey, A. (2015). Kinetic and stoichiometric characterization of organoautotrophic growth of *R* *alstonia eutropha* on formic acid in fed-batch and continuous cultures. *Microbial Biotechnology*, *8*(1), 155–163.

Gunaratne, L. M. W. K., Shanks, R. A., & Amarasinghe, G. (2004). Thermal history

effects on crystallisation and melting of poly(3-hydroxybutyrate). *Thermochimica Acta*, *423*(1), 127–135.

Gökaltun, A., Kang, Y. B. A., Yarmush, M. L., Usta, O. B., & Asatekin, A. (2019). Simple Surface Modification of Poly(dimethylsiloxane) via Surface Segregating Smart Polymers for Biomicrofluidics. *Scientific Reports*, *9*(1), 7377.

Hodge, J. E. (1953). Dehydrated Foods, Chemistry of Browning Reactions in Model Systems. *Journal of Agricultural and Food Chemistry*, *1*(15), 928–943.

Hu, W., Zhang, D., Ftwi, E., Ellis, B. R., & Li, V. C. (2023). Development of sustainable low carbon Engineered Cementitious Composites with waste polyethylene fiber, sisal fiber and carbonation curing. *Resources, Conservation and Recycling*, *197*, 107096.

Hufenus, R., Yan, Y., Dauner, M., & Kikutani, T. (2020). Melt-Spun Fibers for Textile Applications. *Materials*, *13*(19), 4298.

Höhnemann, T. & Windschiegl, I. (2023). Influence of Rheological and Morphological Characteristics of Polyhydroxybutyrate on Its Meltblown Process Behavior. *Materials*, *16*(19), 6525.

INFORS HT (2026). Minifors 2 bench-top bioreactor. Available at: `https://infors-ht.com/en/products/bioreactors/bench-top-bioreactors/minifors` (accessed April 22, 2026).

Iwata, T., Aoyagi, Y., Fujita, M., Yamane, H., Doi, Y., Suzuki, Y., Takeuchi, A., & Uesugi, K. (2004). Processing of a Strong Biodegradable Poly[(*R*)-3-hydroxybutyrate] Fiber and a New Fiber Structure Revealed by Micro-Beam X-Ray Diffraction with Synchrotron Radiation. *Macromolecular Rapid Communications*, *25*(11), 1100–1104.

Jenway (2026). 6320d visible spectrophotometer. Available at: `https://www.tequipment.net/Jenway/632521/Spectrophotometer/` (accessed April 22, 2026).

Juenger, M., Winnefeld, F., Provis, J., & Ideker, J. (2011). Advances in alternative cementitious binders. *Cement and Concrete Research*, *41*(12), 1232–1243.

Kabe, T., Hongo, C., Tanaka, T., Hikima, T., Takata, M., & Iwata, T. (2015). High tensile strength fiber of poly[(R)-3-hydroxybutyrate-co-(R)-3-hydroxyhexanoate] processed by two-step drawing with intermediate annealing. *Journal of Applied Polymer Science*, *132*(2).

Kabe, T., Tsuge, T., Kasuya, K.-i., Takemura, A., Hikima, T., Takata, M., & Iwata, T. (2012). Physical and Structural Effects of Adding Ultrahigh-Molecular-Weight Poly[(R)-3-hydroxybutyrate] to Wild-Type Poly[(R)-3-hydroxybutyrate]. *Macromolecules*, *45*(4), 1858–1865.

Kamnev, A. A., Tugarova, A. V., Dyatlova, Y. A., Tarantilis, P. A., Grigoryeva, O. P., Fainleib, A. M., & De Luca, S. (2018). Methodological effects in Fourier transform infrared (FTIR) spectroscopy: Implications for structural analyses of biomacromolecular samples. *Spectrochimica Acta Part A: Molecular and Biomolecular Spectroscopy*, *193*, 558–564.

Karr, D. B., Waters, J. K., & Emerich, D. W. (1983). Analysis of Poly--Hydroxybutyrate in *Rhizobium japonicum* Bacteroids by Ion-Exclusion High-Pressure Liquid Chromatography and UV Detection. *Applied and Environmental Microbiology*, *46*(6), 1339–1344.

Kerr, B. J., Kellner, T. A., & Shurson, G. C. (2015). Characteristics of lipids and their feeding value in swine diets. *Journal of Animal Science and Biotechnology*, *6*(1), 30.

Kim, B. S., Lee, S. C., Lee, S. Y., Chang, H. N., Chang, Y. K., & Woo, S. I. (1994). Production of poly(3-hydroxybutyric acid) by fed-batch culture of *Alcaligenes eutrophus* with glucose concentration control. *Biotechnology and Bioengineering*, *43*(9), 892–898.

Kookos, I. K., Koutinas, A., & Vlysidis, A. (2019). Life cycle assessment of bioprocessing

schemes for poly(3-hydroxybutyrate) production using soybean oil and sucrose as carbon sources. *Resources, Conservation and Recycling*, *141*, 317–328.

Kumar Singh, A., Kumar, V. R. P., Dehdasht, G., Mohandes, S. R., Manu, P., & Pour Rahimian, F. (2023). Investigating the barriers to the adoption of blockchain technology in sustainable construction projects. *Journal of Cleaner Production*, *403*, 136840.

Kundrat, V., Matouskova, P., & Marova, I. (2019). Facile Preparation of Porous Microfiber from Poly-3-(R)-Hydroxybutyrate and Its Application. *Materials*, *13*(1), 86.

Lan, M., Zhou, J., & Xu, M. (2021). Effect of Fibre Types on the Tensile Behaviour of Engineered Cementitious Composites. *Frontiers in Materials*, *8*.

Lenz, R. W. & Marchessault, R. H. (2005). Bacterial Polyesters: Biosynthesis, Biodegradable Plastics and Biotechnology. *Biomacromolecules*, *6*(1), 1–8.

Leon-Miquel, M., Silva-Retamal, J., Aparicio, D., Rangelov, M., Jin, Q., & Paul, A. (2023). Novel application of Chilean natural pozzolan for sustainable strain-hardening cementitious composite. *Resources, Conservation and Recycling*, *197*, 107098.

Li, J., Wang, Y., Wang, Z., Wang, J., & Wu, D. (2021). Surface chain engineering of chitin nanocrystals towards tailoring the nucleating capacities for poly(-hydroxybutyrate). *International Journal of Biological Macromolecules*, *166*, 967–976.

Li, S.-D., Yu, P. H., & Cheung, M. K. (2001). Thermogravimetric analysis of poly(3-hydroxybutyrate) and poly(3-hydroxybutyrate-co-3-hydroxyvalerate). *Journal of Applied Polymer Science*, *80*(12), 2237–2244. _eprint: https://onlinelibrary.wiley.com/doi/pdf/10.1002/app.1327.

Li, V. (2011). Advances in ECC research. *ACI Special Publication on Concrete: Material Science to Applications*.

Li, V., Wu, C., Wang, S., Ogawa, A., & Saito, T. (2002). Interface tailoring for strain-hardening polyvinyl alcohol-engineered cementitious composite (PVA-ECC). *ACI Materials Journal*, *99*, 463–472.

Li, V. C. (1993). From micromechanics to structural engineering the design of cementitious composites for civil engineering applications. *Doboku Gakkai Ronbunshu*, *1993*(471), 1–12.

Li, V. C. (2003). On Engineered Cementitious Composites (ECC). *Journal of Advanced Concrete Technology*, *1*(3), 215–230.

Liu, H., Lv, F., Li, J., Cao, T., Wan, C., Zhang, W., Li, L., Zheng, G., & Shen, C. (2015). Two-stage drawing process to prepare high-strength and porous ultrahigh-molecular-weight polyethylene fibers: Cold drawing and hot drawing. *Journal of Applied Polymer Science*, *132*(47). _eprint: https://onlinelibrary.wiley.com/doi/pdf/10.1002/app.42823.

Lu, J., Tappel, R. C., & Nomura, C. T. (2009). Mini-Review: Biosynthesis of Poly(hydroxyalkanoates). *Polymer Reviews*, *49*(3), 226–248. _eprint: https://doi.org/10.1080/15583720903048243.

Mango Materials (2025). Mango materials turns methane into biodegradable plastic. Available at: `https://www.mangomaterials.com/news-press/mango-materials-turns-methane-into-biodegradable-plastic/` (accessed August 15, 2026).

Manutsyan, T., Blbulyan, S., Vassilian, A., Semashko, T., Kirakosyan, G., Gabrielyan, L., Trchounian, K., & Poladyan, A. (2024). Gold nanoparticles activate hydrogenase synthesis and improve heterotrophic growth of *Ralstonia eutropha* H16. *FEMS Microbiology Letters*, *371*, fnad138.

Marangoni, C., Furigo Jr., A., & Aragão, G. M. F. (2001). The influence of substrate source on the growth of Ralstonia eutropha, aiming at the production of polyhydroxyalkanoate. *Brazilian Journal of Chemical Engineering*, *18*, 175–180.

Maschke, R., Stalder, M., Eibl, D., Mächler, D., Straumann, M., & Neutsch, L. (2019).

Biological and process-engineering characterization of the minifors 2 laboratory bioreactor. Application Note Minifors 2 Bioreactor for Microorganisms, Zurich University of Applied Sciences, Institute of Chemistry and Biotechnology, Wädenswil, Switzerland. In collaboration with Infors HT.

McAdam, B., Brennan Fournet, M., McDonald, P., & Mojicevic, M. (2020). Production of Polyhydroxybutyrate (PHB) and Factors Impacting Its Chemical and Mechanical Characteristics. *Polymers*, *12*(12), 2908.

Medeiros, E. S., Glenn, G. M., Klamczynski, A. P., Orts, W. J., & Mattoso, L. H. C. (2009). Solution blow spinning: A new method to produce micro- and nanofibers from polymer solutions. *Journal of Applied Polymer Science*, *113*(4), 2322–2330. _eprint: https://onlinelibrary.wiley.com/doi/pdf/10.1002/app.30275.

Meneses, L., Esmail, A., Matos, M., Sevrin, C., Grandfils, C., Barreiros, S., Reis, M. A. M., Freitas, F., & Paiva, A. (2022). Subcritical Water as a Pre-Treatment of Mixed Microbial Biomass for the Extraction of Polyhydroxyalkanoates. *Bioengineering*, *9*(7), 302.

Mettler Toledo (2026). Dsc 1 differential scanning calorimeter. Available at: `https://www.labwrench.com/documents/view/2721/mettler-toledo-dsc-1-differential-scanning-calorimeter-brochure` (accessed April 22, 2026).

Mongili, B., Abdel Azim, A., Fraterrigo Garofalo, S., Batuecas, E., Re, A., Bocchini, S., & Fino, D. (2021). Novel insights in dimethyl carbonate-based extraction of polyhydroxybutyrate (phb). *Biotechnology for biofuels*, *14*(1), 13.

Monteiro, P. J. M., Miller, S. A., & Horvath, A. (2017). Towards sustainable concrete. *Nature Materials*, *16*(7), 698–699.

Morey-Yagi, S. R., Kato, S., Yamaguchi, A., Takemura, A., Kuroishikawa, Y., Terada, K., Morishita, H., & Numata, K. (2026). Acetone-based lysis of marine purple photosynthetic bacterium, *Rhodovulum sulfidophilum,* for efficient biomass utilization. *Bioresource Technology*, *443*, 133846.

Mukhopadhyay, S. & Khatana, S. (2015). A review on the use of fibers in reinforced cementitious concrete. *Journal of Industrial Textiles*, *45*(2), 239–264.

Müller, H. S., Breiner, R., Moffatt, J. S., & Haist, M. (2014). Design and Properties of Sustainable Concrete. *Procedia Engineering*, *95*, 290–304.

Naeimirad, M., Krins, B., & Gruter, G.-J. M. (2023). A Review on Melt-Spun Biodegradable Fibers. *Sustainability*, *15*(19), 14474.

Okutan, M., Boran, F., Ergün, A., Kanca, Y., Özkahraman, B., & Deligöz, H. Hydrophobic surface modification and characterization of melamine foam. *Turkish Journal of Chemistry*, *47*(3), 591–604.

Ozturk, O. & Ozyurt, N. (2022). Sustainability and cost-effectiveness of steel and polypropylene fiber reinforced concrete pavement mixtures. *Journal of Cleaner Production*, *363*, 132582.

Palmeiro-Sánchez, T., O'Flaherty, V., & Lens, P. N. (2022). Polyhydroxyalkanoate bio-production and its rise as biomaterial of the future. *Journal of Biotechnology*, *348*, 10–25.

Paques Biomaterials (2023). Paques biomaterials and looop partner in producing PHA from agri-food side streams. Available at: `https://www.paquesbiomaterials.nl/pha-from-agri-food-side-streams/` (accessed August 15, 2026).

Paques Biomaterials (2024). PHA from sewage sludge is a good business case. Available at: `https://www.paquesbiomaterials.nl/pha-from-sewage-sludge/` (accessed August 15, 2026).

Park, J. M., Kim, T. Y., & Lee, S. Y. (2011). Genome-scale reconstruction and in silico analysis of the Ralstonia eutropha H16 for polyhydroxyalkanoate synthesis, lithoautotrophic growth, and 2-methyl citric acid production. *BMC Systems Biology*, *5*(1), 101.

Patel, S. K. S., Singh, D., Pant, D., Gupta, R. K., Busi, S., Singh, R. V., & Lee, J.-K.

(2024). Polyhydroxyalkanoate Production by Methanotrophs: Recent Updates and Perspectives. *Polymers*, *16*(18), 2570.

Paul, S. C., van Zijl, G. P. A. G., & Šavija, B. (2020). Effect of Fibers on Durability of Concrete: A Practical Review. *Materials*, *13*(20), 4562.

Peña, C., Castillo, T., García, A., Millán, M., & Segura, D. (2014). Biotechnological strategies to improve production of microbial poly-(3-hydroxybutyrate): a review of recent research work. *Microbial Biotechnology*, *7*(4), 278–293.

Poladyan, A., Blbulyan, S., Sahakyan, M., Lenz, O., & Trchounian, A. (2019). Growth of the facultative chemolithoautotroph Ralstonia eutropha on organic waste materials: growth characteristics, redox regulation and hydrogenase activity. *Microbial Cell Factories*, *18*(1), 201.

Puente, J. A. S., Esposito, A., Chivrac, F., & Dargent, E. (2013). Effect of boron nitride as a nucleating agent on the crystallization of bacterial poly(3-hydroxybutyrate). *Journal of Applied Polymer Science*, *128*(5), 2586–2594.

Puppi, D., Pecorini, G., & Chiellini, F. (2019). Biomedical Processing of Polyhydroxyalkanoates. *Bioengineering*, *6*(4), 108.

Pérez-Camacho, I., Chavarría-Hernández, N., Del Rocío López-Cuellar, M., Guerrero-Barajas, C., & Ordaz, A. (2024). Microrespirometric Validation of a Two-stage Process for Polyhydroxyalkanoates Production from Peanut Oil and Propionate with Cupriavidus necator. *The Open Chemical Engineering Journal*, *18*(1), e18741231301420.

Radhakrishnan, N., Chellapandian, M., & Bright Singh, S. (2024). Engineering characteristics, techno-economic feasibility and life cycle assessment of bio-fiber based green engineered cementitious composites. *Journal of Building Engineering*, *96*, 110521.

Ramsay, J. A., Berger, E., Voyer, R., Chavarie, C., & Ramsay, B. A. (1994). Extraction

of poly-3-hydroxybutyrate using chlorinated solvents. *Biotechnology Techniques*, *8*(8), 589–594.

Randl, N., Steiner, T., Ofner, S., Baumgartner, E., & Mészöly, T. (2014). Development of UHPC mixtures from an ecological point of view. *Construction and Building Materials*, *67*, 373–378.

Righetti, M. C., Aliotta, L., Mallegni, N., Gazzano, M., Passaglia, E., Cinelli, P., & Lazzeri, A. (2019). Constrained Amorphous Interphase and Mechanical Properties of Poly(3-Hydroxybutyrate-co-3-Hydroxyvalerate). *Frontiers in Chemistry*, *7*.

RWDC Industries (2023). Lummus and RWDC industries sign MoU accelerating PHA production at scale. Available at: `https://www.rwdc-industries.com/lummus-and-rwdc-industries-sign-mou-accelerating-pha-production-at-scale` (accessed August 15, 2026).

Saab, R., Polychronopoulou, K., Anjum, D. H., Charisiou, N., Goula, M. A., Hinder, S. J., Baker, M. A., & Schiffer, A. (2022). Carbon Nanostructure/Zeolite Y Composites as Supports for Monometallic and Bimetallic Hydrocracking Catalysts. *Nanomaterials*, *12*(18), 3246.

Said, S. H. & Razak, H. A. (2015). The effect of synthetic polyethylene fiber on the strain hardening behavior of engineered cementitious composite (ECC). *Materials & Design*, *86*, 447–457.

Sanhueza, C., Acevedo, F., Rocha, S., Villegas, P., Seeger, M., & Navia, R. (2019). Polyhydroxyalkanoates as biomaterial for electrospun scaffolds. *International Journal of Biological Macromolecules*, *124*, 102–110.

Sanhueza, C., Diaz-Rodriguez, P., Villegas, P., González, , Seeger, M., Suárez-González, J., Concheiro, A., Alvarez-Lorenzo, C., & Acevedo, F. (2020). Influence of the carbon source on the properties of poly-(3)-hydroxybutyrate produced by Paraburkholderia xenovorans LB400 and its electrospun fibers. *International Journal of Biological Macromolecules*, *152*, 11–20.

Santos, A. J. d., Valentina, L. V. O. D., Schulz, A. A. H., & Duarte, M. A. T. (2017). From Obtaining to Degradation of PHB: Material Properties. Part I. *Ingeniería y Ciencia*, *13*(26), 269–298.

Sato, H., Murakami, R., Mori, K., Ando, Y., Takahashi, I., Noda, I., & Ozaki, Y. (2009). Specific crystal structure of poly(3-hydroxybutyrate) thin films studied by infrared reflection–absorption spectroscopy. *Vibrational Spectroscopy*, *51*(1), 132–135.

Scott, F., Yañez, L., Conejeros, R., Araya, B., & Vergara-Fernández, A. (2021). Two internal bottlenecks cause the overflow metabolism leading to poly(3-hydroxybutyrate) production in Azohydromonas lata DSM1123. *Journal of Environmental Chemical Engineering*, *9*(4), 105665.

Shahhosseini, S. (2004). Simulation and optimisation of PHB production in fed-batch culture of Ralstonia eutropha. *Process Biochemistry*, *39*(8), 963–969.

Shimadzu (2026). Nexis gc-2030 gas chromatograph. Available at: `https://www.ssi.shimadzu.com/products/gas-chromatography/gas-chromatograph/nexis-gc-2030/index.html` (accessed April 22, 2026).

Shimadzu Scientific Instruments (2026). What sort of sample concentration should I use for measurements by the KBr pellet method or diffuse reflection method? Accessed: 2026-07-23.

Shoji, D., He, Z., Zhang, D., & Li, V. C. (2022). The greening of engineered cementitious composites (ECC): A review. *Construction and Building Materials*, *327*, 126701.

Siddika, A., Mamun, M. A. A., Ferdous, W., Saha, A. K., & Alyousef, R. (2020). 3D-printed concrete: applications, performance, and challenges. *Journal of Sustainable Cement-Based Materials*, *9*(3), 127–164. _eprint: https://doi.org/10.1080/21650373.2019.1705199.

Silva, D. A., Betioli, A. M., Gleize, P. J. P., Roman, H. R., Gómez, L. A., & Ribeiro, J. L. D. (2005). Degradation of recycled PET fibers in Portland cement-based materials. *Cement and Concrete Research*, *35*(9), 1741–1746.

Singh, B., Ishwarya, G., Gupta, M., & Bhattacharyya, S. K. (2015). Geopolymer concrete: A review of some recent developments. *Construction and Building Materials*, *85*, 78–90.

Soltan, D. G., das Neves, P., Olvera, A., Savastano Junior, H., & Li, V. C. (2017). Introducing a curauá fiber reinforced cement-based composite with strain-hardening behavior. *Industrial Crops and Products*, *103*, 1–12.

Srubar, W. V., Wright, Z. C., Tsui, A., Michel, A. T., Billington, S. L., & Frank, C. W. (2012). Characterizing the effects of ambient aging on the mechanical and physical properties of two commercially available bacterial thermoplastics. *Polymer Degradation and Stability*, *97*(10), 1922–1929.

TA Instruments (2026). Sdt-q600 simultaneous tga/dsc. Available at: `https://www.artisantg.com/Scientific/74393-1/TA-Instruments-SDT-Q600-Simultaneous-TGA-DSC` (accessed April 22, 2026).

Tapadiya, A. & Vasanthan, N. (2017). Crystallization and alkaline hydrolysis of poly(3-hydroxybutyrate) films probed by thermal analysis and infrared spectroscopy. *International Journal of Biological Macromolecules*, *102*, 1130–1137.

TCLGroup (2026). Microcentrifuga refrigerada. Available at: `https://tienda.tclgroup.cl/product/microcentrifuga-refrigerada/` (accessed April 22, 2026).

Thanahiranya, P., Vacharanukrauh, T., Charoensuppanimit, P., Chuetor, S., Chanthanumataporn, M., & Assabumrungrat, S. (2025). Techno-economic and environmental assessment of glycerol valorization to polyhydroxybutyrate using chemical digestion methods. *Process Safety and Environmental Protection*, *195*, 106832.

Thommes, M., Kaneko, K., Neimark, A. V., Olivier, J. P., Rodriguez-Reinoso, F., Rouquerol, J., & Sing, K. S. W. (2015). Physisorption of gases, with special reference to the evaluation of surface area and pore size distribution (IUPAC Technical Report). *Pure and Applied Chemistry*, *87*(9-10), 1051–1069.

Tiwari, M., Mhatre, S., Vyas, T., Bapna, A., & Raghavan, G. (2023). A Validated

HPLC-RID Method for Quantification and Optimization of Total Sugars: Fructose, Glucose, Sucrose, and Lactose in Eggless Mayonnaise. *Separations*, *10*(3), 199.

Turco, R., Santagata, G., Corrado, I., Pezzella, C., & Di Serio, M. (2021). In vivo and Post-synthesis Strategies to Enhance the Properties of PHB-Based Materials: A Review. *Frontiers in Bioengineering and Biotechnology*, *8*, 619266.

United Nations Environment Programme & Global Alliance for Buildings and Construction (2025). Global status report for buildings and construction 2024/2025: Not just another brick in the wall. Technical report, United Nations Environment Programme, Nairobi, Kenya.

Vanheusden, C., Vanminsel, J., Reddy, N., Samyn, P., D'Haen, J., Peeters, R., Ethirajan, A., & Buntinx, M. (2023). Fabrication of poly(3-hydroxybutyrate-co-3-hydroxyhexanoate) Fibers Using Centrifugal Fiber Spinning: Structure, Properties and Application Potential. *Polymers*, *15*(5), 1181.

VaxaSoftware (2026). Densidad del agua líquida entre 0 °C y 100 °C. Available at: `https://www.ugr.es/~elenasb/teaching/densidadtemperatura_agua_tabla.pdf` (accessed April 30, 2026).

Volova, T., Shishatskaya, E., Sevastianov, V., Efremov, S., & Mogilnaya, O. (2003). Results of biomedical investigations of PHB and PHB/PHV fibers. *Biochemical Engineering Journal*, *16*(2), 125–133.

Volova, T. G., Zhila, N. O., Kalacheva, G. S., Brigham, C. J., & Sinskey, A. J. (2013). Effects of intracellular poly(3-hydroxybutyrate) reserves on physiological–biochemical properties and growth of *Ralstonia eutropha*. *Research in Microbiology*, *164*(2), 164–171.

Wang, F. & Lee, S. Y. (1997). Poly(3-Hydroxybutyrate) Production with High Productivity and High Polymer Content by a Fed-Batch Culture of Alcaligenes latus under Nitrogen Limitation. *Applied and Environmental Microbiology*, *63*(9), 3703–3706.

Wang, J., Fang, F., & Yu, H.-Q. (2007). Substrate consumption and biomass growth of

Ralstonia eutropha at various $S0/X0$ levels in batch cultures. *Bioresource Technology*, *98*(13), 2599–2604.

Wang, J., Liu, S., Huang, J., & Qu, Z. (2021). A review on polyhydroxyalkanoate production from agricultural waste Biomass: Development, Advances, circular Approach, and challenges. *Bioresource Technology*, *342*, 126008.

Wellzoom (2026). Wellzoom desktop filament extruder b. Available at: `http://wellzoomextruder.com/product/wellzoom-desktop-filament-extruder-b/` (accessed April 22, 2026).

Wong, L. S. (2022). Durability Performance of Geopolymer Concrete: A Review. *Polymers*, *14*(5), 868.

Xiao, B., Sun, X. F., & Sun, R. (2001). Chemical, structural, and thermal characterizations of alkali-soluble lignins and hemicelluloses, and cellulose from maize stems, rye straw, and rice straw. *Polymer Degradation and Stability*, *74*(2), 307–319.

Xu, J., Guo, B.-H., Yang, R., Wu, Q., Chen, G.-Q., & Zhang, Z.-M. (2002). In situ FTIR study on melting and crystallization of polyhydroxyalkanoates. *Polymer*, *43*(25), 6893–6899.

Xu, P., Wang, Q., Yu, M., Yang, W., Weng, Y., Dong, W., Chen, M., Wang, Y., & Ma, P. (2021). Enhanced crystallization and storage stability of mechanical properties of biosynthesized poly (3-hydroxybutyrate-*co*-3-hydroxyhexanate) induced by self-nucleation. *International Journal of Biological Macromolecules*, *184*, 797–803.

Yabuuchi, E., Kosako, Y., Yano, I., Hotta, H., & Nishiuchi, Y. (1995). Transfer of Two Burkholderia and An Alcaligenes Species to Ralstonia Gen. Nov.: Proposal of Ralstonia pickettii (Ralston, Palleroni and Doudoroff 1973) Comb. Nov., Ralstonia solanacearum (Smith 1896) Comb. Nov. and Ralstonia eutropha (Davis 1969) Comb. Nov. *Microbiology and Immunology*, *39*(11), 897–904.

Yamane, H., Terao, K., Hiki, S., & Kimura, Y. (2001). Mechanical properties and

higher order structure of bacterial homo poly(3-hydroxybutyrate) melt spun fibers. *Polymer*, *42*(7), 3241–3248.

Yoo, D.-Y. & Yoon, Y.-S. (2016). A Review on Structural Behavior, Design, and Application of Ultra-High-Performance Fiber-Reinforced Concrete. *International Journal of Concrete Structures and Materials*, *10*(2), 125–142.

Yousuf, R. G. & Winterburn, J. B. (2016). Date seed characterisation, substrate extraction and process modelling for the production of polyhydroxybutyrate by *Cupriavidus necator*. *Bioresource Technology*, *222*, 242–251.

Yu, J., Plackett, D., & Chen, L. X. L. (2005). Kinetics and mechanism of the monomeric products from abiotic hydrolysis of poly[(*R*)-3-hydroxybutyrate] under acidic and alkaline conditions. *Polymer Degradation and Stability*, *89*(2), 289–299.

Zhang, D., Yu, J., Wu, H., Jaworska, B., Ellis, B. R., & Li, V. C. (2020). Discontinuous micro-fibers as intrinsic reinforcement for ductile Engineered Cementitious Composites (ECC). *Composites Part B: Engineering*, *184*, 107741.

Zhang, J., Wang, J., Dong, S., Yu, X., & Han, B. (2019). A review of the current progress and application of 3D printed concrete. *Composites Part A: Applied Science and Manufacturing*, *125*, 105533.

Zhang, L., Jiang, Z., Tsui, T.-H., Loh, K.-C., Dai, Y., & Tong, Y. W. (2022). A Review on Enhancing Cupriavidus necator Fermentation for Poly(3-hydroxybutyrate) (PHB) Production From Low-Cost Carbon Sources. *Frontiers in Bioengineering and Biotechnology*, *10*.

Zhang, X., Lin, Y., Wu, Q., Wang, Y., & Chen, G.-Q. (2020). Synthetic Biology and Genome-Editing Tools for Improving PHA Metabolic Engineering. *Trends in Biotechnology*, *38*(7), 689–700.

Zhu, Y., Yang, Y., & Yao, Y. (2012). Use of slag to improve mechanical properties of engineered cementitious composites (ECCs) with high volumes of fly ash. *Construction and Building Materials*, *36*, 1076–1081.

Zohaib, M., Afzal, T., Zahir Iqbal, M., Almutairi, B. S., Ali Raza, M., Maqsood, M. F., Raza, M. A., Riaz, S., Naseem, S., & Iqbal, M. J. (2023). Role of time-dependent foreign molecules bonding in the degradation mechanism of polymer field-effect transistors in ambient conditions. *Royal Society Open Science*, *10*(6), 221272.

Şahmaran, M. & Li, V. C. (2009). Durability properties of micro-cracked ECC containing high volumes fly ash. *Cement and Concrete Research*, *39*(11), 1033–1043.

Appendix A

Fermentation Details

This section provides supplementary methodological information related to the fermentation procedures discussed in Chapter 4.

A.1 *A. lata trace*

The composition of the *A. lata* trace is shown in Table A.1:

Table A.1: Composition of the *A. lata* trace element solution used in this work, based on (Wang & Lee, 1997).

Component	**Concentration (g/L)**
$FeSO_4 \cdot 7H_2O$	20.00
H_3BO_3	0.30
$CoCl_2 \cdot 6H_2O$	0.20
$ZnSO_4 \cdot 7H_2O$	0.03
$MnCl_2 \cdot 4H_2O$	0.03
$(NH_4)_6Mo_7O_{24} \cdot 4H_2O$	0.03
$NiSO_4 \cdot 7H_2O$	0.03
$CuSO_4 \cdot 5H_2O$	0.01

A.2 Mineral Medium

The composition of the mineral medium used is shown in Table A.2. The same medium was used for flask cultures, with the addition of 30 μL of gentamicin.

Table A.2: Mineral medium used in all fermentation iterations.

Solution	**Component**	**Concentration (g/L)**	**Volume added**
Solution A	$(NH_4)_2SO_4$	1	600 mL
Solution B	$Na_2HPO_4{\cdot}7H_2O$	6.7	400 mL
	KH_2PO_4	1.5	
	A. lata trace solution	-	1 mL
Solution C	$MgSO_4{\cdot}7H_2O$	200	1 mL

A.3 Culture Medium

The cultures mediums used for the fermentation process are shown in Tables A.3 and A.4:

Table A.3: Initial reactor medium.

Solution	**Component**	**Concentration (g/L)**	**Volume added**
Solution A	$(NH_4)_2SO_4$	2	600 mL
	Antifoam agent	-	500 μL
Solution B	$Na_2HPO_4{\cdot}7H_2O$	3.35	400 mL
	KH_2PO_4	0.75	
Solution C_1	Fructose	1500	30 mL
Solution C_2	Fructose	1500	30 mL
Solution D	$Na_2HPO_4{\cdot}7H_2O$	2	10 mL
	KH_2PO_4	0.4	
	A. lata trace solution	-	2 mL
Solution E	$(NH_4)_2SO_4$	10	20 mL

Table A.4: Final reactor medium.

Solution	**Component**	**Concentration (g/L)**	**Volume added**
Solution A	$(NH_4)_2SO_4$	1.5	100 mL
Solution B	$Na_2HPO_4 \cdot 7H_2O$	3.35	100 mL
	KH_2PO_4	0.75	
Solution C	$Na_2HPO_4 \cdot 7H_2O$	2	20 mL
	KH_2PO_4	0.4	
	A. lata trace solution	-	2 mL
Solution D	Fructose	500	130 mL
Solution E	$(NH_4)_2SO_4$	6	30 mL
Solution F	Gentamicin	-	300 μL
Solution G	Antifoam agent	-	80 mL + 20 mL pure
Solution H	Water	-	600 mL

Appendix B

PHB Characterization

The following section presents all the supplementary material employed for the characterization of PHB in its various formats, including native polymer, processed fibers, and treated specimens. This information includes detailed tables, calculation methods, reference data, and supporting documentation referenced throughout the main chapters of this work.

B.1 Density Calculation

The density of each specimen was calculated from the volume of water displaced during the volumetric-flask measurement. Since the total volume of the flask remained constant before and after introducing the specimen, the displaced water mass was obtained from the difference between the initial and final mass balances.

The density of the specimen was calculated according to Equation B.1.

$$\rho_s = \frac{m_s \, \rho_w}{m_s + m_{fw} - m_{fws}} \tag{B.1}$$

where ρ_s is the density of the specimen, m_s is the specimen mass, ρ_w is the density of water at the measured temperature, m_{fw} is the mass of the flask filled with water up

to the calibration mark, and m_{fws} is the final mass of the flask, water, and specimen after refilling to the same calibration mark.

The term $(m_s+m_{fw}-m_{fws})$ corresponds to the mass of water displaced by the specimen. Dividing this displaced water mass by ρ_w gives the specimen volume, which is then used to calculate ρ_s.

B.2 Water Density

Table B.1 shows the standard density values of water in the range of 21-25°C, according to ASTM D792 (ASTM International, 2026a). These values were used to apply correction factors when the water temperature differed from the standard reference of 23°C.

For temperatures outside this range, additional tabulated density values were obtained from the University of Granada database (VaxaSoftware, 2026), covering a broader interval from 0 to 100°C. When the measured temperature included decimal values and fell outside the ASTM range, the density was approximated using the nearest integer temperature available in the tables.

Table B.1: Standard density of water in the range of 21-25 °C, according to ASTM D792 (ASTM International, 2026a).

x (°C)	**21**	**22**	**23**	**24**	**25**
0.0	997.9948	997.7730	997.5412	997.2994	997.0480
0.1	997.9731	997.7503	997.5174	997.2747	997.0223
0.2	997.9513	997.7275	997.4936	997.2499	996.9965
0.3	997.9294	997.7045	997.4697	997.2250	996.9707
0.4	997.9073	997.6815	997.4456	997.2000	996.9447
0.5	997.8852	997.6584	997.4215	997.1749	996.9186
0.6	997.8630	997.6351	997.3973	997.1497	996.8925
0.7	997.8406	997.6118	997.3730	997.1244	996.8663
0.8	997.8182	997.5883	997.3485	997.0990	996.8399
0.9	997.7957	997.5648	997.3240	997.0735	996.8135

Values are expressed in kg/m^3. For temperatures outside the ASTM range, density values were obtained from extended tabulated data reported by the University of Granada (VaxaSoftware, 2026).

B.3 Molecular-Weight Calculations

The weight-average molecular weight (M_w) and number-average molecular weight (M_n) were calculated from the chromatographic signal according to Equations B.2 and B.3, respectively.

$$M_w = \frac{\sum h_i M_i}{\sum h_i} \tag{B.2}$$

$$M_n = \frac{\sum h_i}{\sum h_i / M_i} \tag{B.3}$$

The dispersity of the molecular-weight distribution was calculated according to Equation B.4.

$$\text{Dispersity} = \frac{M_w}{M_n} \tag{B.4}$$

In these expressions, h_i represents the signal intensity and M_i is the molecular weight assigned to each point of the chromatogram. Since calibration was performed using polystyrene standards, the resulting M_w and M_n values correspond to apparent polystyrene-equivalent molecular weights. They should consequently be interpreted as relative values obtained under the selected chromatographic conditions rather than as absolute molecular weights of PHB.

B.4 Compute of the Mobile and Rigid Amorphous Fractions from DSC

As discussed in Section 5.1.5, PHB follows a three-phase model that satisfies the following relationship:

$$X_{\mathrm{c}} + X_{\mathrm{MAF}} + X_{\mathrm{RAF}} = 1, \tag{B.5}$$

The calculation was performed using PHB as the reference material. The reference values adopted were

$$\Delta H_{\mathrm{m}}^{100\%} = 146 \ \mathrm{J\,g^{-1}}, \tag{B.6}$$

and

$$\Delta C_{\mathrm{p}}^{100\%} = 0.49 \ \mathrm{J\,g^{-1}\,K^{-1}}. \tag{B.7}$$

The latter corresponds to the heat-capacity increment reported for fully amorphous PHB (Czerniecka-Kubicka et al., 2017). Therefore, when this procedure is applied to copolymers, blends, filled materials, or commercial PHA formulations, the resulting fractions are considered apparent values based on the PHB-reference assumption.

B.5 Calculation procedure

The apparent crystalline fraction was obtained from

$$X_{\mathrm{c,app}} = \frac{\sum_i \Delta H_{\mathrm{m},i} - \sum_j \Delta H_{\mathrm{c},j}}{\Delta H_{\mathrm{m}}^{100\%}}. \tag{B.8}$$

The crystallization enthalpies retain the negative sign exported by the DSC software. Consequently, the term $-\Delta H_{\mathrm{c}}$ adds the magnitude of the crystallization event to the numerator. This convention was maintained throughout the calculations.

The MAF was calculated using the heat-capacity increment associated with the mobile glass transition:

$$X_{\mathrm{MAF,app}} = \frac{\Delta C_{\mathrm{p,mob}}}{\Delta C_{\mathrm{p}}^{100\%}} = \frac{\Delta C_{\mathrm{p,mob}}}{0.49}. \tag{B.9}$$

When more than one glass transition was detected, $\Delta C_{\mathrm{p,mob}}$ corresponded only to the transition assigned to the mobile amorphous phase. The heat-capacity increment of the higher-temperature constrained transition was not added to this value.

Finally, the apparent RAF was obtained by complementarity:

$$X_{\mathrm{RAF,app}} = 1 - X_{\mathrm{c,app}} - X_{\mathrm{MAF,app}}. \tag{B.10}$$

Appendix C

Detailed Results of the Fed-Batch Fermentation Campaign

This appendix provides a detailed reactor-by-reactor summary of the fed-batch fermentation campaign carried out for PHB production with *Cupriavidus necator* H16. The objective of this supplementary material is to document the main outcomes, operational problems, and corrective actions associated with each run, thereby providing additional context for the results discussed in Chapter 5. The reactor campaign is presented in sequential stages, from the initial exploratory trials to the final runs in which the target PHB production was achieved under stable operating conditions.

Table C.1: Summary of reactor runs R1-R4 performed during the fed-batch fermentation campaign for PHB production with *Cupriavidus necator* H16.

Reactor	Main outcome	Problem or observation	Consequence / action taken
R1	Introductory reactor run with low biomass growth and low PHB production.	This run served as an initial approach to reactor operation and PHB production. Biomass formation remained limited, and only a low amount of PHB was detected by HPLC.	Confirmed that PHB production under reactor conditions was feasible, but showed that the process still required substantial optimization.
R2	High PHB accumulation with significant culture loss.	PHB accumulation reached approximately 73%, but severe foaming occurred due to high agitation and insufficient antifoam addition. This caused substantial loss of culture.	Demonstrated that high intracellular PHB contents could be achieved, while identifying foam control as a critical operational variable.
R3	High PHB accumulation with significant culture loss.	PHB accumulation reached approximately 83%, but, similarly to R2, severe foaming resulted in important culture losses. The accumulation was quantified by HPLC.	Confirmed the reproducibility of high PHB accumulation under these conditions, but also reinforced the need to improve foam control before continuing process optimization.
R4	Reactor not started.	The inoculum developed in shake flask lost viability before reactor inoculation.	No experimental results were obtained.

Table C.2: Summary of reactor runs R5-R6 performed during the fed-batch fermentation campaign for PHB production with *Cupriavidus necator* H16.

Reactor	Main outcome	Problem or observation	Consequence / action taken
R5*	Excessive biomass growth without successful PHB accumulation.	The culture reached OD values of approximately 50-60 during the growth phase. Under these conditions, oxygen consumption became much higher than expected, leading to depletion of the oxygen supply tank. As a result, the culture died before entering the PHB accumulation stage.	This run revealed that oxygen availability had become a critical problem under the implemented operating conditions, although its underlying cause had not yet been identified at this stage.
R6*	Excessive biomass growth without successful PHB accumulation.	Similarly to R5, the culture exhibited excessive biomass growth and did not reach the PHB accumulation stage. In this run, it became evident that the oxygen transfer capacity of the system was insufficient.	This run allowed the oxygen transfer limitation to be identified more clearly as a critical factor affecting reactor performance. It also contributed to the later recognition that the nitrogen dosage used in the design had promoted excessive biomass growth.

*The agitation system supports speeds of up to 1200 rpm, and the bioreactor is compatible with 1.5 L, 3 L, and 6 L vessels. For this research, the 1.5 L configuration, with a working volume of 1 L, was used. According to the technical analysis presented in (Maschke et al., 2019), and following the selected operating conditions, the volumetric mass transfer coefficient ($k_L a$) for the 1.5 L vessel ranges between 150 and 220 h^{-1}.

Table C.3: Summary of reactor runs R7-R8 performed during the fed-batch fermentation campaign for PHB production with *Cupriavidus necator* H16.

Reactor	Main outcome	Problem or observation	Consequence / action taken
R7	Contaminated run with incomplete growth.	An unknown contaminant consumed fructose faster than RE H16, leading to premature substrate depletion. As a consequence, the culture stagnated at approximately OD 30 and the expected PHB production could not be achieved.	This run failed to meet the experimental objective and prompted a review of chemicals, equipment, and handling procedures used during fermentation.
R8	Contaminated run with incomplete growth.	A contamination event similar to that observed in R7 occurred again. Premature fructose depletion was observed, and the culture stagnated at approximately OD 30 before reaching the intended production stage.	Reinforced the need for stronger contamination control measures. From reactor R9 onward, gentamicin was incorporated into the cultivation protocol to reduce the risk of recurrent contamination.

Table C.4: Summary of reactor runs R9-R10 performed during the fed-batch fermentation campaign for PHB production with *Cupriavidus necator* H16.

Reactor	Main outcome	Problem or observation	Consequence / action taken
R9	First stable PHB-producing run after contamination control.	Gentamicin was incorporated into the cultivation protocol from this run onward. The culture reached approximately OD 65 and achieved a PHB accumulation of 63.48% by GC, corresponding to 10.18 g L^{-1} PHB. Although PHB production was successfully restored, the obtained concentration remained below the design target of 15 g L^{-1}.	Demonstrated that contamination control had been recovered and that PHB production was again feasible under reactor operation.
R10	Stable PHB-producing run, still below target.	Using the same strain source as in R9, the culture reached approximately OD 76 and achieved a PHB accumulation of 63.43% by GC, corresponding to 9.63 g L^{-1} PHB. Although the culture remained stable, the PHB concentration was again lower than expected.	This run provided the basis for revising the ammonium sulfate yield by inverse calculation, suggesting a value close to 1.2 g g^{-1} instead of the initially assumed 1.5 g g^{-1}. This result motivated the kinetic study performed afterward.

Table C.5: Summary of reactor runs R11-R13 performed during the fed-batch fermentation campaign for PHB production with *Cupriavidus necator* H16.

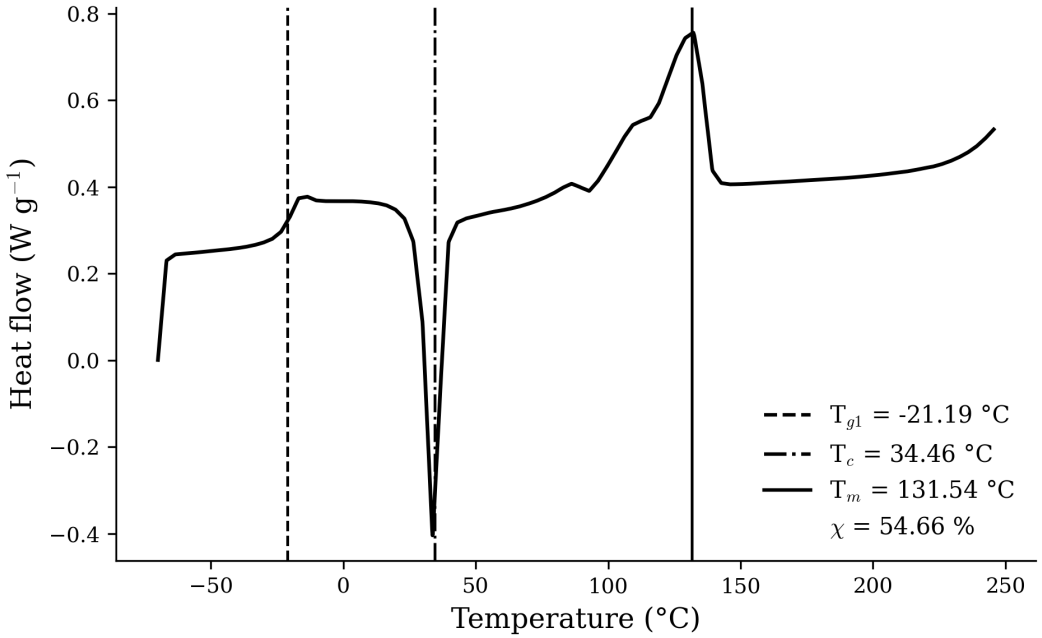
Reactor	Main outcome	Problem or observation	Consequence / action taken
R11	Stable and near-target PHB-producing run.	After updating the ammonium sulfate design basis, the culture reached approximately OD 85 and achieved a PHB accumulation of 73.31% by GC, corresponding to 14.18 g L^{-1} PHB.	Confirmed that the revised nitrogen design substantially improved the fermentation outcome and brought the process close to the target PHB concentration.
R12	Stable target-achieving PHB-producing run.	With the corrected design basis, the culture reached approximately OD 87 and achieved a PHB accumulation of 66.91% by GC, corresponding to 15.26 g L^{-1} PHB.	Confirmed that the process was capable of reaching the target PHB concentration of 15 g L^{-1}.
R13	Stable target-exceeding PHB-producing run.	Under the same revised strategy, the culture reached approximately OD 90 and achieved a PHB accumulation of 71.09% by GC, corresponding to 17.39 g L^{-1} PHB.	Confirmed the reproducibility and robustness of the final fermentation protocol.

Appendix D

DSC Mean Thermograms

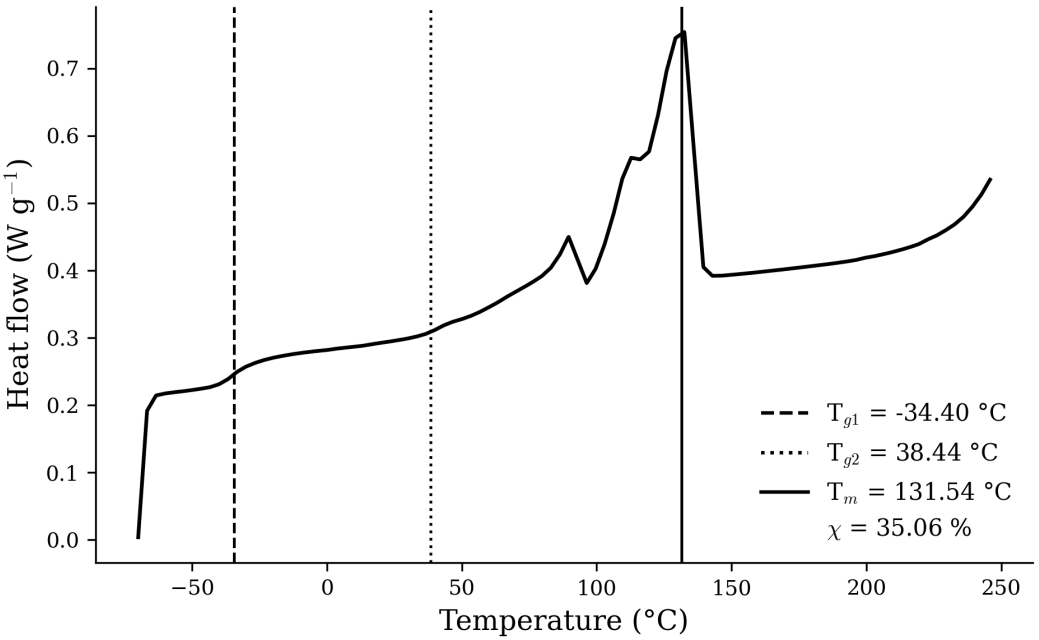
D.1 Differential Scanning Calorimetry

PHAC fiber

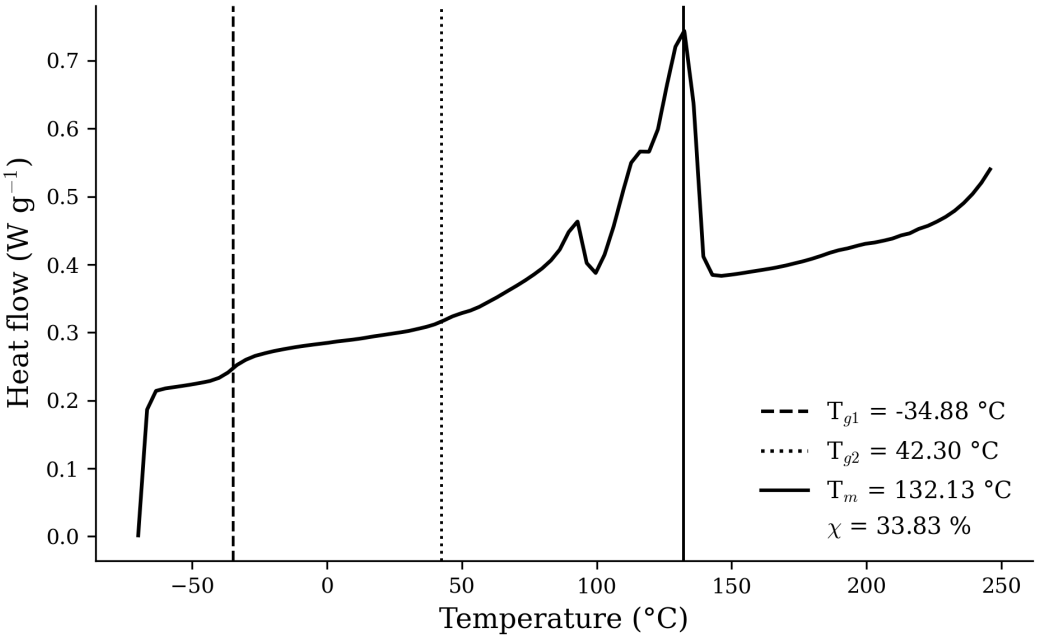


(a) Day 0.

Figure D.1: Individual average DSC thermograms of the PHAC fiber at different aging times.

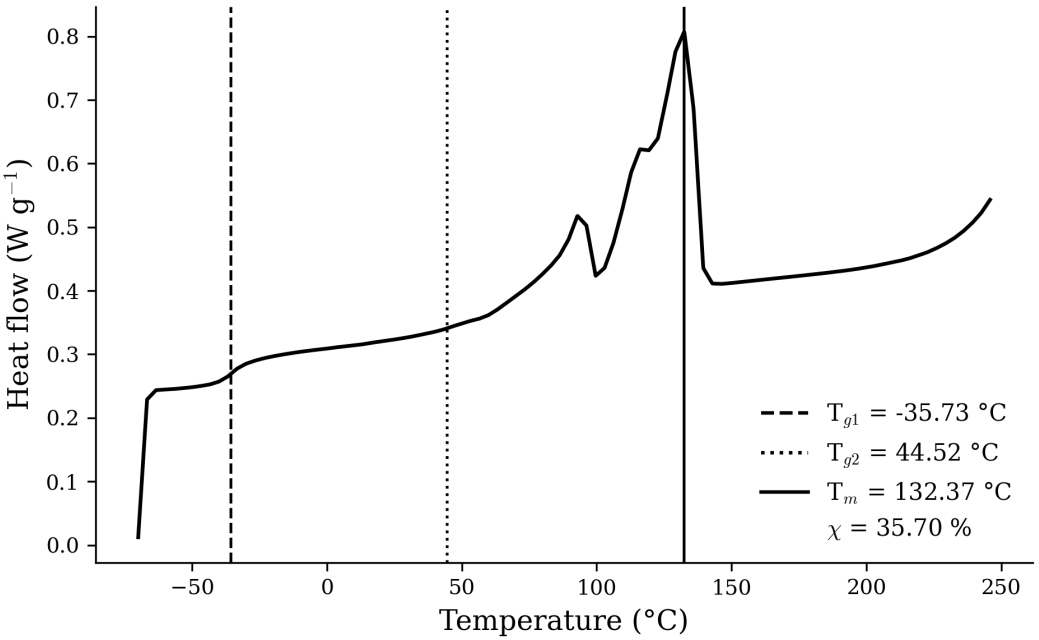


(b) 7 days aged.



(c) 28 days aged.

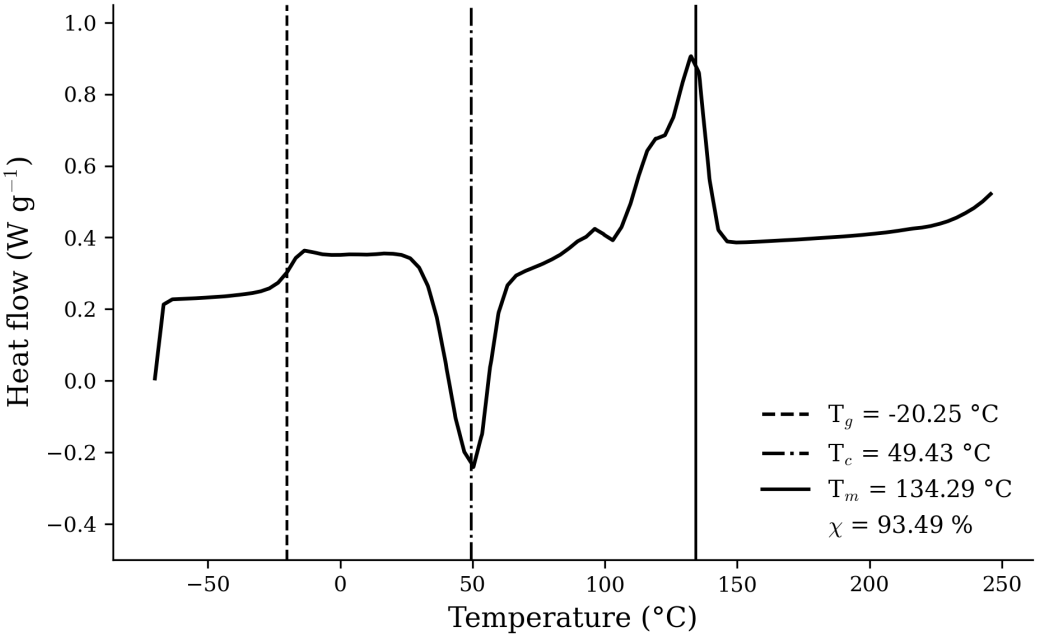
Figure D.1: Individual average DSC thermograms of the PHAC fiber at different aging times.



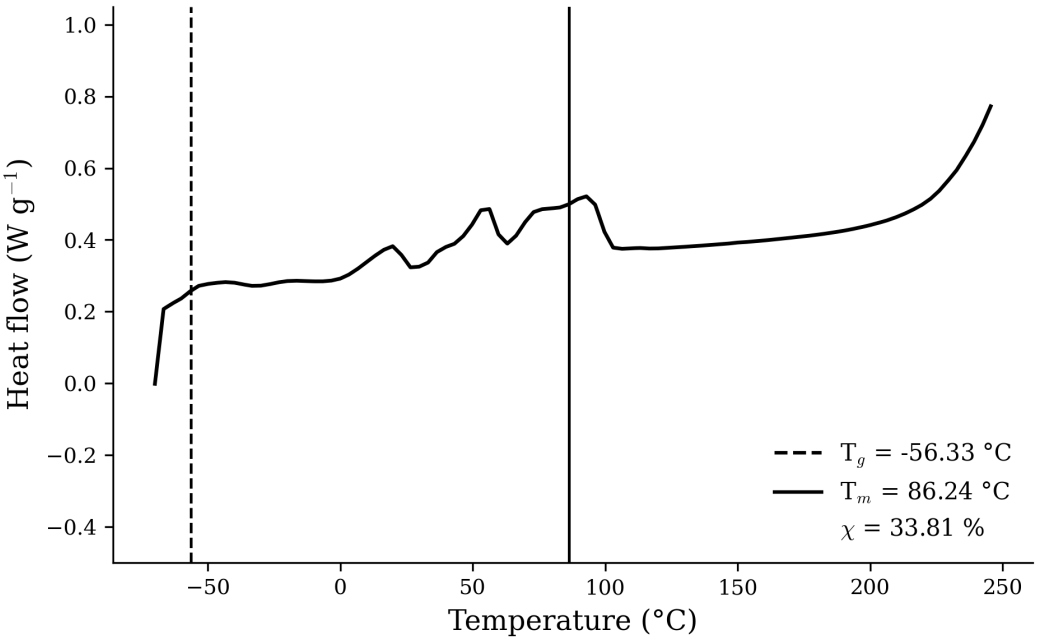
(d) 100 days aged.

Figure D.1: Individual average DSC thermograms of the PHAC fiber at different aging times.

Native film

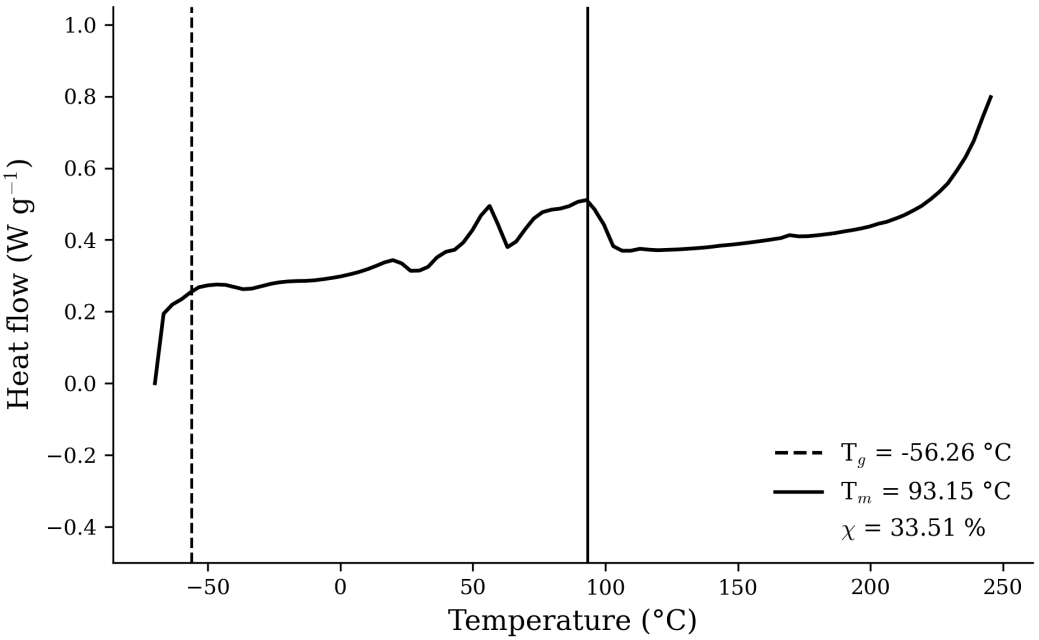


(e) Day 0.



(f) 7 days aged.

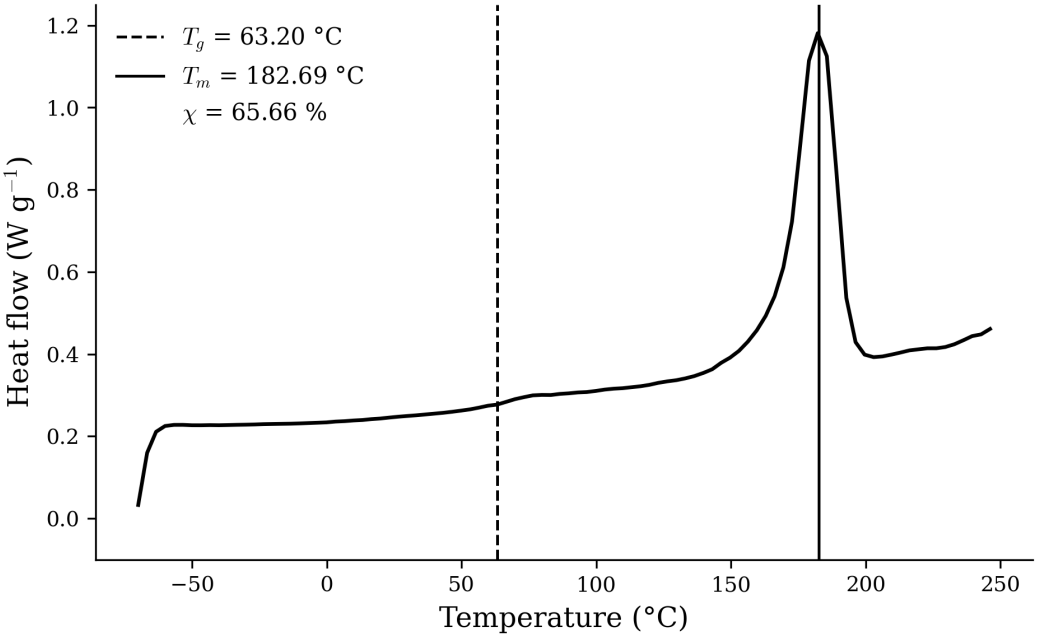
Figure D.2: Individual average DSC thermograms of the locally produced PHB recovered as native film at different aging times.



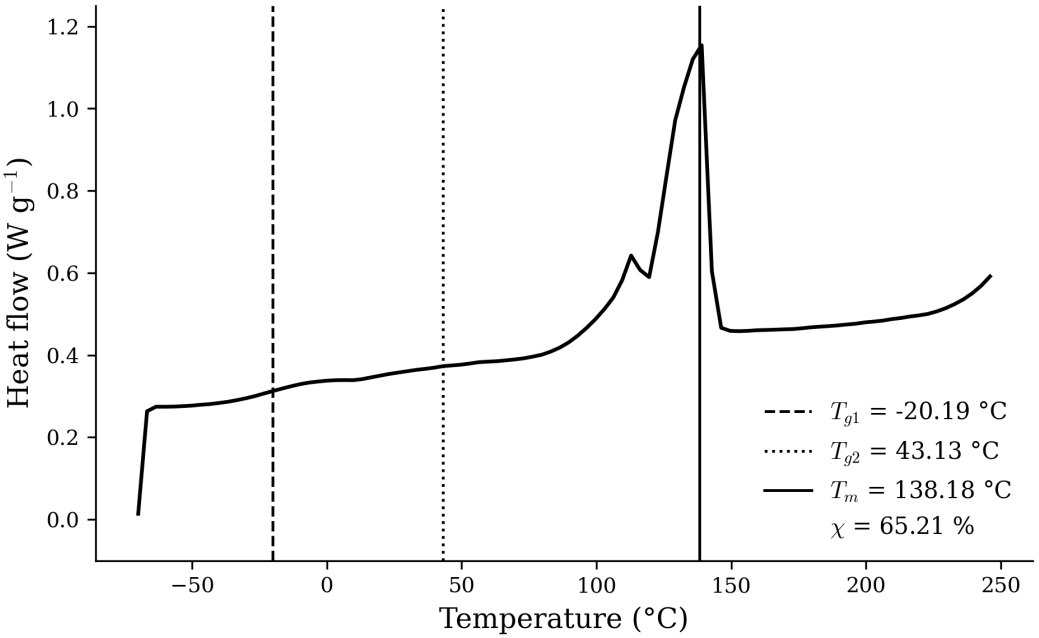
(c) 28 days aged.

Figure D.2: Individual average DSC thermograms of the locally produced PHB recovered as native film.

Commercial PHB pellet



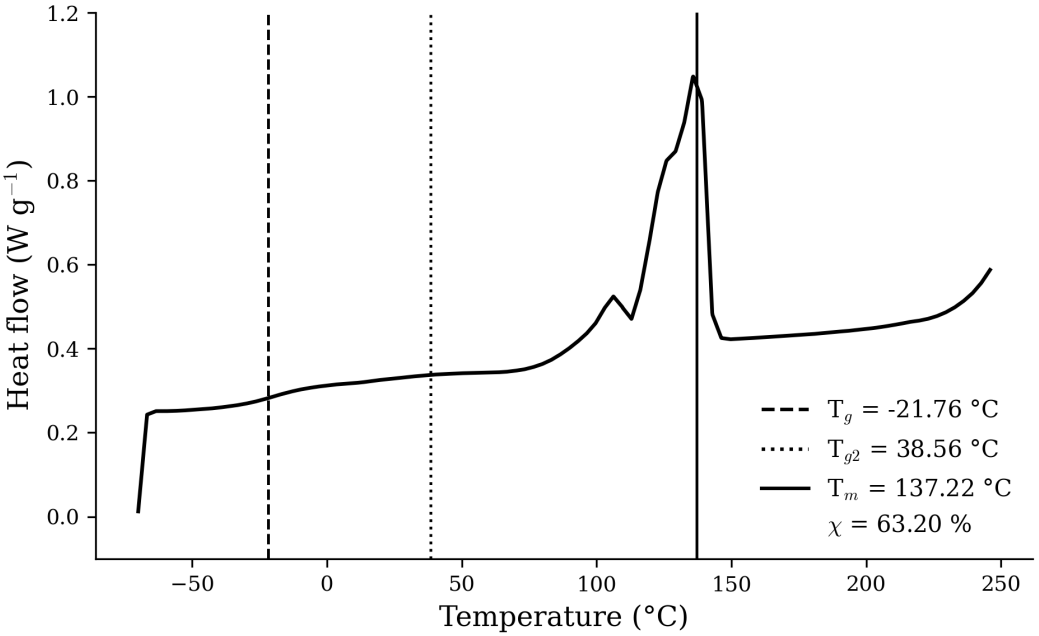
(a) First heating.



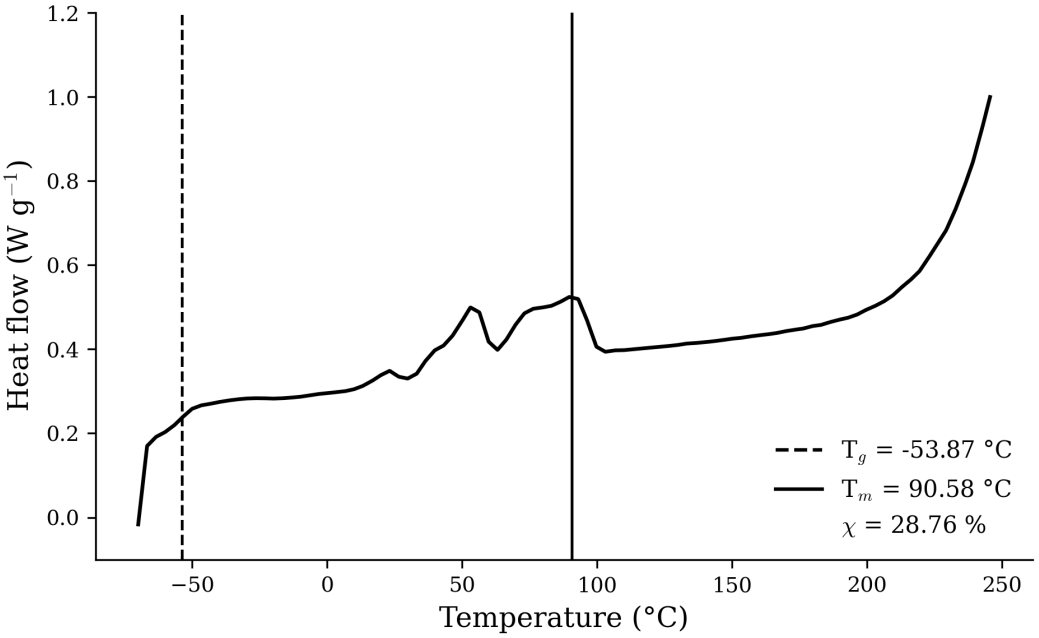
(b) Second heating.

Figure D.3: Individual DSC thermograms of the commercial PHB pellet during the first and second heating cycles.

PHB fiber

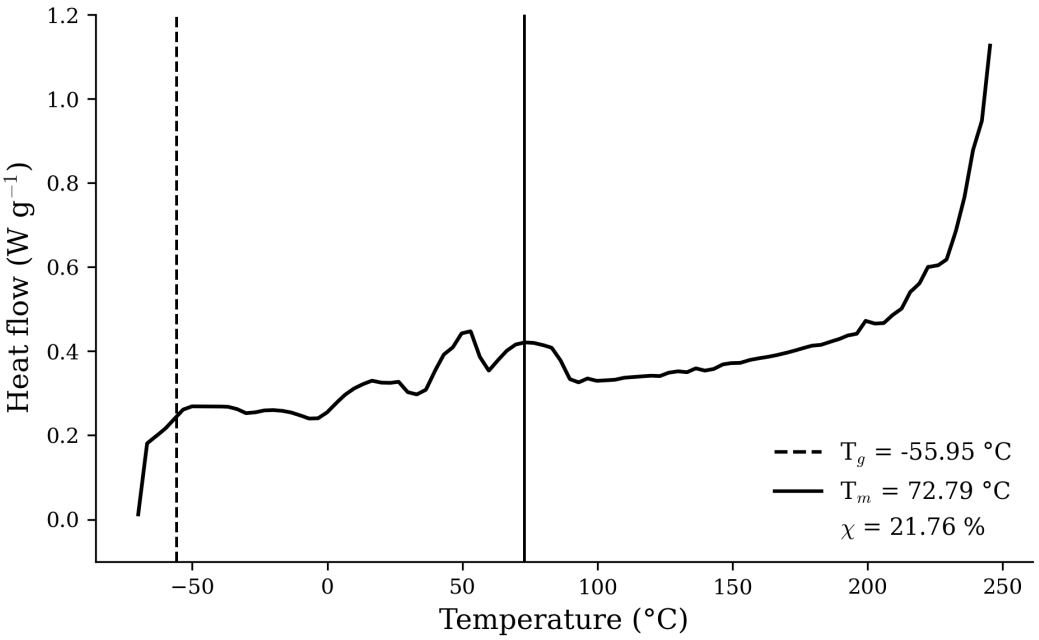


(a) Day 0.



(b) 7 days aged.

Figure D.4: Individual average DSC thermograms of the PHB fiber at different aging times.



(c) 28 days aged.

Figure D.4: Individual average DSC thermograms of the PHB fiber at different aging times.